Electric Thruster Modeling and its Influence on Spacecraft Charging in Varied Plasma Environments

Tejaswi Laxman Shinde

A thesis submitted in fulfilment of the requirements for the degree of Doctor of Philosophy

School of Physics
Faculty of Science
The University of Sydney

June, 2024

Dedicated to my lovely Mother

Thank you for being the reason I fight for my dreams.

Statement of originality

I, Tejaswi Shinde, declare that this thesis titled, "Electric Thruster Modeling and its Influence on Spacecraft Charging in Varied Plasma Environments" and the work presented in it is my own. This thesis has not been submitted for any degree or other purpose. The intellectual content of this thesis is the product of my own work, and all the assistance received in preparing this thesis and the sources are acknowledged.

Tejaswi L. Shinde

Authorship attribution statement

I am primarily responsible for the work conducted in Chapters 2 through 5. Chapter 2 is intended for submission to an AGU journal, while Chapter 3 was published in the conference proceedings of the AIAA Conference 2024. Currently, Chapter 4 is undergoing peer review and was presented at the Australian Space Research Conference 2023. Chapter 5 is scheduled for submission at an upcoming conference. The articles presented in the Appendix are peer-reviewed, published in conference proceedings, and are available online. Specifically, I set up the simulations, ran them, visualized the data, analyzed the results, developed interpretations and figures, and authored reports and conference papers. The contributions of the co-authors were as follows. Cairns: advice on data interpretation, helping to refine the analyses, enhancing the clarity of the findings, and specific comments on writing. Held: Provided general supervision, participated in discussions about the results, offered specific feedback on writing, and guided the project throughout its development. Deprez: SPIS Software technical support, addressed errors that occurred in the software, and assisted in resolving issues efficiently. I am grateful for their combined support and mentorship, which significantly enriched the quality and relevance of this work.

Publications:

- Chapter 2 (Improved results of Appendix A and B) : **Hall Thruster Plume Effects on Spacecraft Charging from 0.067 AU to 1 AU** Tejaswi L. Shinde, Iver H. Cairns, Jason M. Held and Gregory Deprez. Under Review : **Link**
- Chapter 3: **A Comparative Study of Spacecraft Charging Effects with and Without Thrusters from 0.044 AU to 1 AU** Tejaswi L. Shinde, Iver H. Cairns, Jason M. Held and Gregory Deprez. Published at AIAA SciTech 2024 Forum (p. 1141), **Link**
- Chapter 4: **The SPT-100 Hall Thruster and RIT-2X Thruster - Spacecraft Interactions in the Jovian Magnetosphere** Published at (Australian Space Research Conference 2023, Hobart) Tejaswi L. Shinde, Jason M. Held, Iver H. Cairns. **Link**
- Appendix A : **Charge-Exchange Plasma Effects of the SPT-100 Hall Thruster at Heliocentric Distances from 0.044 AU to 1 AU** Tejaswi L. Shinde, Iver H. Cairns , Jason M. Held. Published in AIAA SciTech 2023 Forum (p. 1141), DOI : **Link**

- Appendix B: **Simulation Study of Hall Thruster and their Effects on the Spacecraft at 1 AU and 0.093 AU** Tejaswi L. Shinde, Jason M. Held and Iver H. Cairns. Published in International Electric Propulsion Conference Massachusetts Institute of Technology, Cambridge, MA USA June 19-23, 2022 **Link**

Tejaswi L. Shinde

As the supervisors of the candidature on which this thesis is based, we confirm that the above authorship attribution statements are correct and represent an accurate summary of the student's contribution.

Iver H.Cairns
Primary Supervisor

Jason M.Held
Industrial Supervisor

"The difference between people who make their dreams come true and those who don't is just two things: the courage to start and the discipline to keep going." - Mel Robbins

Acknowledgements

Firstly, I extend my heartfelt gratitude to Prof. Iver H. Cairns and Dr. Jason M. Held for selecting me as a Ph.D. candidate. Their belief in my potential provided an invaluable opportunity to pursue my academic aspirations. I am immensely grateful for their guidance and endless encouragement, which supported my confidence during challenging times.

Secondly, I extend sincere thanks to the Indian government for awarding me a four-year tuition fee scholarship, without which my PhD journey would have been unattainable.

The path toward my Ph.D. was filled with challenges, from securing the scholarship to navigating the obstacles posed by the COVID-19 pandemic. Despite adversity, the unwavering support and encouragement of my supervisors and peers sustained me. To all those who offered assistance or words of encouragement, I am very grateful.

I deeply appreciate the support of my parents and my brother, who stood by me during challenging times and played a crucial role in helping me achieve my goals. To my late grandfather, whose constant motivation inspired me through hard times, I wish he was here to witness this moment. Thank you to my family for being the incredible support that gave me wings to fly so high. To my partner, Om, your unwavering understanding and support were invaluable throughout this journey.

Special thanks to Gregory Deprez for his assistance and technical support with the SPIS software, which significantly contributed to the success of my research.

I would also like to acknowledge the Australian Research Council-CUAVA and Prof. Iver Cairns from the School of Physics for funding this research project. Finally, I am very grateful to everyone who supported me on this journey. Your contributions have not gone unnoticed, and your kindness and generosity truly humble me.

....

Oh wait, I almost forgot! Lastly, but certainly not least, I want to thank... myself! Yes, a big shoutout to me for believing in myself, for all the hard work, for never quitting, and for never taking a day off. Cheers to me for making it happen!

Thank you !

Abstract

As spacecraft travel through space, they encounter various charged particles, including ambient ions, electrons, photoelectrons, and secondary electrons. These particles, collected and emitted by the spacecraft, cause it to accumulate a positive or negative voltage to maintain current equilibrium. However, excessive charging can lead to hazardous surface charging from electrons and ions with energies below 10-100 keV, and deep dielectric charging from electrons with energies above 100 keV, resulting in discharges that pose significant operational challenges. Another source of charging occurs during electric thruster operation, where Charge Exchange (CEX) ions and thruster electrons interact with the spacecraft surface and solar panels, raising scientific and operational concerns. Additionally, the findings apply to electric propulsion missions in interplanetary exploration missions that utilize Hall-effect or ion thrusters. Thus, the thesis aims to investigate the effects of electric thruster-induced charging on spacecraft potential under varying ambient plasma and solar photon conditions, comparing scenarios with and without thruster operation. The main research question is whether the spacecraft's negative charging induced by electric thrusters varies with changing ambient plasma and solar-photon flux conditions and whether ambient plasma particles and solar photons amplify or alleviate negative charging.

Chapter 1 provides an introduction and literature review, covering the solar wind's impact on spacecraft charging and its interaction with the electric thruster plume. It also discusses plasma simulation techniques and operational guidance for using the Spacecraft Plasma Interaction Software (SPIS). Chapter 2 examines the effects of ambient plasma and electric thruster-induced charging on spacecraft potential, showing stable potential despite variations when the thruster is active. Chapter 3 analyzes the impact of varying densities of CEX ions and thruster electrons, with the RIT-2X thruster achieving a lower negative potential than the SPT-100 Hall thruster. Higher densities of CEX ions and thruster electrons lead to more positive spacecraft potential. Chapter 4 reveals that the electric thruster backflow plume mitigates negative charging in solar wind conditions and the Jovian magnetosphere. Chapter 5 explores the impact on solar panels, showing the Sunward-facing side becoming more positive compared to the conductive-coated backside and spacecraft surface. In summary, this thesis provides a deep understanding of spacecraft charging with and without an electric thruster in diverse plasma environments, crucial for the preliminary design phase to ensure the safety of sensitive instruments and satellite health.

Contents

Contents **xiii**

List of Figures **xvii**

List of Tables **xxiv**

1 Introduction **2**

1.1 Solar Physics 6
1.1.1 Brief history 6
1.1.2 The Solar Structure 8
1.1.2.1 Sun's Interior 8
1.1.2.2 Sun's Atmosphere 8
1.1.3 Corona 10
1.1.3.1 Coronal Holes 11
1.1.4 Solar Wind 12
1.1.4.1 Brief History of the Solar Wind 13
1.1.4.2 Isothermal Parker Solution 14
1.1.4.3 Radial Dependencies 17
1.2 Jovian Magnetosphere 18
1.3 Spacecraft- Solar Wind Interaction 21
1.3.1 Brief History of Spacecraft Charging 21
1.3.2 Spacecraft Charging Basic Concepts 22
1.3.3 Sources of Spacecraft Charging 24
1.3.3.1 Debye Length and Sheath Formation 25
1.3.3.2 Potential Barriers 26
1.4 Electric Propulsion Systems 27
1.4.1 Types of Electric Propulsion Systems 28
1.4.1.1 Gridded Ion thruster (GIT) 29
1.4.1.2 The Hall thruster 30
1.4.2 Plume Characteristics 32
1.4.3 Spacecraft-Electric Plume Interactions 33
1.4.3.1 Physical Effects 33
1.4.3.2 Mechanical Effects 34

1.4.3.3 Electrical Effects 34
1.4.3.4 Electrostatic Discharges 34
1.5 Plasma Simulations 35
1.5.0.1 Particle in Cell (PIC) 36
1.5.0.2 Particle in Cell- Monte Carlo Simulation in the SPIS software 37
1.6 Spacecraft Plasma Interaction Software (SPIS) 39
1.6.1 SPIS Basic Principles 39
1.6.2 Simulation Setup 42
1.6.2.1 Geometry 42
1.6.2.2 Group Editor 43
1.6.2.3 Electric Circuit 45
1.6.2.4 Global Parameter Settings 45
1.6.2.5 Simulation Phase 45
1.6.2.6 Simulation Control 46
1.6.2.7 Data Mining and Post-Processing 47
1.6.3 SPIS Limitation 47
1.7 Research Aims and Outlines 51

2 Hall Thruster Plume Effects on Spacecraft Charging from 0.067 AU to 1 AU 53
2.1 Abstract 53
2.2 Introduction 54
2.3 Simulation setup 57
2.4 Results 59
2.4.1 Variations of the Potential from 0.067 AU to 1 AU 59
2.4.1.1 Fitting Curve 62
2.4.2 Collected and Emitted currents 63
2.4.3 Ram, Wake, and Side Potential Profiles 67
2.4.4 With and Without the Thruster: Role of Secondary Electrons 71
2.4.5 With and Without the Thruster: Role of Photoelectrons 75
2.4.6 With the Thruster: Without Secondaries and Photoemission 78
2.5 Conclusion 80

3 A Comparative Study of Spacecraft Charging Effects with and Without RIT-2X and SPT-100 Thrusters from 0.044 AU to 1 AU 83
3.1 Abstract 83
3.2 Introduction 84
3.3 Simulation Model and Setup 86
3.4 SPIS Simulated Results 88

3.4.1 Variation in spacecraft potential from 0.044 AU to 1 AU 88
3.4.2 Comparison of collected and emitted current with and without the thruster 91
3.4.3 Ram, wake and side potential 94
3.4.4 Role of Photoelectrons on Spacecraft Potential 100
3.5 Conclusion 101

4 SPT-100 Hall Thruster and RIT-2X Thruster-Spacecraft Interaction in Jovian Magnetosphere 103
4.1 Abstract 103
4.2 Introduction 104
4.3 Simulation Description 106
4.4 SPIS Simulated Results 108
4.4.1 Variation of the spacecraft potential at Jovian's Magnetospheric Plasma 108
4.4.2 Spacecraft Charging Effects in the Absence of sunlight 111
4.4.3 Ram, wake, and side potential profiles 112
4.5 Conclusions 115

5 The Effects of SPT-100 and RIT-2X Thruster Plumes on Solar Panels at 0.044 AU and 1 AU 117
5.1 Abstract 117
5.2 Introduction 118
5.3 SPIS Simulation Setup 119
5.4 SPIS Simulation Results 121
5.4.1 Case A: Solar Panel opposite the Thruster 121
5.4.1.1 With and without sunlight at 1 AU 121
5.4.1.2 With and without sunlight at 0.044 AU 126
5.4.2 Case B: Thruster-facing Solar Panel Configuration 131
5.4.2.1 In the Presence of sunlight at 1 AU: 131
5.4.2.2 In the Presence of sunlight at 0.044 AU: 133
5.5 Conclusion 135

6 Conclusion 138
6.1 Limitations 144
6.2 Future Work 144

A Charge-Exchange Plasma Effects of the SPT-100 Hall Thruster at Heliocentric Distances from 0.044 AU to 1 AU 147
A.1 Abstract 147

A.2 Introduction 148
A.3 Simulation Modeling 150
A.4 Simulation Results 151
A.4.1 Simulation results from 0.044 AU to 1 AU 151
A.4.2 With and Without thruster from 0.044 AU to 0.093 152
A.4.3 With and Without thruster from 0.11 to 0.25 AU 157
A.4.4 With and Without thruster from 0.25 to 1 AU 158
A.4.5 Ram wake and side potential profiles 160
A.4.6 Effects on spacecraft charging with and without the Secondary electrons 162
A.5 Conclusion 164

B Simulation Study of Hall Thruster and their Effects on the Spacecraft at 1 AU and 0.093 AU **166**
B.1 Abstract 166
B.2 Introduction 166
B.3 Simulation setup 168
B.4 Simulation results 169
B.4.1 Without the SPT-100 Hall thruster 170
B.4.1.1 S1 Simulation: Far away from the Sun At 1AU 170
B.4.1.2 S2 Simulation: Near-Sun environment at 0.093 AU 171
B.4.2 With the SPT-100 Hall thruster 173
B.4.2.1 S3 Simulation: Far away from the Sun at 1 AU 173
B.4.2.2 S4: Near-Sun environment at 0.093 AU 177
B.5 Conclusion 178

C Variation in Spacecraft Potential with Different Sizes and Geometries **179**
C.1 Different spacecraft sizes and potential variation 179
C.2 Different spacecraft geometry at 1AU and 0.044 AU 181
C.3 Cubical Spacecraft with Solar Panels 184
C.4 Conclusion 186

List of Figures

1.1 The Sun's composition, various regions, temperature (Kelvin), and densities (Kg/m³). Sourced from (Priest, 2014) 9

1.2 Mean variation of temperature and density in the solar atmosphere with height according to the VAL (Vernazza-Avrett-Loeset) model. Image Credit: (Lang, 2001) 10

1.3 A coronal hole on the Sun captured in this 193-degree (angular extent) Extreme Ultraviolet (EUV) image from the Atmospheric Imaging Assembly (AIA) aboard the Solar Dynamics Observatory (SDO). Image credit: NASA/SDO 12

1.4 A model of the equatorial heliosphere from a plasma (top) and neutral (bottom) perspective. The top panel includes a colour bar illustrating plasma temperature, with arrows denoting plasma flow. Markings for the termination shock, heliopause, and bow shock are provided. In the bottom panel, a colour bar indicates H density, with the hydrogen wall in front of the heliopause labelled, and trajectories of the Voyager spacecraft illustrated. Figure sourced from (Zank et al., 2022) 13

1.5 The spherically symmetric hydrodynamic expansion (radial) speed $v(r)$ of an isothermal solar corona with temperature T_0 is depicted as a function of r/a, where a represents the radius of the base of the solar corona, set at 10^6 km. Image sourced from (Parker, 1958) 15

1.6 Radial dependence of solar wind parameters on density (N), magnetic Field (B), speed (V), and temperature (T) in the ecliptic plane as a function of radial distance. Observations include solar corona (diamonds) and in situ observations (hourly) of HE1 and HE2 at 0.3-1 AU, and in situ observations (hourly) of P101, P11, VY1, and VY2 at 1-61 AU. Figure sourced from Köhnlein (1996) 17

1.7 Illustration of Jupiter's magnetosphere. Image credit: NASA 19

1.8 Illustration of spacecraft charging caused by ambient plasma and electric thruster plume. 25

1.9 Schematic of typical DC discharge Gridded Ion thruster. Image sourced from NASA website 30

1.10 Schematic of typical RF discharge Gridded Ion thruster. Image sourced from NASA website . . . 31
1.11 Schematic of Hall Thruster. Image sourced from (Ashkenazy et al., 2007) . . 31
1.12 A typical thruster beam depicting the ion distribution, CEX-ions, and sputtered material. Figure sourced from (Goebel et al., 2023) . . . 33
1.13 Typical cycle of PIC simulation. Image sourced from (Loureiro, 2010) 37
1.14 Typical Cycle of PIC-MCC simulation. Image sourced from (Loureiro, 2010) 38
1.15 Representation of a CEX collision. Image sourced from (Loureiro, 2010) . . . 42
1.16 Visualization of the GMSH Interface featuring the CAD Model and Gamma Value Statistics Bar. . . . 43
1.17 Group Editor in SPIS with Default Properties for Spacecraft (SC) and Boundary Conditions (BC) (*Spis User Manual* n.d.) . . . 44
1.18 The SPIS simulation code features a hierarchical structure illustrated here. Nested boxes denote the structure of the code. Arrows signify the simulation's computational steps and time evolution, crucial information for user understanding. The image is taken from the (*Spis User Manual* n.d.) 46
1.19 The SPIS simulation data visualisation panel . . . 48
1.20 The SPIS simulation data visualisation panel . . . 48

2.1 GMSH spacecraft model with a meshing grid (green/yellow), the void boundary is the simulation boundary, and the blue conical shape represents the ion plume. . . . 59
2.2 Plot showing the spacecraft potential (volts, x-axis) with and without the SPT-100 Hall thruster, as a function of heliocentric distance (AU, y-axis). The solid blue and orange lines represent the spacecraft potential considering solar photon flux, while the dotted orange and blue lines illustrate the potential variation when solar photon flux is excluded. . . . 60
2.3 Best-fit curves without and with a thruster vs. heliocentric distance: (Left) 0.044 AU to 1 AU, (right): 0.067 to 1 AU. . . . 63
2.4 With the thruster on collected and emitted currents (on the primary axis) and spacecraft potential (on the right-hand axis) versus heliocentric distance. 65
2.5 Without the thruster collected and emitted currents (on the primary axis) and spacecraft potential (on the right-hand axis) versus heliocentric distances. . . . 66
2.6 Cross comparisons of 2D potential maps with and without the SPT-100 Hall thruster at varying heliocentric distances, corresponding to Figure 2.1 and the 3D potential cut in the $y = 1$ plane. sunlight and the solar wind come from the left (the -x direction) . . . 71

2.7 The potential profiles along the ram direction (-x axis), wake direction (x-axis) and the sheath direction (z-axis), obtained from Figure 2.6. Figures 2.7a and 2.7b illustrate the ram potential with and without the thruster, positioned at the top left and top right, respectively. Figures 2.7c and 2.7d depict the wake potential with and without the thruster, located in the middle left and middle right panels. Finally, Figures 2.7e and 2.7f show the side potential with and without the thruster, placed at the bottom left and bottom right panels. 72
2.8 Spacecraft potential with and without secondary electrons at 1 AU and 0.067 AU, from left to right: a.) with the thruster and b.) without the thruster 74
2.9 Collected and emitted currents with and without the thruster at 0.067 AU and 1 AU. 74
2.10 Spacecraft potential with and without photoelectrons at 1 AU and 0.067 AU, from left to right: a.) with the thruster on and b.) without the thruster . 76
2.11 Collected and emitted currents with and without the thruster at 0.067 AU and 1 AU. From top left to bottom right, respectively: With the thruster at (a) 0.067 AU, and (b) 1AU and without the thruster at (c) 0.067 AU and (d) 1AU. 76
2.12 Collected and emitted currents with the thruster on but no photoemission and secondary electrons at (a.) 0.067 AU and b.) 1 AU 79

3.1 GMSH spacecraft model with a meshing grid (green/yellow), the void boundary is the simulation boundary, and the blue conical shape represents the ion plume. 87
3.2 Spacecraft potential with the SPT-100 Hall thruster, the RIT-2X thruster and without thruster versus heliocentric distance. 90
3.3 Collected and emitted currents (on the primary axis) and spacecraft potential (on the right-hand axis) versus heliocentric distance a.) With RIT-2X, b.) SPT-100 Hall thruster, and c.) without the thruster. Note that for SPT-100 Hall thruster the simulation at 0.044 AU are not performed due to SPIS technical issues 93
3.4 Cross comparisons of 2D spacecraft potential maps with and without RIT-2X thruster at varying heliocentric distances, corresponding to Figure 3.1, cut in y = 1 plane. sunlight and solar wind directions are on the left. 97

3.5 The plot shows the potential profile with (on left) and without (on right) the RIT-2X thruster along the ram direction (-x axis), wake direction (x-axis), and the sheath direction (z-axis) obtained from Figure 3.4. Figures 3.5a and 3.5b illustrate the ram potential with and without the thruster, positioned on the top left and top right, respectively. Figures 3.5c and 3.5d depict the wake potential with and without the thruster, located in the middle left and middle right panels. Finally, Figures 3.5e and 3.5f show the side potential with and without the thruster, placed in the lower left and lower right panels. 98
3.6 Spacecraft potential with and without photoelectrons a.) 0.067 AU (on the left) and b.) 1 AU (on the right) 101

4.1 GMSH spacecraft model with a meshing grid (green/yellow), the void boundary is the simulation boundary, and the blue conical shape represents the ion plume. 107
4.2 Spacecraft potential versus radial distance from Jupiter with and without the thruster. The dark blue region represents Europa at 9.5 R_j, the light blue region shows Ganymede 15 R_j, and the white region denotes Callisto at 26.1 R_j 109
4.3 Collected and emitted currents without the thruster at the Europa, Ganymede, and Callisto. 'Se' stands for secondary electrons and 'ph' for photoelectrons. 109
4.4 Collected and emitted currents with the thruster at the Europa, Ganymede, and Callisto.'Se' stands for secondary electrons and 'ph' for photoelectrons. 110
4.5 Spacecraft potential with and without photoelectrons at a.) Europa, b.) Ganymede, and c.) Callisto 111
4.6 Cross comparisons of 2D spacecraft potential maps with and without thrusters at the Europa (left column), Ganymede (middle) and Callisto (right panel), corresponding to Figure 1, cut in y = 1 plane. sunlight directions are on the left 113
4.7 From top to bottom rows, the potential profile along the ram direction (-x axis), wake direction (x-axis) and the sheath direction (z-axis) obtained from Figure 6 a.) Europa (top row) b.) Ganymede (middle row) and c.) Callisto (bottom row) 114

5.1 Integration of GMSH spacecraft model with the solar panels and the mesh grid. The void indicates the domain/simulation boundary and the conical shape symbolizes the ion plume. 120

5.2 Influence of sunlight on Spacecraft and Solar Panel Surface Potential with and Without Thruster at 1 AU. Spacecraft Surface on the Left, Solar Panel Back Surface (Marked in Red Border) and Solar Panel Front Surface on the Right 122
5.3 Cross comparisons of 2D potential maps with and without the SPT-100 Hall thruster and RIT-2X thruster at 1 AU, corresponding to Figure 1 and the 3D potential cut in the x = 1 plane. sunlight and solar wind come from the left (the -x direction) for each panel. 124
5.4 Collected and emitted currents at 1AU on the spacecraft surface and rear side of the solar panel (on the primary axis) and spacecraft potential (on the right-hand axis) versus heliocentric distance 125
5.5 Collected and emitted currents on the front side of the solar panel (on the primary axis) and spacecraft potential (on the right-hand axis) versus heliocentric distance 125
5.6 Influence of sunlight on Spacecraft and Solar Panel Surface Potential with and Without Thruster at 0.044 AU. Spacecraft Surface on the Left, Solar Panel Back Surface (Marked in Red Border) and Solar Panel Front Surface on the Right 127
5.7 2D potential maps with and without the RIT-2X thruster at 0.044 AU, corresponding to Figure 1 and the 3D potential cut in the x = 1 plane. sunlight and the solar wind come from the left (the -x direction) 129
5.8 Collected and emitted currents at 0.044 AU on the spacecraft surface and rear side of the solar panel (on the primary axis) and spacecraft potential (on the right-hand axis) versus heliocentric distance 130
5.9 Collected and emitted currents on the front side of the solar panel (on the primary axis) and spacecraft potential (on the right-hand axis) versus heliocentric distance. 130
5.10 2D potential maps with SPT-100 Hall thruster (on left) and RIT-2X thruster (on right) at 1 AU facing the thruster, corresponding to Figure 1 and the 3D potential cut in the x = 1 plane. sunlight is coming from the right (in +x direction). 132
5.11 Comparison of collected and emitted currents on the front side of solar panels relative to the heliocentric distance at 1AU: Thruster-facing solar panel vs. Thruster-away from the solar panel Configurations 133
5.12 2D potential maps with the RIT-2X thruster (on right) at 0.044 AU facing the thruster, corresponding to Figure 1 and the 3D potential cut in the x = 1 plane. sunlight is coming from the right (in +x direction). 134

5.13 Comparison of collected and emitted currents on the front side of solar panels relative to the heliocentric distance at 1AU: Thruster-Facing solar panel vs. Thruster-away from the solar panel Configurations 135

A.1 GMSH model of the simple cylindrical spacecraft and meshing grid (green and yellow) used in the SPIS simulation. The ovoid boundary is the simulation box. The blue conical shape shows the ion plume 151
A.2 Illustration of Spacecraft potential and Population densities with the thruster on vs helio distances 153
A.3 Simulation result for the 0.044 AU case representing the population densities with (left) and without the thruster (right). The solar wind and Sun direction on the left side for all the simulations 154
A.4 Cross comparison of spacecraft potential with and without the thruster for various helio distances from 0.044 AU to 1 AU 157
A.5 Without the thruster collected and emitted currents versus heliocentric distances 158
A.6 With the thruster collected and emitted currents versus heliocentric distances 159
A.7 The plot shows the potential profile along the ram direction (-x axis). The origin of the graph is at point D in Figure A.1. The left panel is with the thruster on, and the right panel is without the thruster 161
A.8 The plot shows the potential profile along the wake direction (x-axis). The origin of the graph is at point C in Figure A.1. The left panel is with the thruster on, and the right panel is without the thruster 161
A.9 The plot shows the potential profile along the sheath direction (z axis). The origin of the graph is in the z-direction from Figure A.1. The left panel is with the thruster on, and the right panel is without the thruster 162
A.10 Collected currents and spacecraft potential with and without secondaries at 0.067 AU when the thruster is on 162
A.11 Collected currents and spacecraft potential with and without secondaries at 1 AU when the thruster is on 163

B.1 GMSH model of the simple cylindrical spacecraft and meshing grid (green and yellow) used in the SPIS simulation. The void boundary is the simulation box. The blue conical shape shows the ion plume 168
B.2 Population density logarithmic maps without the thruster for 1AU a) photoelectrons, b) H+ ion density, c) ambient electron density, d) secondary electrons density 171

B.3 Maps of the plasma potential for the 1 AU case without the thruster: a) with photoelectrons, b) without photoelectrons, c) without secondary electrons.pa172
B.4 Population density logarithmic maps without the thruster for 0.093 AU a) photoelectrons, b) H+ ion density, c) ambient electron density, d) secondary electrons density 172
B.5 Maps of the plasma potential at 0.093 AU case without the thruster: a) with photoelectron (-7.29 V), b) without photoelectron (-7.98), c) without secondary electrons (-38.9 V) 172
B.6 Population density logarithmic maps with the thruster for 1AU: a) CEX-ion, b) thruster electrons, c) ambient ions H+, d) thermal electrons, e) secondary electrons, f) photoelectrons 174
B.7 Maps of the plasma potential at 1 AU case with the thrusters operating: a) with photoelectron (-4.84 V), b) without photoelectron (-4.90 V), c) without secondary electrons (-4.85 V) 174
B.8 Population density logarithmic maps with the thruster for 0.093 AU: a) CEX-ion, b) thruster electrons, c) ambient ions H+, d) thermal electrons, e) secondary electrons, f) photoelectrons 176
B.9 Population density logarithmic maps with the thruster for 0.093 AU: a) CEX-ion, b) thruster electrons, c) ambient ions H+, d) thermal electrons, e) secondary electrons, f) photoelectrons 176

C.1 Spacecraft potential variation with size and geometry at 1 AU without thruster 180
C.2 Spacecraft potential distributions for cylindrical (1m in radius and 1 m long) and cubical geometries (1m x 1m x 1m) at 1 AU and 0.044 AU. The top panels show the potential for the cylindrical spacecraft to be (left) +9.15 V at 1 AU and (right) -28 V at 0.044 AU. The bottom panels show the potential of the cubic spacecraft to be (left) +9.22 V at 1 AU and (right) -12 V at 0.044 AU. sunlight is incident from the left side in both cases. 182
C.3 2D potential distributions of a cubical spacecraft (1m in length, width, and height) with solar panels (3m in length, 1m in width, and 0.5 m in height) at 1 AU (left) and 0.044 AU (right). sunlight is incident from the left side in both cases. 184

List of Tables

1.1 Cross-section parameters of CEX-collisions. Table from (Miller et al., 2002) . 42
1.2 Description of Simulation Parameters (*Spis User Manual* n.d.) 47

2.1 Gmsh Geometry Dimensions and Thruster Specifications. 58
2.2 Physical Parameters Used in SPIS To Simulate Various Environments Charging Effects from (Guillemant, 2014) 58

3.1 Parameters used for SPIS simulation. 87

4.1 Parameters used for SPIS simulation. Plasma Parameters taken from (Rudolph, 2012; Holmberg et al., 2019) 107

5.1 Geometry Dimensions and Thrusters Specifications used in SPIS 121

A.1 Gmsh Geometry Dimensions and Thruster Specifications. 152

B.1 Gmsh Geometry Dimensions and Thruster Specifications. 169

Chapter 1

Introduction

The early beginnings of spacecraft-plasma interaction studies trace back to the dawn of space exploration, catalyzed by milestones like the Soviet Sputnik probe in 1957. This era ushered in a new understanding of the intricate interplay between spacecraft and the space environment. Some subsequent missions, such as SCATHA launched in 1979, were intended to unravel the complexities of spacecraft interactions with the surrounding plasma environment. They helped to understand and mitigate some of the challenges posed by spacecraft charging phenomena. Based on their analyses, researchers identified risks associated with electrostatic discharges and other charging-related effects on spacecraft components, electronics, and mission objectives. These insights were crucial in shaping the development of mitigation strategies and design guidelines aimed at fortifying satellites against the adverse impacts of charging events. As spacecraft technology evolved, propulsion systems underwent a significant transformation. Electric thrusters emerged as an alternative to traditional chemical thrusters, offering improved efficiency and enabling long-duration space missions. In 1964, National Aeronautics and Space Administration's (NASA) Space Electric Rocket Test 1 (SERT-1) marked the first flight of a demonstrated electric thruster, showcasing its potential. Subsequently, NASA's Deep Space 1 mission in 1998 became the first to employ ion propulsion for an interplanetary mission, demonstrating its suitability for long-duration missions.

However, the operation of electric thrusters introduced a challenge: The exhaust plume undergoes a charge-exchange process, where the fast ions emitted from the plume combine with slow neutrals, producing slow ions and fast neutrals. Some of the slow ions, known as Charge Exchange Ions (CEX-ions), and electrons (from the neutralizer) tend to return to the surface of the spacecraft, leading to the accumulation of electrostatic charge on the surface of the spacecraft. Additionally, interactions between the backflow plume and solar wind can further influence the spatial charge distribution, causing variations in the potential of different parts of the spacecraft. The low-energy CEX-ions and thruster electrons may interfere with sensitive instruments, leading to measurement errors and data contamination. Hence, it becomes important to examine the influence of thruster-induced plasma and solar wind on spacecraft charging across different environments to prevent (or at least understand) operational irregularities and failures. However, conducting precise measurements of these complex interactions in a vacuum chamber poses challenges due to scale limitations and the inability to fully replicate the solar-wind conditions. Such experiments are often time-consuming, inaccurate, and costly. Consequently, numerical simulations serve as crucial tools for predicting thruster-spacecraft interactions, offering a more comprehensive understanding of charging characteristics compared to ground or even in-space testing.

This thesis is relevant to several space mission scenarios, including the Parker Solar Probe, which operates at small heliocentric distances with intense photoelectron fluxes and high-density plasma, and the Juno mission, which navigates Jupiter's magnetosphere with highly energetic plasma conditions. Understanding the behavior of electric thruster plumes under such diverse environments is critical for predicting spacecraft charging, particularly in the presence of high-energy particles and dense magnetospheric plasma. Additionally, interplanetary missions employing electric propulsion face unique challenges due to interactions between thruster plumes and ambient plasma. By investigating these interactions under varying plasma conditions, this thesis provides insights into spacecraft charging dynamics, essential for protecting sensitive instruments and maintaining satellite health in extreme environments.

To achieve these objectives, this thesis explores the interactions between electric thruster plasma and spacecraft plumes using the Spacecraft Plasma Interaction Software (SPIS). Four key parameters were examined across the chapters, with the thruster configured to face radially toward the Sun in all cases. This specific alignment was chosen to study the direct interaction of photoelectrons, abundant on Sunlit surfaces, with the thruster plume and their subsequent effect on spacecraft potential.

1. Varying solar wind - Given that the electric thruster backflow plume returns to the spacecraft surface, altering charge distributions and spacecraft potential, there is a gap in understanding how ambient plasma conditions affect the spacecraft potential during thruster operation. Specifically, it is unclear whether the spacecraft's potential varies with the density and temperature of the solar wind when the thruster is active.To address this, Chapter 2 investigates the ion-induced charging phenomenon by analyzing the behavior of charged particles, such as ambient electrons, ions, photoelectrons, secondary electrons, charge exchange (CEX) ions, and thruster electrons, both with and without the thruster active. The investigation spans various heliocentric distances from 0.044 to 1 AU. The findings presented in Chapter 2 reveal that charge-exchange (CEX) ions and thruster

electrons dominate the spacecraft environment, achieving a low, stable, and negative potential across all heliocentric distances examined. This negative potential is attributed to thruster electrons having a thermal speed higher than that of ions. Consequently, the study demonstrates that with the thruster active, the spacecraft's potential remains stable across varying plasma densities, unlike the significant variations observed from 0.044 AU to 1 AU when the thruster is inactive.

2. Comparison between high-performance thrusters: Chapter 2 addressed the fact that the variation in ambient plasma does not significantly affect the spacecraft potential when the SPT-100 Hall thruster is activated, in contrast to the scenario without the thruster. It reveals that, regardless of ambient plasma variation, the spacecraft maintains a low, stable negative potential because of the dominance of CEX-ions and thruster electrons in both the spacecraft and surrounding plasma. The stability persists across heliocentric distances ranging from 0.044 AU to 1 AU. Building on this finding, Chapter 3 investigates whether changes in the density of CEX-ions and thruster electrons impact the spacecraft's potential. To explore this, the RIT-2X thruster, known for its high thrust of 180 mN compared to the SPT-100 Hall thruster's 35 mN, is selected. Chapter 3 presents a comparative analysis of these two electric thrusters, examining their effects on spacecraft potential as thrust levels increase.

3. Jupiter's magnetospheric plasma: Chapters 2 and 3 established that the density of CEX-ions and thruster electrons plays a crucial role in determining the spacecraft potential. Specifically, the findings showed that higher densities of CEX-ions and thruster electrons result in more stable and lower negative potentials, with minimal variation, as observed in the RIT-2X thruster case. Furthermore, when the density of CEX-ions and thruster electrons exceeds that of the ambient plasma, the influence of ambient plasma particles, such as photoelectrons and secondaries, on spacecraft potential becomes negligible during thruster operation. Building on these insights, Chapter 4 investigates the effects of the Jovian magnetospheric plasma on spacecraft charging at three distinct orbital locations: Ganymede, Callisto, and Europa. These environments represent vastly different plasma conditions compared to the solar wind, characterized by high-energy particles and dense magnetospheric plasma. The study examines the spacecraft potential with and without thruster operation, analyzing how the backflow plume interacts with the unique plasma characteristics of Jupiter's magnetosphere. The findings in Chapter 4 closely align with those of Chapters 2 and 3, showing that the electric thruster's backflow plume consistently maintains a low, stable negative potential, even in the presence of Jovian magnetospheric plasma. This demonstrates that the dominance of CEX-ions and thruster electrons over the ambient plasma continues to mitigate the effects of the

surrounding environment on spacecraft charging.

4. Solar panels and thruster plume interactions: Chapter 5 investigates how electric thruster plumes from the SPT-100 and RIT-2X thrusters impact the charging of solar panels at distances of 1 AU and 0.044 AU. The potential values differ from those in Chapters 2 and 3 due to the use of a different geometry, as demonstrated in Appendix C, which highlights how geometry variations influence spacecraft potential. The findings reveal that the front side of the solar panel (non-conductive material, Sun-facing) achieves a low negative potential with the SPT-100 Hall thruster and a low positive potential with the RIT-2X thruster, regardless of sunlight exposure or panel orientation relative to the thruster. In contrast, the backside of the solar panel (conductive material, anti-Sunward) and the spacecraft surface consistently achieve a low negative potential when the thruster is active. Without the thruster, large variations in spacecraft potential and solar panel potential are observed on both dielectric and conductive surfaces due to the influence of ambient plasma and solar photons. Additionally, the front side of the solar panel, coated with dielectric material, tends to charge more positively due to higher charge dissipation compared to the backside and spacecraft surface, which are coated with conductive materials. This charging behavior is significantly influenced by material composition, the use of resistors to limit current flow from the solar panels to the spacecraft, and the area exposed to sunlight. The study further demonstrates that the electric thruster plume's impact on dielectric surfaces is notably less significant compared to the conductive-coated backside and spacecraft surface. These results highlight how the combination of dielectric material properties and the emission of charge-exchange (CEX) ions and thruster electrons contribute to achieving a more positive and stabilized potential on the front side of the solar panel.

The rest of this chapter sets the groundwork for the thesis by starting with essential insights into solar physics, focusing on understanding the formation of the solar wind and its variation with distance from the Sun. Through this foundational knowledge, a deeper understanding of the environmental factors that influence spacecraft behavior is gained. Section 2 delves into the fundamentals of spacecraft charging, clarifying how it interacts with particles from the solar wind and the subsequent impacts on spacecraft systems. In Section 3, the focus shifts to the operational principles of electric thrusters and their interactions with spacecraft. Exploring these interactions is vital for assessing the efficacy of electric propulsion systems in mitigating spacecraft charging issues. Section 4 introduces various techniques used in plasma simulation, providing a comprehensive overview of the methodologies used in the study. Understanding these simulation techniques is essential for accurately modeling spacecraft-plasma interactions. Finally, Section 5 provides an in-depth explanation of the foundational concepts behind the Spacecraft Plasma Interaction Software (SPIS), an open-source tool for simulation that employs the particle-in-cell (PIC) technique.

Through these foundational elements and comprehensive analyses, this thesis aims to contribute to the advancement of electric thruster-spacecraft-plasma interaction studies and pave the way for enhanced spacecraft design and operation in challenging space environments.

1.1 Solar Physics

1.1.1 Brief history

The study of the Sun has a rich history in astronomy, with notable contributions from Galileo Galilei, Heinrich Schwabe, Gustav Kirchhoff, and many other scientists. Sunspots were observed as early as ancient times, with records from civilizations such as the Chinese and Greeks. However, Galileo's telescopic observations in 1610 marked a significant advancement, as he systematically studied Sunspots and used them as evidence to support Copernicus' heliocentric theory (Vokhmyanin et al., 2018). In the 19th century, Schwabe discovered the existence of an 11-year Sunspot cycle, laying the foundation for understanding the cyclic nature of solar activity and its impact on Earth's climate and technology (Priest, 2014). In the mid-19th century, Gustav Kirchhoff and Robert Bunsen conducted experiments that proved that analyzing the spectrum of the Sun could help determine its chemical and physical composition. Their work led to the identification of various elements, such as hydrogen and helium, present in the Sun's atmosphere (Meadows, 2016). In the mid-to-late nineteenth century, Richard Carrington conducted observations on Sunspot activity by recording the position, size, and shapes of the Sunspots over an extended period. His observations revealed that Sunspots tend to emerge at higher latitudes and migrate towards lower latitudes as the Sun cycle progresses. The pattern of Sunspot distribution over time can be effectively illustrated using the butterfly diagram, a concept developed by Edward Walter Maunder and Annie Scott Dill Maunder in the early 1900s.

The early researchers, including Richard Carrington , estimated that the Sun's rotation period ranged between 25 and 28 days. Over time, with refinements in observational techniques and the development of more precise instruments such as helioseismology and Space-based observation, it is today known that the average rotation period of the Sun's equator is approximately 25.4 days. However, because of differential rotation, this period varies with latitude, and higher latitudes have longer rotation periods (Carrington, 1863).

On 1 September 1859, Richard Carrington observed one of the most significant solar flares in recorded history at his private observatory, witnessing it erupting from a group of Sunspots. This event, later known as the Carrington Event, was a powerful geomagnetic storm caused by the ejection of a massive coronal mass from the Sun that interacted with Earth's magnetosphere. The Carrington event led to strong auroras that were visible throughout much of the Earth, even at low latitudes. It also disrupted telegraph communication systems and sparked electrical fires. These effects provided early evidence of the potential impact of solar flares on Earth's atmosphere and technology (Carrington, 1863). As space exploration advanced through the 20th century, scientists gained a better understanding of solar activity and its effects on Earth by establishing multiple observatories across the world.

Before the 1930s, there was limited progress in understanding the Sun's corona (the outermost layer of its atmosphere). Historically, observing the corona was only feasible during total solar eclipse events, when the moon fully obscured the photosphere, presenting challenges to observation. This led to the invention of the coronagraph by Bernand Lyot (1952), a telescope equipped with an attachment to obstruct direct sunlight, enabling the study of the corona even under full daylight conditions (D'Azambuja, 1952).

The 21st century has witnessed significant progress in understanding solar physics and solar activity. Ground-based solar observatories have undergone significant upgrades in instrumentation and observational techniques. New telescopes equipped with advanced adaptive optics and imaging technologies have provided high-resolution views of the Sun's surface, allowing scientists to study fine-scale features such as granulation, Sunspots, and solar flares with unprecedented detail (Priest, 2014).

A suite of satellites and space missions, including Skylab (1973, which conducted significant solar observations as part of its varied experiments), Yohkoh (1991), Ulysses (1992), SoHo (1995), ACE (1997), TRACE (1998), RHESSI (2002), STEREO (2006), Hinode (2006), SDO (2010), GOES (2016), DSCOVR (2016), Parker Solar Probe (2018), and Solar Orbiter (2022), have revolutionized understanding of solar physics. These missions, operated by agencies such as NASA, ESA (European Space Agency), JAXA (Japanese Aerospace Exploration Agency) and NOAA (National Oceanic and Atmospheric Administration), provide a comprehensive view of the Sun's dynamic behavior, ranging from its surface features to its outer atmosphere and solar wind. By capturing high-definition images, monitoring solar activity, and measuring solar wind parameters, these satellites enable scientists to study solar phenomena such as Sunspots, solar flares, coronal mass ejections

(CMEs), and solar wind variability. Through continuous observation and data collection, these satellites contribute invaluable insights into the fundamental processes driving solar variability and its influence on space weather, Earth's magnetosphere, and technological systems. In 2023, the Indian Space Research Organization (ISRO) launched the Aditya L1 spacecraft, specifically designed to study the solar corona, the outer atmosphere of the Sun, using a coronagraph. Its mission is to investigate the solar atmosphere, monitor solar magnetic storms, and assess their effects on the Earth's environment (Singh et al., 2011).

1.1.2 The Solar Structure

1.1.2.1 Sun's Interior

The Sun is a huge ball composed of hot gas comprised mainly of Hydrogen (92%) and Helium (8%) by number, mostly ionized because of the high temperature. The Sun's interior is divided into three regions as sketched in Figure 1.1, namely the core, the radiative zone, and the convection zone (Priest, 2014). The core is the region where nuclear fusion takes place. Hydrogen is converted to helium, where the temperature is about 1.5×10^7K. The energy generated in the core leaks continuously outward in a very gentle manner across the radiative zone by radiative diffusion. In this region, photons are absorbed and emitted many times, and it takes many years to cross it. The radiative zone is characterized by extremely high temperatures, but the energy process is slow because the dense plasma restricts the swift travel of photons. Above the radiative zone lies the convection zone, where energy transfer occurs primarily through the movement of hot plasma. In this region, the hot plasma rises towards the surface similar to the bubbles rising in boiling water. As the hot plasma reaches the surface of the Sun, it begins to cool. The energy released from the surface of the Sun is radiated out into space, causing the plasma to lose heat. As it cools, the plasma becomes denser and begins to sink back down into the convective zone. This process is called convection. In the convection zone, the energy is transported from the Sun's core to its surface, where it further radiates out into space (Priest, 2014).

1.1.2.2 Sun's Atmosphere

The Sun's outer layer, also known as the solar atmosphere, consists of three regions with gradually transitioning physical properties: the photosphere, chromosphere, and corona. The photosphere, the thinnest layer, is a few hundred kilometres thick and emits most

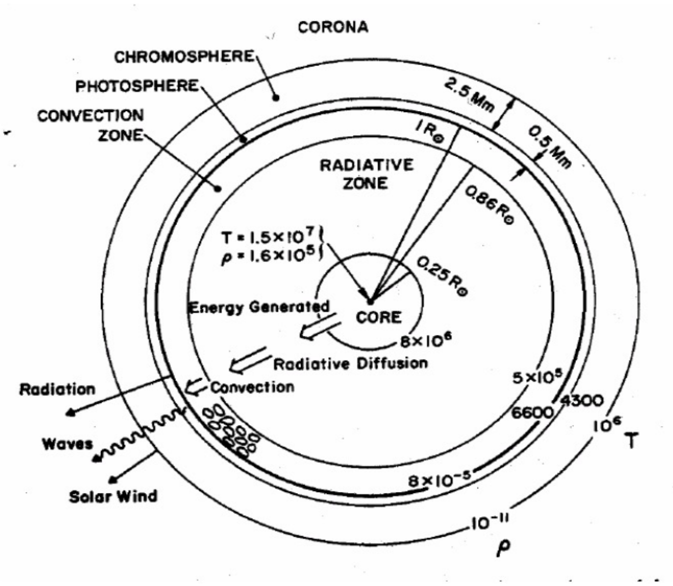

Figure 1.1: The Sun's composition, various regions, temperature (Kelvin), and densities (Kg/m³). Sourced from (Priest, 2014)

of the Sun's light. It is relatively dense, with densities typically around $10^{23}\,\mathrm{m}^{-3}$, and is opaque due to its high density. Above the photosphere lies the chromosphere, which gradually transitions from the photosphere and becomes less dense and more transparent, with densities ranging from $10^{23}\,\mathrm{m}^{-3}$ at the base to approximately $10^{17}\,\mathrm{m}^{-3}$ at the top. This layer exhibits a mix of dynamic phenomena and rising temperatures. The outermost region is the corona, which begins above the chromosphere and transitions smoothly through the so-called transition region. The corona is highly diffuse, with densities decreasing from $10^{15}\,\mathrm{m}^{-3}$ near the transition region to about $10^{7}\,\mathrm{m}^{-3}$ at Earth's orbit (1 AU). The density continues to drop with increasing distance from the Sun, reaching approximately $10^{5}\,\mathrm{m}^{-3}$ in the interstellar medium. These gradual changes in density and temperature across the layers are critical for understanding solar dynamics and interactions with the solar wind (Priest, 2014).

Figure 1.2 shows the mean variation in temperature and density as a function of height above the photosphere based on the popular VAL model (Vernazza et al., 1973; Vernazza et al., 1976; Vernazza et al., 1981). The VAL model of the solar atmosphere is a semi-empirical one-dimensional model that successfully fits a number of spectral lines from different regions, and it has been extremely useful. However, a representation of Figure 1.2 oversimplifies it, focusing only on the mean properties. As seen in Figure 1.2, it is clear that the photospheric temperature of 6000 K rises to 50,000 K in the chromosphere (which is partially ionized). Then, over a few hundred kilometers known as the transition region, the temperature increases dramatically to beyond 100,000 K in the fully ionized corona.

This layer is called the 'transition region' as this layer exists between the relatively cool chromosphere and the million-degree corona. Further, the corona expands outward to form the solar wind, a variable but consistent flow of plasma that creates a cavity in the interstellar medium known as the heliosphere. Within this region, the pressure of the solar wind is equal to that of the interstellar gas (Holzer, 1989; Golub et al., 2010). Most researchers describe the corona and its structures as extending roughly a few to perhaps 5-10 solar radii from the Sun (Zirker, 1977; Cranmer, 2009; Waldmeier, 1956). Terms such as solar wind or interplanetary medium refer to larger heliocentric distances where the plasma is primarily moving approximately radially away from the Sun. This thesis will simulate various heliocentric distances ranging from 0.044 AU to 1 AU, as well as the Jovian magnetospheric plasma at 5.2 AU.

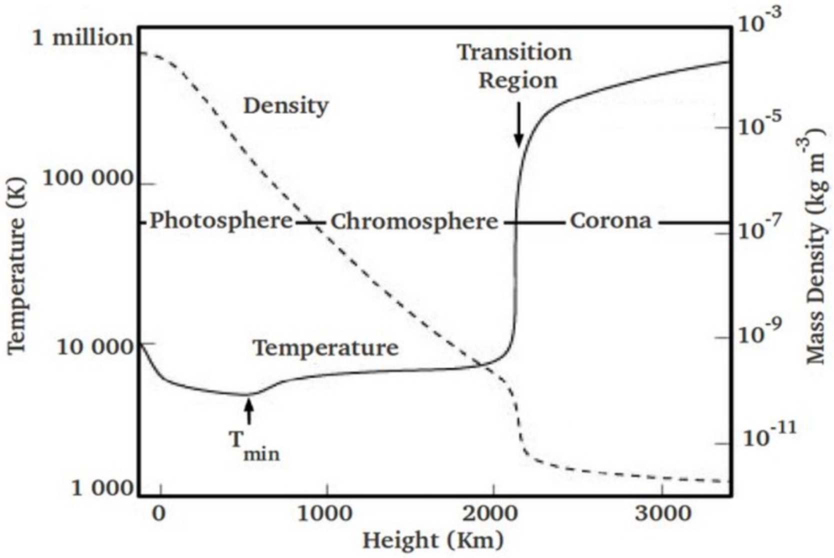

Figure 1.2: Mean variation of temperature and density in the solar atmosphere with height according to the VAL (Vernazza-Avrett-Loeset) model. Image Credit: (Lang, 2001)

1.1.3 Corona

The corona, the Sun's hottest layer, diffuses outward from the solar surface and is dominated by its magnetic field. It eventually merges with the solar wind (Cravens et al., 1997; Golub et al., 2010). Before the 1930s, observing the corona was only possible during eclipses, where it appeared as a faint halo of low density about 10^{15} m^{-3} and high temperature, approximately 2×10^6 K. The intensity of the solar corona, roughly 10^{-6} of the solar disk's brightness, is comparable to that of the full moon (Priest, 2014). However, observing during a total solar eclipse posed challenges for researchers, as these occur only about once a year and take about 3 minutes, making it rare and difficult to study the corona. This complexity stimulated Lyot to replicate the eclipse by means of a coronagraph, as mentioned earlier in Amo et al. (2022). Hence the coronagraph has made it routine to study the properties of the corona by blocking the disk of the Sun and measuring the intensity and (linear) polarization of the white light from the corona. Observing the corona is best done by using X-rays and extreme ultraviolet regions of the spectrum because these wavelengths can penetrate the lower layers of the Sun's atmosphere and reveal details of the corona, which are otherwise obscured by the brighter layers closer to the Sun's surface. However, the Earth's atmosphere blocks most of the spectrum at shorter wavelengths.

The corona exhibits a three-part structure in X-rays consisting of (relatively dark) coronal holes, coronal loops, and bright X-ray points (Priest, 2014). Coronal holes are cooler areas where plasma escapes outward along open magnetic fields, contributing to the fast solar wind. The solar wind from these coronal holes influences space weather and contributes to auroras near Earth's polar regions. Coronal loops, on the other hand, are magnetically closed and connect opposite-polarity regions of the photosphere. Lastly, X-ray bright points scattered across the solar disc comprise the tiny loops.

1.1.3.1 Coronal Holes

The coronal holes, identified as extended regions of open magnetic field lines, exhibit lower density and cooler temperatures (Zirker, 1977; Cranmer, 2009; Waldmeier, 1956). They were first named and studied within the green spectral lines (5303 Å) using a coronagraph. Subsequent detailed analysis of Skylab images (1973-74) revealed vast coronal features, exemplified by an image captured by the Atmospheric Imaging Assembly on board the Solar Dynamics Observatory, as shown in Figure 1.3. The ultraviolet coronagraph spectrometer on the Solar and Heliospheric Observatory (SOHO) and the ultraviolet coronal spectrometer (UVCS) provided quantitative measurements of temperature and flow speed within the coronal and solar wind, conclusively establishing coronal holes as the source of the fast solar wind (Kohl et al., 2006).

During periods near solar minimum, large coronal holes with opposing magnetic-field polarities cover the north and south polar caps, persisting for 7 to 8 years, making them the longest-lived solar features. Furthermore, observations indicate that polar holes decrease in size approximately two years before the solar maximum, often disappearing entirely for one or two years around the maximum (Priest, 2014). Although some coronal holes may endure across all solar latitudes during solar minimum, their lifespan typically spans only a few months. Notably, low-latitude holes frequently adjoin complex active regions and can merge with polar holes of the corresponding polarity.

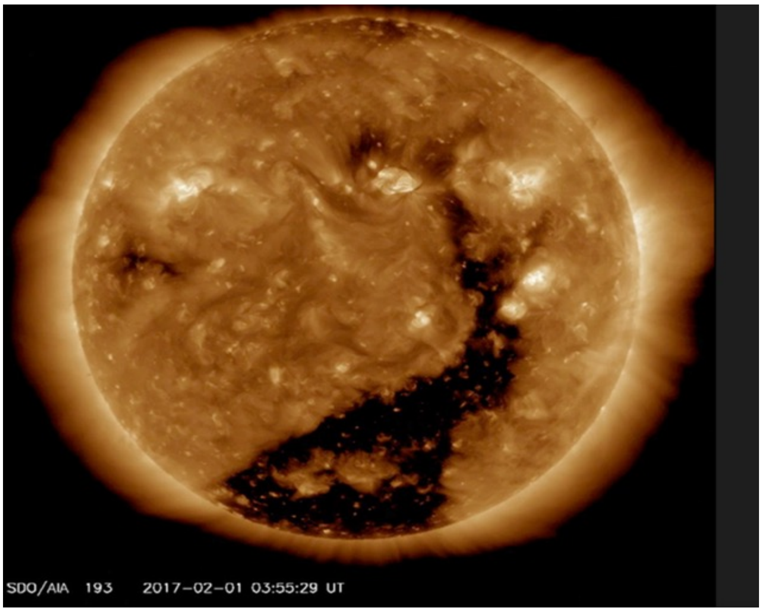

Figure 1.3: A coronal hole on the Sun captured in this 193-degree (angular extent) Extreme Ultraviolet (EUV) image from the Atmospheric Imaging Assembly (AIA) aboard the Solar Dynamics Observatory (SDO). Image credit: NASA/SDO

While Coronal Loops and X-ray Bright Points are other significant solar features, they are outside the scope of this thesis. However, briefly, coronal loops are arch-like structures formed by closed magnetic field lines in the Sun's corona, while X-ray bright points are small-scale regions of intense X-ray emissions caused by localized heating of the corona (Priest, 2014). The next section will provide a brief history of the study of the solar wind.

1.1.4 Solar Wind

The solar wind, consisting of heated electrons and ions, continuously expands from the outer solar corona and fills interplanetary space. As the solar wind moves outward, it encounters various obstacles, such as non-conducting moons, asteroids, comets, and both magnetized and unmagnetized planets. Eventually, the solar wind reaches the interstellar medium, passing through the termination shock and then diverting down the tail of the heliosphere (the shock or shock wave is the speed at which the solar wind drops below the speed of the sound in the medium). Figure 1.4 illustrates the steady-state, two-dimensional configuration of the solar wind's interaction with interstellar plasma, characterized by a two-shock heliosphere structure. The top panel's color bar depicts the temperature distribution of both the solar wind and interstellar plasma, while the bottom panel illustrates the density distribution of neutral hydrogen. Arrows in the top panel indicate the flow of both the solar wind and interstellar plasma. The plasma temperature is presented logarithmically, whereas the neutral density is depicted linearly. Distances from the x- and y-axes are measured in astronomical units (AU). Notably, the Sun and the heliosphere move at a velocity of 23 km/s relative to the interstellar medium. The heliopause represents the outer boundary of the heliosphere, inside which lies the termination shock. At the termination shock, the solar wind's bulk velocity diminishes and the density and temperature increase abruptly. This phenomenon was observed directly by both Voyager spacecraft during their exploration of the termination shock region (Gopalswamy et al., 2010).

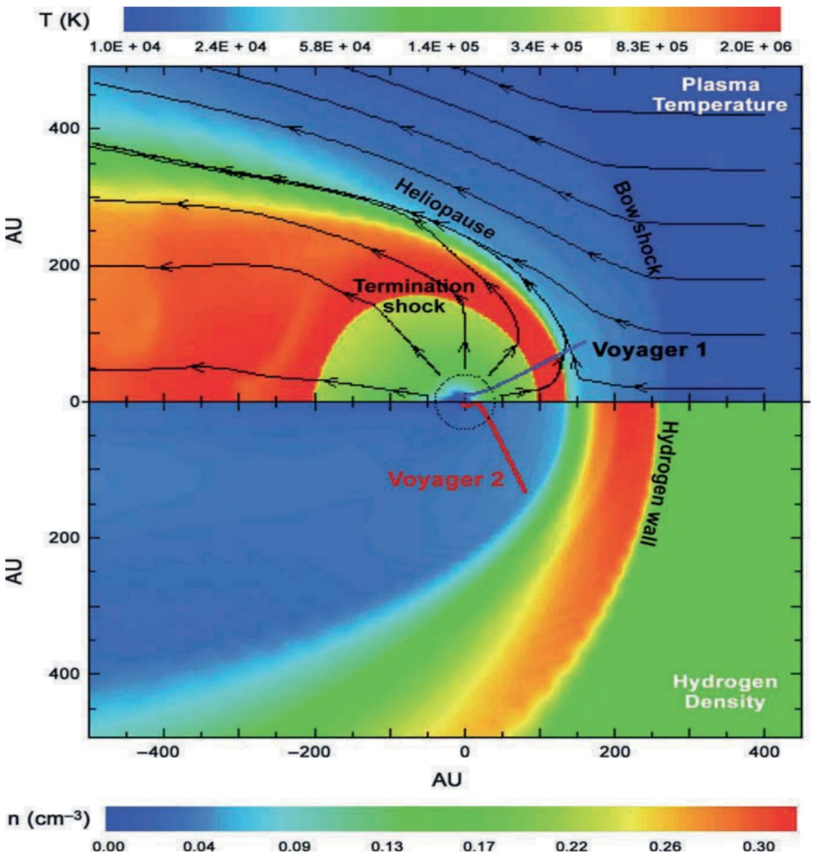

Figure 1.4: A model of the equatorial heliosphere from a plasma (top) and neutral (bottom) perspective. The top panel includes a colour bar illustrating plasma temperature, with arrows denoting plasma flow. Markings for the termination shock, heliopause, and bow shock are provided. In the bottom panel, a colour bar indicates H density, with the hydrogen wall in front of the heliopause labelled, and trajectories of the Voyager spacecraft illustrated. Figure sourced from (Zank et al., 2022)

1.1.4.1 Brief History of the Solar Wind

In 1859, the British scientist Richard Carrington observed a solar flare for the first time. Approximately 17 hours later, a geomagnetic storm occurred as the associated coronal mass ejection (CME) reached Earth, suggesting a connection between solar and geomagnetic events (Carrington, 1859). A Norwegian scientist named Kristian Birkeland suggested that magnetic storms and auroral displays were caused by a beam of electrons continuously emitted from the Sun (Egeland, 2009). Three years later, in 1919, Frederick Lindemann suggested that the Sun ejects particles of both charge polarities, protons as well as electrons (Lang, 2009).

Later, in the mid-1950s, spectroscopic work identified the solar spectral lines as lines corresponding to very highly ionized and hot ionic species and provided the first evidence that the temperature of the solar corona is approximately one million degrees Celsius. Later, in 1951, while observing cometary ions, Bierman proposed that the ejection of plasma from the Sun contained an equal number of ions and electrons (Lang, 2009).

The term "solar wind" was first used by the American astrophysicist Eugene Parker (Parker, 1958). In 1958, Parker showed that despite the Sun's coronal plasma being strongly attracted by solar gravity, since solar gravity decreases with increasing distance from the Sun, the outer corona atmosphere can escape supersonically into interplanetary space (Parker, 1958). The first actual measurement of solar wind was made in 1961 by a particle detector on Explorer 10. The following year, Mariner 2 confirmed that the solar wind was a continuous medium (Snyder et al., 1963).

1.1.4.2 Isothermal Parker Solution

In 1958, Parker proposed that the corona is expanding and not in static equilibrium. He assumed that the corona is isothermal, symmetric in spherical terms, and in a steady state (Parker, 1958). The expansion of the corona is considered to have a radial velocity of $v(r)$, where r is the heliocentric distance (AU). Parker used an approximation for the total (electron plus ion) plasma pressure, $p{=}2nkT_0$, where $n(r)$ is the ion number density, T_0 is the temperature of the ions and electrons, and k is the Boltzmann constant. In addition, he assumed that the electron and ion densities and temperatures are the same. Using the conservation of particle flux and the momentum equation, he obtained the following analytic relation for the plasma flow velocity (Gombosi et al., 2018):

$$\left[\frac{v^2}{v_m^2} - \ln\left(\frac{v^2}{v_m^2}\right)\right] = 4\ln\left(\frac{r}{a}\right) + \frac{v_{esc}^2}{v_m^2}\left(\frac{a}{r}\right) - 4\ln\left(\frac{{v_{esc}}^2}{v_m^2}\right) - 3 + \ln 256\,. \tag{1.1}$$

Here a is the radius of the hot coronal base (Parker used a value of $a = 10^6$ km), v_{esc} is the gravitational escape speed at radius a ($v_{\mathrm{esc}}^2 = \frac{2GM_\odot}{a}$, G is the gravitational constant, $M_\odot$ is the solar mass, v_m is the most probable particle speed with $v_m^2 = \frac{2kT_0}{m_p}$, and m_p is the proton mass. In Equation (1.1), the integration constant was selected to ensure that the velocity remains real and positive for all values of $r > a$. In addition, only solutions that met the criteria $v_0^2 \geq 2kT_0/m$ and $v(r \to \infty) > v_m$ were taken into account. The selection was made under the assumption of a negligible expansion velocity at the hot corona base (v_0), as Parker focused on a hydrodynamic escape scenario. Subsequently, this solution became known as the "solar wind." Figure 1.5 shows a graphical representation of the solutions of speed $v(r)$ for the escaping coronal plasma (Parker, 1958; Gombosi et al., 2018).

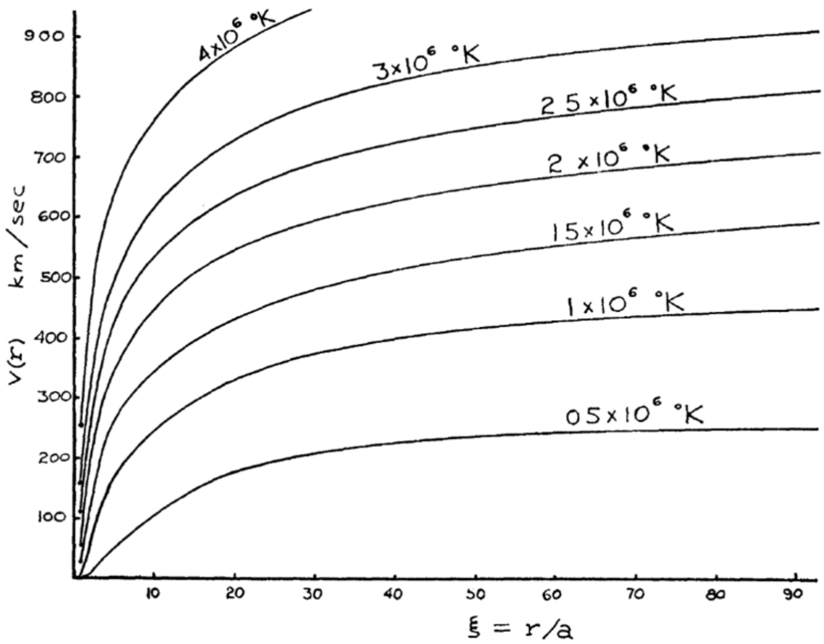

Figure 1.5: The spherically symmetric hydrodynamic expansion (radial) speed $v(r)$ of an isothermal solar corona with temperature T_0 is depicted as a function of r/a, where a represents the radius of the base of the solar corona, set at 10^6 km. Image sourced from (Parker, 1958)

In his seminal 1958 paper, Parker suggested that the plasma emanating from the Sun carries magnetic field lines that stretch out radially as the plasma moves away from the Sun and that the magnetic footpoints move as the Sun rotates. This results in a so-called "Parker spiral" shape for the field lines. Parker predicted that the radial component of the solar magnetic field decreases approximately as *1/r^2* in interplanetary space. The magnetic field lines follow an Archimedean spiral described by Equation (1.2) (Gombosi et al., 2018):

$$\frac{r}{R_s} - \ln\left(\frac{r}{R_s}\right) = 1 + \frac{v_s}{R_s \Omega_\odot}\left(\phi - \phi_s\right) \,. \tag{1.2}$$

Here $\Omega_\odot$ is the angular velocity of the Sun, ϕ is the solar azimuth angle and ϕ_s is the azimuth angle of the magnetic field line at distances R_s (Parker, 1958 and Gombosi et al., 2018).

Equation (1.2) represents the mathematical relationship between the position of a point in the Parker spiral, represented by the distance from the Sun r and its azimuthal angle ϕ_s. The equation essentially tells us that the distance a point is from the Sun (r) and the number of times it has wrapped around the Sun (determined by $\varphi - \varphi_s$) are related through a logarithmic term and the Sun's rotation. This relationship gives rise to the characteristic spiral shape of the magnetic field lines.

Assuming a value of $R_s = 5R_s$, the magnetic field vectors obtained by Parker varied as follows (Gombosi et al., 2018):

$$B_r(r,\theta,\phi) = B(\theta,\phi_s)\left(\frac{R_s}{r}\right)^2 \tag{1.3}$$

$$B_\theta(r,\theta,\phi) = 0 \tag{1.4}$$

$$B_\phi(r,\theta,\phi) = B(\theta,\phi_s)\Omega_\odot\,(r - R_s)\sin\theta/v_s\left(\frac{R_s}{r}\right)^2 . \tag{1.5}$$

Here v_s is the asymptotic speed of the solar wind that is reached at a heliocentric distance r,$B(\theta,\phi_s)$ is the radial component of the magnetic field at the origin of the field line (on the $r = R_s$ sphere). Equation (1.3) suggests that the strength of the radial component of the magnetic field (B_r) is inversely proportional to the square of the distance $(1/r^2)$. This indicates that the farther away from the Sun the weaker the radial magnetic field becomes. Similarly, the strength of the azimuthal component of the magnetic field (B_ϕ) decreases away from the Sun but at a slower rate than the radial component. It decreases proportionally to the inverse of the distance $(1/r)$. Because the azimuthal component decreases less rapidly than the radial component, the magnetic field lines become "wound up" in a helical or spiral pattern. This means that the magnetic field lines start to coil around the Sun's rotation axis as they extend into interplanetary space. Another important consequence of the Parker solution was that the particle density in the interplanetary medium would decrease farther away from the Sun. A mathematical derivation of how plasma density decreases with radial distance incorporates principles of fluid dynamics and mass conservation. In spherical coordinates, the continuity equation takes the form:

$$\frac{\partial\rho}{\partial t} + \frac{1}{r^2}\frac{\partial}{\partial r}\left(r^2\rho U\right) = 0 \tag{1.6}$$

Equation (1.6) describes how the density varies with respect to time and position. The first term, $\frac{\partial \rho}{\partial t}$, represents the local rate of change in plasma density over time. In this case, steady-state conditions are assumed, where the density does not change significantly over time, and so the first term equals zero. The second term, $\frac{1}{r^2}\frac{\partial}{\partial r}\left(r^2 \rho U\right)$, represents the convective flux term, which accounts for the change in density due to the radial velocity component U. Integrating this expression shows that the plasma density is inversely proportional to the square of the radial distance, represented as $n \propto r^{-2}$.

The data collected by various spacecraft so far confirm these predictions, which are shown in the next section.

1.1.4.3 Radial Dependencies

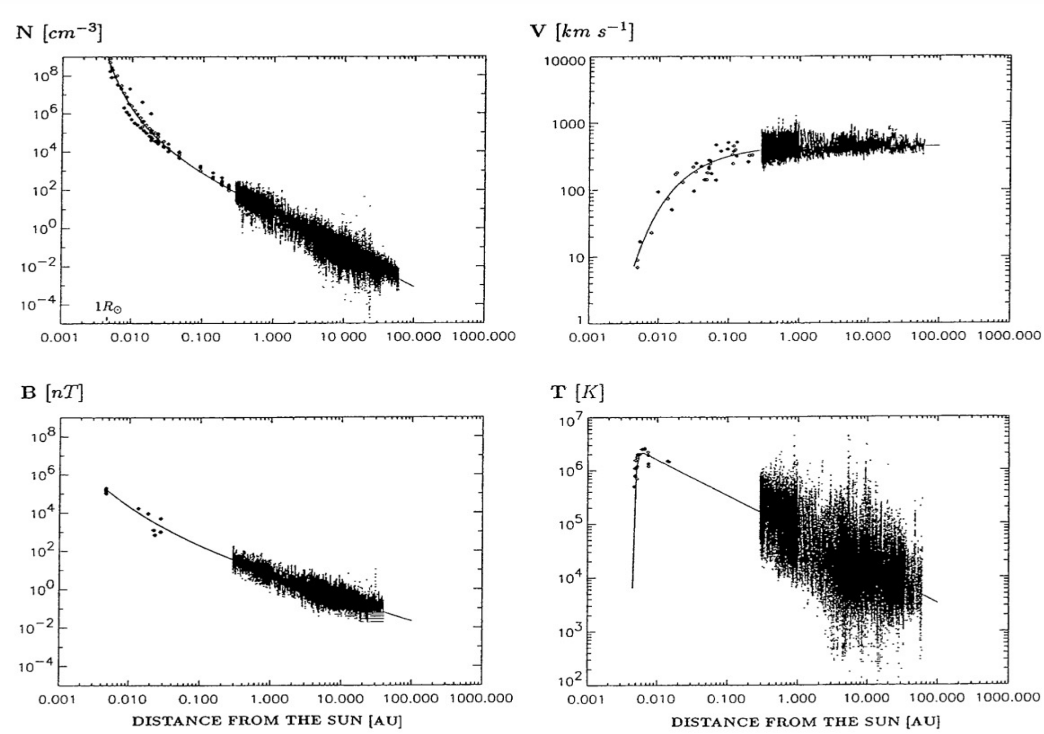

Figure 1.6: Radial dependence of solar wind parameters on density (N), magnetic Field (B), speed (V), and temperature (T) in the ecliptic plane as a function of radial distance. Observations include solar corona (diamonds) and in situ observations (hourly) of HE1 and HE2 at 0.3-1 AU, and in situ observations (hourly) of P101, P11, VY1, and VY2 at 1-61 AU. Figure sourced from Köhnlein (1996)

Köhnlein (1996) analyzed the radial variations of four key parameters in the solar wind: plasma density (N), radial speed (V), temperature (T), and the magnitude of the interplanetary magnetic field (B). The data were utilized from remote sensing observations of the solar corona and in situ measurements within the heliosphere. Inner heliosphere data (from 0.3 to 1 AU) were obtained from Helios-1 (HE1) and Helios-2 (HE2), while Pioneer

10 and 11 (P10, P11) and Voyager 1 and 2 (VY1, VY2) provided measurements from the outer heliosphere (1 AU to 61 AU), as shown in Figure 1.6.

In the data analyzed (Figure 1.6), the plasma density exhibited an approximately exponential decrease from 1.1 solar radii ($R_{\odot}$) to 0.3 AU, followed by a power-law decrease outward to 61 AU (a linear feature in the log-log plot), with a power-law index of 1.93 given in Köhnlein (1996). Thus, indicating the quadratic nature of the decrease in plasma density with increasing distance from the Sun. In contrast, the magnitude of the interplanetary magnetic field (B) decreased more gradually. Its reduction was inversely proportional to the radial distance, which aligns reasonably well with the prediction of the Parker theoretical model (Parker, 1963). The solar wind speed increased from the base of the solar corona to an upper level (reaching approximately 450 km/s) and remained relatively constant around this value up to 61 AU. Furthermore, the temperature exhibited a decrease with distance from the Sun, although the rate of decline was generally gradual.

1.2 Jovian Magnetosphere

The continuous flow of charged particles from the solar wind travels at high speed, carrying energy and a magnetic field. When the solar wind encounters a planet with a magnetic field such as Earth or Jupiter, it interacts with the planet's magnetic field lines. The lines extend from the planet's pole into space, creating a magnetic field that surrounds the planet. Jupiter's magnetosphere is formed by the most powerful planetary magnetic field in the Solar System, which extends millions of kilometers into space. The study of Jupiter's magnetosphere is a contribution of many researchers starting with Van Allen's early work on the structure of Jupiter's magnetosphere by analyzing data collected from Pioneer 10 and 11 from Allen et al. (1974). In the late 1970s, Chris Goertz focused on a detailed analysis using data from Pioneer 10 and Voyager 1 to understand the dynamics of Jupiter's magnetosphere. His studies introduced geometric parameters to describe the current sheet (Goertz, 1981). Further, in 1983, Jupiter's magnetosphere was characterized using the Divine-Garret model from Divine et al. (1983). The model incorporated data obtained from spacecraft missions such as Pioneer and Voyager. These spacecraft provided valuable in situ measurements of the magnetic field, charged particle populations, plasma properties, and other parameters within Jupiter's magnetosphere. By analyzing these data, scientists could gain an understanding of the structure and dynamics of the magnetosphere. In addition, Earth-based telescopes and instruments were also utilized in developing the model, as they provided complementary information to spacecraft data, helping to validate and refine the model.

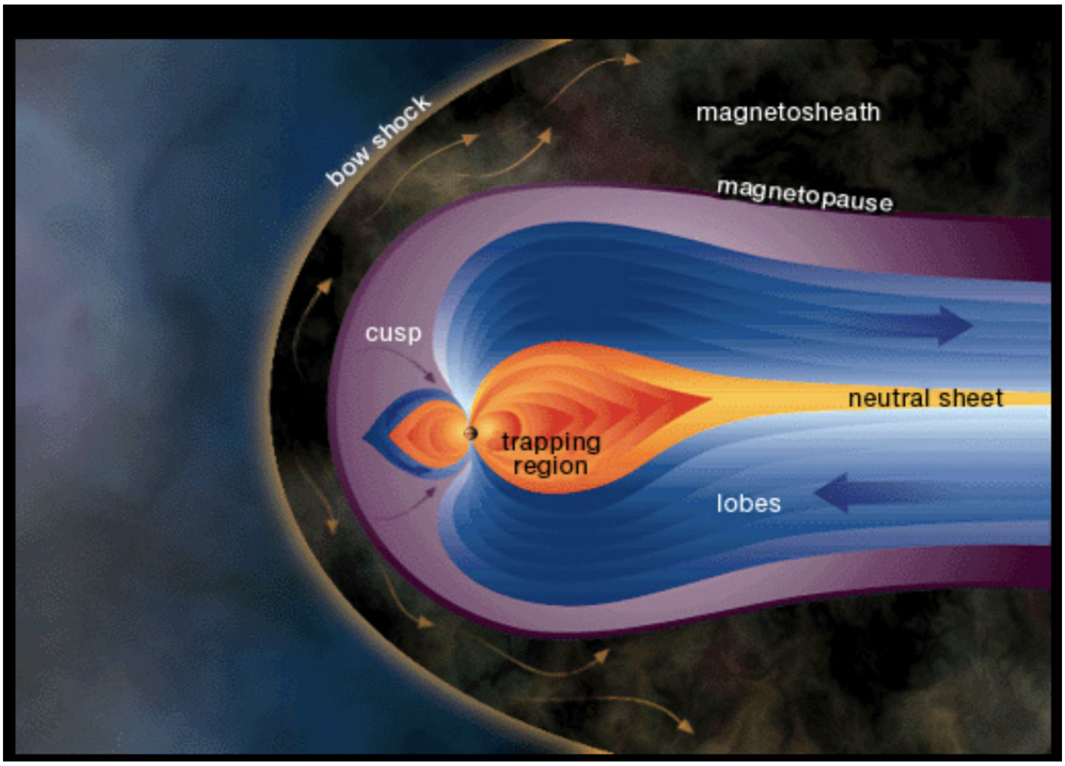

Figure 1.7: Illustration of Jupiter's magnetosphere. Image credit: NASA

Figure 1.7 illustrates the intricate structure of Jupiter's magnetosphere, which includes components such as the bow shock, magnetosheath, magnetopause, and magnetotail (Khurana et al., 2004). The internal magnetic field of Jupiter plays a crucial role in diverting the solar wind away from the planet's atmosphere, forming a cavity in the solar wind flow known as the magnetosphere. This magnetosphere consists of charged particles and serves as a protective shield for the planet. Similarly to Earth's magnetosphere, the boundary that separates the outer region of Jupiter's magnetosphere from the surrounding plasma is termed the magnetopause (Khurana et al., 2004). At the magnetopause, there is a balance between the radially outward pressure of the solar wind and the Sunward pressure exerted by the planet's magnetic field. Additionally, the interaction between the solar wind and Jupiter's magnetic field gives rise to a bow shock upstream of the magnetopause. The region between the bow shock and the magnetopause is known as the magnetosheath (Khurana et al., 2004). Beyond Jupiter, the magnetic field lines are elongated into a tail-like structure called the magnetotail, which extends away from the Sun. This magnetotail formation is the result of the solar wind exerting pressure against Jupiter's magnetic field (Russell, 2001).

The magnetospheric environment of Jupiter is significantly influenced by three key factors, as outlined by (Garrett and Hoffman, 2000): the tilt of its magnetic field (11 degrees) relative to its spin axis, its rapid rotational speed, and the presence of its moon Io (at a radial distance of 5.9 R_j (Jovian radii). Io, a volcanically active moon, continuously generates vast toruses of gas and ions, contributing significantly to Jupiter's magnetospheric dynamics. This torus, known as the Io plasma torus is a dense, doughnut-shaped region of plasma encircling Jupiter along Io's orbit. It is primarily composed of sulfur and oxygen ions sourced from Io's volcanic activity, which are ionized and energized by interactions with Jupiter's strong magnetic field. The Io torus is a critical feature of Jupiter's magnetosphere, significantly influencing plasma distribution and dynamics within the system. Jupiter's rotation rate is exceptionally rapid, with a rotational period of approximately 10 hours, compared to Earth's 24-hour day. The fast rotation, combined with Jupiter's strong magnetic field, results in the cold plasma trapped within its magnetosphere being forced to co-rotate at velocities much higher than those typically encountered by spacecraft in Earth's magnetosphere. For instance, while a spacecraft in Earth's orbit typically travels at speeds around 8 km/s, in Jupiter's outer magnetosphere, these speeds can exceed 100 km/s. The corotation speed varies, ranging from approximately 45 km/s at 4 R_j to 200 km/s at 20 R_j (Garrett and Hoffman, 2000). According to Garrett and Hoffman (2000), Jupiter's magnetospheric environment can be categorized into three distinct types of plasmas : cold plasma, intermediate plasma, and the radiation environment. The cold plasma associated with the Io torus is characterized by high densities (2000 cm-3) and low energies, consisting of ions such as hydrogen, oxygen, sulfur, and sodium. The intermediate plasma has moderate energies (electrons around 1 keV, protons around 30 keV) with densities decreasing exponentially from 5 cm^3 near Jupiter to 0.001 cm^3 beyond 40 RJ, and varying co-rotation velocities. The radiation environment contains high-energy particles (more than 100 keV), which form intense radiation belts that pose a significant threat to spacecraft (Garrett and Hoffman, 2000). Each of these populations exhibits unique characteristics and plays a significant role in shaping the overall dynamics of Jupiter's magnetosphere.

Jupiter's so-called Galilean moons, initially observed by the Italian astronomer Galileo Galilei in 1610, are Io, Europa, Ganymede, and Callisto. These moons interact with Jupiter's magnetic field and are influenced by the charged particles and radiation trapped within the magnetosphere. Chapter 4 of this study focuses exclusively on understanding spacecraft charging in Jupiter's magnetosphere. Europa, in particular, holds significance because of its subsurface ocean and its potential to sustain human life. Upcoming missions, such as ESA's Jupiter Icy Moons Explorer (JUICE) and NASA's Europa Clipper, aim to investigate the habitability of Europa and other Galilean moons by studying their plasma environments, magnetospheric interactions, and surface compositions. These missions face significant challenges, including navigating Jupiter's intense radiation belts and understanding spacecraft charging effects in its dynamic magnetosphere (Meitzler et al., 2023). This thesis provides valuable insights into spacecraft charging in such environments, contributing to safer mission operations and better spacecraft design. Overall, the Galilean moons are integral components of Jupiter's magnetospheric system, and studying them is crucial for ensuring spacecraft safety and functionality, comprehending surface interactions and plasma environments, and evaluating the potential habitability of these fascinating worlds.

1.3 Spacecraft- Solar Wind Interaction

The solar wind comprises charged particles emitted from the Sun, flowing outward into space. Typically, its radial speed ranges between 300 and 1200 km/s, with an average speed of about 400 km/s. However, during periods of solar minimum, there are high-speed streams with velocities reaching up to 700 km/s, recurring approximately every 27 days. The solar wind's speed, density, and magnetic field parameters play a critical role in the energy transfer to the magnetosphere, which can lead to spacecraft phenomena such as surface charging and radiation effects (Gonzalez et al., 1994). Surface charging occurs when an excess of electrons or ions accumulates on a surface, causing an imbalance in surface currents. Other forms of charging include internal charging, also known as dielectric charging, which involves energies above 100 keV that tend to penetrate the surface materials of the spacecraft (Sorensen, 2006). The large accumulation of electrons can lead to high electric fields inside the spacecraft, resulting in electrostatic discharges. The internal charging effects due to high-energy electrons (above 100 keV to 3 MeV) are not addressed in this thesis. Instead, the focus will be on surface charging (energies below 1-100 keV) and how the spacecraft's potential changes in various plasma environments (Mikaelian, 2009).

1.3.1 Brief History of Spacecraft Charging

The first effects of spacecraft charging were documented by Johnsons and Meadows (1955) by analyzing the spacecraft charging data from the rocket-borne spectrometer (Johnson et al., 1955). The early recognition of spacecraft's interaction with its surrounding environment can affect the performance of onboard instruments laid the groundwork for the future research. Further the launch of Sputnik in 1957, showed significant progress in understanding spacecraft charging. The early work on spacecraft charging Chopra (1961) laid the groundwork for the theoretical understanding of spacecraft charging. The spacecraft potential was first measured by Sputnik 3 , given in , Mikaelian (2009). These early works, both the review paper and the measurements from Sputnik 3 confirmed the presence of spacecraft charging and highlighted its possible operational risks. Progress continued from 1965 to 1980, marked by sophisticated theories and a concentration on spacecraft-plasma interactions. The 1973 failure of a US Air Force Defense Space System Communication Satellite highlighted the urgency of addressing spacecraft charging issues, leading to collaborative efforts between NASA and the Air Force (Bedingfield et al., 1996). The era also witnessed the development of predictive computer codes such as NASCAP (NASA/ Air Force Charging Analyzer Program for Geosynchronous orbits) and the establishment of design guidelines outlined in various technical reports and standards from Katz et al. (1979). The launch of SCATHA in 1979 aimed to collect data on spacecraft surface charging effects and plasma interactions, ultimately paving the way for the development of charging control methods and advancing scientific understanding of plasma phenomena from Mulen et al. (1980). Other well-equipped satellites for studying surface charging include the Los Alamos National Laboratory (LANL) geosynchronous satellites (Bame et al., 1993), and the latest additions to the Geostationary Operational Environmental Satellites (GOES) (Dichter et al., 2015). Ongoing research efforts are being made to deepen people's understanding of these effects, contributing to improved spacecraft design, operational safety, and progress in space exploration.

1.3.2 Spacecraft Charging Basic Concepts

Langmuir (1960) and Chen (1965) state that when a spacecraft is in a plasma environment, it functions similarly to a Langmuir probe by interacting with the surrounding plasma. The interaction causes the spacecraft to collect electrons and ions, leading to the accumulation of charge on its surface. This implies that its surfaces collect surrounding charges, causing fluctuations in the probe's electrostatic potential. The spacecraft potential is described as floating with respect to the plasma potential, which is assumed to be zero at an infinite distance from the satellite (Guillemant, 2014). As the satellite accumulates charges, it enters a state of spacecraft charging, which includes :

a) Absolute charging occurs when the overall spacecraft potential of the structure is different from the plasma potential, which is referred to as absolute charging (Guillemant, 2014).

b) Surface charging occurs when the electrical charges accumulate on the spacecraft surface leading to variation in the electrostatic potential of the surface relative to the background plasma. Electrons with energies between 1 and 100 keV can contribute to surface charging (Mikaelian, 2009).

c) Differential charging refers to differences in surface potential across the surface of the satellite, which can reach thousands of volts depending on the material and environmental factors. Such charging can lead to destructive arcing (Guillemant, 2014).

d) Internal charging occurs when the charged particles have a high enough energy (typically higher than 100 KeV to 3MeV) to penetrate the surface and enter dielectric materials and/or isolated internal conducting surfaces. Internal charging poses potential hazards, such as breakdowns of insulators or electrical components and thus their associated circuits (Mikaelian, 2009).

Surface charging occurs in every spacecraft because of the difference in velocities between thermal electrons and ions. Electrons, being lighter and more mobile, collide with the spacecraft's surface more frequently than the heavier ions. This discrepancy leads to a significant build-up of thermal electrons on the surface, causing it to acquire a negative charge. The accumulation of this negative charge is a result of the higher mobility and greater number of electron impacts compared to ions in the plasma environment. Furthermore, to achieve equilibrium with the spacecraft and its surroundings, the net current collected and emitted from the spacecraft's surface must balance out, reaching a steady state as shown in Equation (1.7) and Equation (1.8) where the net total current, summing over all types of currents, all net currents linking to or on the satellite body equals zero (Mikaelian, 2009; Lai and Pradipta, 2022; Garrett, 1981).

$$I_{\mathrm{net}}(V) = I_{\mathrm{e}}(V) - [(I_{\mathrm{i}}(V) + I_{\mathrm{se}}(V) + I_{\mathrm{si}}\,(V) + I_{\mathrm{be}}(V) + I_{\mathrm{ph}}(V) + I_{\mathrm{b}}\,(V)] \tag{1.7}$$

where V is the surface potential relative to the plasma and all currents are functions of the surface potential. These currents include: I_e, the incident net electron current on the satellite surface, I_i, the incident net ion current on the satellite surface, I_{se}, the secondary electron net current due to Ie, I_{si}, the secondary electron net current due to Ii , I_{be}, the net backscattered electron current due to Ie, I_{ph}, the net photoelectron current, and I_b, the net current from active sources such as charged particle beams, ion thrusters, etc.

The equilibrium condition is therefore given by:

$$I_{\mathrm{net}}(V) = 0\,. \tag{1.8}$$

In this situation, the spacecraft's charging process stabilizes and reaches a state of equilibrium, in which the net current is zero and the spacecraft's electrical potential floats at a non-zero potential relative to the plasma potential.

1.3.3 Sources of Spacecraft Charging

Spacecraft charging can significantly and routinely affect the operation of spacecraft electronics and systems (Mikaelian, 2009). The charging is caused by several factors such as multiple components of electrons and ions (e.g., not just the thermal particles but also high energy particles from solar flares and other sources) hitting the spacecraft surface, plus the net emissions of photoelectrons and secondary electrons, as illustrated in Figure 1.8.

In Figure 1.8, we see a comprehensive depiction of the spacecraft charging environment. On the left side of the figure, solar photons and solar wind particles (indicated by arrows) strike the spacecraft surface, causing the emission of photoelectrons and thermal electrons. Photoelectrons are emitted when sunlight strikes the surface, with the photoelectron flux depending on solar flux, material, and incident angle. Secondary electrons are generated from the incident collisions of thermal electrons or ions with the surface, a process detailed in the figure. These interactions give rise to secondary electrons, classified as secondary electron emission under electron impact (SEEE) and secondary electron emission under proton impact (SEEP) (Lai and Pradipta, 2022; Garrett, 1981). The generation of secondary electrons is determined by the Secondary Electron Yield (SEY), which depends on the material, the primary electron energy, and the angle of incidence (Guillemant, 2014).

The right side of the figure illustrates the impact of ion thrusters on spacecraft charging. The thruster ion-plume, composed of xenon neutrals, can cause a backflow of charge-exchange ions (CEX-ions) and thruster electrons onto the spacecraft surface, altering the current distribution and spacecraft potential. The figure shows the direction of these backflow particles, emphasizing the interactions between the electric thruster plumes, the spacecraft, and the surrounding plasma. A detailed study of these interactions will be addressed in Section 1.4.3.1.

The presence of charges that accumulate on the surfaces of spacecraft is a leading factor in the formation of a sheath and a potential barrier. The sheath arises predominantly from the electric fields generated by the accumulated charges on the surface, which exert electrostatic forces on the charged particles (Guillemant, 2014). The thickness of this layer varies depending on the emission and collection rates of electrons and ions on the spacecraft surface, determined by the Debye length, defined in the next subsection. The Debye length, in turn, is influenced by factors such as the temperature and density of the thermal plasma. However, the potential barrier refers to the difference in electric

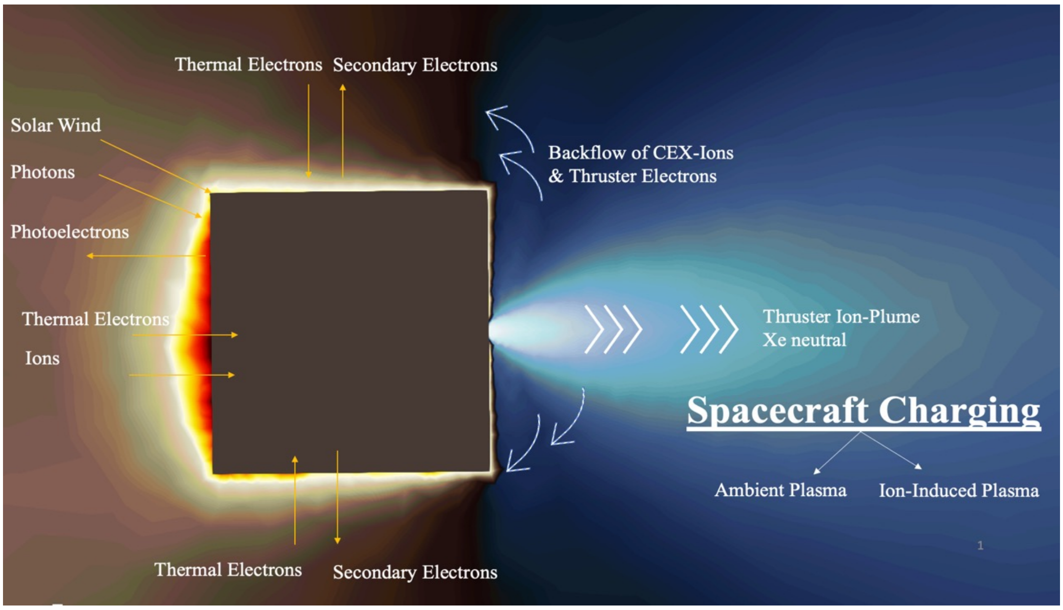

Figure 1.8: Illustration of spacecraft charging caused by ambient plasma and electric thruster plume.

potential between the spacecraft surface and the surrounding plasma. Sheaths and potential barriers are important concepts for understanding spacecraft charging dynamics, which influence the distribution of charges on spacecraft surfaces and regulate the flow of charged particles within the surrounding plasma environment. The following sections provide detailed information.

1.3.3.1 Debye Length and Sheath Formation

In plasma physics, the Debye length (λ_D) is a fundamental parameter that determines the scale over which electric potential disturbances are shielded, maintaining approximate charge neutrality in the plasma. This characteristic length depends on the temperature and density of charged particles and is essential for understanding sheath formation and plasma behavior near boundaries (Gurnett et al., 2005). The characteristic length over which (approximate charge) neutrality is established is called the Debye length λ_D and is expressed as:

$$\lambda_D = \sqrt{\frac{\varepsilon_0 k_b T}{n_0 e^2}} \tag{1.9}$$

where ε_0 is the vacuum permittivity, k_b is Boltzmann's constant, T is the temperature, n_0 is the plasma number density, and e is the elementary charge. In more detail, this is the Debye length for the ambient plasma electrons, which equals the ambient ion Debye length if the ambient ions and electrons have the same temperature, and other electron (and ion) components in principle have their own Debye lengths.

The Debye length represents the scale at which the electric field is screened out by the presence of electrons. Consider an object with a negative charge in the presence of an electric field. Plasma ions are attracted while the electrons are repelled, resulting in a polarization of the charges. The attracted ions gradually form a shield, creating a layer between the material and its surrounding environment with a net positive charge to eliminate the object's negative charge from the plasma seen from a macroscopic distance. Therefore, the Debye length defines the thickness of this layer directly around the material, often referred to as the sheath (Guillemant, 2014). Inside this sheath, the particles act independently, influenced mainly by electromagnetic forces. This means that the plasma is not evenly charged neutral, especially close to objects such as satellites, where particles are emitted and collected.

If the Debye length exceeds the dimensions of the spacecraft ($\lambda D \gg R_{sc}$), called the Thick Sheath limit, the satellite and the plasma are electrically connected. Consequently, the potential is the same everywhere on the satellite's surface (Guillemant, 2014). In this scenario, the electric field extends many Debye lengths into space from the surface of the object. Conversely, if the Debye length is less than the size of the spacecraft ($\lambda D \gg R_{sc}$), the system is considered to be decoupled, with each component interacting primarily with nearby surfaces. Under these conditions, the Thin Sheath approximation holds (Guillemant, 2014). This suggests that the different parts of the spacecraft are only slightly influenced by each other's electrical characteristics because of the screening effect. Here, the electric field is localized close to the surface of the object, which leads to a drop in potential.

1.3.3.2 Potential Barriers

The photoelectrons and secondary electrons emitted from the spacecraft's surface can accumulate near the satellite rather than immediately disperse into space. As these electrons accumulate, they create a build-up of negative electric charge in the surrounding space near the satellite. The negative potential acts like a barrier for other electrons coming from the spacecraft, particularly those with low energy. These low-energy electrons do not have enough energy to overcome the potential barrier. As a result, they get trapped or slow down near the spacecraft, unable to escape into space. Subsequently, this often leads to the recollection of low-energy particles on the spacecraft surface, which may further interfere with the sensitive instruments and can significantly impact scientific observations and low-plasma measurements.

The ATS-6 spacecraft observed the recollection of photoelectrons and secondary electrons due to the potential barrier, which led to the development of the theory of a spherically symmetric photoelectron sheath that included the effect of ions, thermal electrons, and secondaries (Whipple Jr, 1976). The theory's aim was to understand whether a potential barrier leads to the recollection of photoelectrons or secondary electrons. However, it was too complicated to explain the data by model. Further, Thiebault et al. (2015) explored the potential barrier within the electrostatic sheath enveloping magnetospheric spacecraft, specifically focusing on conductive types like Geotail and Cluster. They developed theoretical and numerical methods to create a software model that confirmed the existence of a non-monotonic potential profile with a negative potential barrier encircling a positively charged spacecraft (Thiebault et al., 2015).

Later, both Ergun et al. (2010) and Guillemant et al. (2012) conducted research on spacecraft interactions in close proximity to the Sun, specifically focusing on the Solar Probe Plus mission at a distance of 0.044 AU. Ergun et al. (2010) utilized a self-consistent PIC code, while Guillemant used a PIC simulation using SPIS software. The study of Ergun et al. (2010) revealed that despite the presence of a high photoelectron density, the spacecraft developed a negative potential because of the significant density and temperature of thermal electrons, resulting in the formation of potential barriers. Guillemant et al. (2012) findings corroborated this, finding a high negative potential for the spacecraft at 0.044 AU. Both studies demonstrated that, despite the high density of photoelectrons, the spacecraft acquired a negative charge because of the formation of dense sheaths of low-energy secondary electrons and photoelectrons, which created potential barriers. Consequently, these low-energy electrons had insufficient energy to overcome the strong potential barrier, and this resulted in substantial recollection. Similar results to Guillemant et al. (2012) are found in this thesis, which will be discussed in detail in Chapter 2.

1.4 Electric Propulsion Systems

The electric thruster operates by utilizing an electric field to propel charged particles at high velocities, thereby generating thrust. It functions on the basis of the principles of electrostatic or electromagnetic acceleration. The thruster consists of an anode for introducing the propellant, an ionization chamber, and a cathode that serves both to neutralize charge and to ionize the propellant gas through electron emission. In ion thrusters, an acceleration grid is used to accelerate ions, whereas Hall thrusters rely on a magnetic field to confine electrons and generate thrust (Goebel et al., 2023). Within the ionization chamber of Ion and Hall thrusters, a commonly used propellant, Xenon gas undergoes ionization through electron bombardment or alternative methods. The electrons within the thruster are mostly confined by magnetic fields, while ions are further accelerated by the electric field. Consequently, the positively charged ions are accelerated to high speeds, producing thrust in the reverse direction. Furthermore, it is essential for thrusters to neutralize the exiting ion beam by introducing electrons into the beam using a neutralizer, such as a hollow cathode or other electron-emitting devices (Goebel et al., 2023). The mechanism enables the electric thruster to achieve high thrust, thereby reducing propellant consumption compared to chemical propulsion. Consequently, this reduction in propellant usage allows more space for payload systems and decreases launch mass, facilitating the utilization of smaller launch vehicles at a lower cost. Electric propulsion has become increasingly important in modern space exploration missions. For instance, the Double Asteroid Redirection Test (DART) mission employed the NASA Evolutionary Xenon Thruster–Commercial (NEXT-C) ion propulsion system, showcasing its precision in trajectory adjustments. Similarly, ESA's BepiColombo mission to Mercury utilizes solar electric propulsion to navigate its complex interplanetary trajectory, emphasizing the versatility of electric propulsion systems.

However, certain missions, such as the Parker Solar Probe (PSP) and Juno, rely on chemical propulsion to meet high-thrust requirements and navigate unique mission environments, including intense radiation belts and highly energetic plasma conditions. Additionally, missions like the Jupiter Icy Moons Explorer (JUICE) also use chemical thrusters to operate in Jupiter's dynamic magnetosphere. These examples highlight the diverse propulsion needs across missions and underscore the role of electric thrusters in enabling longer and more efficient missions, as evidenced by ESA's SMART-1 mission. While PSP, Juno, and JUICE do not utilize electric thrusters, the research in this thesis provides valuable insights into spacecraft charging mitigation for future missions that may incorporate electric propulsion systems in similar plasma environments.

1.4.1 Types of Electric Propulsion Systems

Electric thruster types are generally categorized on the basis of their method of acceleration to produce thrust. Table 1.1 displays the thrust and specific impulse values for various thrusters. Electric thrusters are primarily divided into three main categories:

1. Electrothermal:
    - Propellant heated by resistive or arc heating methods. They are expanded through a nozzle for high-speed plume.
    - Examples: Resistor thruster, Arcjet thruster

2. Electrostatic:
   - Propellant acceleration by applying forces to ionized particles.
   - Examples: Hall thruster, Gridded Ion Thruster (GIT), and FEEP/Electrospray Thruster
3. Electromagnetic:
   - Propellant acceleration by combined electric and magnetic fields.
   - Examples: Pulsed Plasma thruster (PPT), Magnetohydrodynamic thruster (MPD)

This thesis investigation will focus on electrostatic thrusters, particularly focusing on the SPT-100 Hall thruster and the Radiofrequency thruster (a type GIT thruster), with detailed information provided in the following section (Goebel et al., 2023).

Electric thruster types	**Thrust (mN)**	**Specific Impulse (s)**
Electrothermal	0.1mN − 1 N	20 − 350
Electrosprays	20μN − 20mN	225 − 3000
Gridded Ion thruster	0.1 − 20mN	500 − 3000
Hall Effect thruster	0.25 − 55mN	200 − 2000

Table 1.1: Thrust and specific impulse range for various thrusters (Goebel et al., 2023).

1.4.1.1 Gridded Ion thruster (GIT)

In this propulsion system, a xenon propellant is introduced into a ionization chamber through an anode and subjected to electron bombardment (through an internal cathode or radio frequency), leading to the creation of energetic electrons and ions, thereby forming a plasma. Following this, a magnetic field is generated to steer electrons within the chamber, while ions are propelled through grids by varying electric potentials. GIT thrusters provide a high specific impulse but a low thrust, as shown in Table 1.1. Multiple methods exist to generate ions from the discharge chamber:

1. Direct-Current (DC) Discharge: The propellant is ionized by electron bombardment to establish potential differences between the cathode and anode. This is done using an internal hollow cathode as shown in Figure 1.9.

2. Radio Frequency (RF) Discharge: In this case, there is no internal hollow cathode. The propellant is ionized via the radio frequency or microwave excitation of an RF generator as shown in Figure 1.10.

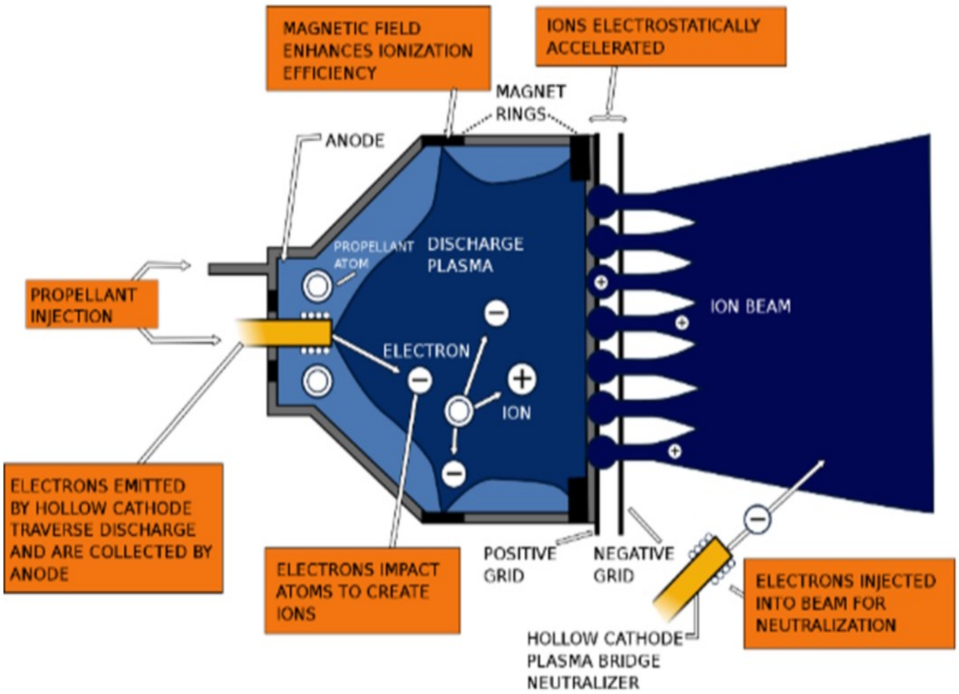

Figure 1.9: Schematic of typical DC discharge Gridded Ion thruster. Image sourced from NASA website

The thesis will explore the charging associated with a radio frequency thruster (RIT) thruster in Chapter 3. A variant of the Gridded Ion Engine (GIE), the RIT-2X thruster employs a high-frequency electromagnetic field to ionize xenon atoms through collisions with electrons. Once ionized, the positively charged ions are propelled outwards by an electric field, generating significant thrust. In particular, the RIT-2X thruster is the largest in its class and offers optimal mass savings for all-electric spacecraft. Thrust levels range from 80mN to 205mN, catering to diverse mission requirements.

1.4.1.2 The Hall thruster

Hall thrusters, a type of electric propulsion system, have been widely used for spacecraft propulsion due to their ability to efficiently accelerate ions and generate thrust using a combination of electric and magnetic field. Figure 1.11 presents a schematic of a Hall thruster, which comprises a discharge chamber, an anode, and a cathode. Xenon propellant enters through the anode, diffusing within the thruster chamber. The hollow cathode

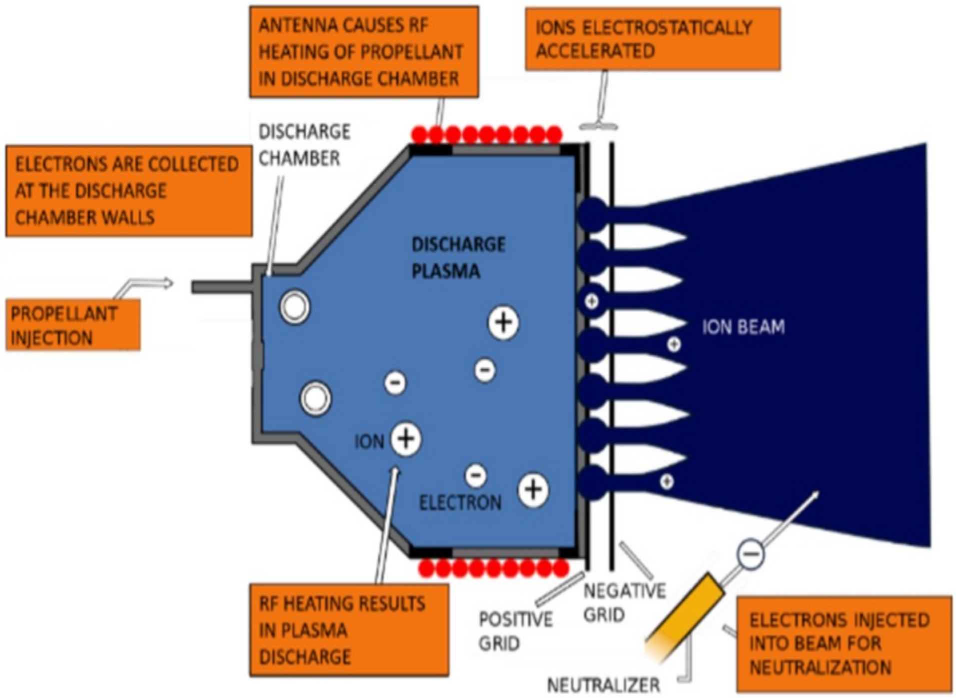

Figure 1.10: Schematic of typical RF discharge Gridded Ion thruster. Image sourced from NASA website

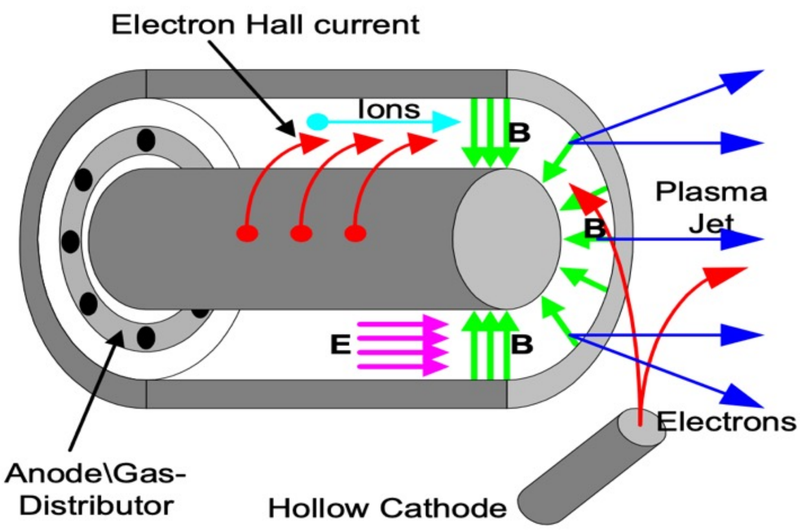

Figure 1.11: Schematic of Hall Thruster. Image sourced from (Ashkenazy et al., 2007)

emits electrons, ionizing the propellant. A radial magnetic field confines electrons, trapping them in the cross-product of the axial electric and radial magnetic fields (E×B), while ions are accelerated by the electric field. Upon exiting, ions attract an equal number of electrons to exit with them, resulting in a neutral plasma plume. Hall thrusters, also known as Hall effect thrusters (HETs), stationary plasma thrusters (SPTs), and magnetic layer thrusters, are the same devices but are distinguished by the use of dielectric insulating walls in the plasma chamber. Compared to ion thrusters, Hall thrusters provide higher thrust and demand less power, albeit with lower efficiency and specific impulse. The thrust and the specific impulse are provided in Table 1.1.

1.4.2 Plume Characteristics

Figure 1.12 illustrates the general characteristics of the thruster plume. Firstly, the main ion beam that exhausts from the thruster is known as a thruster plume, which does not interact with the spacecraft due to the weak electromagnetic force. The thruster plume exhibits an envelope and a distribution of ion currents within that envelope. Secondly, as indicated in the grey circle, energetic ions emitted from the plume undergo the charge exchange process. In this process, fast ions interact with slow neutrals via the movement of an electron from a neutral to an ion, resulting in the formation of slow ions and fast neutrals without changes in momentum. CEX-ions travel radially, returning to the spacecraft's surface and potentially bombarding the spacecraft components in the vicinity. Third, energetic ions are emitted at larger angles from the thruster axis, mainly because of the edge effect (fringe effect) or the scattering of ions caused by the background gas. Finally, impurities generated from the wear of the thruster component can lead to erosion, sputtering, and deposition of surface material which changes the surface properties such as transparency, emissivity, etc. (Goebel et al., 2023).

As mentioned earlier, the main aim of this thesis is to investigate the impact of charge-exchange ions (CEX-ions) on spacecraft surfaces and their resultant effects. The presence of CEX-ions, coupled with associated electrons, induces changes in the properties of the plasma surrounding the spacecraft. The modification in the charge distribution introduces an additional current that influences the potential of the spacecraft. Our thesis research focuses primarily on the surface charging phenomena caused by CEX-ions, deliberately omitting the aspects of erosion, sputtering, and contamination. More information on these effects can be found in the subsequent subsection.

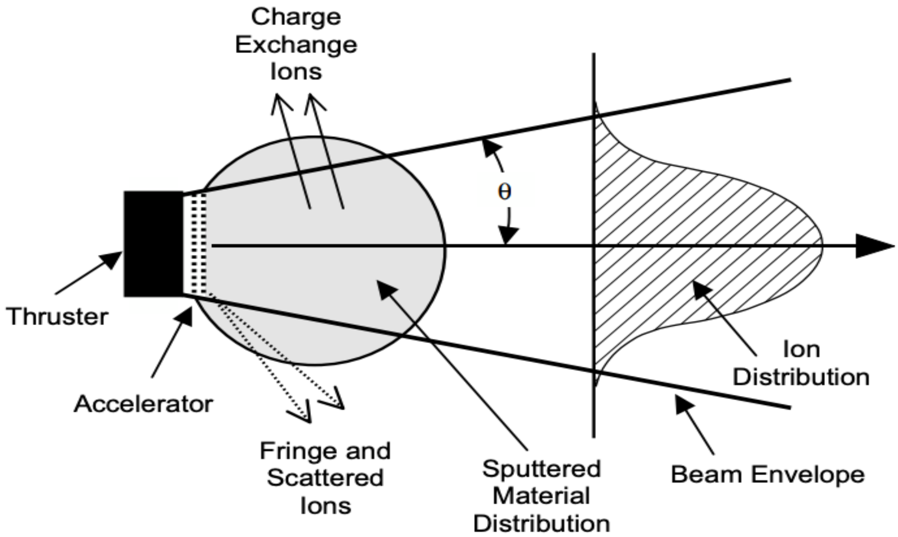

Figure 1.12: A typical thruster beam depicting the ion distribution, CEX-ions, and sputtered material. Figure sourced from (Goebel et al., 2023)

1.4.3 Spacecraft-Electric Plume Interactions

Designing a spacecraft that incorporates an electric thruster requires understanding of the interactions between the thruster and the spacecraft. Thruster plumes can have an immediate effect on the spacecraft due to their current-carrying capability, which may result in erosion or contamination of surfaces with materials ejected from thruster wear, in addition to interacting with subsystems and altering the spacecraft's potential. These direct interactions can influence spacecraft operations, while prolonged effects can affect the lifetime of the spacecraft. The primary impact on the spacecraft during electric thruster operation stems from CEX-ions produced by the collision of the main ion beam with neutral gas, which play a crucial role in the dynamics of interactions between the spacecraft and the ion plume. The high density charge-exchange ions released by the thruster result in multiple effects on the spacecraft, which are systematically categorized and examined subsequently (Goebel et al., 2023).

1.4.3.1 Physical Effects

Sputtering

Sputtering involves an exchange of momentum between incident and target particles, leading to the dislocation of target particles from their lattice sites. As a result, these incident particles can compromise the structural integrity of the spacecraft. The sputtering process is influenced by the energy and angular distribution of the incoming particles, along with the material properties of the surfaces they strike (Sentís, 2023).

Contamination

The operation of an electric thruster commonly results in spacecraft contamination, which can be in two forms: direct and indirect contamination. Direct contamination arises from particles deposited into or onto the spacecraft, originating either from the propellant or impurities ejected from the thruster. Indirect contamination, on the other hand, occurs when sputtered particles result from the impact of the plume on a surface.

1.4.3.2 Mechanical Effects

Forces and Torques

The direct impact of ions from the thruster exerts forces and torques on the spacecraft. These can lead to the destabilization of a spacecraft because the forces are not always aligned with the center of gravity and sometimes counteract the desired thrust.

1.4.3.3 Electrical Effects

Two types of charging can occur, surface charging and internal charging, depending on the energies of the charged particles impacting. Surface charging typically occurs at energies between 1 to 100 keV, as detailed in Section 1.3.2. In this scenario, low-energy charged particles with substantial currents become trapped on the spacecraft's surface. In contrast, internal charging arises from highly energetic particles above 100 KeV that deposit themselves in the internal components of the spacecraft. Spacecraft charging is a significant concern during satellite operation due to the electric fields that can be generated, which can adversely affect spacecraft systems. The electric field induced by charging can also accelerate particles towards the spacecraft's surface, leading to increased erosion and contamination.

1.4.3.4 Electrostatic Discharges

Spacecraft charging can result in powerful electrostatic discharges either due to a high electrostatic field between two objects or from direct contact transfer due to surface or internal charging.

1.5 Plasma Simulations

This section explores the different types of numerical simulation code and the plasma modeling techniques used in the Spacecraft Plasma Interaction Software (SPIS). This will provide detailed insights into how SPIS facilitates the simulation of electric thruster plumes interacting with spacecraft, further enriching understanding of spacecraft-plasma interactions.

Numerical modeling for plasma simulations can be done using three approaches: kinetic, fluid, and hybrid modeling. Kinetic modeling, rooted in Ludwig Boltzmann's statistical concepts, tracks the behaviors and interactions of individual plasma particles by solving the Boltzmann equation or its reduced forms (e.g., Vlasov equation). This approach provides highly detailed results but requires significant computational resources.In contrast, fluid modeling simplifies plasma behavior by treating it as a macroscopic fluid using averaged quantities such as density, velocity, and pressure. Fluid models are derived from kinetic theory by taking moments of the Boltzmann equation and assuming conditions such as local thermodynamic equilibrium and negligible wave-particle interactions. Although computationally efficient, fluid models sacrifice precision, particularly in non-equilibrium conditions.Hybrid modeling bridges these two approaches by combining the precision of kinetic theory for certain particle populations with the efficiency of fluid modeling for others. For example, in SPIS, fast-moving electrons are often treated as a fluid, while ions are modeled kinetically. This allows for a balance between accuracy and computational feasibility, making hybrid modeling suitable for simulating complex real-world scenarios (Loureiro, 2010).

The Boltzmann Equation can be written as :

$$\frac{\partial f_i}{\partial t} + \mathbf{v}_i \cdot \frac{\partial f_i}{\partial \mathbf{x}} + \frac{\mathbf{F}_i}{m_i} \cdot \frac{\partial f_i}{\partial \mathbf{v}_i} = S \sum_{j=1} \int \int \left(f_i' f_j' - f_i f_j \right) g_{ij} d\sigma \tag{1.10}$$

where f_i is the distribution function for species i, $\mathbf{v}_i$ is the velocity of the particles, $\mathbf{F}_i$ is the force acting on the particles, and m_i is the mass of the particles. The term $\frac{\partial f_i}{\partial t}$ represents the rate of change of the distribution function with respect to time, $\mathbf{v}_i \cdot \frac{\partial f_i}{\partial \mathbf{x}}$ describes the advection of particles, and $\frac{\mathbf{F}_i}{m_i} \cdot \frac{\partial f_i}{\partial \mathbf{v}_i}$ accounts for the influence of external forces. The right-hand side represents the collision integral, where f_i' and f_j' are the post-collision distribution functions, g_{ij} is the relative velocity, $d\sigma_{ij}$ is the differential cross section, and the integral is taken over the velocity space of particles of species j. This equation captures the evolution of the distribution function, incorporating changes due to particle motion, external forces, and collisions.

1.5.0.1 Particle in Cell (PIC)

In many plasmas, particle collisions are typically rare or insignificant compared to the influence of other forces, such as electromagnetic interactions. In such scenarios, the Boltzmann equation can be reformulated into a non-collisional form known as the Vlasov equation. The Vlasov equation is a kinetic equation that tracks the evolution of the distribution function of charged particles under the influence of external fields. By setting the right-hand side of equation 1.10 to zero, the Vlasov equation can be expressed as

$$\frac{\partial f_i}{\partial t} + \mathbf{v}_i \frac{\partial f_i}{\partial \mathbf{x}} + \frac{\mathbf{F}_i}{m_i} \frac{\partial f_i}{\partial \mathbf{v}_i} = 0 \tag{1.11}$$

Further, the particle-in-cell method is used to address the non-collisional Boltzmann equation (Vlasov equation). In the PIC method, the plasma is simulated using so-called superparticles or macro-particles, which each represent many real particles, for instance millions of electrons or ions. A superparticle contains average information on the mass and velocity of the represented particles.

The basic code of a PIC simulation is depicted in Figure 1.13. Initially, a set of initial conditions is loaded into the simulator, which initiates the generation of superparticles. These superparticles are subsequently assigned initial microscopic properties that include mass, charge, position, and velocity. Moreover, the simulator is provided with initial electric and magnetic fields, along with defined boundary conditions, before the code commences. Once the initial conditions are established, the simulation loop begins. In this loop, the positions of the superparticles are calculated on the basis of the forces acting on each superparticle and its initial position and velocity vector, leading to their movement within the simulation domain. After the movement of all superparticles, each superparticle's physical charge density and current are mapped onto the nodes of its current mesh cell utilizing a linear weighting process. This method assigns portions of the charge density and current to each node of the cell, depending on their distances from the superparticles. Lastly, the accumulated charge quantities within the grid are used to calculate the electric potential on each node by solving the Poisson equation given as:

$$\nabla^2 \phi + \frac{\rho}{\epsilon_0} = 0\,. \tag{1.12}$$

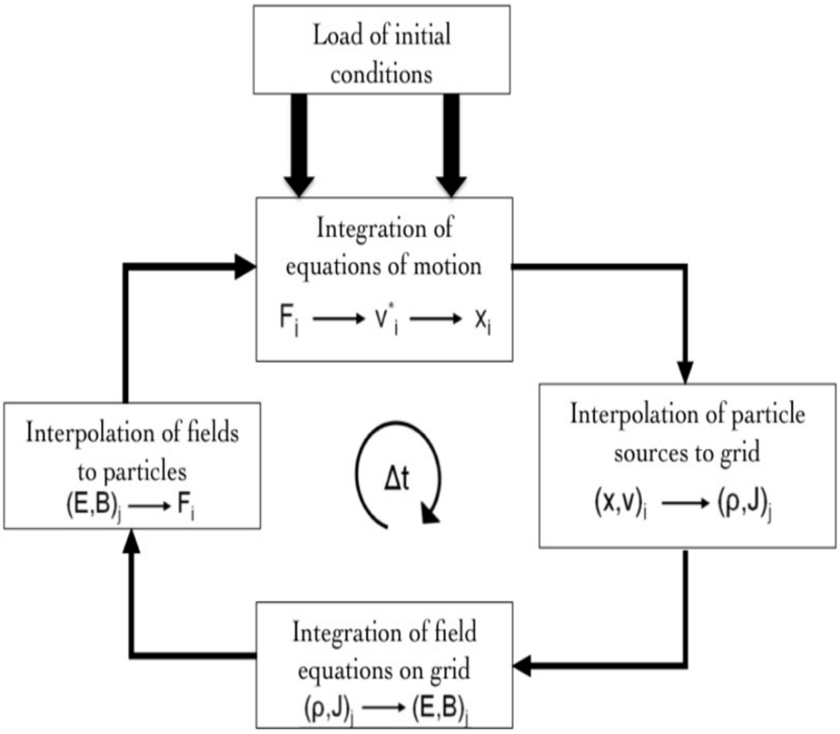

Figure 1.13: Typical cycle of PIC simulation. Image sourced from (Loureiro, 2010)

Here, ϕ represents the electric potential, ρ indicates the charge density, and ε_0 denotes the permittivity in a vacuum.

Upon computing the potential for each node, the electric fields are calculated. (Similarly, currents are used to calculate the magnetic fields.) These fields are then used to determine the total force exerted on each superparticle, providing the quantities required to compute the new velocities and positions for each particle in the next time step. Subsequently, the cycle is re-commences and the system is iterated until the final time selected by the user.

1.5.0.2 Particle in Cell- Monte Carlo Simulation in the SPIS software

The SPIS software employs both Particle-in-Cell (PIC) and Monte Carlo Collision (MCC) methods to simulate the behavior of charged particles in plasma. The PIC method is utilized to investigate the collective behavior of charged particles within the plasma, while the MCC method focuses on calculating the probability of collisions between macroparticles, which allows for the determination of the new particle velocities and eventually the plasma evolution through time. Figure 1.14 displays a block diagram of the PIC-MCC.

Within the SPIS software, the dynamics of the plasma is solved using a modified Boltzmann Equation, which incorporates both PIC and MCC methods to accurately depict the complex interactions and behavior of charged particles in plasma environments:

$$\frac{\partial f_i}{\partial t} + \mathbf{v}_i \cdot \frac{\partial f_i}{\partial \mathbf{x}} + \frac{\mathbf{F}_i}{m_i} \cdot \frac{\partial f_i}{\partial \mathbf{v}_i} = \iint (f_i' G_g' - f_i G_g) g_{ij} \, d\sigma_{ij} \, d\mathbf{v}_j \tag{1.13}$$

The distribution G_g in Equation 1.13 represents the background particles, and the index g denotes the background gas particles. Equation 1.13 holds only for collisions involving background neutrals. Specifically, within the SPIS software, only charge-exchange collisions (CEX) are accounted for, while all elastic collisions between various particle types are disregarded. Figure 1.14 below illustrates the typical cycle of the PIC-MCC technique.

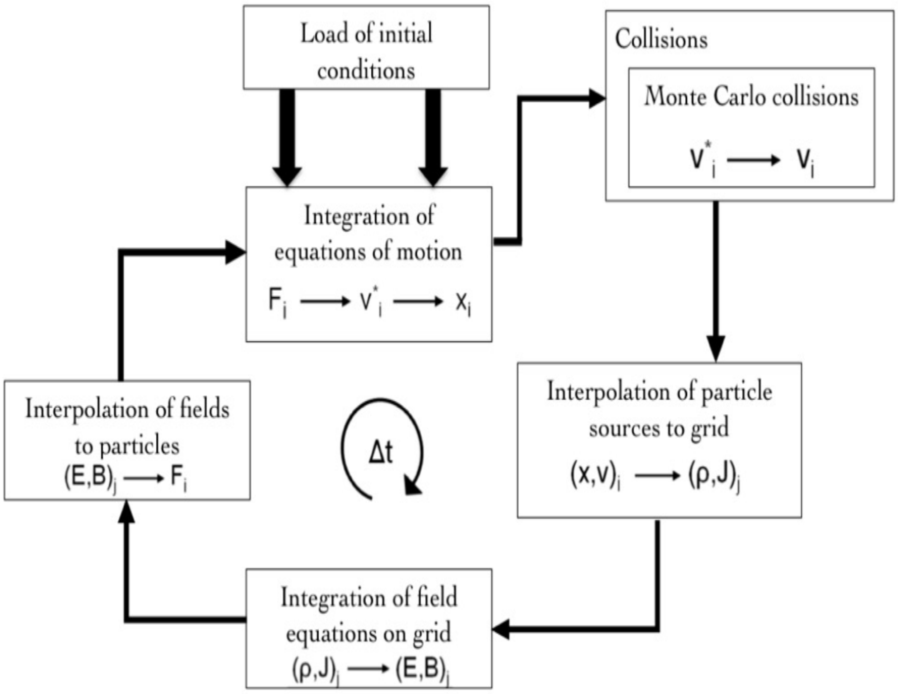

Figure 1.14: Typical Cycle of PIC-MCC simulation. Image sourced from (Loureiro, 2010)

The PIC cycle is modified by the integration of the Monte Carlo Collision method. In SPIS thruster simulations, superparticles are emitted from a surface with specified velocities and positions, establishing the initial conditions for the simulation. As the simulation progresses with each time step, new particles are introduced into the simulation volume and processed alongside existing particles. Initially, in SPIS, the superparticles are randomly distributed on the ejection surface. The structure of the PIC-MCC simulation demonstrates that particle collisions are incorporated as an additional module within the code, positioned between the calculation of superparticle positions and the assignment of their properties to the mesh grid. The remainder of the loop continues as described in conventional PIC simulations (Loureiro, 2010).

1.6 Spacecraft Plasma Interaction Software (SPIS)

1.6.1 SPIS Basic Principles

The Spacecraft Plasma Interaction Software (SPIS) version 6.1.0 (*SPIS - Spacecraft Plasma Interaction Software* n.d.) is an open-source simulation tool that solves the electrostatic potential and motion of charged and neutral particles in 3D, using an unstructured mesh, around a spacecraft with complex and realistic geometries to compute spacecraft-plasma interactions, variations in spacecraft potential, and detailed sheath structures around a spacecraft. SPIS simulations are based on the particle-in-cell (PIC) method, but it offers the possibility to switch between different versions of the PIC method, such as full-PIC (where all charged species are modeled as particles) or hybrid-PIC (where electrons are simulated as fluids) for example, in (Wartelski, Ardura, et al., 2011 and Sarrailh, Matéo-Vélez, et al., 2015). In our study, the SPIS simulation employed the hybrid particle-in-cell method, where CEX-ions and neutrals are modeled using a PIC method, and electrons are modeled using a fluid method, see, e.g., (Loureiro, 2010; Wartelski, Ardura, et al., 2011). The simulation tool is widely used for spacecraft charging simulations in different environments such as in LEO, GEO, and electric thruster operations; see, e.g., (Lee et al., 2011; Wartelski, Theroude, et al., 2013; Wartelski, Ardura, et al., 2011; Thiebault et al., 2015; and Filleul et al., 2021).

The spacecraft charging is determined through an equivalent electric circuit, accounting for its interaction with the surrounding plasma, by calculating the currents between the plasma and spacecraft using a circuit solver. Within SPIS, the spacecraft potential is obtained by solving a linear or non-linear Poisson equation for densities typical of most electric thrusters; the quasi-neutrality assumption (which also assumes the Boltzmann relation) yields the same outcome as solving the Poisson equation, offering a faster and more stable solution as shown in Biagioni et al. (2003) and Wartelski, Ardura, et al. (2011). Therefore, it is possible to implement in SPIS the quasi-neutrality equations with constant or variable electron temperature. Nevertheless, the user can switch between the Poisson solver and the quasi-neutrality approach from the SPIS Graphical User Interface (GUI). If the quasi-neutrality approach with a constant electron temperature is selected, the plasma potential is calculated from Equation 1.14 given in (Wartelski, Ardura, et al., 2011):

$$\Phi_p = \frac{k_b T_e}{e} \ln\left(\frac{n_i}{n_{\text{ref}}}\right) + \Phi_{\text{ref}}\,, \tag{1.14}$$

where Φ_p is the plasma potential (in V), k_b is Boltzmann's constant, T_e is the electron temperature (in eV), e is the elementary charge, n_i is the density of ions, and n_{ref} and

Φ_{ref} are respectively the plasma density and plasma potential at a certain point. This Boltzmann relation only holds for isothermal, unmagnetized, and collisionless electrons.

For full PIC modeling, the 3D mesh resolution in the simulation domain must be finer than that of the local Debye length to resolve the sheath and electron dynamics. Given the extremely small Debye length downstream of the thruster, it is computationally demanding to meet the mesh resolution of the simulations (Filleul et al., 2021). Hence an alternative method is chosen: treating the neutralizer electrons as an isothermal fluid population (all the thruster electrons are assumed to have the same temperature throughout the simulation). The electron density on the simulation mesh is then determined by the local plasma potential according to Boltzmann's relation, thus simplifying the simulation, as explained in .To simplify and more accurately model the thruster plume and spacecraft interactions, quasi-neutrality was assumed ($n_e = n_i$), where the electron and ion populations are treated differently for computational purposes. The ions are modeled kinetically using the Particle-In-Cell (PIC) method, while the electrons are treated as a non-isothermal fluid population, obeying the polytropic law shown in Equation 1.15 (Wartelski, Ardura, et al., 2011; Filleul et al., 2021):

$$T_e n_e^{1-\gamma} = C \,. \tag{1.15}$$

Here γ is the polytropic constant (with $\gamma = 1$ corresponding to the iso-thermal case and $\gamma = \frac{5}{3}$ for an adiabatic plasma) and C is a temperature constant.

This polytropic law describes how the pressure and density of these electrons vary, representing a limitation of the code. In particular, this led to a major drawback explained in Filleul et al. (2021), where the forced quasi-neutrality showed an inability to accurately describe the sheath near the spacecraft, especially the solar array impacted by the CEX-ions. In addition, the finding states that measurements from space and laboratory experiments show that the value of γ (which represents the thermal behavior of the plasma) usually falls between 1 and 1.3. This range is lower than the adiabatic coefficient, which is 5/3. The value of γ can change in different parts of the plasma thruster plume. Hence, the polytropic constant was varied between the isothermal case ($\gamma = 1$) and the adiabatic one ($\gamma = \frac{5}{3}$) so that the simulation can accurately reflect the thermal properties and potential distribution of the plasma in different regions of the thruster plume. Finally, the only available solution to address the computational limitation was to combine. By integrating Equation 1.15 with the Vlasov equation under the assumption of quasi-neutrality, the electric potential is derived as Equation 1.16, as referenced in Wartelski, Ardura, et al. (2011); Filleul et al. (2021):

$$\Phi_p = \frac{k_b \gamma T_{e,\mathrm{ref}}}{e(\gamma - 1)} \left(\frac{n_i}{n_{\mathrm{ref}}} \right)^{\gamma - 1} + \Phi \tag{1.16}$$

In this thesis, the spacecraft model in the SPIS software computes the spacecraft potential using Equation 1.16. Using the polytropic model for electron cooling and assuming quasineutrality allows for control of the plasma potential within the simulation volume. This method is unconventional compared to the standard PIC approach to solve Poisson's equation, as it involves setting the volume potentials directly by choosing a specific value of γ. Thus, varying the γ value determines the potential gradients that lead to the expected charge-exchange (CEX) backflow density distributions and fluxes to the spacecraft surfaces.

The Hall thruster model in SPIS utilizes a Monte-Carlo method (MCC) to simulate collisions between CEX-ions, neutrals and various other species (neutral Xe, Xe+, and Xe++) within the computational regions. Figure 1.16 illustrates the CEX collision. In this interaction, a fast ion collides with a slow neutral, exchanging electrons and generating fast neutrals and slow ions. Two types of CEX-ions are described using Equations 1.17 and 1.18 in the SPIS simulations.

$$Xe^{+}_{\mathrm{fast}} + Xe_{\mathrm{slow}} \rightarrow Xe_{\mathrm{fast}} + Xe^{+}_{\mathrm{slow}} \tag{1.17}$$
$$Xe^{++}_{\mathrm{fast}} + Xe_{\mathrm{slow}} \rightarrow Xe_{\mathrm{fast}} + Xe^{++}_{\mathrm{slow}} \tag{1.18}$$

$\mathrm{Xe}_{\mathrm{fast}}$ particles do not contribute significantly to charging and $\mathrm{Xe}_{\mathrm{slow}}$ is assumed to not be modified by collisions since ion-ion and ion-neutral elastic collisions are ignored, as justified elsewhere (Wartelski, Ardura, et al., 2011). The earlier work of Wartelski, Ardura, et al. (2011) and Wartelski, Theroude, et al. (2013) provides justifications for the accuracy of plume models for various electric thrusters in SPIS, demonstrating a strong correlation between experimental and in-flight data and simulated outcomes. More detailed information on SPIS and its modeling capabilities can be found in the work of Sarrailh, Matéo-Vélez, et al. (2015).

In SPIS software, the initial distribution of particles remains constant both before and after charge-exchange (CEX) ion collisions, and only their velocities change. This means that while CEX-ion collisions primarily result in the creation of new slow ions, the total particle count is not altered. Likewise, the distribution of neutrals remains unchanged; the initial slow neutral is not removed and no new fast neutral is generated. This approach simplifies the simulation by assuming that the initial conditions, including ion and neutral distributions, are unperturbed and constant. Consequently, these initial unperturbed

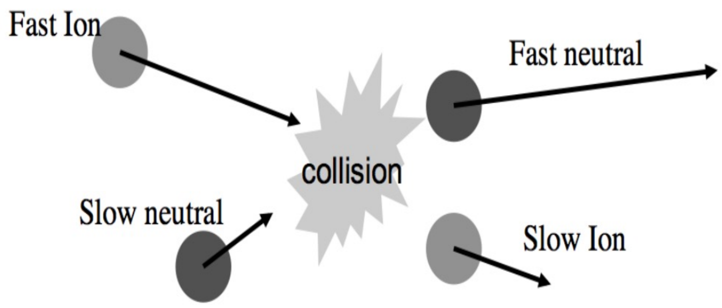

Figure 1.15: Representation of a CEX collision. Image sourced from (Loureiro, 2010)

conditions are used to calculate the rates of CEX ion production. For thruster modeling in SPIS, only ions and neutrals are simulated with PIC particles, whereas electrons are modeled as a fuid method by Wartelski, Ardura, et al. (2011). Recent experimental data from Miller et al. (2002), provides the basis for the cross section parameters used in CEX collisions, as shown in Equation 1.19. During the simulation, equation 1.19 is used to calculate the cross section for CEX collisions at each time step based on the relative velocities of the particles.

$$\sigma(\Delta v) = a - b \ln(\Delta v) \tag{1.19}$$

where σ is the CEX cross section and ΔV the relative velocity between the two particles, given in ms^{-1}.The constant parameters a and b are determined by fitting the experimental curves performed by Miller et al. (2002). The values of a and b for both types of collisions are provided in Table 1.2 ensuring that the simulation is based on real-world measurements.

Table 1.1: Cross-section parameters of CEX-collisions. Table from (Miller et al., 2002)

Type of collision	Parameter a (m^2)	Parameter b (m^2)
(Xe^+, Xe)	1.71×10^{-18}	1.18×10^{-19}
(Xe^{2+}, Xe)	1.03×10^{-18}	7.7×10^{-20}

1.6.2 Simulation Setup

1.6.2.1 Geometry

To initiate the simulation process, a CAD model is designed using the GMSH software, which is a 3D finite element grid generator equipped with an integrated CAD engine and postprocessor. The geometry used in the SPIS must include key components such as the surface of the spacecraft, the external boundaries, and the computational volume, as shown in Figure 1.16. According to the SPIS guidelines, assuming that the external boundary is three times the Debye length is crucial for achieving accurate results. The computational volume, representing the surrounding plasma, is specified in GMSH under the "physical element" tab.

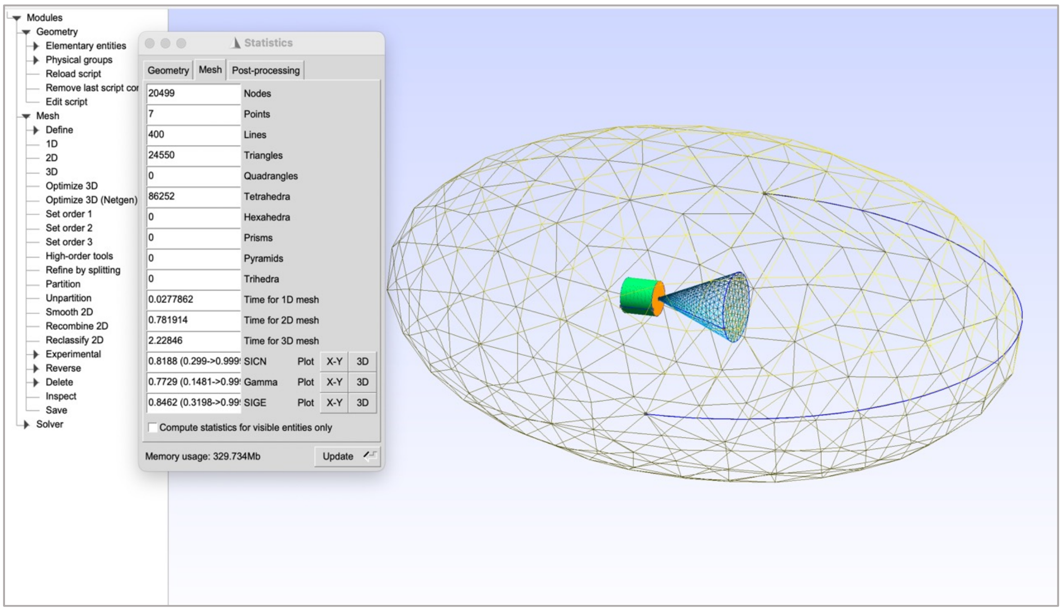

Figure 1.16: Visualization of the GMSH Interface featuring the CAD Model and Gamma Value Statistics Bar.

In addition, the user must define the mesh size for each point in the satellite structure. The mesh size for the external boundary is set to one-third of the Debye length to ensure precise results. Following meshing, it is essential to examine the statistics tab in the Tools section and verify the Gamma value. To achieve accuracy, the Gamma value (which represents the ratio of the inscribed to circumscribed sphere radius) should exceed 0.6 (as shown in Figure 1.16). Once the meshing is complete, the file should be saved in (.msh) format and loaded into SPIS.

1.6.2.2 Group Editor

After importing the file into the SPIS, the subsequent phase involves identifying various physical groups within the mesh (surfaces, volumes, boundaries) along with their specific associated properties. Users have the option to define the materials of different spacecraft components, incorporate thrusters, and allocate electrical node numbers for each group. Various types of physical groups and their associated properties are illustrated in Figure 1.17 (*Spis User Manual* n.d.).

Group type		Property type	Description
Spacecraft surface group	***Mandatory Properties***	*S/C Plasma population BC*	Define all characteristics related to the plasma model on the boundary defined by the S/C surface.
		Electrical node model	Select the electrical node for the present group. Please notice, that this property care shared with other groups.
		S/C conductivity model	Define all characteristics related to the conductivity model.
		S/C electric field	Define all characteristics related to the electric field model on the present S/C surface boundary.
		S/C macroscopic characteristics	Define all macroscopic characteristics, including thickness and temperature .
		S/C thin elements	Set if the present group corresponds to a thin element or not. See the corresponding section.
		S/C sources and interactors	Defined all characteristic related to the interactions models and sources.
		S/C material	Select the material for the present group.
		S/C mesh properties	Define all characteristics of the mesh model for the inner boundary defined by the S/C surface.
	Optional Properties	*S/C instrument support*	Set if the present group correspond to an instrument on the S/C surface or not. This option is not supported on all SPIS versions.
External boundary group	***Mandatory Properties***	*Ext. Bound. Plasma Population BC*	Define all characteristics of the plasma model on the external boundary defined by far plasma.
		Ext. Bound. Electric field BC	Define all characteristics of the electric field model on the external boundary defined by far plasma.
		Ext. Bound. mesh properties	Define all characteristics related to the mesh model the external boundary defined by far plasma.
	Optional Properties	*N/A*	N/A
Computational volume group	***Mandatory Properties***	*Volume plasma model*	Define all characteristics related to the plasma model on the external boundary defined by far plasma.
		Volume mesh properties	Define all characteristics related to the mesh model the external boundary defined by far plasma.
	Optional Properties	*N/A*	N/A

Figure 1.17: Group Editor in SPIS with Default Properties for Spacecraft (SC) and Boundary Conditions (BC) (*Spis User Manual* n.d.)

1.6.2.3 Electric Circuit

SPIS simplifies and establishes an internal circuit that interconnects spacecraft components with various instruments or thrusters, and the satellite system and surfaces. This circuit may include resistors (R), capacitors (C), or voltage generators (V) to simulate actual electrical characteristics. In the simulation, a resistor is placed between the thruster and the spacecraft to isolate the thruster from the spacecraft system. This arrangement ensures electrical decoupling, preserving isolation between the systems without mutual interaction. A representative example is given by: R 01 5000, with 'R' representing a resistor, '01' marking the node specified in the group editor, and '5000' being the resistance in Ohms.

1.6.2.4 Global Parameter Settings

The Global Parameters are used to define the global physical values of the space environment, particle interactions, and simulation setup(e.g., density, temperature, velocity, solar photon flux , simulation duration, and simulation time steps, etc.). Users can define environments within the global parameter by selecting their distribution function. *Spis User Manual* (n.d.) provides details of different distribution functions applicable to various plasma scenarios. Note that throughout our thesis, the PIC distribution is consistently employed.

1.6.2.5 Simulation Phase

Figure 1.18 illustrates the overall architecture of the SPIS software, which is divided into two primary components: the spacecraft circuit and the plasma solver. The spacecraft circuit component is tasked with resolving the electrical circuit, taking into account the currents collected from and emitted to the plasma. Users can define the circuit by specifying the resistances and capacitances of different components. Further, the plasma solver tab comprises two distinct phases as depicted in Figure 1.18, labeled fields and matter, and employs the PIC method to calculate plasma evolution. In this section, the primary focus is on the plasma part of the code as it pertains directly to the scope of this study. To the best of my understanding, spacecraft circuit solving is an integral part of SPIS simulations for scenarios where spacecraft charging effects need to be coupled with electrical circuits. However, when this functionality is not used, SPIS continues to simulate plasma dynamics without the spacecraft circuit component, treating the spacecraft as a fixed or passive boundary condition

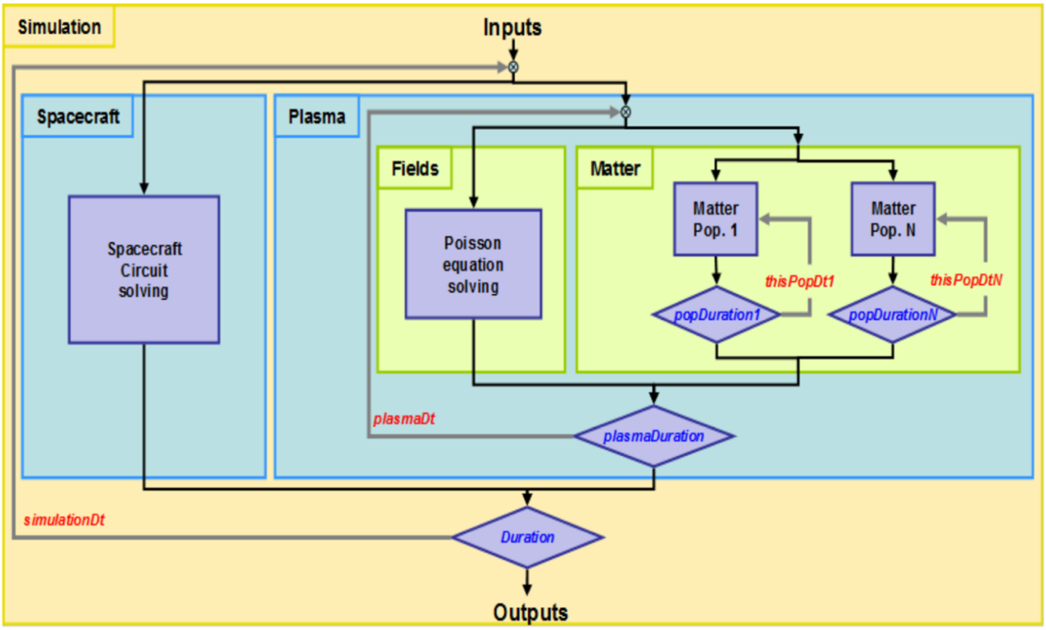

Figure 1.18: The SPIS simulation code features a hierarchical structure illustrated here. Nested boxes denote the structure of the code. Arrows signify the simulation's computational steps and time evolution, crucial information for user understanding. The image is taken from the (*Spis User Manual* n.d.)

- **Field part:** In this segment, the plasma fields are resolved either through a Poisson solver or by assuming a quasineutral plasma, where simpler techniques are utilized.
- **Matter part:** This segment is responsible for the creation and movement of particles, utilizing the fields determined in the preceding part of the cycle.

1.6.2.6 Simulation Control

Simulation convergence relies on the user-specified values for time steps and durations to achieve a steady state equilibrium. Table 1.2 presents descriptions and guidelines for time steps and durations in SPIS. *PlasmaDt* (the time step for plasma particles) is calculated on the basis of the ambient electron plasma frequency (ω_{pe}), which represents the plasma frequency in rad/s. It is derived from the formula $\omega_{pe} = \sqrt{\frac{n_e \cdot e^2}{m_e \cdot \varepsilon_0}}$, where e is the elementary charge, m_e is the electron mass, and ε_0 is the permittivity of the free space. *PlasmaDt* is then obtained from Equation 1.20:

$$Plasmadt = 0.2 \times \frac{2\pi}{\omega_{pe}} \tag{1.20}$$

Table 1.2: Description of Simulation Parameters (*Spis User Manual* n.d.)

Parameter	Description
Simulation Duration	The estimated time to reach the stable steady-state equilibrium. To achieve convergence, the user needs to do trial and error to choose the right value for the capacitance C_{sat} of the satellite (in these simulations, it usually is between 10^{-7} and 10^{-6} F).
SimulationDt	The simulation time step. It is recommended to have at least $SimulationDt \leq \frac{Duration}{100}$.
SimulationDtInit	The initial simulation time step, set as $\leq \frac{Duration}{1000}$.
PopDt = PopDuration	Time for each plasma population pop to cross the entire simulation box. Thus, it has to be set as the size of the box over the mean pop velocity.
PlasmaDt	The time step for global plasma dynamics. It is recommended to set it as a fraction of the plasma period for the stability of PIC plasma modeling: $PlasmaDt \leq 0.2 \times \frac{2\pi}{\omega_{pe}}$.
PlasmaDuration	It is recommended to use $PlasmaDuration > 2 \times PlasmaDt$.

1.6.2.7 Data Mining and Post-Processing

Figure 1.19 illustrates the simulation running and control panel; it enables continuous monitoring and tracking of the simulation progress in real-time. The monitors update automatically as the simulation evolves.

Once the simulation is completed, the results are sent back to the user interface, allowing users to export them in .vtk format. The examination of these results uses 3D visualization tools such as Cassandra or Paraview, as shown in Figure 1.20. Through this application, one can identify each property exported for every cell within the simulation volume, thereby revealing the plasma profile throughout the volume. Visualization of potential profiles, densities, and currents is possible. In Chapters 2, 3, 4, and 5 present the detailed analysis of these results using SPIS and Paraview software.

1.6.3 SPIS Limitation

In understanding the capabilities and constraints of the SPIS software, it is essential to recognize the challenges that it encounters when simulating complex plasma environments. These limitations arise primarily from computational constraints and the inherent complexity of plasma dynamics. One notable area of limitation lies in SPIS's ability to accurately model dense plasma scenarios, particularly in the context of plasma thruster

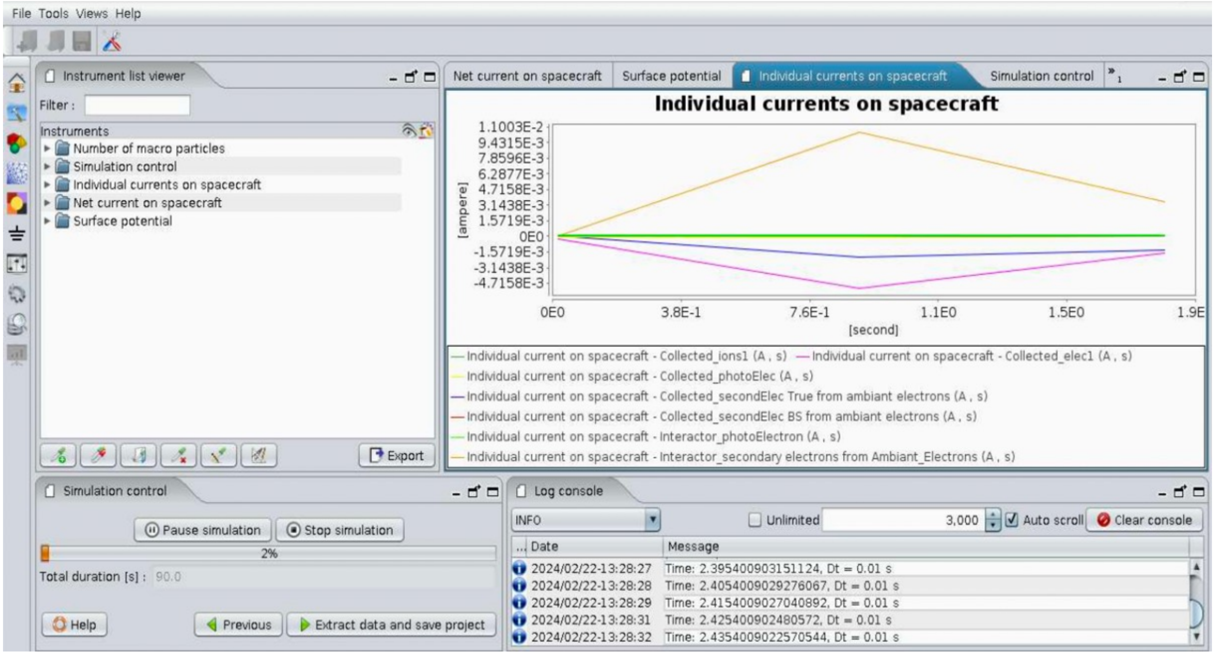

Figure 1.19: The SPIS simulation data visualisation panel

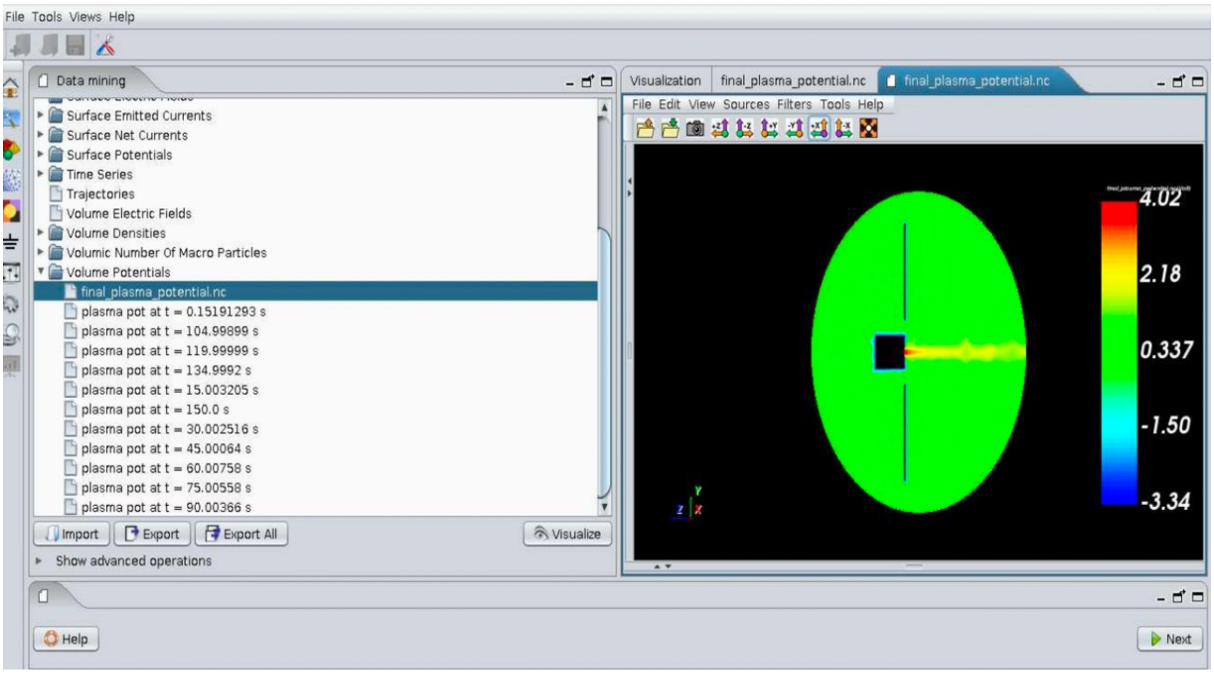

Figure 1.20: The SPIS simulation data visualisation panel

plumes. Here, the interplay between computational resources, simulation methods, and physical precision presents significant hurdles to achieving accurate results. The particular constraints and difficulties encountered by SPIS are described below, informed by direct discussions with a technical expert from the SPIS software team (Deprez, 2024) and papers published by software developers (Wartelski, Theroude, et al., 2013; Wartelski, Ardura, et al., 2011 and Sarrailh, Matéo-Vélez, et al., 2015).

1. Computational Environment Constraints:

   - SPIS, with its base solver, faces challenges when computing electrons and ions using the full Particle-In-Cell (PIC) method, particularly in dense plasmas. For example, in the Low Earth Orbit (LEO) environment, where short collision lengths and time scales lead to frequent interactions, the computational demands of resolving every particle's dynamics become impractical. Instead, the *KineticMaxwellBoltzmannVolDistrib* model (akin to the Global Maxwell-Boltzmann distribution) is used for electrons, assuming their thermalization occurs much faster than the overall plume expansion time. Similarly, in electric thruster plume simulations, the PIC method is applied specifically to *CEX-ions* and neutrals, as charge-exchange collisions dominate over other interactions. Electrons, on the other hand, are modeled using the *global Maxwell-Boltzmann distribution*, which assumes rapid equilibration relative to ion motion. These approximations ensure computational efficiency while maintaining accuracy in environments with high plasma densities (Deprez, 2024).

2. Limitations in Plume Simulation for Thrusters:

   - SPIS faces challenges in accurately simulating plasma thruster plumes, particularly when electron and ion densities are excessively high (Deprez, 2024). Although the particle-in-cell (PIC) method is mathematically accurate under certain constraints, the computational resources required for dense-plume simulations may exceed practical limits.

   - To address this limitation, SPIS employs a hybrid-fluid approach to simulate ions and electrons in plume a, incorporating an electron cooling law as explained in Section 1.5 (Filleul et al., 2021). The choice of cooling law, including options such as adiabatic, polytropic, or specifically calibrated laws, affects the accuracy of the results.

   - Using a cooling law that has been calibrated and validated using experimental data for particular thrusters, such as the SPT-100 Hall thruster, can produce accurate results within certain limits (Wartelski, Ardura, et al., 2011). However, extrapolating this approach to other thrusters (including the RIT-2X thruster) may push the limits of validity and accuracy (Deprez, 2024). It should be noted that the RIT-2X thruster simulation was carried out for the first time in our thesis using the SPIS simulation with the help of Deprez (2024) technical help. However, it requires validation through experimental data for the RIT-2X thruster.

3. Hybrid fluid approach for denser plasma environments:

   - In scenarios involving denser plasma environments, SPIS may utilize a hybrid fluid approach to solve plasma dynamics. This approach is applicable under specific conditions: Firstly, the hybrid approach is applicable when the thermal speed of a population significantly exceeds its group speed (where 'group speed' denotes the propagation speed of this electron wave packet in a medium). Secondly, if the spacecraft's overall shape is convex, then this method is considered valid and has been confirmed during SPIS developments through comparisons with spacecraft data (including measurements from Langmuir probes and spacecraft potentials) (Deprez, 2024).

4. Limitations with additional features and assumptions:

   - Incorporating elements such as ion-ion and ion-neutral elastic collisions into SPIS simulations could improve the fidelity of plume dynamics and energy distributions, but this may introduce challenges as these features are not included in the existing version of SPIS software (Wartelski, Ardura, et al., 2011). The inclusion of such features could impact computational efficiency and require further validation to ensure accuracy within the SPIS framework.

5. Validation of Simulation Results:

   - Despite the inherent challenges and limitations of SPIS discussed above, this thesis addresses simulation accuracy through validation efforts based on prior research. The AISEPS project, funded by ESA, demonstrated that SPIS models for various electric thrusters, such as the SPT-100 and RIT-10, align well with experimental data, showing excellent agreement in plume axis behaviour and satisfactory agreement in the backflow region (Wartelski, Ardura, et al., 2011). Similarly, SPIS-based spacecraft charging models have been validated with experimental data at ESA facilities, including the SMART-1 mission, which successfully replicated spacecraft ground potential behaviours and solar array effects (Wartelski, Theroude, et al., 2013). Building on this foundation, the work in this thesis began with simulations based on the geometry used in Guillemant (2014) study. We simulated spacecraft potential without the thruster, from 0.044 AU to 1 AU, and observed alignment with Guillemant's results, with slight variations in potential values. The source of these variations—whether due to differences in domain size or meshing resolution—remains unclear. To investigate, we varied the meshing size at 1 AU for the same domain size and found that spacecraft potential remained unchanged, suggesting meshing resolution does not significantly influence the results. While this thesis does not include ground-based experiments due to the challenges of replicating solar wind environments in vacuum chambers, these prior validations and our comparative analysis provide confidence in the reliability of the results.

1.7 Research Aims and Outlines

This thesis undertakes, for the first time, a comprehensive numerical simulation study to investigate the interaction between electric thrusters and spacecraft across a wide range of plasma environments. These include varying heliocentric distances from 0.044 AU to 1 AU and diverse Jovian magnetospheric plasma conditions at 5.2 AU. While similar methodologies may have been applied to various mission, the integration of electric thruster interactions with such vastly different plasma environments in a single study is unprecedented. As discussed earlier, spacecraft exposure to the space environment can result in either excessive positive or negative charging, leading to spacecraft anomalies. Furthermore, the operation of electric thrusters introduces additional currents through the backflow plume, altering the spacecraft's potential and the 3D environment around the spacecraft. Thus the primary objective of this thesis is to investigate the negative charging of spacecraft when the thruster is activated under widely varying plasma conditions. This includes analyzing the effects of different thrusters, examining the impact of the thruster facing sunlight, exploring scenarios with and without sunlight, studying the role of secondary electrons, evaluating the influence on solar panels, and assessing the effects of varying spacecraft geometry size and shape

Chapter 2 explores the effect of the SPT-100 Hall thruster plume on spacecraft potential by comparing scenarios with and without the thruster across different heliocentric distances. This chapter builds upon the preliminary results presented in Appendix 1 and Appendix 2, where solar photon flux was not considered, leading to inaccuracies in the spacecraft potential values. Consequently, all simulations were redone to ensure accurate results. Chapter 2 demonstrated that considering an accurate solar photon flux resulted in a substantial shift in spacecraft potential values, particularly in cases without the thruster. This difference is attributed to the accurate inclusion of solar-photon flux and the associated photoelectron emission. By refining these aspects, Chapter 2 offers a more comprehensive and accurate investigation. Furthermore, an in-depth examination is conducted to analyze the ram, wake, and sheath potential profiles across various heliocentric distances, aiming to enhance understanding of how the potential barrier and sheath affect the spacecraft's potential. Finally, the impact of photoelectrons and secondary electrons on spacecraft charging is evaluated, providing insights into their influence under diverse conditions.

Chapter 3 explores the dynamics of charged particles and their impact on spacecraft potential across varying heliocentric distances by comparing scenarios with and without RIT-2X and SPT-100 Hall thrusters. The primary objective is to analyze the consequences of the increased densities of CEX-ions and thruster electrons, using a high-performance RIT-2X thruster with a thrust capacity of 180 mN, and to examine its interactions with the surrounding plasma.

Chapter 4 investigates the impact on spacecraft potential in Jovian magnetospheric plasma environments for scenarios with and without RIT-2X and SPT-100 Hall thrusters. Chapter 4 analyses three distinct locations, Europa, Ganymede, and Callisto, to determine if electric thrusters exhibit consistent patterns in mitigating spacecraft charging.

Chapter 5 focuses on analyzing the impact of electric thruster plumes on solar panels, considering scenarios both with and without the thruster in two distinct locations: at 1 AU in the vicinity of Earth and another at 0.044 AU in the proximity of the Sun. It further examines the effects of changing the orientation of the solar panel's front side in relation to the thruster plume. In the final chapter, Chapter 6, conclusions are derived from the preceding research and directions for future studies are outlined.

In summary, this thesis provides a profound understanding of spacecraft charging in various plasma environments, with and without the influence of thrusters. By investigating how spacecraft potential is influenced by varying distances from the Sun, the absence of photoelectrons and secondary emissions, potential barriers, sheath effects, the plasma within Jupiter's magnetosphere, and the impacts on solar panels. Thus the research contributes to improving satellite safety and longevity strategies to mitigate the risks associated with spacecraft charging.

CHAPTER 2

Hall Thruster Plume Effects on Spacecraft Charging from 0.067 AU to 1 AU

Prepared for Journal Submission : Tejaswi L. Shinde, Iver H. Cairns, Jason. M. Held and Gregoire Deprez (Improved result of Appendices A and B)

2.1 Abstract

The backflow plume from an electric thruster can lead to the accumulation of electrostatic charge on the spacecraft, leading to a negative charge. Interactions between the plume and solar wind can further influence the charge distribution, resulting in variations in spacecraft potential and interference with sensitive instruments. A 3D Particle-In-Cell (PIC) simulation tool within the Spacecraft Plasma Interaction Software (SPIS) is used to compute spacecraft charging effects from 0.067 to 1 Astronomical Unit (AU) for the Stationary Plasma Thruster (SPT-100). Although 0.044 AU is included in the simulations without the thruster, results with the thruster were omitted due to slow and fluctuating convergence in simulations caused by high ambient plasma density and temperature. Further the study examines the dynamic behavior of ambient electrons and ions, thruster electrons, and CEX-ions, as well as photoemission and secondary electrons, and solar-photon flux impact on the spacecraft potential. The main finding is the demonstration that the high dominance of CEX-ions and thruster electrons helps to achieve a low and stable negative potential ranging from -2 to -6 V from 0.067 AU to 1 AU when the thruster is on, as opposed to the varying range of -5 to +9 V with the thruster off. Other findings show that the elimination of photoelectrons or secondary electrons has a comparatively greater impact on spacecraft potential when the thruster is off, as opposed to when the

thruster is on. Both CEX-ions and thruster electrons significantly contribute to the mitigation and regulation of spacecraft potential towards a less negative potential in situations where photoemission or secondary electrons are absent or relatively unimportant.

2.2 Introduction

In recent years, there has been a growing interest in electric propulsion systems for commercial, scientific, and interplanetary missions, mainly due to their high specific impulse, thruster controllability, and proven reliability (Goebel et al., 2023; Kuninaka et al., 2011; and Garner et al., 2013). Electric thrusters offer higher delta-V compared to chemical propulsion, which allows for additional payload capacity (Goebel et al., 2023). However, it is important to note that electric propulsion systems have some drawbacks. One significant drawback is the significantly longer time-to-destination compared to chemical propulsion systems. The prolonged journey increases the risk of major changes in the spacecraft charging while passing through the solar wind environment, e.g., in (Goebel et al., 2023; and Liu et al., 2013). The solar wind particles can cause variations in the spacecraft's electrostatic potential, severely disturbing low-energy particle and electric field measurements shown by Guillemant et al. (2012). Additionally, when an electric thruster operates in different plasma environments, spacecraft surface charging variations are expected , e.g., in (Wang, 1997 and Na et al., 2019). The effects caused by electric thruster operations have long raised both scientific and operational concerns. The plume backflow can contaminate and interact with spacecraft payload systems, potentially leading to unfavorable consequences for the mission lifetime, e.g. in (Wang, 1997; Tajmar, 2002; Lee et al., 2011; Na et al., 2019; Filleul et al., 2021).

Backflow plumes from an electric thruster consist of low-velocity charge-exchange ions (CEX-ions) that result from collisions between fast-beam ions and propellant neutrals within the main ion beam and thruster electrons emitted from the cathode as discussed in Goebel et al. (2023). These low-energy ions and electrons flow back toward the spacecraft, giving rise to two primary effects. First, effluent deposition causes contamination of optical sensors, solar arrays, thermal control systems, and other communication devices. Secondly, the presence of CEX-ions and associated electrons modify the properties of the solar wind surrounding the spacecraft, leading to an additional current that can influence the spacecraft potential and plasma instrument observations, as discussed in Wang (1997). Consequently, studying thruster-induced plasma and solar wind effects on spacecraft charging in different environments is crucial to avoid operational and measurement anomalies and failures. However, performing such complex interaction measurements in a vacuum chamber presents challenges due to the physical scale of the system and the inability to fully replicate the solar wind environment, which makes it time-consuming, often inaccurate, and expensive. Therefore, numerical simulations play a vital role in predicting thruster-spacecraft interactions and provide a more comprehensive way to gain valuable insights into charging characteristics compared to ground tests.

Referring to solar wind effects on spacecraft charging at various heliocentric distances, Guillemant et al. (2012) investigated variations in spacecraft potential, electrostatic sheath, and potential barrier with distance to the Sun using the Spacecraft Plasma Interaction Software (SPIS). The simulation result revealed that the spacecraft charged positively by a few volts from 1 AU to around 0.3 AU. However, within 0.3 AU, the potential barrier generated by photoelectrons and secondary electrons caused the potential to become negative. These low-energy electrons tended to surround the spacecraft, generating a potential barrier that significantly affected the plasma potential and led to high recollection of low-energy electrons. Consequently, these low-energy electrons could interfere with plasma sensors and particle detectors, biasing the particle distribution functions measured by the instruments, as shown in Guillemant et al. (2012).

Numerical simulations conducted by several researchers explore the interaction between the surface of the spacecraft and the thruster plume. A consistent finding across simulations is the significant impact of the backflow plume of charge-exchange (CEX) ions, since their density is much higher compared to the ambient density, as documented in various studies (Wang, 1997; Tajmar, 2002; Lee et al., 2011; Na et al., 2019; Filleul et al., 2021). Acting as a neutralizer, CEX-ions and thruster electrons play a crucial role in mitigating the negative potential of the spacecraft. Real flight data collected from the SMART-1 spacecraft led to significant insights into the behavior of Charge Exchange (CEX) ions in the spacecraft environment. The study identified two groups of CEX ions with distinct energy levels of approximately 35 eV and 65 eV. The group with 35 eV energy was found to dominate, as it primarily consists of singly charged ions, while the group with 65 eV energy, attributed to doubly charged ions, had a much lower density and was therefore considered negligible (Na et al., 2019). In a separate flight, the Cluster spacecraft was observed to acquire a high positive potential due to substantial currents from photoelectrons. The strong electrostatic sheath that enveloped the spacecraft introduced disruptions in the measurements of the electric field and the particle field (Torkar et al., 2001). To mitigate this challenge, the Cluster spacecraft integrated an indium-ion emitter, capable of producing ions within the 5 to 9 keV energy range, at currents ranging in the tens of microamperes. The Active Spacecraft Potential Controller (ASPOC), an instrument on board the Cluster spacecraft, showcased significant reductions in spacecraft potential, leading to enhancements in particle measurements; see (Torkar et al., 2001). Similar favorable results were also observed in the case of the Double Star TC-1 spacecraft by K. Torkar et al. (2005). The phenomenon demonstrates the benefits of the presence of a positive ion beam in lowering and stabilizing the potential, reducing potential variation, and enhancing particle measurements.

However, understanding these complex interactions and their implications for spacecraft potential remain elusive, particularly considering variations in solar wind conditions, the presence or absence of photoelectrons, and secondary electrons. Consequently, the aim of our research is to investigate ion-induced charging effects on spacecraft potential across various heliocentric distances using the Spacecraft Plasma Interaction Software (SPIS). The investigation will be based on factors involving ambient electrons and ions, secondary electrons and photoelectrons, CEX-ions and thruster electrons, and solar photon flux. In my first conference paper, the impact of the SPT-100 Hall thruster on spacecraft potential at heliocentric distances of 1 AU and 0.093 AU was examined by Shinde, Held, and Cairns (2022). The results revealed that both CEX-ions and thruster electrons dominate the satellite's plasma environment at both distances, resulting in negative spacecraft potentials because of the higher thruster electron impact rate. Moreover, at 0.093 AU, the effects of photoelectrons and secondary electrons become slightly more significant than at 1AU, leading to more positive spacecraft potentials. Another study by Shinde, Held, and Cairns (2023) showed the effects of ion-induced charging from 0.044 AU to 1 AU by comparing spacecraft potential variations and current evaluations for various sources with thruster on and off. The study demonstrated that electric thrusters can effectively maintain a low negative potential over a wide range of heliocentric distances. In particular, when the thruster is active, a substantial reduction in the spatial size of the sheath and the potential barrier was observed. However, it is important to note that the study by Shinde, Held, and Cairns (2023) did not account for the inverse distance squared fall-off of the solar photon flux.

The purpose of this paper is to investigate the effects of various factors on spacecraft charging in different solar wind conditions when the SPT-100 Hall thruster is switched on and off. These factors include ambient electrons and ions, thruster electrons and CEX-ions, photoemission and secondary electrons, and the solar photon flux at different heliocentric distances. The spatial profiles of the ram, wake, and electrostatic sheath structure for all heliocentric distances will also be examined. To achieve this, SPIS software will be used for simulation setup and modeling of physical parameters (Section 2). The paper will then show the result in Section 3. Section 3.1 shows the analysis of the spacecraft potential variation and derives a best-fit equation for conditions with and without the thruster across the range from 0.067 AU to 1 AU. Please note that 0.044 AU is included in the simulations without the thruster, results with the thruster were omitted due to slow and fluctuating convergence in simulations caused by high ambient plasma density and temperature. Additionally, the collected and emitted currents on the satellite's surface will be studied under different thruster conditions (Section 3.2). Detailed potential profiles of the ram, wake, and sheath surrounding the spacecraft will be presented in Section 3.3. Section 3.4 will focus on the role of secondary electrons at 0.067 AU and 1 AU, with and without the thruster. The importance of photoelectrons in influencing spacecraft potential will be discussed in Section 3.5 for these distances, with and without the thruster. Finally, in Section 3.6, the combined effect of neglecting secondary electrons and photoelectrons on the spacecraft potential will be examined at 0.067 AU and 1 AU, with and without the thruster. By addressing these aspects comprehensively, the paper aims to provide a thorough understanding of spacecraft charging under different solar wind conditions and the influence of the SPT-100 Hall thruster on spacecraft potential.

2.3 Simulation setup

Spacecraft Plasma Interaction Software (SPIS) version 6.1.0 is an open-source simulation tool which solves the electrostatic potential and motion of charged and neutral particles in 3D. The setup for the simulation involves specifying the spacecraft's geometry, computational mesh, material properties, internal circuitry, and the simulated environment. In this paper, the same spacecraft model is employed as in the prior research by Shinde, Held, and Cairns (2022) and Shinde, Held, and Cairns (2023) representing it as a cylinder with a 1 m radius and a 2 m long, coated with indium tin oxide (ITO) material. The dimensions of the simulation domain vary based on the Debye length, and accordingly, the mesh refinement are applied. According to the SPIS user manual [*Spis User Manual* n.d.] the domain dimension must be larger than three times the (thermal electron) Debye length (3 x Debye length). Meanwhile, the mesh resolution within the domain is always less than one-third of the Debye length, resulting in 50,000 to 100,000 mesh tetrahedrons. The spacecraft mesh size is based on the thermal and photoelectron electron Debye lengths (one-third of the local plasma Debye length). The satellite model is created using the Gmsh software, version 4.10.5 which is free software to generate a mesh geometry and to perform post-processing, available online at (*GMSH* n.d.), as shown in Figure 2.1 and Table 2.1. The physical parameters for simulating various heliocentric distances are adopted from Guillemant (2014) as shown in Table 2.2. The simulation considers varying plasma properties, such as density, temperature, and bulk velocity, varying photon flux, and timesteps for ions, thermal electrons, secondary electrons, and photoelectrons. Additionally, the solar photon flux is taken into account. For simplification, the satellite is assumed to be stationary relative to the Sun. Therefore, only the solar wind ion drift velocity, directed along the x-axis, is simulated. The corresponding electron drift is neglected since it is small compared with the electron thermal speed, which is not true for the ions.

Table 2.1: Gmsh Geometry Dimensions and Thruster Specifications.

Parameters	**Value**
Geometry	1m radius, 2m long, cylinder
Surface Material	Indium Tin Oxide
Photoelectron temperature	3eV
Thruster Electron Temperature	0.5eV
Ambient Ion type	H+
Ion modelling	PIC
Electron modelling	PIC
Magnetic Field	Not considered
Thruster Specification	
Ion Thruster	SPT-100 Hall
Thrust	0.035 N
Specific Impulse	1840s
Cathode Temperature	5 eV
Mass Flow rate (Xe)	1.91×10^{-6} Kg/s
Current	1.43 A
Power	723 W

Table 2.2: Physical Parameters Used in SPIS To Simulate Various Environments Charging Effects from (Guillemant, 2014)

Distance (AU)	**1**	**0.42**	**0.72**	**0.25**	**0.162**	**0.11**	**0.093**	**0.067**	**0.044**
Solar Flux	1	1.93	4.73	16.0	38.10	82.64	115.62	222.7	516.53
$N_e = N_i$ (m^{-3})	6.93e6	1.35e7	3.67e7	1.19e8	3.10e8	8.03e8	1.14e9	1.94e9	7.0e9
$T_e(eV)$	8.14	10.41	14.52	22.95	31.77	41.50	48.33	59.25	84.47
$T_i(eV)$	8.00	11.21	17.00	30.76	39.90	49.00	55.82	67.00	87.25
Vram(km/s)	430.00	429.00	400.00	401.40	366.00	355.00	350.00	335.00	300.00
Debye length (m)	8.06	6.52	4.67	3.27	2.38	1.69	1.53	1.30	0.82
Debye length of photoelectrons (m)	0.98	0.71	0.45	0.25	0.16	0.11	0.09	0.07	0.04
Secondaries $T_e(eV)$	0.28	0.35	0.45	0.7	0.95	1.2	1.32	1.55	1.92

During simulations, the thruster is assumed to be electrically isolated from the spacecraft chassis, while the spacecraft surface floats with the plasma. The anode and cathode of the thruster are isolated from the spacecraft using a resistor. To manage excessive charging, a 500 kilo Ohm resistor is introduced between the thruster and the spacecraft, providing a return path for leakage currents. The resistor ensures a high degree of isolation between the thruster and the spacecraft surface, thus limiting potential charging issues (Liu et al., 2013). It is crucial to note that the ground of the spacecraft is distinct from the ground of the electric thrusters. This configuration is adopted primarily to reduce spacecraft contamination caused by thruster plumes, as discussed in Liu et al. (2013). During the simulations, the magnetic field and backscattered electrons are not considered. Figure 2.1 shows the center of the cylinder representing the spacecraft located at the origin of the Cartesian coordinate system (0, 0, 0). The orientation of the plane is as follows: the x-axis points along the thruster axis (i.e., the length of the cylinder), the y-axis points vertically upward along the plane of the paper, and the z-axis points outward from the plane.

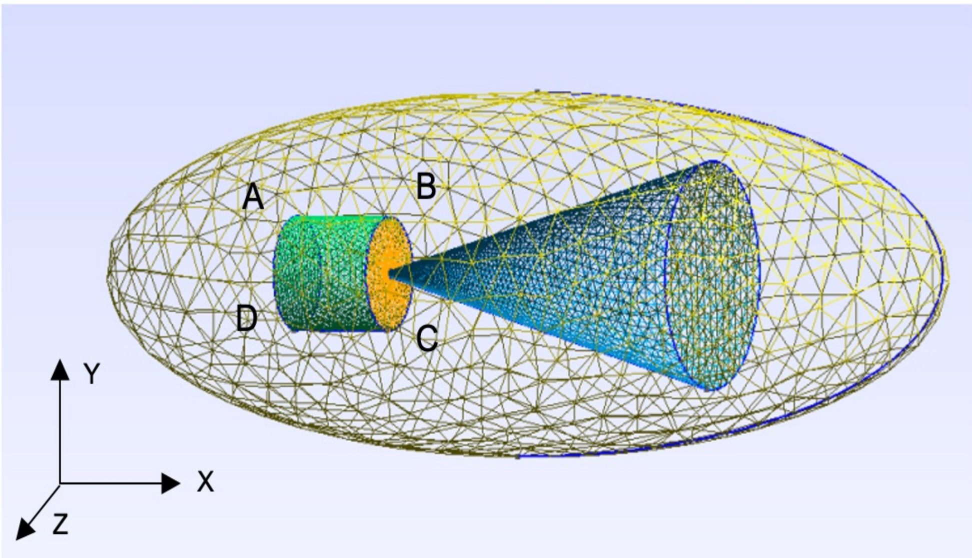

Figure 2.1: GMSH spacecraft model with a meshing grid (green/yellow), the void boundary is the simulation boundary, and the blue conical shape represents the ion plume.

2.4 Results

2.4.1 Variations of the Potential from 0.067 AU to 1 AU

The variation in spacecraft potential across a range of heliocentric distances is significantly influenced by the presence of the thruster and solar-photon flux. Figure 2.2 highlights these variations, distinguishing between scenarios with and without solar-photon flux. The dotted curve indicates the spacecraft potential without the solar-photon flux, while the solid curves indicate with the solar-photon flux. Consider a distance greater than 0.25 AU, without the thruster, where the charging effects are less critical compared to a near-Sun environment. The region is dominated by photoelectrons (without the thruster) due to their much higher density of 10^8 m^{-3} compared to other number densities (ambient ions 10^7 m$^{-3.}$, thermal electron 10^7 m^{-3}, secondaries 10^7 m^{-3}) which all vary with the inverse squared distance from the Sun, see (Shinde, Held, and Cairns, 2022). The decreasing mean energy of thermal electrons reduces the secondary emission rate. Moreover, the ambient ions become a source of secondary electrons due to proton impact (SEEP) on the spacecraft surface and so increase the secondary electron density. As shown in Figure 2.2, outside 0.25 AU the spacecraft potential (without thruster) is positive and increases monotonically with increasing distance. The positive charging of the spacecraft can be explained by the emission of photoelectrons in the thick-sheath approximation, which holds validity in this instance (Guillemant, 2014). This is also referred to as the Orbital Motion Limited model, where spacecraft charging is affected by the spacecraft's motion through the surrounding plasma, as explained in Guillemant (2014). When the Debye length of photoelectrons is greater than the spacecraft's size, the potential barrier (shown in Section 2.4.3) does not restrict the escape of photoelectrons and secondary particles, thereby resulting in the spacecraft's positive charging. The recollection of secondary electrons in this region is simply due to the positive potential of the spacecraft.

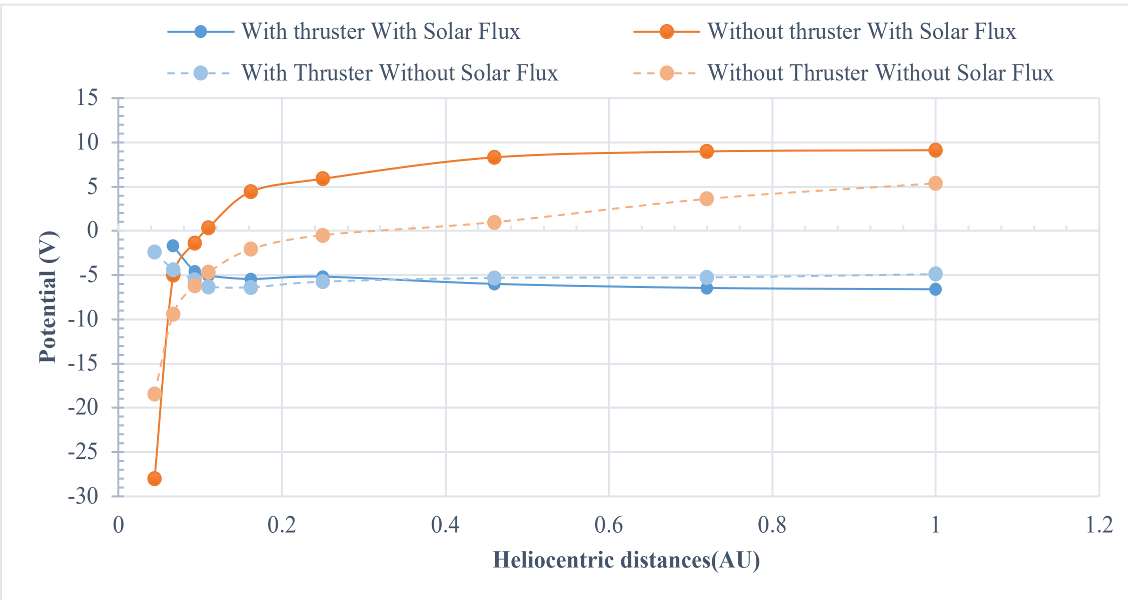

Figure 2.2: Plot showing the spacecraft potential (volts, x-axis) with and without the SPT-100 Hall thruster, as a function of heliocentric distance (AU, y-axis). The solid blue and orange lines represent the spacecraft potential considering solar photon flux, while the dotted orange and blue lines illustrate the potential variation when solar photon flux is excluded.

Below 0.25 AU, close to the Sun, the spacecraft charging effects become more critical because of the hot and dense ambient environment, despite higher photoemission and secondary emission rates from the surfaces exposed to the plasma. As shown in Figure 2.2 without the thruster, the satellite potential decreases to -28.6 V at 0.044 AU. The negative charging can be explained by the fact that the high thermal electron density of 10^9 m^{-3} and temperature of about 100 eV dominate and charge the spacecraft negatively despite the high photoemission; see, e.g., (Guillemant, 2014 and Ergun et al., 2010). This result might appear contradictory when considering photoemission, but it can be explained by the fact that the temperature of thermal electrons is much higher compared to that of photoelectrons and secondary electrons. As a result, the local potential barrier (detailed in Section 2.4.3) is closer to the surface, restricting the escape of photoelectrons and secondary electrons and leading to a high level of recollection. The study Guillemant (2014) demonstrates that recollection of photoelectrons and secondary electrons is extremely efficient in achieving a current balance with a negative spacecraft potential. This phenomenon corresponds to a thin sheath, also known as the space-charge limited model, which holds true when the Debye length of photoelectrons is smaller than the spacecraft size, for a detailed explanation see (Guillemant, 2014). In such cases, spacecraft charging is primarily influenced by the space charge, which dominates plasma behavior. In the previously reported paper by Shinde, Held, and Cairns (2023), similar behavior is observed; however, when an accurate solar photon flux is included, a substantial shift in spacecraft potential values is evident in Figure 2.2, particularly, without the thruster. This difference is attributed to the accurate inclusion of solar-photon flux and associated photoelectron emission.

In contrast, when the thruster is operating, a low and stable negative potential is obtained (from -2 V to -6 V) over a wide range of heliocentric distances from 0.067 AU to 1 AU. The primary reason is due to the CEX-ions and the electrons from the cathode dominating the surface and surrounding plasma, since their number densities are much higher, 10^{10} m^{-3} and 10^{11} m^{-3}, respectively. The CEX-ions create a dense cloud surrounding the spacecraft that interacts with the charged particles present near the spacecraft. The thruster electrons follow the same path as CEX-ions but with a much higher thermal speed and charging current, which leads to a negative charge and potential on the spacecraft. The CEX-ions act as a protective shield between the spacecraft and the surrounding plasma, thereby reducing the impact of ambient electrons. As a result, the operation of an electric thruster provides additional current that controls and stabilizes the spacecraft's potential to a low negative potential. For example, at 0.067 AU, the spacecraft potential converges to -1.74 V instead of -4.36 V without the thruster. A significant difference in spacecraft potential with and without the thruster (from 0.067 AU to 1AU) is mainly due to the high dominance CEX-ions and thruster electrons that reduce the potential barrier (as shown in Section

2.4.3) surrounding the spacecraft, which no longer restrict the escape of photoelectron and secondaries, thus leading to a much less negative potential.

At a distance of 0.044 AU from the Sun, the potential of the spacecraft with the thruster is uncertain due to slow and fluctuating convergence. Multiple simulations using the PIC distribution have been performed to assess the spacecraft's potential convergence, which appears to lie within the range of -1 to -3 V. However, as of the present date, the simulations exhibit a significant fluctuation with time and have not yet reached convergence. To verify these results, a similar simulation was rerun using the assumption of Maxwell-Boltzmann distributions where thermal electrons are treated as fluid. In this case, the spacecraft's potential lies within the same range of -1 to -3 V, but the convergence is slower, albeit more stable. The sluggish convergence may be due to the high ambient electron and ion temperature and density, which are on the order of 100eV. These factors are likely impeding the attainment of a faster convergence in the PIC and Maxwell-Boltzmann distribution simulations.

The previous paper Shinde, Held, and Cairns (2023) achieved qualitatively similar results. However, the paper considered a constant solar photon flux, leading to an inaccurate spacecraft potential without the thruster, as shown in Figure 2.2 by the differences between the light orange dotted curve and points (without the correct photon flux) and the solid dark orange lines and points (with the correct photon flux). Interestingly, there were only very small variations in spacecraft potential with the thruster active in Figure 2.2 for the accurate (dark blue solid curve and points) and constant (light blue dotted curve and points) solar flux cases. Therefore, the current study validates that the solar photon flux doesn't significantly impact spacecraft charging when the thruster is on, in contrast to the scenario without the thruster. It also demonstrates that electric thrusters consistently contribute to reducing and stabilising the spacecraft potential at small negative values across various solar wind conditions, charging it to a low negative potential regardless of solar photon flux.

2.4.1.1 Fitting Curve

to analyze the relationship between spacecraft potential and heliocentric distances, fitting curves are used to derive mathematical models for both cases. Figure 2.3 demonstrates these fitted curves, providing insights into the potential trends with and without the SPT-100 Hall thruster. A non-linear least square Mathematica model is used to fit the curve and estimate the equation for both cases. Equation 2.1 gives the potential in volts without the SPT-100 Hall thruster on for the simulated spacecraft from 0.044 AU to 1 AU:

$$\Phi = 8.4 - \frac{0.00077}{x^4} + \frac{0.0293}{x^3} - \frac{0.362}{x^2} + \frac{0.542}{x} + 0.623x^2 \quad \text{(V)} \tag{2.1}$$

Here the heliocentric distance x is in the unit of AU. Similarly, Equation 2.2 predicts the potential of the same spacecraft with the SPT-100 Hall thruster operating for the same geometry from 0.067 AU to 1 AU (0.044 AU is not considered due to the uncertain value of spacecraft potential):

$$\Phi = -6.2 - \frac{0.00002}{x^5} + \frac{0.0009}{x^4} - \frac{0.012}{x^3} + \frac{0.0673}{x^2} - 0.495x^2 \quad \text{(V)} \tag{2.2}$$

These equations can be used to predict the spacecraft potential at values of r that have not been simulated. It's worth noting that while we've simplified the terms in the fitting equations by selectively retaining only those terms that significantly contribute to reducing the residual error between the simulated data and the curve. The equations remain a combination of polynomial terms, which are necessary to accurately represent the underlying data and functions over the entire range of distances considered.

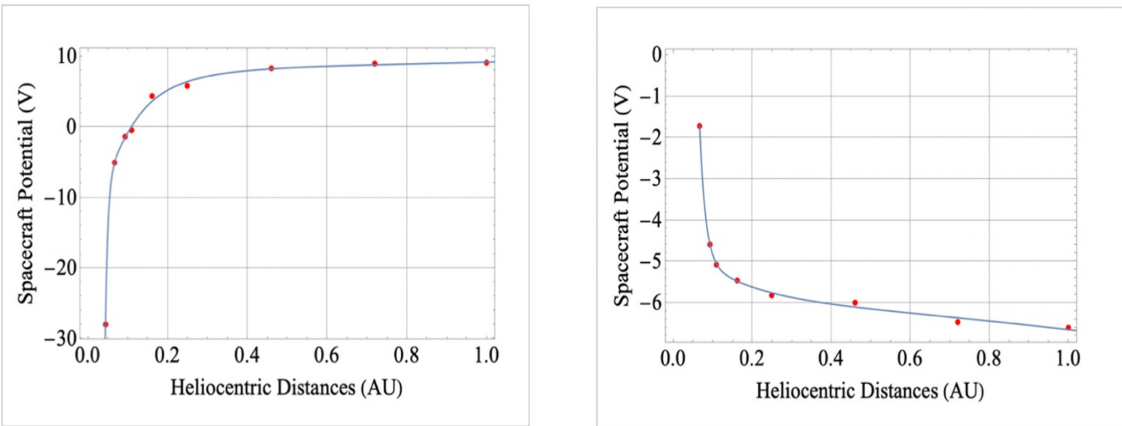

Figure 2.3: Best-fit curves without and with a thruster vs. heliocentric distance: (Left) 0.044 AU to 1 AU, (right): 0.067 to 1 AU.

2.4.2 Collected and Emitted currents

Understanding how different particle currents vary with heliocentric distance is crucial for evaluating spacecraft charging dynamics. Figure 2.4 presents the collected and emitted currents for various particles, including solar wind and thruster particles, across distances from 0.067 AU to 1 AU. The photoelectron, secondary electron, thermal electron and thruster electron currents increase monotonically in magnitude with increasing distance from the Sun from 0.067 AU to 1 AU. On the other hand, it is apparent that the collected CEX-ion current is closely constant for all helio distances considered. (Note that all currents are considered positive for simplicity). An orange-dotted curve indicates the spacecraft's potential for various heliocentric distances from 0.067 AU to 1 AU. Table 3 provides the main output current values with and without the thrusters for all the simulation cases.

Considering the region further away from the Sun, beyond 0.25 AU, a consistently low and negative potential is observed from 0.25 AU to 1 AU in Figure 2.4. In this region, the low mean energy of ambient thermal electrons reduces the occurrence of secondary electron emission. The spacecraft surface is primarily influenced by photoelectrons, resulting in positive charging when the thruster is off. However, when the thruster is operated, the positively charged surface becomes enveloped by a dense cloud of CEX-ions, which are associated with higher-speed thruster electrons that are attracted to the positively charged surface. The surface accumulates more thruster electrons to neutralize the positive charge. Since the thermal speed of electrons is much higher than ions the surface collects more negative electrons per unit time, so we often obtain a negative potential when the thruster is on. It is evident from Figure 2.4 that the collected current of CEX-ion and thruster electrons at 1 AU is about 6.8 mA and 5.7 mA, respectively, which is much higher than the thermal electron current of 0.004 mA. Thus, the thruster backflow plume dominates the solar wind effects in this region.

Between 0.162 AU and 0.093 AU, the dominance of CEX-ions and thruster electrons current is much higher than that of thermal electrons. Concurrently, the photoelectron emission and secondary electron emission significantly increase with a smaller distance to the Sun. At the distance of 0.067 AU, the collection current of CEX-ions of about 7.7 mA is slightly higher than the collection current of thermal electrons, which stands at 6.4 mA. Nevertheless, the currents of photoemission and secondary electron emission far exceed that of the thermal electrons. These factors collaboratively contribute to the mitigation of the spacecraft's negative charge. For instance, at 0.067 AU, the spacecraft's negative potential diminishes to a lower value of -1.70 V, as opposed to the value of -5.01 V when the thruster is off. However, it's important to note that the CEX-ions and thruster electron neutralizing effects can lose their validity, if the CEX-ions are smaller than that of the thermal electron collection current. In such a case, the high-energy ambient electrons will dominate the spacecraft, resulting in a substantial negative potential. Notably, the condition at 0.044 AU and 0.025 AU is omitted due to its instability and longer duration to obtain the convergence.

Analysis of Figure 2.4 shows that from 0.11 AU to 0.067 AU, the thruster electron collection current increases monotonically as the spacecraft approaches the Sun. One possible explanation for this phenomenon is that prior to the thruster's operation, the spacecraft's surface carries a negative charge due to the presence of a high thermal electron density. However, upon thruster activation, the dense cloud of CEX-ions plays a significant role in neutralizing the spacecraft's negative charge. The neutralization occurs primarily by diminishing the strong electrostatic sheath that surrounds the spacecraft. Consequently, photoelectrons and secondary electrons are more prone to escaping from the spacecraft's surface, contributing to the reduction of the negative charge. As a result, the surface tends to attract more of the low-energy thruster electrons in order to attain equilibrium between the emitted and collected currents. The recollection of secondary electrons at 0.067 AU is notably reduced from 12 mA to 5.5 mA, which may result in diminished interference with low plasma measurements. Similarly, the recollection of photoelectrons at 0.067 AU is reduced from 19 mA to 16 mA. Thus, the study indicates that near-Sun environment, CEX-ions and thruster electrons emitted from the thruster play a crucial role in mitigating the negative charging of the spacecraft. Furthermore, the finding suggests that the CEX-ions and thruster electrons are an crucial parameter in determining the spacecraft's final potential when the thruster is on.

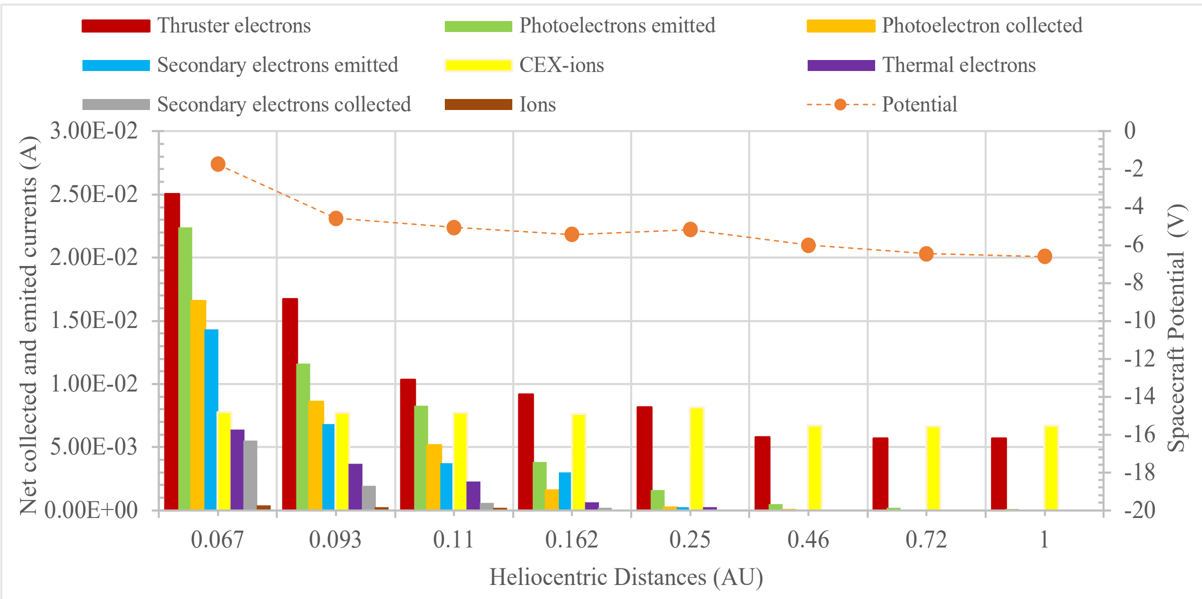

Figure 2.4: With the thruster on collected and emitted currents (on the primary axis) and spacecraft potential (on the right-hand axis) versus heliocentric distance.

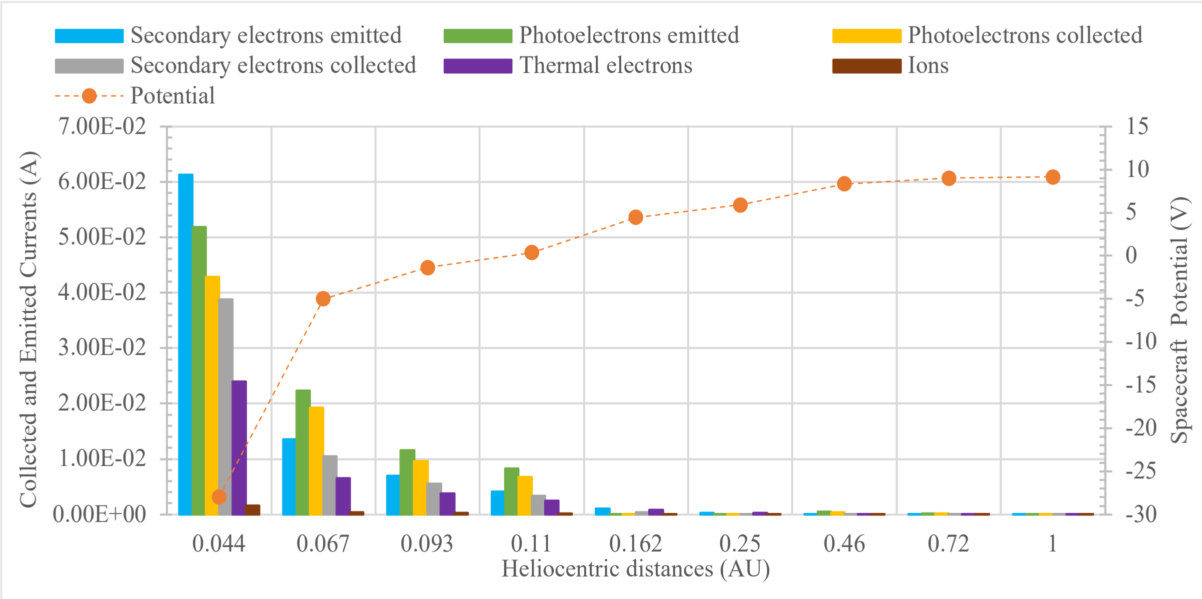

Figure 2.5: Without the thruster collected and emitted currents (on the primary axis) and spacecraft potential (on the right-hand axis) versus heliocentric distances.

In contrast, in the absence of the thruster, when the spacecraft is far away from the Sun (beyond 0.25 AU), the main charging factor is photoelectrons, due to the low mean energy of thermal electrons that reduces the rate of secondary electron emission. As shown in Figure 2.5, at 0.025 AU, the emitted current of photoelectrons is 0.1mA, which is significantly higher than the collected current of thermal electrons at approximately 0.021 mA. Higher photoemission currents result in a positively charged surface. Moving closer to the Sun, within 0.11 AU, the spacecraft's potential decreases sharply and becomes strongly negative, converging to approximately -28 V (at 0.044 AU), despite the presence of high photoelectron and secondary electron emission. As explained in Section 2.4.3 , the electrostatic sheath becomes closer to the spacecraft and restricts the escape of photoelectrons and secondary electrons. Due to their insufficient kinetic energy, photoelectrons and secondary electrons do not overcome the strong potential barrier, resulting in high recollection and their return to the spacecraft's surface (Ergun et al., 2010 and Guillemant, 2014). The secondary electrons, totaling 38 mA, are recollected back to the spacecraft, leading to the build-up of negative charge. In this scenario, an equilibrium is reached when a significant amount of photoelectron current and secondary electron is collected (Guillemant, 2014). However, the recollection of these low-energy electrons interferes with the measurement of a low-energy plasma and contaminates the data. Therefore, having an electric thruster can be beneficial as it provides a stabilizing effect on the spacecraft potential restricting it to small negative values in the range of -2V to -6V and enhances the accuracy of low-plasma measurements, considering that the CEX-ion and thruster electron density is much larger than the ambient density.

2.4.3 Ram, Wake, and Side Potential Profiles

Figure 2.6 demonstrates the intrinsically 2D (rotationally symmetric) nature of the potential structure of the spacecraft, which is obtained by cutting Figure 1 along the y = 1 plane to vary the heliocentric distances. The ram direction is in the negative x-axis direction, and the wake direction is along the positive x-axis. The left images depict the potential with the thruster on from 0.067 to 1 AU, while the right-hand images show the potential without the thruster activated, for distances from 0.044 to 1 AU. The negative potential wells due to photoelectrons and secondary electrons are visible in the ram direction (left side) for all helio distances when the thruster is on and for distances less than 0.25 AU when the thruster is off. In the wake direction the thruster makes the potential positive at all distances, but when the thruster is off a negative well in the potential is visible within about 0.25 AU. This is the standard potential well caused by the exclusion of ambient ions streaming from the Sun by the spacecraft body, whereas the ambient electrons can easily access this region due to their large thermal speeds, making the net charge and potential negative. On the sides (e.g., the +/- z direction), the potential shows a relatively standard sheath.Figure 7 illustrates the evolution of the potential profiles in the ram, wake, and z directions with and without the thruster at various heliocentric distances.

Figures 2.7a and 2.7b show the ram potential, with and without the thruster, in the top left and top right panels, respectively. With the thruster on, as the spacecraft moves from 1 AU to 0.46 AU, it experiences a minimum ram potential near -4 to -5 V, likely due to the accumulation of thruster electrons (Figure 2.7a). A localized minimum in potential ranging from -7 to -11 V is observed interior to 0.25 AU. The localized minimum can act as a potential barrier or a trap depending on the particle charge. However, the CEX-ions play a crucial role in neutralizing this potential barrier, maintaining the spacecraft's potential at a more positive value. It is evident from Figure 2.7a at 0.067 AU, where the potential barrier is reduced from -14 to -8 V, mainly due to the presence of CEX-ions that help neutralize the charge surrounding the spacecraft. However, without the thruster, a positive ram potential is observed in the range of 0.6 to 9 V from 1 AU to 0.25 AU (as shown in Figure 2.7 b). Interior to 0.11 AU, a similar minimum in potential occurs even when the thruster is inactive, although the potential is much more negative than when the thruster is on. For example, at 0.067 AU, the potential barrier reaches -14.1 V without the thruster, while it is only -8.3 V with the thruster on. Furthermore, at 0.044 AU, the ram barrier reaches -34 V when the thruster is off, leading to a significant recollection of secondary electrons emitted from the spacecraft. Therefore, the ram potential barriers are substantially reduced when the electric thruster operates near the Sun.

Figures 2.7c and 2.7d show the wake potential structure with and without the thruster in the middle left and middle right panels, respectively. A stable positive potential of approximately +25 V is observed at the satellite when the thruster is on, with the potential decreasing monotonically with increasing distances from the spacecraft (Figure 2.7c). Note that the potential profiles are essentially independent of helio distance when the thruster is on, consistent with the thruster plume dominating all other charging influences. Taken together, the wake region behind the spacecraft is filled with ions and electrons emitted from the thruster. As a result, it develops a plasma sheath which acts as a barrier to ambient electrons directly impacting the spacecraft's surface. The sheath's reduction of potential with increasing distance into the plasma is primarily due to larger electron densities. Overall, the presence of positive ions in the wake of an electric thruster can play a significant role in reducing spacecraft charging and managing potential barriers, contributing to the safe and stable operation of the spacecraft in the space environment. On the other hand, without the thruster on (Figure 2.7d), the wake potentials at and above 0.25AU decrease monotonically with increasing distance from the spacecraft. However, interior to 0.162 AU the profile develops a localized minimum near x = 1 m with a magnitude that increases as the heliocentric distance decreases. For instance, at 0.067 AU this wake barrier reaches -14 V when the thruster is off. Further towards the Sun at 0.044 AU, the wake barrier reaches -40 V which may result in the return of low-energy electrons back to the surface and enhancing spacecraft charging dynamics. Thus, when the thruster is off the spatial profiles of the potential in the ram and wake directions are surprisingly similar, presumably because of increased electron densities due to increased photoelectron effects (ram direction) and hotter, denser, ambient electrons in the wake cavity, respectively.

Figures 2.7e and 2.7f show the sheath profiles (perpendicular to the ram and wake axis) with and without the thruster in the bottom left and bottom right panels, respectively. Figure 2.7e shows a low, negative potential in a small range of -2 to -6 V from 0.067 AU to 1 AU with the thruster on compared to Figure 7f having a large range of -40 to +9 V with the thruster off from 0.044 AU to 1 AU, respectively. With the thruster on the spatial profiles are reminiscent of a standard sheath for cold dense electrons (small Debye length) about a negative potential object for R > 0.093 AU. Similarly, for R > 0.093 AU and the thruster off the monotonic potential profile appears appropriate for a standard sheath about a positively charged object for warm dilute electrons (large Debye length). Only for R< 0.093 AU do the perpendicular sheaths change character and evolve to having

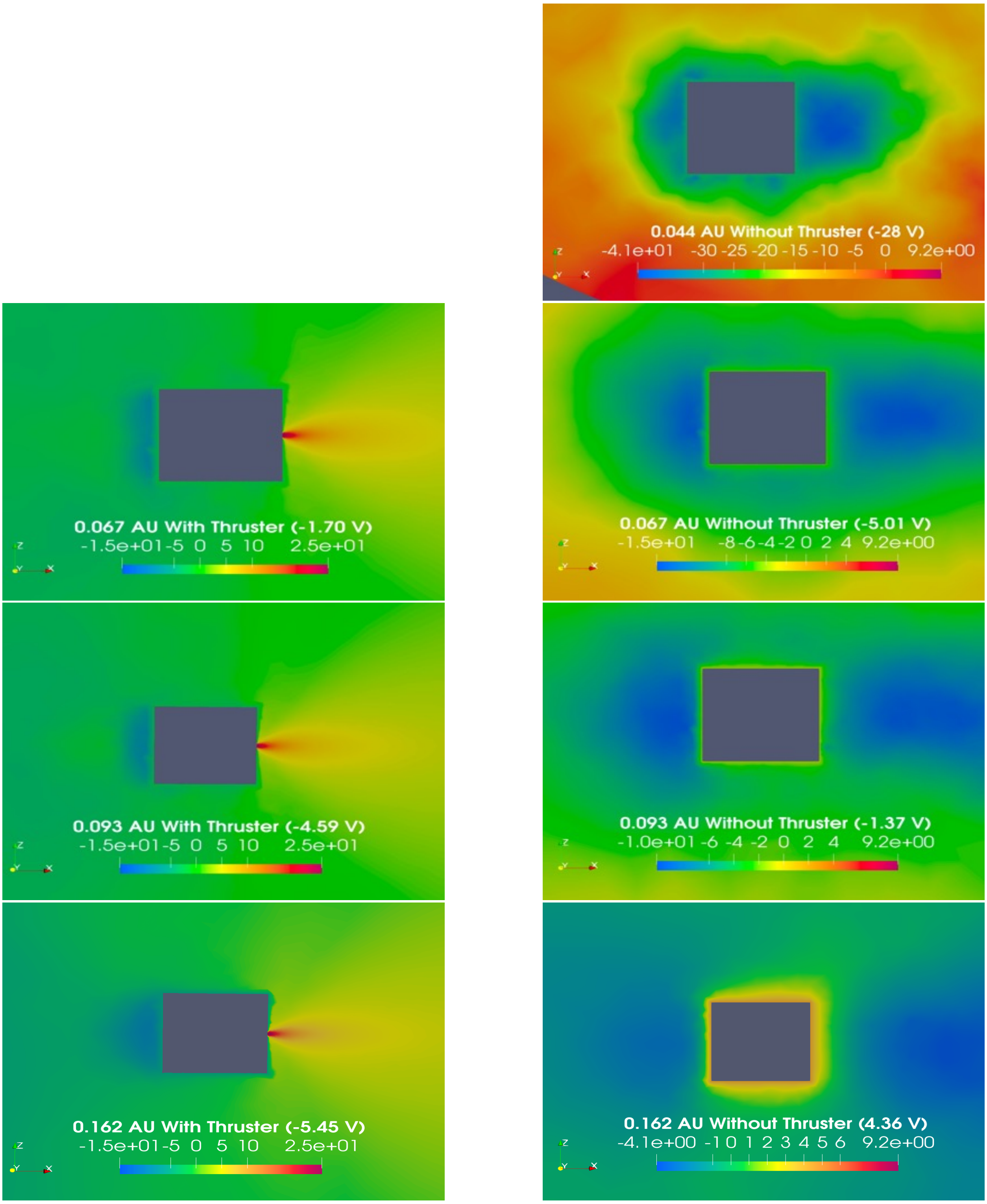
0.044 AU Without Thruster (-28 V)
-4.1e+01 -30 -25 -20 -15 -10 -5 0 9.2e+00
0.067 AU With Thruster (-1.70 V)
-1.5e+01 -5 0 5 10 2.5e+01
0.067 AU Without Thruster (-5.01 V)
-1.5e+01 -8 -6 -4 -2 0 2 4 9.2e+00
0.093 AU With Thruster (-4.59 V)
-1.5e+01 -5 0 5 10 2.5e+01
0.093 AU Without Thruster (-1.37 V)
-1.0e+01 -6 -4 -2 0 2 4 9.2e+00
0.162 AU With Thruster (-5.45 V)
-1.5e+01 -5 0 5 10 2.5e+01
0.162 AU Without Thruster (4.36 V)
-4.1e+00 -1 0 1 2 3 4 5 6 9.2e+00

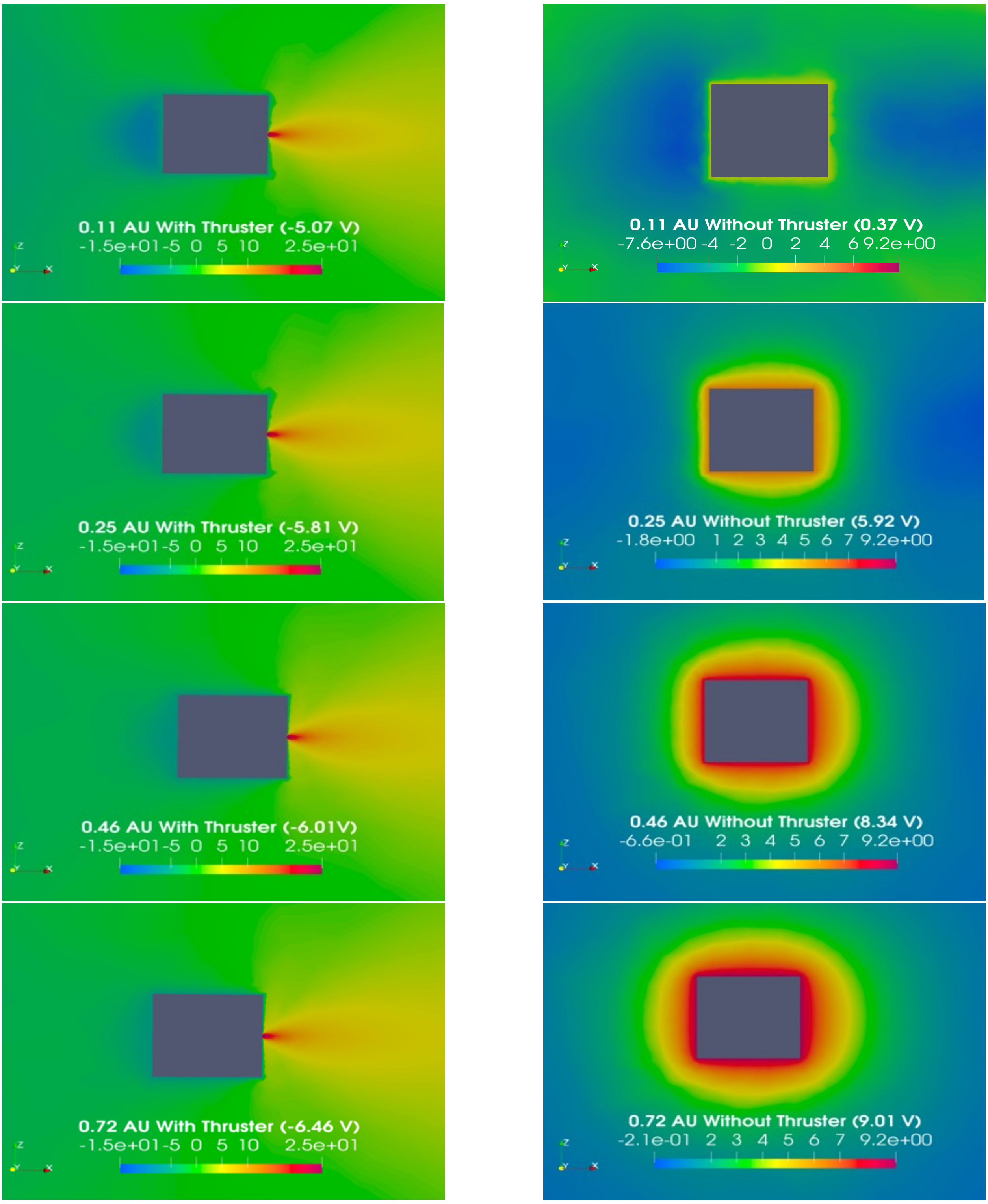
0.11 AU With Thruster (-5.07 V)
-1.5e+01 -5 0 5 10 2.5e+01
0.11 AU Without Thruster (0.37 V)
-7.6e+00 -4 -2 0 2 4 6 9.2e+00
0.25 AU With Thruster (-5.81 V)
-1.5e+01 -5 0 5 10 2.5e+01
0.25 AU Without Thruster (5.92 V)
-1.8e+00 1 2 3 4 5 6 7 9.2e+00
0.46 AU With Thruster (-6.01V)
-1.5e+01 -5 0 5 10 2.5e+01
0.46 AU Without Thruster (8.34 V)
-6.6e-01 2 3 4 5 6 7 9.2e+00
0.72 AU With Thruster (-6.46 V)
-1.5e+01 -5 0 5 10 2.5e+01
0.72 AU Without Thruster (9.01 V)
-2.1e-01 2 3 4 5 6 7 9.2e+00

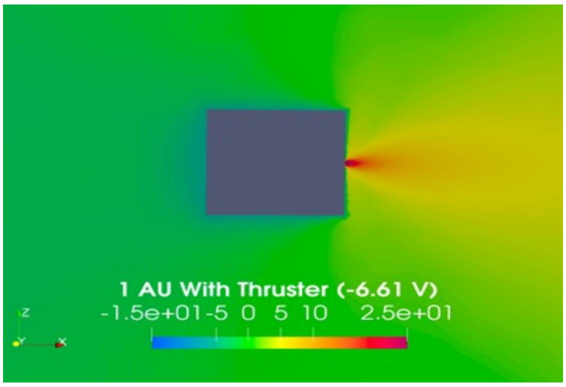

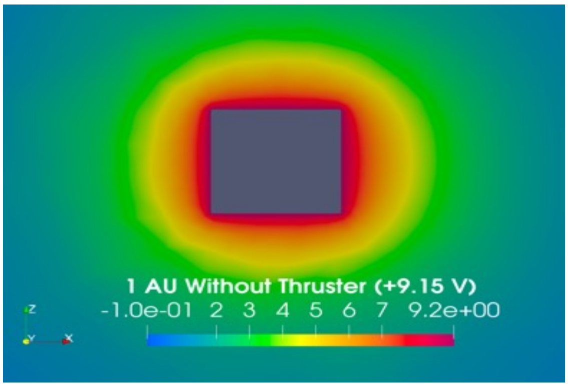

Figure 2.6: Cross comparisons of 2D potential maps with and without the SPT-100 Hall thruster at varying heliocentric distances, corresponding to Figure 2.1 and the 3D potential cut in the $y = 1$ plane. sunlight and the solar wind come from the left (the -x direction)

a negative potential well when the thruster is off. Note that the satellite potentials are the same in the ram and z directions (Figures 2.7a, 2.7b, 2.7e and 2.7f), as expected for a conducting spacecraft surface, and that the potential in the wake direction (Figure 2.7c) is different due to the thruster and satellite surface being isolated by a resistor.

2.4.4 With and Without the Thruster: Role of Secondary Electrons

Figure 2.8 illustrates the impact of secondary electrons on the spacecraft potential at distances of 0.067 AU and 1 AU with and without the thruster. It is apparent from Figure 2.8a that at 1 AU, the influence of secondary electrons on the spacecraft potential is negligible, while at 0.067 AU there is a significant variation when the thruster is on. As expected, the inclusion of secondary electrons leads to the satellite potential becoming more positive. However, without the thruster from Figure 2.8b, it is evident that secondary electrons have a greater influence on the spacecraft potential at 0.067 AU than at 1 AU. Figures 2.9a and 2.9b display the collected and emitted current with the thruster at 0.067 AU in the top left and 1 AU in the top right, respectively. Meanwhile, Figures 2.9c and 2.9d depict the collected and emitted current without the thruster at 1 AU in the bottom left and 1 AU in the bottom right, respectively.

The emission of secondary electrons during thruster operation depends on both ambient and thruster electrons that impact the spacecraft. In Figure 2.8a (right) at 0.067 AU when the thruster is on, the spacecraft charges to -3.5 V instead of -1.74 V. A detailed analysis, as shown in Figure 2.9a, reveals that the thruster electron collection greatly increases from 25 mA to 200 mA when the secondaries are eliminated, while the thermal electron collection current decreases from 6.9 mA to 2.1 mA, reducing the return of photoelectrons

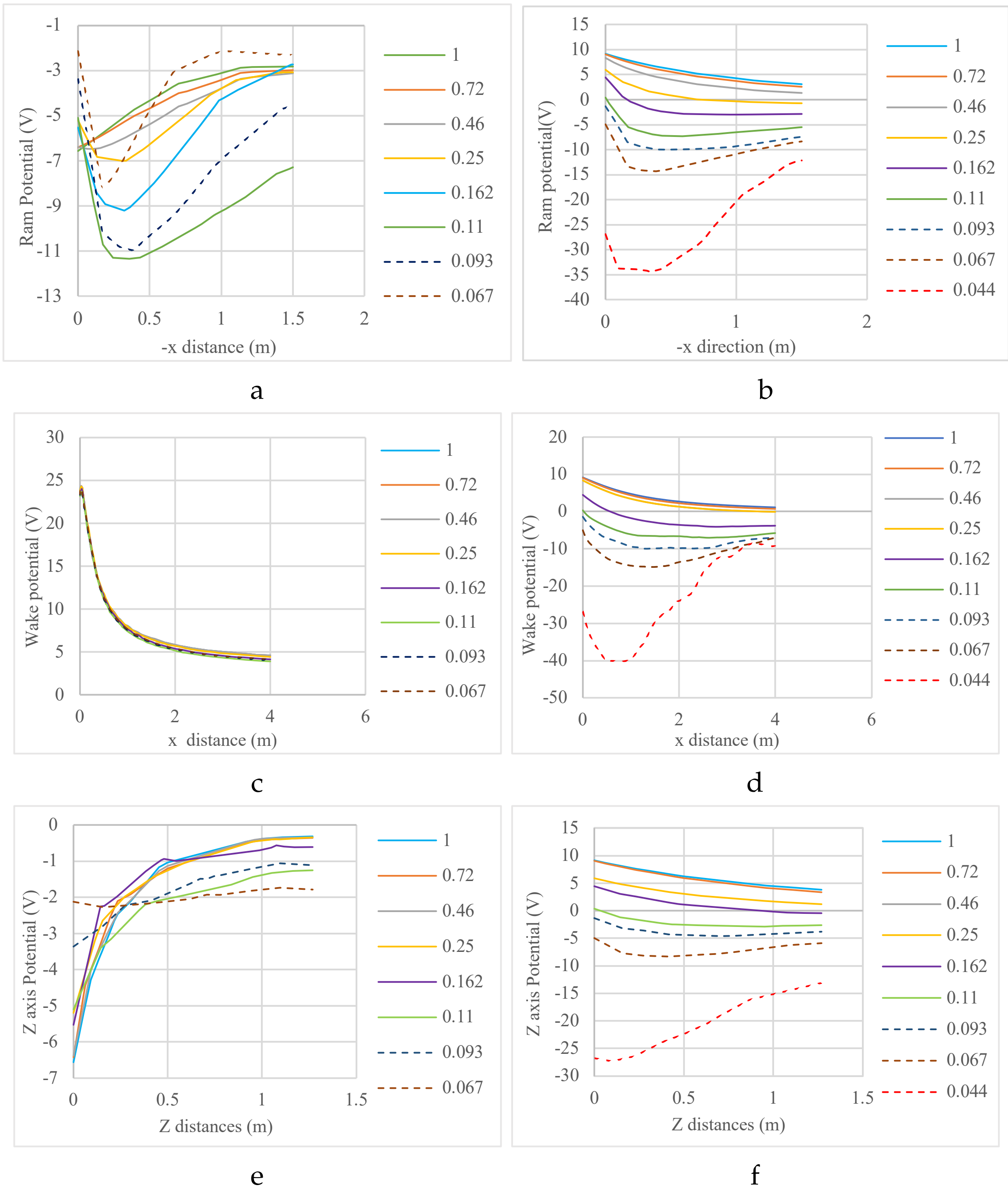

Figure 2.7: The potential profiles along the ram direction (-x axis), wake direction (x-axis) and the sheath direction (z-axis), obtained from Figure 2.6. Figures 2.7a and 2.7b illustrate the ram potential with and without the thruster, positioned at the top left and top right, respectively. Figures 2.7c and 2.7d depict the wake potential with and without the thruster, located in the middle left and middle right panels. Finally, Figures 2.7e and 2.7f show the side potential with and without the thruster, placed at the bottom left and bottom right panels.

current from 18 mA to 3.8 mA. The sudden increase in thruster electron current is probably attributed to the reduction in spacecraft potential and secondary electrons, leading to a reduction in thermal electron current. The negatively charged surface attracts CEX-ions, causing a slight rise in their current from 7 mA to 10 mA. With the combined effects of CEX-ions and photoelectron emission, the negative spacecraft potential diminishes, resulting in a greater accumulation of thruster electrons. Consequently, the spacecraft becomes charged to a slightly larger negative potential, approximately -3.1 V instead of -1.7 V. It's important to note that despite the substantial current collection of the thruster electron the spacecraft does not excessively charge the spacecraft to a highly negative potential due to relatively low temperature of thruster electrons (0.5 eV) in comparison to ambient electrons or any other currents. In conclusion, in the near-Sun environment, the emission of secondary electrons has a significant influence on the spacecraft and surrounding plasma potentials during thruster operation.

On the other hand, at 1 AU, when the thruster is active, there is a negligible difference in spacecraft potential with or without secondaries. The spacecraft charges at -4.9 V (without secondaries) instead of -4.8 V (with secondary electrons), as shown in Figure 8a (right). In this case, the low-density thermal electrons from the ambient plasma are dominated by the CEX-ions and thruster electrons (Figure 2.9b). The low mean energy of thermal electrons decreases the rate of secondary electron emission, allowing CEX-ions and thruster electrons to dominate the spacecraft and the surrounding plasma. Since the solar-photon flux is reduced at 1 AU, the effect of photoelectrons on spacecraft charging is negligible, as will be explained in detail in Section 2.4.5. In Figure 2.9b, it is evident that the collected current of thermal electrons and photoelectrons is much lower than the currents of thruster electrons and CEX-ions, both with and without secondaries. Hence, secondary electrons are less important and do not significantly affect the spacecraft's potential when far away from the Sun.

In Figure 2.9c, at 0.067 AU without the thruster, minor variations in the collection of thermal electron and photoelectron currents are noticeable. However, at 1 AU (Figure 2.9d), the currents remain consistent regardless of whether secondaries are present or not. When the thruster is off, at 0.067 AU, the spacecraft potential has a significantly more negative value of -13.1 V than -5.01 V due to the high dominance of thermal electrons (as shown in Figure 2.8b). Since secondary electrons are not present, there is no potential barrier, which results in a much higher ram potential of -16.3 V and wake potential of -23.6 V. The absence of secondary electrons reduces the collected thermal electron current from 7 to 5.5 mA and the photoelectron current from 18 to 13 mA (as shown in Figure 2.9c). The emitted photoemission current is constant regardless of the presence or absence of

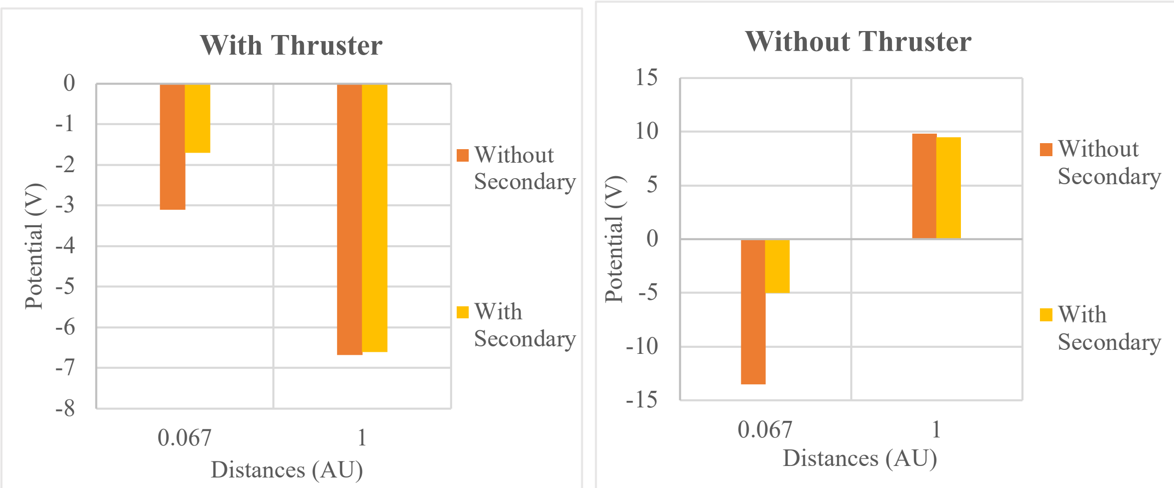

Figure 2.8: Spacecraft potential with and without secondary electrons at 1 AU and 0.067 AU, from left to right: a.) with the thruster and b.) without the thruster

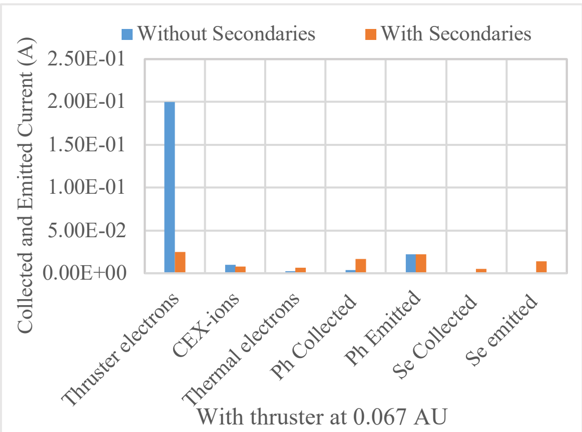

a. With the thruster at 0.067 AU

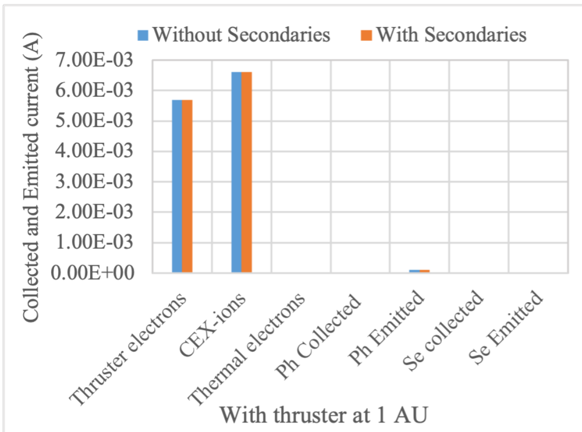

b. With the thruster at 1 AU

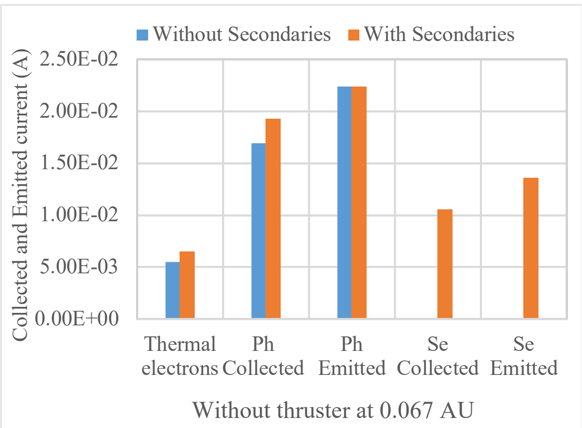

c. Without the thruster at 0.067 AU

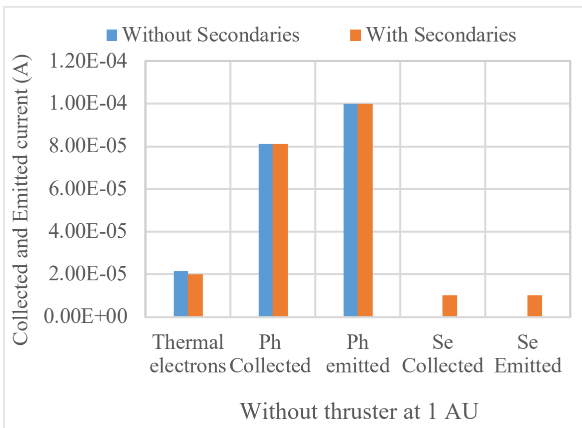

d. Without the thruster at 1 AU

Figure 2.9: Collected and emitted currents with and without the thruster at 0.067 AU and 1 AU.

secondaries. In such cases, the surface accumulates high-temperature ambient electrons with zero emission, leading to a large negative potential. Thus, in the vicinity of the Sun at 0.067 AU, secondary electrons play a crucial role in reducing the negative potential of the satellite when the thruster is off. In contrast, at 1 AU, without the thruster, the elimination of secondary electrons has a negligible impact on the spacecraft potential due to the low mean energy of thermal electrons (as shown in Figure 2.8b). In Figure 2.9d, it is evident that the collected and emitted currents at 1 AU are constant with or without secondary electrons.

In summary, the findings suggest that the secondary electrons significantly help mitigate the spacecraft's negative charge in close proximity to the Sun, irrespective of whether the thruster is on or off. Indeed, the absence of secondary electrons makes the spacecraft's potential more negative when the thruster is on, albeit to a significantly lesser degree than in the absence of the thruster and secondary electrons. In contrast, the impact of secondary electrons on the spacecraft potential is negligible near Earth (relatively far away from the Sun) irrespective of the thruster being on or off.

2.4.5 With and Without the Thruster: Role of Photoelectrons

Figure 2.10 shows the effect of photoelectrons on the spacecraft potential at distances of 0.067 AU and 1 AU, both in the presence and absence of the thruster. As shown in Figure 2.10a, when the thruster is on, the influence of photoelectrons on the spacecraft potential at 1 AU is negligible. However, at 0.067 AU, Figure 2.10a demonstrates a noticeable factor of two variations in the spacecraft potential. The spacecraft at 0.067 AU charges to -4.45 V instead of -1.70 V. The possible explanation is similar to the case without secondary electrons discussed in Section 2.4.4, where the high-density CEX-ions and thruster electrons dominate the plasma and the spacecraft environment, diminishing the importance of photoelectrons. Figure 2.10b when the thruster is off further highlights the significant impact of photoemission on the spacecraft potential at both the location at 1 AU and 0.067 AU. As expected, the inclusion of photoelectrons leads to a more positive spacecraft potential at both distances and when the thruster is on or off. Figures 2.11a and 2.1b display the collected and emitted current with the thruster at 0.067 AU in the top left and 1 AU in the top right, respectively. Meanwhile, Figures 2.11c and 2.11d depict the collected and emitted current without the thruster at 1 AU in the bottom left and 1 AU in the bottom right, respectively.

From Figure 2.11a, it is evident that at 0.067 AU with the thruster, the collected current of

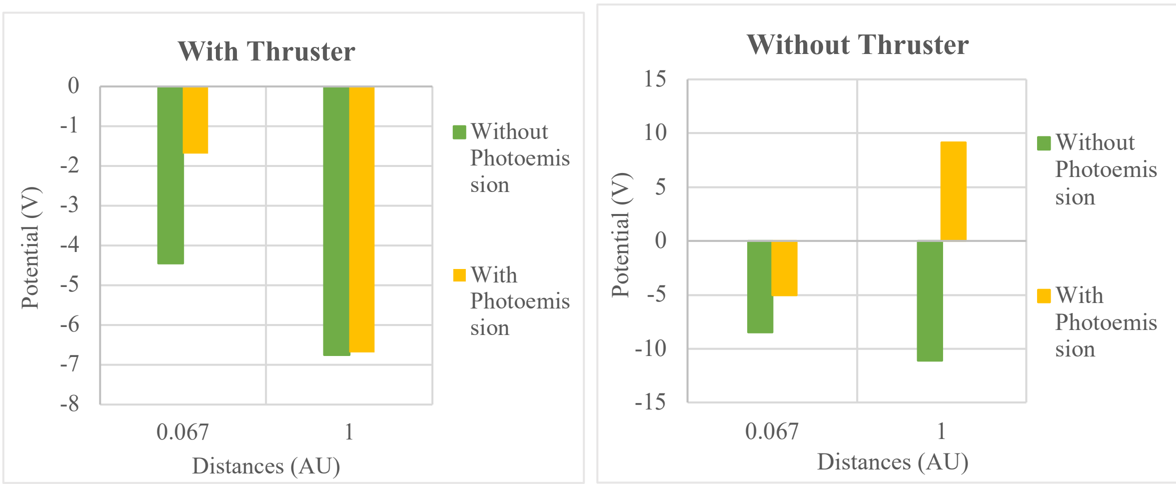

Figure 2.10: Spacecraft potential with and without photoelectrons at 1 AU and 0.067 AU, from left to right: a.) with the thruster on and b.) without the thruster

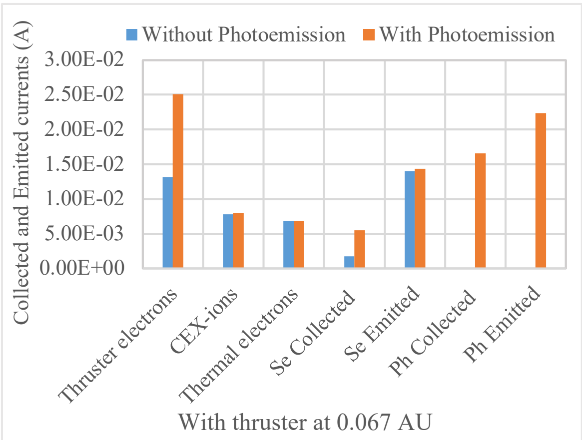

a. With the thruster at 0.067 AU

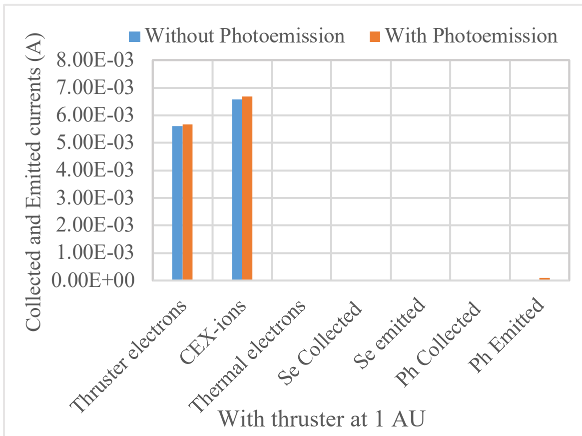

b. With the thruster at 1 AU

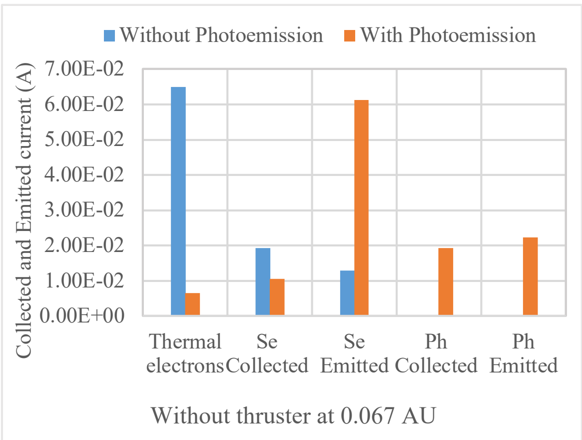

c. Without the thruster at 0.067 AU

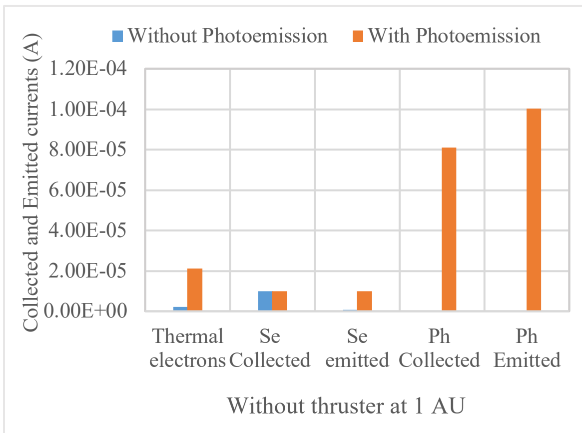

d. Without the thruster at 1 AU

Figure 2.11: Collected and emitted currents with and without the thruster at 0.067 AU and 1 AU. From top left to bottom right, respectively: With the thruster at (a) 0.067 AU, and (b) 1AU and without the thruster at (c) 0.067 AU and (d) 1AU.

thermal electrons and CEX-ions remains constant with or without photoemission. However, a decrease in thruster electron current is observed from 25 mA to 13 mA when photoelectrons are neglected and the potential becomes more negative. One possible reason could be that the spacecraft is exposed to a hot and dense environment, resulting in the penetration of the surface by high-temperature thermal electrons (few 10 to 100 eV). Consequently, it leads to high secondary electron emission that helps to remove the negative charge. Similarly, the CEX-ions contribute significantly to reducing the negative potential of the spacecraft. However, because of the relatively high temperature of the thermal electrons compared to other charged particles, the spacecraft tends to settle at a negative potential and thus repels the thruster electrons. As a result, thruster electron accumulation on the surface is dependent on photoelectron and secondary electron emission. From Figure 2.11b it is clear that at 1 AU, the thruster electrons and CEX-ions dominate the photoelectron effect and have negligible impact on the spacecraft potential irrespective of the presence or absence of photoemission.

Moving to the scenario without the thruster, from Figure 2.11c it is clear that eliminating photoemission at 0.067 AU and 1 AU leads to a significant variation in spacecraft potential. In both cases, the photoelectric effects are important and make the spacecraft significantly positive. Indeed, at 1 AU a significant change in spacecraft potential is seen from -11 V to + 9V when photoelectrons are included. While at 0.067 AU, the spacecraft potential without photoemission is -8.4 V instead of -5.01 V (as shown in Figure 2.10b). Close to the Sun, photoemission is quite strong, but it has a minor effect on making the spacecraft positive. The seemingly contradictory result is explained in section 2.4.3, in terms of the high density of thermal electrons generating a strong potential barrier that hinders the escape of photoelectrons and secondary electrons, leading to a significant accumulation of electrons on the spacecraft's surface. The same can be observed in Figure 2.11c, where the thermal electron collected current on the surface increases from 6.5 mA to 65 mA. In such a situation, the return of the secondary electron increases from 10 mA to 19 mA, and the emission rate is significantly lowered from 61 mA to 13 mA without photoemission. Thus, close to the Sun at 0.067 AU, despite its high solar photon flux, the spacecraft charges to a negative potential, and in the absence of photoemission, its potential becomes more negative.

Conversely, at 1 AU without the thruster, the spacecraft potential in the absence of photoemission converges to -11.1 V instead of +9 V (as shown in Figure 2.10b). At this distance, photoemission is the primary charging factor that causes the spacecraft to become positively charged, due to the low density of thermal electrons. However, in the absence of sunlight the thermal electrons tend to accumulate on the spacecraft, leading to a large negative potential. From Figure 2.11d, it is evident that the lack of photoelectrons results in a substantial decrease in the collected current of thermal electrons, due to a strong build-up of the negative charge that repels the incoming electrons. On the other hand, in the presence of photoemission, the current of photoelectrons dominates the thermal electron current by a factor of 10, making the spacecraft charge positively and leading to the attraction of thermal electrons.

In summary, the simulations show that photoemission plays a pivotal role in mitigating the negative charge of the spacecraft close to the Sun, irrespective of whether the thruster is on or off. Indeed, the absence of photoemission impacts the spacecraft's potential when the thruster is on, albeit to a significantly lesser degree than in the absence of the thruster and photoemission. For example, at a distance of 0.067 AU, with the thruster but without photoemission, the spacecraft charges at -4.45 V, while without both the thruster and photoemission, the spacecraft's potential converges to a higher negative value of -8.47 V. Similarly, when situated far from the Sun at 1 AU, the spacecraft's potential without the thruster and without photoemission reaches a substantial negative value of -11.1 V. In contrast, with the thruster but without photoemission, the potential stabilizes at -6.7 V. As such, the roles of CEX-ions and thruster electrons are essential in maintaining a low negative potential in the absence of photoemission, both at the location of 0.067 AU and 1 AU.

2.4.6 With the Thruster: Without Secondaries and Photoemission

Figure 2.12 illustrates the impact of simultaneously eliminating secondaries and photoelectrons on spacecraft potential at 0.067 AU and at 1 AU. The results specifically focus on the thruster's operation and do not include a scenario without the thruster, as the primary objective is to understand spacecraft charging during thruster operation. In this scenario, the photoelectrons and secondary electrons are eliminated at 0.067 AU, and the spacecraft charges to a significantly higher negative potential of -11.1 V instead of -1.7 V, despite the presence of high-density CEX-ions and thruster electrons. This is in contrast to -3.1 V without secondaries only and -4.5 V without photoemission only (from sections 2.4.4 and 2.4.5). Thus, the combined absence of photoelectrons and secondary electrons can lead to high negative charging of the spacecraft. The large negative charging can be explained by the fact that the spacecraft, being exposed to a hot and dense environment, experiences significant charging by high-temperature thermal electrons (few 10 to 100 eV). The absence of photoemission and secondary electrons prevents the removal of electrons from the surface, resulting in a large negative potential. Since the thermal electron temperature is so high compared to the energies of any other particles it controls the spacecraft potential. The combined elimination of secondary electrons and photoemission causes the spacecraft to charge to a large negative potential. The CEX-ions and thruster electrons compensate if either of them is not present and charges the spacecraft to a much less negative potential (as shown in sections 2.4.4 and 2.4.5). Hence in order to achieve equilibrium, the incoming ambient electron current must be equal to that for the net photoelectrons, secondary electrons, CEX-ions and thruster electrons. Figure 12a clearly demonstrates that the collected current of thruster electrons is significantly reduced from 25 mA to 1.8 mA due to the repulsion caused by the strongly negative surface potential when secondaries and photoemission are not included. Thus, the presence of photoelectrons and secondary electrons is crucial in maintaining a smaller magnitude of negative potential when the thruster is active. The absence of either one may not have a significant impact, but their combined elimination can result in excessive negative charging of the spacecraft.

On the other hand, Figure 2.12b shows that the simultaneous elimination of secondary and photoelectrons at 1 AU has a negligible effect on spacecraft potential, owing to the decreased energy and density of thermal electrons. The final spacecraft potential at 1 AU converges to -6.75 V, only very slightly different from the potential of -6.72 V. In summary, at 0.067 AU, photoelectrons and secondary electrons play a vital role in preventing excessive negative potential, while the absence of either may have a significant but smaller impact on the spacecraft potential. However, at 1 AU, the simultaneous elimination of photoelectrons and secondary electrons shows negligible effects on the spacecraft potential when the thruster is active.

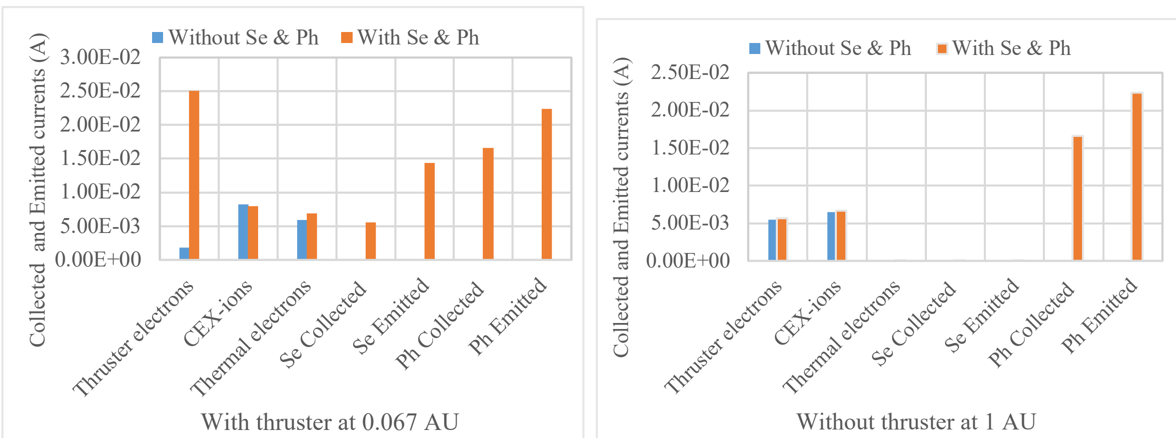

Figure 2.12: Collected and emitted currents with the thruster on but no photoemission and secondary electrons at (a.) 0.067 AU and b.) 1 AU

2.5 Conclusion

The study investigated the effects of spacecraft charging induced by the operation of the SPT-100 Hall thruster in various space environments, ranging from 0.067 AU to 1 AU. The analysis considered factors such as ambient electrons and ions, CEX-ions and thruster electrons, photoelectrons, secondary electrons, and solar photon flux. The results revealed significant variations in space charge and potential barriers when comparing thruster-on and thruster-off scenarios. During thruster operation, the spacecraft potential tends to settle at a low, stable, and negative potential, ranging from -2 V to -6 V from 0.067 AU to 1 AU, respectively. The low negative potential is primarily attributed to the presence of thruster electrons and high-density CEX-ions, which dominate the in situ plasma. In contrast, without the thruster, the spacecraft potential exhibited a wide range from 0.044 A to 1 AU, ranging from -28 V to +9V, respectively. The spacecraft potential without the thruster is primarily influenced by the increasing energy and number density of thermal electrons and the increasing roles of photoelectrons and secondary electrons as the spacecraft approaches closer to the Sun. It is crucial to emphasize that the stabilizing effect of the thruster, particularly in relation to maintaining a low negative potential, relies on factors such as the density of charge-exchange ions (CEX-ions), thruster electron, ambient electron density, photoelectrons, secondary electrons, and the spacecraft's geometry. Above all, the finding of this paper suggests that under various conditions, the SPT-100 Hall thruster can effectively maintain and stabilize the spacecraft potential, mainly due to the influence of high-density CEX-ions and thruster electrons. The presence of CEX-ions and thruster electrons emerged as a critical factor in determining the spacecraft's final potential when the thruster is active.

The findings for distances ranging from 0.067 AU to 1 AU can be summarized as follows: Firstly, when the SPT-100 Hall thruster is operational, the spacecraft maintains a low, stable, and negative potential from -2V to -6V across a wide range of heliocentric distances. The variation in spacecraft potential is significantly reduced compared to when the thruster is off. Without the thruster, the spacecraft exhibits a large variation in potential, ranging from +9 V to -28 V. The negative potentials when the thruster is on are primarily due to the dominance of the CEX-ions and thruster electrons over the ambient plasma and the effects of both photoelectrons and secondary electrons. The negative potentials are mainly the result of the collection of thruster electrons. Secondly, the potential structures of the spacecraft are intrinsically 3D (in detail, rotationally symmetric 2D) with different potential structures of the ram, wake and side (perpendicular to the ram-wake axis) due to the importance of the thruster CEX-ions and electrons, photoelectric and secondary electron emission and collection, and the wake void region. These effects often lead to potential hills/wells (depending on particle charge) and associated reflection and trapping effects on particles. In general, these effects appear to combine non-linearly, and all are quantitatively important, albeit less so when the thruster particles dominate the ambient plasma. Third, during thruster operation, the magnitudes of the changes in the sheath potential and the potential barrier are significantly reduced because of the high dominance of CEX-ions over the ambient plasma. This leads to a less restrictive escape of secondary electrons and photoelectrons, thereby minimizing their recollection. Consequently, low recollection of secondary electrons may reduce the disturbances and enhance the accuracy of low-energy plasma measurements. In contrast, without the thruster, close to the Sun the plasma near the spacecraft experiences a strong potential barrier, which limits the escape of photoelectrons and secondary electrons, resulting in large recollection. In such cases, the spacecraft charges to a large negative potential, and recollection of the low-energy electrons has a high chance of interfering with spacecraft instruments.

Moreover, in close proximity to the Sun, both photoelectrons and secondary electrons play a significant role in reducing the negative potential of the spacecraft (making the potential more positive), regardless of whether the thruster is on or off. Indeed, the absence of photoemission or secondary electrons makes the spacecraft more negatively charged when the thruster is on, albeit to a significantly lower degree than without the thruster in the absence of photoemission or secondary electrons. Far away from the Sun, near 1 AU, the influence of photoelectrons and secondary electrons is negligible when the thruster is on. However, when the thruster is off, the absence of photoelectrons can lead to high negative charging. In this situation, the operation of the thruster helps maintain and stabilize the spacecraft's potential to a low negative potential. For example, at 1 AU, the spacecraft's potential without the thruster and without photoemission reaches a substantial negative value of -11.1 V. In contrast, with the thruster but without photoemission, the potential stabilizes at -6.7 V. Without the thruster far away from the Sun, secondary electrons have negligible impact on spacecraft potential because of the low mean energy of thermal electrons.

Furthermore, when the thruster is on, the elimination of either photoemission or secondary electrons can lead to a higher negative charge of the spacecraft, although to a lesser extent when compared to the combined elimination of both photoelectrons and secondary electrons. In combined elimination, the spacecraft can acquire a considerably high negative potential when the thruster is on, corresponding to these processes combining nonlinearly rather than linearly. For instance, at 0.067 AU from the Sun, when secondary electrons and photoemission are both eliminated simultaneously, the spacecraft becomes charged to a significantly substantial negative potential of approximately -11.1 volts, as opposed to -1.70 volts (when photoelectrons and secondaries are considered).

Lastly, the solar photon flux has a relatively small effect on the spacecraft's potential when the thruster is turned on compared to when it is off, resulting in a significant shift in spacecraft potential. Photoelectric effects always make the spacecraft potential more positive in this chapter's simulations, as does secondary electron emission. The accumulation of thruster electrons on the spacecraft's surface depends on the presence and absence of photoemission and secondary emission, and on the magnitude and sign of the spacecraft's potential. Overall, these findings have significant implications for how the thruster's operation can assist in maintaining and controlling spacecraft charging under various solar-wind conditions. This newfound understanding should aid in enhancing the preflight design assessment of electric thruster-induced charging and ensure the safety of sensitive instruments on board. Future studies will evaluate the effects of different electric thruster plumes on the spacecraft potential in the solar wind, magnetospheric environments, and terrestrial LEO orbits.

CHAPTER 3

A Comparative Study of Spacecraft Charging Effects with and Without RIT-2X and SPT-100 Thrusters from 0.044 AU to 1 AU

Published as: Tejaswi L Shinde, Iver H Cairns, Jason M Held, and Gregoire Deprez at AIAA 2024-1141, https://arc.aiaa.org/doi/10.2514/6.2024-1141

3.1 Abstract

The research aims to understand the impact of the RIT-2X thruster compared to the SPT-100 Hall thruster and the absence of the thruster. The objective is to analyze how various electric thrusters affect the spacecraft potential under solar-wind conditions ranging from 0.044 AU to 1 AU. To investigate the effects on spacecraft potential, the Spacecraft Plasma Interaction Software (SPIS) is utilized. The main finding indicates that the RIT-2X thruster exhibits a stronger stabilizing effect, resulting in a consistently lower, stable and negative potential within the range of -3 to -4 V compared to the SPT-100 Hall thruster, -2 to -6 throughout the helio distances. In contrast, without the thruster, the variation in the spacecraft potential is significant, ranging from -28 to 9 V from 0.044 AU to 1AU. In particular, at 0.044 AU, the RIT 2X thruster significantly reduces the negative potential from -28 to -3.2 V. Thus, the study emphasises the vital role of the RIT-2X thruster in decreasing the negative potential, contributing to enhanced stability in the presence of ambient ions and electrons, photoelectrons and secondary electrons, CEX-ions and thruster electrons and solar photon flux. The electrostatic sheath interior to 0.11 AU experiences a notable reduction in potential due to the presence of high-density CEX-ions and thruster electrons, leading to a decrease in the recollection of secondary and photoelectrons. Furthermore,

the study emphasizes the minimal variation in spacecraft potential in the absence of sunlight when the RIT-2X thruster is on, in contrast to the slight variations observed with the SPT-100 Hall thruster and significant variation when the thruster is inactive.

3.2 Introduction

Hall-effect thrusters (HET) and gridded-ion engines (GIE) have gained recognition as prominent electric propulsion technologies for a wide range of scientific, commercial, and interplanetary missions. These technologies offer enhanced propulsive capability and reduced propellant consumption compared to conventional chemical thrusters (Goebel et al., 2023; Kuninaka et al., 2011; Garner et al., 2013; and Liu et al., 2013). Operating within power ranges ranging from hundreds of watts to tens of kilowatts, and with specific impulse (Isp) values ranging from thousands to tens of thousands of seconds, these thrusters typically produce thrust levels in the fraction-of-a-Newton range (Goebel et al., 2023; Amo et al., 2022). The RIT-2X thruster, a variant of the GIE, utilizes a high-frequency electromagnetic field to ionize xenon atoms by colliding them with electrons. Once ionized, the positively charged ions are accelerated by an electric field, thus producing high thrust (Porst et al., 2017). On the other hand, Hall thrusters are ionized by electron impact and their acceleration is driven by the axial electric field, with the magnetic field playing a role in electron confinement (Goebel et al., 2023). The present paper focuses on the charging effects of the RIT-2X thruster by comparing it with the SPT-100 Hall thruster and without the thruster. The RIT-2X thruster stands out as a promising Gridded Ion Engine, offering the highest specific impulse and optimal mass savings for all-electric spacecraft. It caters to a wide range of thrust levels, ranging from 50 μN to 205 mN, making it suitable for diverse space missions (Porst et al., 2017). However, with these thrusters, the backflow exhausts have low-energy ions and electrons which interact with spacecraft systems and charge the spacecraft negatively (Na et al., 2019; Wang, 1997; Lee et al., 2011; Tajmar, 2002).

The backflow plumes generated by these thrusters consist of low-velocity charge-exchange ions (CEX ions), resulting from collisions between fast-beam ions and propellant neutrals within the main ion beam (Goebel et al., 2023). Some of these CEX-ions flow back toward the spacecraft, leading to two primary effects. Firstly, the deposition of effluent causes contamination of optical sensors, solar arrays, thermal control systems, and other communication devices (Wang, 1997). Second, the CEX-ions and associated electrons will modify the properties of the ambient plasma flowing around the spacecraft by inducing an additional current that may influence the spacecraft potential and plasma instrument observations (Wang, 1997). The effects caused by the electric thruster operations have long raised both scientific and operational concerns, as the plume's backflow contaminates and interacts with spacecraft systems and results in ion-induced charging. Thus, it is important to study the complex interaction of the thruster-induced and ambient plasma and their effects on spacecraft charging in various environments to avoid spacecraft operational and measurement anomalies and failures. In the previous studies, the dynamic interaction between the SPT-100 Hall thruster plume and spacecraft surface under different solar wind conditions were explored, ranging from 0.044 AU to 1 AU. examining the influence of various variables, including the presence or absence of solar-photon flux and the inclusion or exclusion of photoemission and secondary electrons. The main finding suggests that the electric thrusters provide low, stable, and negative potential throughout a wide range of heliocentric distances and effectively mitigate the issue of spacecraft negative charging in diverse scenarios. Specifically, it is found that photoelectrons and secondary electrons play a crucial role near the Sun when the thruster is on, maintaining a low negative potential for the spacecraft, shown in Shinde, Held, and Cairns (2022); Shinde, Held, and Cairns (2023); and Shinde, Held, Cairns, and Deprez (2024)

The present paper expands on previous research by Shinde, Held, Cairns, and Deprez (2024) examining the charging effects generated by the RIT-2X thruster and its implications for spacecraft potential. A comprehensive comparative analysis is undertaken, comparing the RIT-2X thruster, the SPT-100 Hall thruster, and scenarios without a thruster, considering the presence of ambient electrons and ions, thruster electrons and CEX-ions, photoemission, secondary electrons, and solar photon flux. The investigation delves into the complex interaction between the electric thruster backflow plume and the spacecraft in solar wind conditions, aiming to develop a dynamic understanding of charging in diverse plasma environments and the impact of charged particles on spacecraft potential to ensure the safety of sensitive instruments. To achieve these objectives, the study employs SPIS software for the setup of the simulation and the modeling of physical parameters (Section II). Subsequently, Section III of the paper shows the variation in spacecraft potential. Section III evaluated the collected and emitted currents on the surface of the satellite, comparing scenarios with and without thruster operation over a wide range of helio distances. Section IV provides detailed potential profiles for the ram, wake, and side areas surrounding the spacecraft. Finally, Section IV investigates the significance of photoelectrons in influencing spacecraft potential, considering scenarios with and without thruster operation.

3.3 Simulation Model and Setup

The study employs SPIS, an open source simulation tool that utilizes a 3D electrostatic solver based on the particle-in-cell (PIC) method to compute the interaction between plasma and spacecraft. The tool is commonly utilized for simulations of spacecraft charging across diverse environments in LEO, GEO, and electric thruster operations by using full or hybrid Particle in Cell (PIC), Monte Carlo, and other techniques (Wartelski, Theroude, et al., 2013; Wartelski, Ardura, et al., 2011; Thiebault et al., 2015). The spacecraft charging is determined through an equivalent electric circuit, accounting for its interaction with the surrounding plasma, calculating the currents between the plasma and spacecraft using a circuit solver. Within SPIS, the spacecraft potential is obtained by solving a linear or non-linear Poisson equation (for densities typical of most electric thrusters, the quasi-neutrality assumption yields the same outcome as solving the Poisson equation, offering a faster and more stable solution) (Thiebault et al., 2015). In current simulations, a PIC model is employed to calculate all species (ions, thermal electrons, photoelectrons, and secondary electrons) outside a spacecraft integrated with the SPT-100 Hall thruster. The Hall thruster model in SPIS utilizes a Monte-Carlo method to simulate collisions between CEX-ions and various other species (neutral Xe, Xe+, Xe++) within the computational regions. Fast Xe particles are excluded from the simulation as they do not contribute to charging (Thiebault et al., 2015). The simulation incorporates electric fields and magnetic fields in the modeling of plasma populations, with the electric field derived from the plasma flow field (Thiebault et al., 2015). Table 1 provides specifications for the SPT-100 thruster. Additional details on the simulation method, plume validation, and governing equations of this software can be found on the SPIS software websites (*SPIS - Spacecraft Plasma Interaction Software* n.d.).

In this paper, the same spacecraft model is used as in Chapter 2 and the previous research by Shinde, Held, and Cairns (2022); Shinde, Held, and Cairns (2023); and Shinde, Held, Cairns, and Deprez (2024), representing it as a cylinder with a radius of 1 m and a length of 2 m, coated with indium tin oxide (ITO) material as shown in Figure 3.1. The dimensions of the simulation domain vary on the basis of the Debye length, and accordingly mesh refinements are applied. The domain dimension must be smaller than three times the thermal electron's Debye length (3 x Debye length). Meanwhile, the mesh resolution within the domain is always less than one-third of the Debye length, resulting in 50,000 to 100,000 mesh tetrahedrons. The spacecraft mesh size is based on the thermal electrons and photoelectron Debye lengths (one-third of the local plasma Debye length). The satellite model is created using the GMSH software, as shown in Figure 3.1 and Table 3.1. The physical parameters for different heliocentric distances are adopted from Guillemant

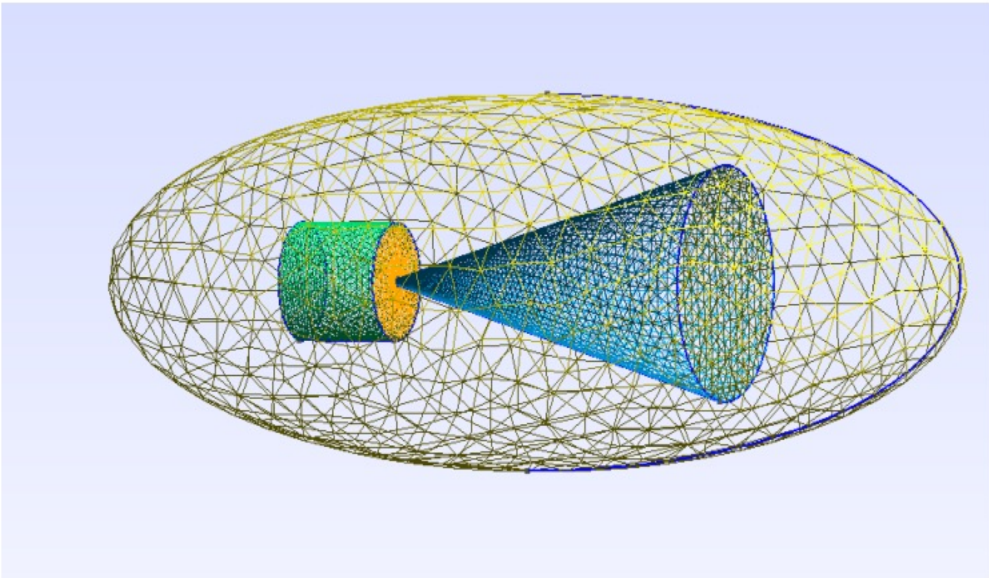

Figure 3.1: GMSH spacecraft model with a meshing grid (green/yellow), the void boundary is the simulation boundary, and the blue conical shape represents the ion plume.

Table 3.1: Parameters used for SPIS simulation.

Parameters	**Value**	
Geometry	1 m radius, 2 m long, cylinder	
Material	Indium Tin Oxide	
Secondary electron temperature	2eV	
Photoelectron temperature	3eV	
Ambient Ion type	O+	
Ion modelling	PIC	
Electron modelling	PIC	
Magnetic Field	Not considered	
Thruster Specification		
Electric Thruster	SPT-100 Hall	RIT-2X Thruster
Thrust (N)	0.035	0.180
Specific Impulse (s)	1840	2966
Cathode Temperature (eV)	5	5
Mass Flow rate (Xe) (kg/s)	1.91×10^{6}	$6.19 \times 10^{-}6$
Current (A)	1.43	3.99
Power (W)	723	6025

(2014). The simulation considers varying plasma properties, such as density, temperature, solar wind velocity, and timesteps for ions, thermal electrons, secondary electrons, and photoelectrons. Additionally, the solar-photon flux is taken into account. For simplification, the satellite is assumed to be stationary relative to the Sun. Therefore, only the solar wind ion drift velocity, directed along the x-axis, is simulated. The corresponding electron drift is neglected because it is small compared with the electron thermal speed, which is not true for the ions. During simulations, the thruster is assumed to be electrically connected to the spacecraft chassis, while the spacecraft surface floats with the plasma. The anode and cathode of the thruster are isolated from the spacecraft. To manage excessive charging, a 500 kilo ohm resistor is introduced between the thruster and the spacecraft, providing a return path for leakage currents. The resistor ensures a high degree of isolation between the thruster and the spacecraft surface, thus limiting potential charging issues (Liu et al., 2013;Wartelski, Theroude, et al., 2013). It is crucial to note that the ground of the spacecraft is distinct from the ground of the electric thrusters. The configuration is adopted primarily to reduce spacecraft contamination caused by thruster plumes (Liu et al., 2013). During the simulations, the magnetic field and backscattered electrons are not considered. Figure 3.1 shows the center of the cylinder representing the spacecraft located at the origin of the Cartesian coordinate system (0, 0, 0). The plane's orientation is as follows: the x-axis points along the thruster axis (that is, the length of the cylinder), the y-axis points vertically upward along the plane of the paper, and the z-axis points outward from the plane.

3.4 SPIS Simulated Results

3.4.1 Variation in spacecraft potential from 0.044 AU to 1 AU

Figure 3.2 shows the variation in spacecraft potential for a wide range of heliocentric distances with the RIT-2X thruster, the SPT-100 Hall thruster and without the thruster. Let's consider when the electric thruster is switched on. As evident in Figure 3.2, a low and stable negative potential is obtained from -3 to -4 V for the RIT-2X thruster from 0.044 AU to 1 AU while -2 to -6 V for the SPT-100 Hall thruster from 0.067 AU to 1AU. The primary reason is due to the CEX-ions and the thruster electrons of the cathode dominating the spacecraft and surrounding plasma since their number of densities are much higher, 10^{10} m^{-3} and 10^{11} m^{-3}, respectively. The CEX-ions create a dense cloud surrounding the spacecraft that interacts with the charged particles present near the spacecraft (Shinde, Held, and Cairns, 2023 and Shinde, Held, Cairns, and Deprez, 2024). The thruster electrons follow the same path as CEX-ions but with a much higher thermal speed and charging current, which leads to a negative charge and potential on the spacecraft. The CEX-ions act as a protective shield between the spacecraft and the surrounding plasma, thereby reducing the impact of ambient electrons. As a result, the operation of an electric thruster provides additional current that controls and stabilizes the spacecraft's potential to a low negative potential. For example, at 0.044 AU with the RIT-2X thruster, the spacecraft potential converges to -3.5 V instead of -28.6 V without the thruster. A significant difference in spacecraft potential with and without the thruster is mainly due to the high dominance of the CEX-ions and thruster electrons that reduce the potential barrier (as shown in Section 3.4.3) surrounding the spacecraft which no longer restrict the escape of photoelectrons and secondaries, thus leading to a much less negative potential. Similarly, with the SPT-100 Hall thruster at 0.067 AU, the spacecraft potential converges to -1.74 V instead of -4.36 V without the thruster. However, at 0.044 AU with the SPT-100 Hall thruster, the spacecraft potential is uncertain due to slow and unstable convergence. Multiple simulations using the PIC distribution have been performed to assess the spacecraft's potential convergence, which appears to lie within the range of -1 to -3 V. However, as of the present date, the simulations exhibit instability and have not yet reached convergence. A detailed study on spacecraft charging with the SPT-100 Hall thruster can be found in the previous work by (Shinde, Held, Cairns, and Deprez, 2024).

In contrast without the thruster, as shown in Figure 3.2 it is apparent that the spacecraft potential decreases monotonically from 1 AU to 0.25 AU and non-monotonically from 0.11 AU to 0.044 AU. Let's consider further away from the Sun (above 0.25 AU), without the thruster, where the charging effects are less critical. The region is dominated by photoelectrons (without the thruster) due to their much higher density of 10^8 m^{-3}compared to other number densities (ambient ions 10^7 m^{-3} , thermal electron 10^7 m^{-3}, secondary densities 10^7 m^{-3}) which all vary with the inverse squared distance to the Sun (Shinde, Held, and Cairns, 2023) and (Shinde, Held, Cairns, and Deprez, 2024). The decreasing mean energy of thermal electrons reduces the secondary emission rate. Moreover, the ambient ions become a source of secondary electrons due to proton impact (SEEP) on the spacecraft surface and so increase the secondary electron density nearby. As shown in Figure 3.2, outside 0.25 AU the spacecraft potential without the thruster is positive and decreases monotonically. The positive charging of the spacecraft can be explained by the fact that since the photoelectron Debye length is larger than the spacecraft size, it gives rise to a 3D thick sheath phenomenon where the potential barrier does not restrict the escape of photoelectrons and secondaries (Shinde, Held, and Cairns, 2023; Shinde, Held, Cairns, and Deprez, 2024; Ergun et al., 2010; and Guillemant, 2014). The partial recollection of secondary electrons in this region is simply due to the positive potential of the spacecraft.

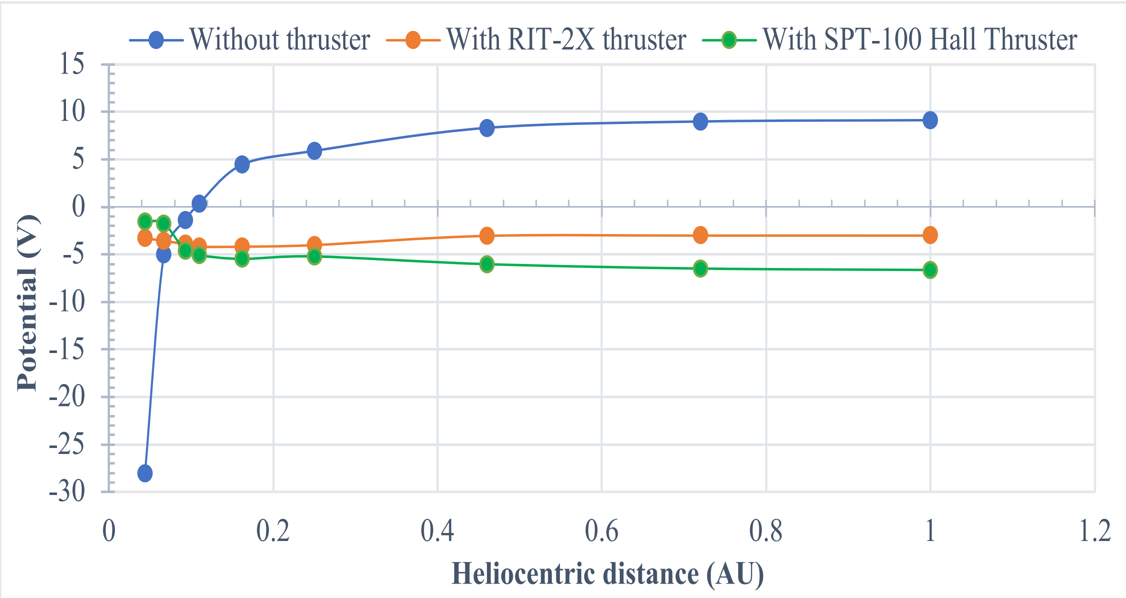

Figure 3.2: Spacecraft potential with the SPT-100 Hall thruster, the RIT-2X thruster and without thruster versus heliocentric distance.

Below 0.25 AU, near the Sun, the impact of spacecraft charging becomes increasingly critical because of the hot and dense ambient environment. As illustrated in Figure 3.2, the spacecraft potential decreases sharply below 0.25 AU, charging the spacecraft to a significantly negative potential of -28.6 V at 0.044 AU. Negative charging can be explained by the fact that the high thermal electron density of 10^9 m^{-3} and temperature of about 100 eV dominate and charge the spacecraft negatively despite high photoemission (Shinde, Held, Cairns, and Deprez, 2024; Ergun et al., 2010; and Guillemant, 2014). The result might seem contradictory when considering photoemission, but it can be explained by the fact that the Debye length of the photoelectron is smaller than the spacecraft size, which moves the local potential barrier close to the surface and restricts the escape of photoelectrons and secondary electrons. This phenomenon corresponds to a thin sheath, also known as the space-charge limited model, which holds true when the Debye length of photoelectrons is smaller than the spacecraft size (Ergun et al., 2010 and Guillemant, 2014). Consequently, the simulation suggests that the final spacecraft potential is primarily influenced by the density and temperature of thermal electrons, photoelectrons, secondary electrons, and solar photon flux in the absence of a thruster.

In a previous paper Shinde, Held, and Cairns (2023), comparable results were achieved. However, considering a constant solar photon flux rather than a varying solar photon flux with respect to the distance to the Sun led to inaccurate results (Shinde, Held, and Cairns, 2023). Interestingly, subsequent work shows that, considering a constant solar flux as a function of heliocentric distance, there were only minor fluctuations in the spacecraft potential with the thruster on than without the thruster (Shinde, Held, Cairns, and Deprez, 2024). Thus, the study from reference Shinde, Held, Cairns, and Deprez (2024) validates that solar photon flux does not significantly impact spacecraft charging when the thruster is on, in contrast to the scenario without the thruster. It also demonstrates that electric thrusters consistently contribute to reducing and stabilizing spacecraft potential at small negative values across various solar wind conditions, charging it to a low negative potential regardless of solar photon flux (Shinde, Held, Cairns, and Deprez, 2024).

3.4.2 Comparison of collected and emitted current with and without the thruster

Figure 3.3 shows the collected and emitted currents on the surface of the spacecraft, comparing scenarios with and without the SPT-100 Hall thruster and the RIT-2X thruster. The section specifically examines the charging effects of the RIT-2X thruster and its impact on spacecraft potential, contrasting it with the SPT-100 Hall thruster and the absence of any thruster. As shown in Figures 3.3a and 3.3b, the currents of thruster electrons and CEX-ions are significantly higher than other currents across heliocentric distances. The photoelectron, secondary electron, CEX-ions, and thruster electron currents consistently increase in magnitude with the distance from the Sun, ranging from 0.044 AU to 1 AU. In contrast, when the SPT-100 Hall thruster is utilized, CEX-ions are consistently collected at all heliocentric distances, while the thruster electrons and other currents monotonically increase with the distance from the Sun, spanning from 0.067 AU to 1 AU. A detailed study on the SPT-100 Hall thruster is provided in Chapter 2 and a previous published study (Shinde, Held, Cairns, and Deprez, 2024). The spacecraft potential at various heliocentric distances is represented by an orange dotted curve for the RIT-2X thruster, green for the SPT-100 Hall thruster, and a blue dotted curve for without the thruster

Far away from the Sun, above 0.25 AU, and in the absence of the thruster, photoelectrons dominate because of the low mean energy of thermal electrons. The photoelectron electron density is much higher, of the order of $10^8\,\mathrm{m}^{-3}$, compared to other number densities (ambient ions $10^7\,\mathrm{m}^{-3}$, thermal electrons $10^7\,\mathrm{m}^{-3}$, secondaries $10^7\,\mathrm{m}^{-3}$), which all vary with the inverse squared distance from the Sun. In this region, without the thruster, the spacecraft potential undergoes a positive charge, decreasing monotonically from 9 V to 5 V from 0.25 to 1 AU.

However, when the thruster is operated, the positively charged surface becomes enveloped by a dense cloud of CEX-ions with a density of approximately $10^{10}\,\mathrm{m}^{-3}$, which are associated with higher-speed thruster electrons having a density of $10^{11}\,\mathrm{m}^{-3}$ that are attracted to the positively charged surface. The surface accumulates more thruster electrons to neutralize the positive charge. Because the thermal speed of electrons is much higher than that of ions, the surface collects more negative electrons per unit time, so often a negative potential is obtained when the thruster is on.

Figure 3.3a illustrates that with the RIT-2X thruster, the collected current of CEX-ions and thruster electrons at 1 AU is approximately 51 mA, significantly surpassing the thermal electron current of 0.004 mA. Consequently, the thruster backflow plume dominates over solar wind effects, charging the spacecraft to about -3.0 V from 0.25 AU to 1 AU. Similarly, with the SPT-100 Hall thruster, the collected current of thruster and CEX-ions, approximately 6.8 mA and 5.7 mA, respectively, dominates over thermal electrons and charges the spacecraft in the range of -6 to -5 V. A noticeable difference in the collected current of CEX-ions, thruster electrons, and spacecraft potential between the two thrusters may be attributed to the lower thrust of the SPT-100 Hall thruster (35 mN) compared to the RIT-2X thruster (180 mN).

As the spacecraft approaches the Sun, below 0.25 AU, the thermal electron density and temperature increase and dominate the spacecraft and surrounding plasma. As apparent in Figure 3.3c, despite high photoemission and secondary electron emission, the spacecraft charges to a negative potential within 0.25 AU mainly due to the strong thermal electron dominance. For example, at 0.044 AU, the thermal electron density of 10^9 m^{-3} and the temperature of 100 eV dominated the photoelectron and secondary electrons, developing a strong electrostatic sheath that restricts their escape from the surface of the spacecraft (Shinde, Held, Cairns, and Deprez, 2024). Given their low kinetic energy, both photoelectrons and secondary electrons are unable to overcome the strong potential barrier, leading to high recollection and the build-up of negative charge on the spacecraft of -28.6 V. The recollection of these low-energy electrons helps to lower the negative charge, but they might interfere with the low-energy plasma measurements and contaminate the data.

In contrast, during the operation of the RIT-2X thruster, it maintains a consistently low and negative potential within the range of -3 V to -4.5 V from 0.162 to 0.044 AU. A notable observation occurs at 0.044 AU, where the potential decreases from -28 V to -3.25 V when the thruster is active. This significant reduction is primarily attributed to the high dominance of CEX-ions and thruster electrons over other charged particles, which diminish the potential barrier surrounding the spacecraft (as detailed in Section 3.4.3). Consequently, this reduction no longer constrains the escape of photoelectrons and secondary electrons, resulting in a lower negative potential. At a distance of 0.044 AU, when the RIT-2X thruster is on, the recollection of secondary electrons and photoelectrons is

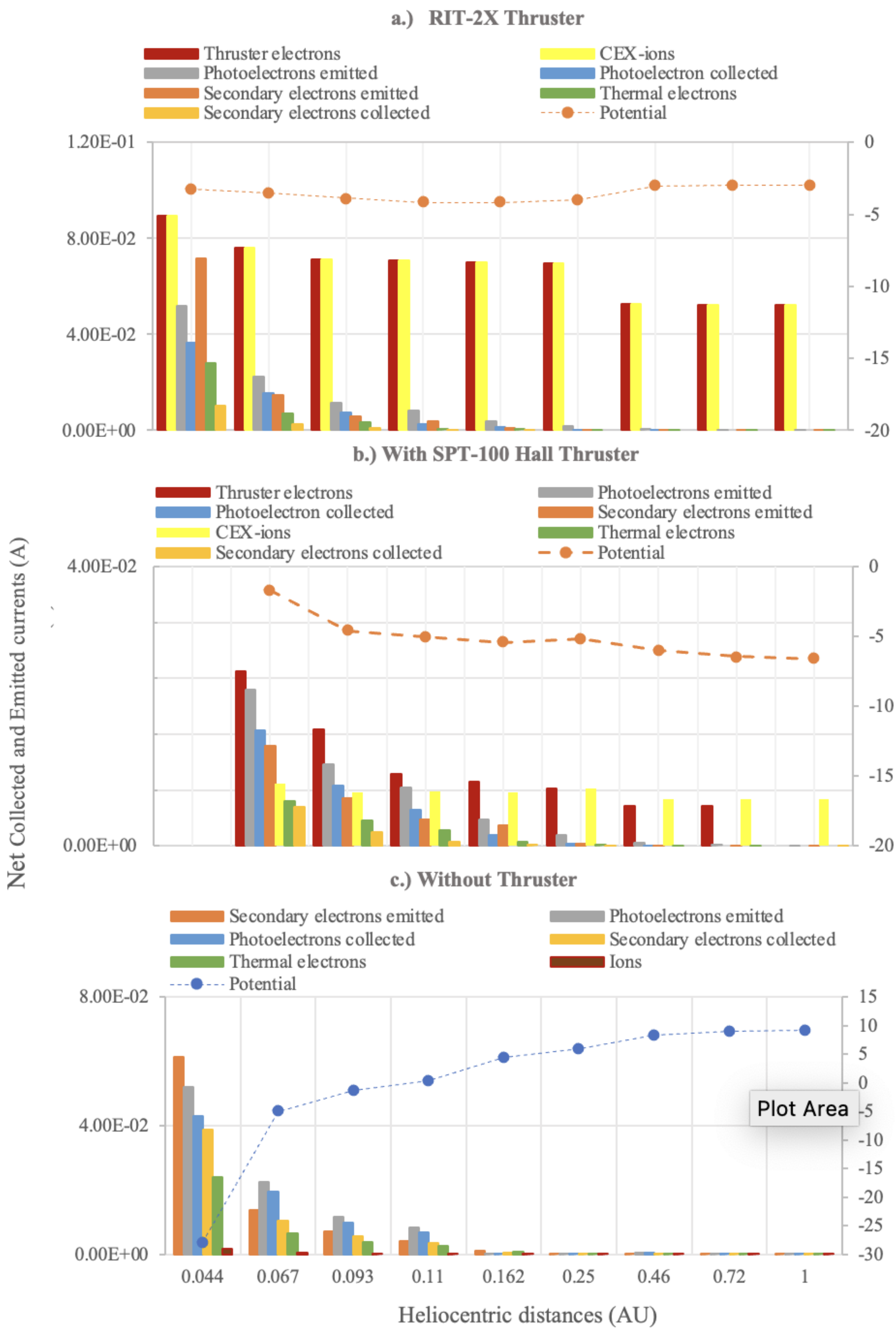

Figure 3.3: Collected and emitted currents (on the primary axis) and spacecraft potential (on the right-hand axis) versus heliocentric distance a.) With RIT-2X, b.) SPT-100 Hall thruster, and c.) without the thruster. Note that for SPT-100 Hall thruster the simulation at 0.044 AU are not performed due to SPIS technical issues

significantly reduced to 10 mA and 36 mA, respectively. The reduction in recollection of these low-energy electrons may enhance the accuracy of low plasma measurements, compared to without the thruster recollection of 38mA and 42 mA at 0.044 AU. In summary, the RIT-2X thruster consistently maintains a low and negative potential across heliocentric distances ranging from 0.044 AU to 1 AU, providing a stabilizing effect that surpasses the SPT-100 Hall thruster. In particular, a noticeable reduction in spacecraft potential is observed at 0.044 AU, decreasing from -28.6 V to -3.25 V. During thruster operation, the final potential of the spacecraft is determined by the density of CEX-ions and thruster electrons in relation to the ambient plasma density. The higher density and current of the CEX-ions and thruster electrons, in comparison to the ambient plasma, contribute to a much lower negative potential.

3.4.3 Ram, wake and side potential

In this section, the evolution of ram, wake, and side potential structures will be discussed, focusing on with and without the RIT-2X thruster. Detailed potential profiles of the SPT-100 Hall thruster can be found in previous work (Shinde, Held, Cairns, and Deprez, 2024). Figure 3.4 demonstrates the intrinsically 2D (rotationally symmetric) nature of the potential structure of the spacecraft which is obtained by cutting Figure 3.1 along the y=1 plane for varying heliocentric distances. The ram direction is in the negative x-axis direction, and the wake direction is along the positive x-axis. The left images show the potential with the RIT-2X thruster, while the right images show the potential without the thruster on, for distances from 0.044 AU to 1 AU. The negative potential wells due to photoelectrons and secondary electrons are visible in the ram direction (left side) for distances of 0.044 AU when the thruster is on and less than about 0.25 AU when the thruster is off. In the wake direction the thruster makes the potential positive at all distances, but when the thruster is off a negative well in the potential is visible within about 0.25 AU. This is the standard potential well caused by the exclusion of ambient ions streaming from the Sun by the spacecraft body, whereas the ambient electrons can easily access this region due to their large thermal speeds, making the net charge and potential negative. On the sides (e.g., the +/- z direction), the potential shows a relatively standard sheath.

Figures 3.5a and 3.5b show the ram potential, with and without the RIT-2X thruster, in the top left and top right panels, respectively. With the thruster on, as the spacecraft moves from 1 AU to 0.067AU, it experiences a minimum ram potential in the range of -3 to -4 V, likely due to the accumulation of thruster electrons. A localized minimum in the potential of -7 V is observed only at 0.044 AU, as shown in Figure 3.5a (top left panel). The localized minimum can act as a potential barrier or a trap depending on the particle charge.

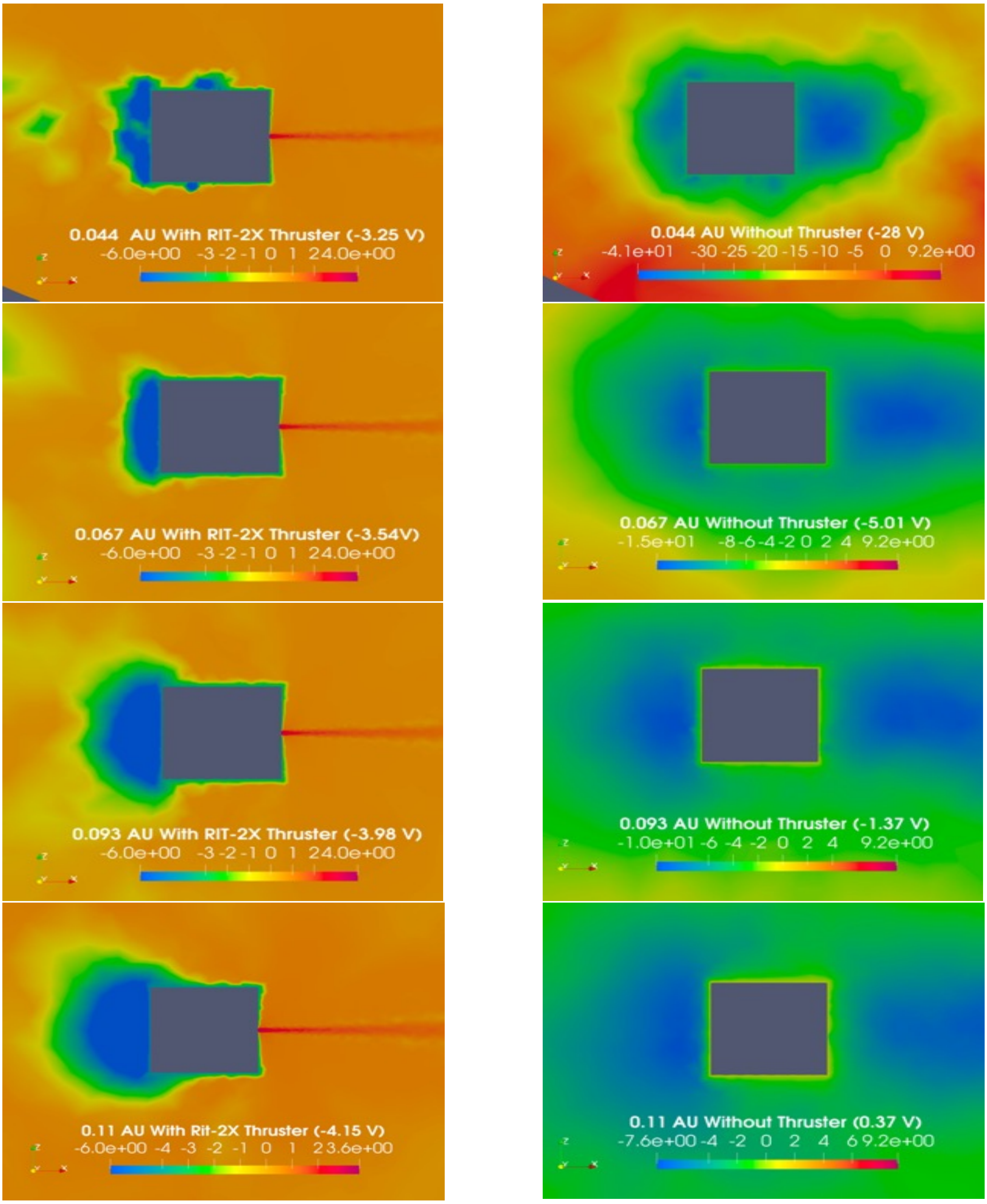
0.044 AU With RIT-2X Thruster (-3.25 V)
-6.0e+00 -3 -2 -1 0 1 24.0e+00
0.044 AU Without Thruster (-28 V)
-4.1e+01 -30 -25 -20 -15 -10 -5 0 9.2e+00
0.067 AU With RIT-2X Thruster (-3.54V)
-6.0e+00 -3 -2 -1 0 1 24.0e+00
0.067 AU Without Thruster (-5.01 V)
-1.5e+01 -8 -6 -4 -2 0 2 4 9.2e+00
0.093 AU With RIT-2X Thruster (-3.98 V)
-6.0e+00 -3 -2 -1 0 1 24.0e+00
0.093 AU Without Thruster (-1.37 V)
-1.0e+01 -6 -4 -2 0 2 4 9.2e+00
0.11 AU With Rit-2X Thruster (-4.15 V)
-6.0e+00 -4 -3 -2 -1 0 1 23.6e+00
0.11 AU Without Thruster (0.37 V)
-7.6e+00 -4 -2 0 2 4 69.2e+00

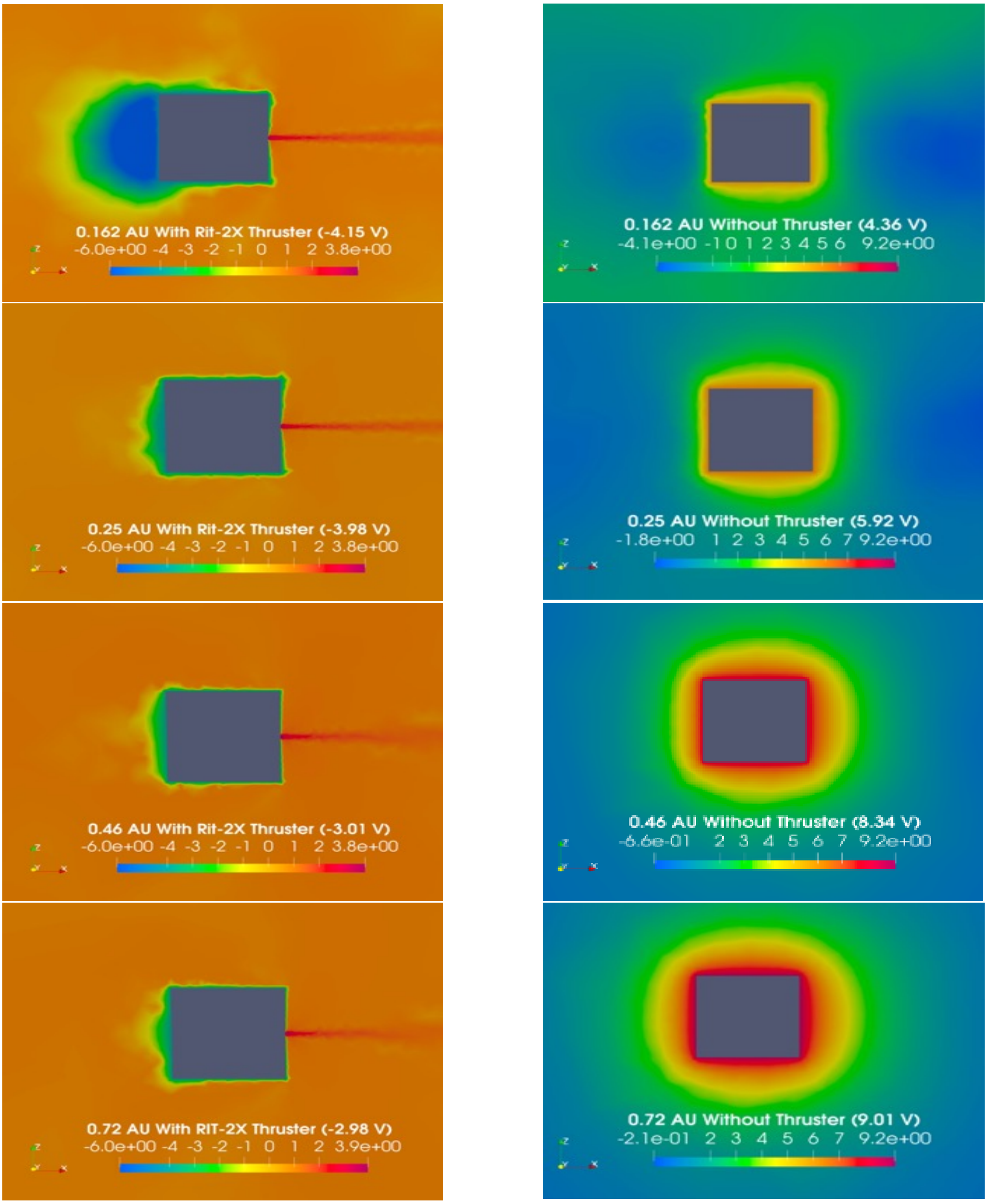
0.162 AU With Rit-2X Thruster (-4.15 V)
-6.0e+00 -4 -3 -2 -1 0 1 2 3.8e+00
0.162 AU Without Thruster (4.36 V)
-4.1e+00 -1 0 1 2 3 4 5 6 9.2e+00
0.25 AU With Rit-2X Thruster (-3.98 V)
-6.0e+00 -4 -3 -2 -1 0 1 2 3.8e+00
0.25 AU Without Thruster (5.92 V)
-1.8e+00 1 2 3 4 5 6 7 9.2e+00
0.46 AU With Rit-2X Thruster (-3.01 V)
-6.0e+00 -4 -3 -2 -1 0 1 2 3.8e+00
0.46 AU Without Thruster (8.34 V)
-6.6e-01 2 3 4 5 6 7 9.2e+00
0.72 AU With RIT-2X Thruster (-2.98 V)
-6.0e+00 -4 -3 -2 -1 0 1 2 3.9e+00
0.72 AU Without Thruster (9.01 V)
-2.1e-01 2 3 4 5 6 7 9.2e+00

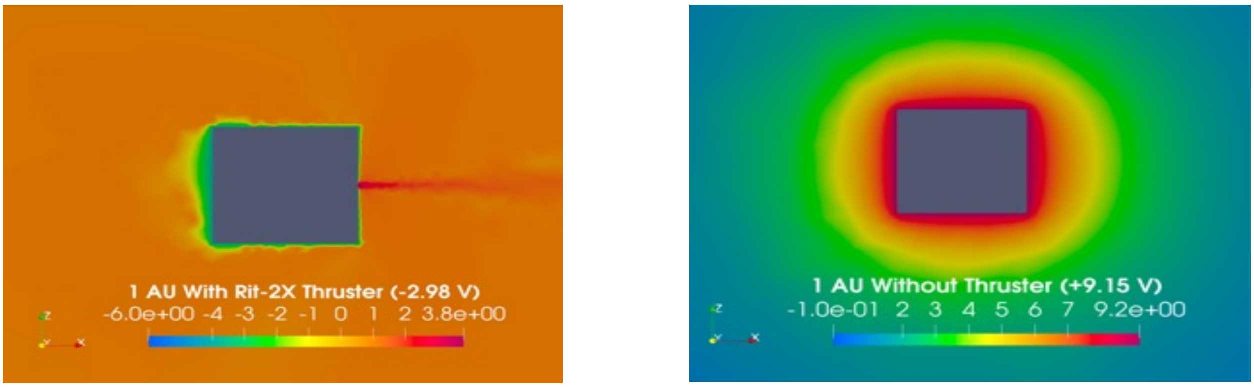

Figure 3.4: Cross comparisons of 2D spacecraft potential maps with and without RIT-2X thruster at varying heliocentric distances, corresponding to Figure 3.1, cut in y = 1 plane. sunlight and solar wind directions are on the left.

However, CEX-ions and thruster electrons play a crucial role in neutralizing this potential barrier, maintaining the spacecraft potential at a more positive value. It is evident from Figures 3.5a and 3.5b at 0.044AU, where the potential barrier is reduced from -35 V (without thruster) to -7 V (with thruster), mainly due to the presence of CEX-ions that help neutralize the charge surrounding the spacecraft. In contrast, without the thruster, a positive ram potential is observed in the range of 0.6 to 9 V from 1 AU to 0.25 AU (as shown in Figure 3.5b). Within a distance of 0.11 AU from the Sun, the formation of a potential barrier begins, and the potential becomes significantly more negative than when the thruster is active. Specifically, at 0.067 AU, the potential barrier is -14.1 V without the thruster, in contrast to a mere +0.5 V when the thruster is on. Below 0.11 AU, without the thruster, the ram barrier potential spans from -7V to -34V, causing a notable accumulation of secondary electrons emitted from the spacecraft. However, with the RIT-2X thruster active, the ram potential barriers are significantly lowered to a range of -3 to -7 V within 0.11 AU, enhancing the precision of sensitive instruments and thereby promoting the mission's safety and success.

Figures 3.5c and 3.5d show the wake potential structure with and without the RIT-2X thruster in the middle left and middle right panels, respectively. A stable positive potential of approximately +3.5 V is observed in the satellite when the thruster is on, the potential decreasing monotonically with increasing distances from the spacecraft (Figure 3.5c). Note that the potential profiles are essentially independent of helio distance when the thruster is on, consistent with the thruster plume dominating all other charging influences. Together, the wake region behind the spacecraft is filled with ions and electrons emitted from the thruster. As a result, it develops a plasma sheath that acts as a barrier to ambient electrons directly impacting the spacecraft's surface. The sheath reduction of

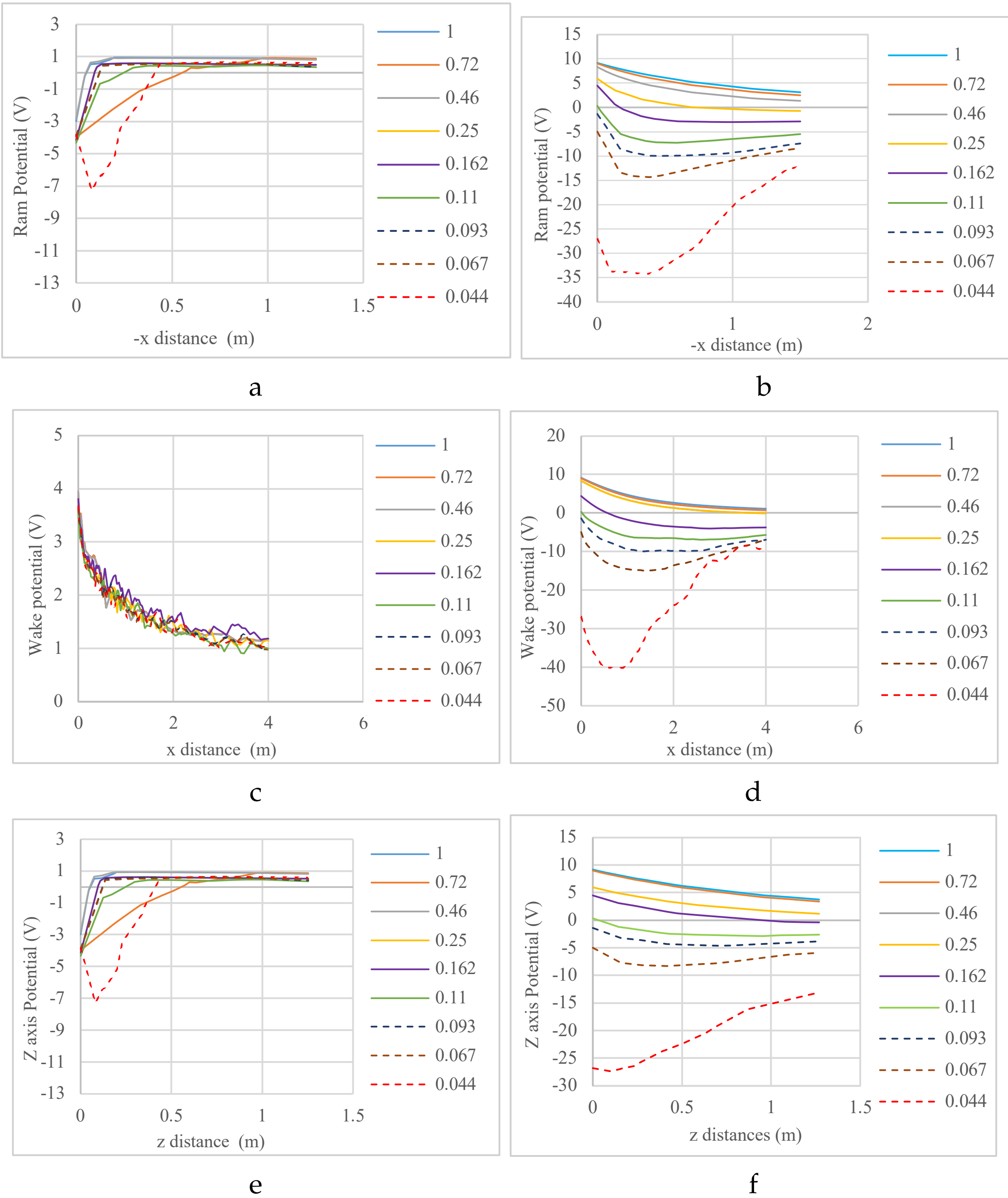

Figure 3.5: The plot shows the potential profile with (on left) and without (on right) the RIT-2X thruster along the ram direction (-x axis), wake direction (x-axis), and the sheath direction (z-axis) obtained from Figure 3.4. Figures 3.5a and 3.5b illustrate the ram potential with and without the thruster, positioned on the top left and top right, respectively. Figures 3.5c and 3.5d depict the wake potential with and without the thruster, located in the middle left and middle right panels. Finally, Figures 3.5e and 3.5f show the side potential with and without the thruster, placed in the lower left and lower right panels.

potential with increasing distance into the plasma is mainly due to larger electron densities. In general, the presence of positive ions in the wake of an electric thruster can play a significant role in reducing spacecraft charging and managing potential barriers, contributing to the safe and stable operation of the spacecraft in the space environment. However, without the thruster (Figure 3.5d), the wake potentials at and above 0.25 AU decrease monotonically with increasing distance from the spacecraft. However, interior to 0.162 AU the profile develops a localized minimum near x = 1 m with a magnitude that increases as the heliocentric distance decreases. For instance, at 0.067 AU this wake barrier reaches -14 V when the thruster is off. Further towards the Sun at 0.044 AU, the wake barrier reaches -40 V which may result in the return of low-energy electrons back to the surface and enhancing spacecraft charging dynamics. Thus, when the thruster is off the spatial profiles of the potential in the ram and wake directions are surprisingly similar, presumably because of increased electron densities due to increased photoelectron effects (ram direction) and hotter, denser, ambient electrons in the wake cavity, respectively.

Figures 3.5e and 3.5f show the side profiles (perpendicular to the ram and wake axis) with and without the thruster in the lower left to lower right panels, respectively. Figure 3.5 shows a low negative potential in a small range of -3 to -7 V from 0.067 AU to 1 AU with thruster on compared to Figure 3.5f, which has a large range of -40 to +9 V with the thruster off from 0.044 AU to 1 AU, respectively. With the thruster on the spatial profiles is reminiscent of a standard sheath for cold dense electrons (small Debye length) about a negative potential object for R > 0.067AU. Similarly, for R > 0.093 AU when the thruster is off the monotonic potential profile appears appropriate for a standard sheath about a positively charged object for warm dilute electrons (large Debye length). Only for R< 0.067 AU do the perpendicular sheaths change character and evolve to have a negative potential well.

Referencing the earlier research in Chapter 2 by (Shinde, Held, Cairns, and Deprez, 2024), the SPT-100 thruster exhibited comparable effects by decreasing the potential barrier near the Sun and reducing negative charging compared to operations without the thruster. In particular, at the ram barrier at 0.067 AU, the potential barrier decreased from -14 V (without thruster) to -8 V (with SPT). However, this was still not as effective as the RIT-2X thruster at the same distance, where the potential barrier dropped from -14 V to +0.5 V (with RIT), and the wake potential for both thrusters stabilized at +3.5 V for the RIT-2X and 25 V for the SPT-100 Hall thruster, in contrast to the significant fluctuations from 9 V to -40 V observed without the thruster. In summary, the RIT-2X thruster proved more effective in consistently lowering the spacecraft's minimum negative potential across heliocentric distances compared to the SPT-100 Hall thruster, primarily due to higher CEX-ions and thruster electron density.

3.4.4 Role of Photoelectrons on Spacecraft Potential

Figure 3.6 illustrates the impact of photoelectrons on spacecraft potential at distances of 0.067 AU and 1 AU, considering both the absence of a thruster and the presence of the RIT-2X and SPT-100 Hall thrusters. At 0.067 AU, Figure 3.6a shows a notable potential variation without the thruster, while the SPT-100 Hall thruster results in a comparatively minor change. As expected, the inclusion of photoelectrons leads to a more positive satellite potential. However, with the RIT-2X thruster, the impact on the spacecraft potential is exceptionally small. In contrast, at 1 AU (Figure 3.6b), it becomes evident that without the thruster there is a significant change in potential, while the SPT-100 Hall thruster results in a relatively minor variation. In particular, the operation of the RIT-2X thruster has a minimal impact on spacecraft potential compared to the SPT-100 and the absence of a thruster.

As depicted in Figure 3.6a, when the thruster is off, at 0.067 AU near the Sun, the photoelectrons efficiently contribute to maintaining a low negative spacecraft potential. Without photoemission and thruster at 0.067 AU, the spacecraft's potential reaches -8.3 V instead of -5.0 V. Similarly, the SPT-100 Hall thruster induces variations in spacecraft potential in the absence of sunlight, with the potential converging at -4.5 V instead of -1.7 V compared to no thruster. In contrast, the impact of the RIT-2X thruster on the spacecraft potential is minimal, with the potential varying by a very small factor, almost unaffected, regardless of whether sunlight is present or not. The phenomenon is possibly attributed to the high collected current of CEX-ions and thruster electrons, which tend to dominate the spacecraft and surrounding plasma. The results also highlight that a higher thruster and CEX-ion density, in comparison to ambient density, leads to a lower negative charging of the spacecraft, eliminating the effects of the ambient environment. At 1 AU, as shown in Figure 3.6b, spacecraft charging becomes less critical due to the low mean energy of thermal electrons. In this region, photoelectrons dominate the current, positively charging the spacecraft to +9V. However, the absence of sunlight can result in a large negative potential of approximately -13 V (as indicated in Figure 3.6b). In contrast, with both the SPT-100 Hall thruster and the RIT-2X thruster, the influence of photoelectrons on the spacecraft potential is notably negligible. In summary, the RIT-2X thruster effectively mitigates the negative charging of the spacecraft, demonstrating negligible impact at 1 AU and exceptionally low variation in spacecraft potential at 0.067 AU in the absence of photoelectrons. The effectiveness persists regardless of the presence or absence of sunlight, highlighting the thruster's consistent ability to maintain spacecraft stability.

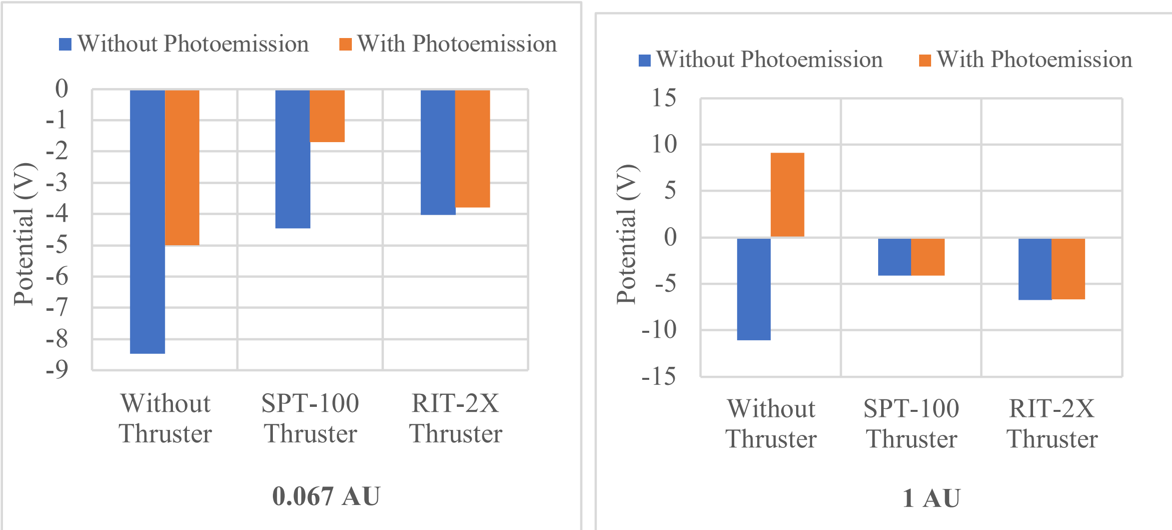

Figure 3.6: Spacecraft potential with and without photoelectrons a.) 0.067 AU (on the left) and b.) 1 AU (on the right)

3.5 Conclusion

The study examined the impact of ambient electrons and ions, thruster electrons and CEX-ions, along with photoemission and secondary electron effects at different heliocentric distances, using the RIT-2X thruster, the SPT-100 Hall thruster, and no thruster. The results revealed that the RIT-2X thruster effectively maintains spacecraft potential at a consistently low negative level, ranging from -3 to -4 V, contrasting with a substantial variation between +9 V and -28 V. During RIT-2X thruster operation at 0.044 AU, there was a significant decrease in spacecraft potential, dropping from -28 V to -3.25 V. This reduction is attributed to high-density CEX-ions and thruster electrons, reducing the potential barrier around the spacecraft from -35 V to -7 V. Consequently, there was a notable decrease in the recollection of photoelectrons and secondary electrons, with values of 10 mA and 36 mA, respectively, compared to 38 mA and 42 mA at 0.044 AU. The finding suggests that the RIT-2X thruster behaves similarly to the SPT-100 Hall thruster, maintaining a low, stable, and negative spacecraft potential across solar wind conditions from 0.044 AU to 1 AU. The discrepancy in spacecraft potential between the two thrusters may be due to differences in the density and current of CEX-ions and thruster electrons accumulating on the spacecraft's surface. When the thruster is activated, the spacecraft's final potential depends on the density and current of CEX-ions and thruster electrons in relation to ambient plasma density. A higher density of CEX-ions and thruster electrons compared to ambient plasma density leads to a reduction in the spacecraft's potential to a more positive level, as observed in the RIT-2X thruster compared to the SPT-100 Hall thruster.

Another finding is that the RIT-2X thruster has a remarkable ability to mitigate the impact of photoemission on the spacecraft potential, making this effect nearly negligible at both 1 AU and 0.067 AU. This contrasts to the SPT-100 Hall thruster, where photoemission appears to play a more substantial role in varying the spacecraft potential at 0.067 AU. The RIT-2X electric thruster, with its capacity to minimize the influence of photoemission, emerges as a promising solution, particularly in scenarios where the spacecraft operates in eclipse. The finding emphasizes the ability of the RIT-2X thruster to effectively manage spacecraft potential variation, even under conditions of varying solar illumination, thereby enhancing the overall reliability of spacecraft systems. In conclusion, this study provides valuable insight into different electric thruster behaviors in spacecraft charging across a wide range of heliocentric distances. Understanding ion-induced charging can aid in selecting the appropriate electric thruster based on the mission's purpose at specified distances. Future work will focus on understanding the effects of spacecraft charging on solar panels with and without the RIT-2X thruster.

CHAPTER 4

SPT-100 Hall Thruster and RIT-2X Thruster-Spacecraft Interaction in Jovian Magnetosphere

Peer Reviewed at Australian Space Research 2023 Conference: Tejaswi L Shinde, Jason M Held, Iver H Cairns

4.1 Abstract

The SPT-100 Hall and RIT-2X thruster models are simulated using Spacecraft Plasma Interaction Software (SPIS) to predict the variation in spacecraft potential across different magnetospheric plasma environments around Jupiter at 5.2 AU. The analysis is conducted in three distinct regions: Europa at 9.5 Jovian radii (R_j), Ganymede at 15 R_j, and Callisto at 26.1 R_j. Since magnetospheric environments significantly differ from solar wind conditions, the objective is to gain insights into the impact of Jovian magnetospheric plasma on the spacecraft potential with and without the RIT-2X thruster and the SPT-100 Hall thruster. The primary findings show that both electric thrusters effectively maintain a low, stable, and negative potential within a small range of -3 to -6 V in the Jovian magnetosphere, as opposed to the varying range of -25 to 11 V without the thruster. Interestingly, the RIT-2X thruster exhibits a stronger stabilizing effect compared to the SPT-100 Hall thruster, potentially due to its higher CEX-ion and thruster electron density. Furthermore, in the absence of sunlight, a spacecraft's potential tends to charge to a substantially more negative level, especially in Europa's orbit. However, using an electric thruster significantly mitigates this negative potential, stabilizing the spacecraft potential to a low negative value. Thus, the study affirms that the use of an electric thruster can be advantageous in maintaining and stabilizing the spacecraft's potential, not only in solar wind conditions but also in planetary magnetospheres.

4.2 Introduction

As the spacecraft travels through various plasma conditions, it encounters a variety of charged particles. These particles bombard the spacecraft, causing its surface to charge (Lai and Cahoy, 2016). Furthermore, an integrated electric thruster with the spacecraft, essential for propulsion, expels CEX-ions and thruster electrons to form a backflow plume (Goebel et al., 2023). Low-velocity charge-exchange ions (CEX ions) are formed due to collisions between fast-beam ions and propellant neutrals within the main ion beam, and thruster electrons are emitted from the cathode (Goebel et al., 2023). These low-energy ions and electrons flow back toward the spacecraft, giving rise to two primary effects. Firstly, the deposition of effluent causes contamination on optical sensors, solar arrays, thermal control systems, and other communication devices (Wang, 1997). Secondly, the presence of CEX-ions and associated electrons modify the properties of the ambient plasma surrounding the spacecraft, leading to an additional current that can influence the spacecraft potential and plasma instrument observations (Wang, 1997). These two factors, the ambient plasma and electric thruster plasma, combine to create a dynamic and complex charging environment, causing variation in the spacecraft's potential. The excess negative or positive potential of the spacecraft can lead to a range of operational issues, disrupting the normal functioning of electronic systems onboard and resulting in electrical discharges that can harm or interfere with delicate instruments. It also produces a strong electrostatic sheath that envelopes the spacecraft, leading to the accumulation of low-energy electrons that interfere with the sensitive instruments (Guillemant, 2014). As a result, a thorough study of the interactions between electric thrusters and spacecraft in various plasma conditions is imperative to prevent operational and measurement anomalies and failures. However, performing such complex interaction measurements in a vacuum chamber presents challenges due to the physical scale of the system and the inability to fully replicate the solar wind environment, making it time-consuming and often inaccurate and costly. Consequently, numerical simulations are crucial in forecasting interactions between thrusters and spacecraft, offering a more detailed method of acquiring essential knowledge about charging behaviors as opposed to ground tests.

In prior investigations, scientists conducted simulations of the Jupiter Icy Moons Explorer (JUICE) spacecraft to gain insight into the plasma environment within Jupiter's magnetosphere (Holmberg et al., 2019). They employed Spacecraft Plasma Interaction Software (SPIS) to examine the variation in spacecraft potential across different regions of Europa, Ganymede, and Callisto. Their findings revealed that the spacecraft orbiting Europa exhibited a negative charge potential, primarily due to the prevalence of ambient electrons. As the spacecraft moved farther away to the Ganymede and Callisto regions, it exhibited an increasingly positive potential due to the greater influence of secondary and photoelectrons, respectively (Holmberg et al., 2019). Similarly, other researchers utilized SPIS software to model various spacecraft designs for prospective Jupiter missions, such as the Jupiter Ganymede Orbiter (JGO) and the Jupiter Europa Orbiter (JEO) within the Europa Jupiter System Mission. These simulations considered the spacecraft's exposure to the solar wind and Jupiter's magnetospheric plasma. The results indicated that in sunlight, both at Ganymede and Callisto, the spacecraft exhibited a positive charge potential (Rudolph, 2012). However, in the absence of sunlight, the spacecraft's potential significantly increased to a high negative value (Rudolph, 2012). It should be noted that these simulations did not incorporate the presence of an electric thruster (Holmberg et al., 2019; Rudolph, 2012). Earlier research Shinde, Held, and Cairns (2023); Shinde, Held, and Cairns (2024); Shinde, Held, Cairns, and Deprez (2024) involved simulations to investigate the interactions between the SPT-100 Hall thruster, RIT-2X thruster plume and the surface of the spacecraft under varying solar wind conditions, ranging from 0.044 to 1 AU. These studies assessed the effects of different factors, such as whether solar-photon flux was present or absent, and whether photoemission and secondary electrons were included or excluded. The main finding suggests that electric thrusters provide low, stable and negative potential throughout a wide range of heliocentric distances and effectively mitigate the issue of spacecraft negative charging in various scenarios, shown in Shinde, Held, and Cairns (2023); Shinde, Held, Cairns, and Deprez (2024). Specifically, it was found that photoelectrons and secondary electrons play a crucial role near the Sun when the thruster is on, making the potential more positive but maintaining a low negative potential for the spacecraft.

The primary objective of the present paper is to explore the implications of spacecraft charging within different regions of the Jovian magnetospheric plasma, specifically focusing on Europa (9.5 R_j), Ganymede (15 R_j), and Callisto (26.1 R_j). The investigation will involve evaluating the impact of activating and deactivating either the SPT-100 Hall thruster or the RIT-2X thruster. The factors considered in the simulations are ambient electrons and ions, thruster-generated electrons and CEX-ions, photoemission, and secondary electrons, as well as the solar photon flux at varying radial distances from Jupiter. The spatial profiles of the configurations of the ram, wake, and electrostatic sheath within these three regions, spanning a radial distance ranging from 9.5 R_j to 26.1 R_j will also be examined. To achieve these objectives, SPIS software is used to simulate the spacecraft charging in Jovian magnetospheric plasma. Section 4.3 discussed the simulation setup and plasma parameters used. Following this, Section 4.4 will detail the simulation results, which include variations in spacecraft potential and the measurements of currents emitted and collected at the satellite's surface under different conditions of thruster activity across Europa, Ganymede, and Callisto. The role of photoelectrons in affecting spacecraft potential will be examined in further detail in Section 4.5, considering various radial distances and thruster operations. Section 4.6 then illustrates two-dimensional and detailed potential profiles of the ram, wake, and sheath around the spacecraft. Through a thorough examination of these elements, this paper aims to provide an in-depth analysis of spacecraft charging in the Jovian magnetospheric plasma, specifically focusing on the effects of the SPT-100 and RIT-2X thrusters on spacecraft potential.

4.3 Simulation Description

The study employs the Spacecraft Plasma Interaction Software (SPIS) simulation tool, a 3D electrostatic solver that operates on the Particle in Cell (PIC) method. This tool is widely employed for spacecraft charging simulations in different environments (LEO, GEO, electric thruster operations). Similarly to the previous chapters and papers Shinde, Held, and Cairns (2022); Shinde, Held, and Cairns (2023); Shinde, Held, and Cairns (2024); Shinde, Held, Cairns, and Deprez, 2024, a similar model of the spacecraft is modeled as a cylinder with a radius of 1m and a length of 2m, coated with indium tin oxide material (ITO). The dimensions of the simulation domain vary on the basis of the Debye length, and accordingly the mesh refinements are applied. The domain dimension must be smaller than three times the thermal electron's Debye length (3 x Debye length). Meanwhile, the mesh resolution within the domain is always less than one-third of the Debye length, resulting in 50,000 to 100,000 mesh tetrahedrons. To maintain accuracy, the simulation adjusts the mesh size based on the thermal, photoelectron, and secondary electron Debye lengths (half of the local plasma Debye length). The satellite model is created using the GMSH software, as shown in Figure 4.1. The physical parameters for the Jovian magnetospheric plasma shown in Table 4.1 are taken from Rudolph (2012) for Ganymede and Callisto and and for Europa from Holmberg et al. (2019). The simulation considers varying plasma properties, such as density, temperature, plasma drift velocity, and timesteps for ions, thermal electrons, secondary electrons, and photoelectrons. Additionally, the solar-photon flux is taken into account. In the simulations, a PIC model is used to compute all species (protons, thermal electrons, photoelectrons, and secondary electrons) within a spacecraft integrated with the SPT-100 Hall thruster. In the SPIS Hall thruster and RIT-2X models, the Monte Carlo method is employed to simulate collisions between CEX-ions and various other species (neutral Xe, Xe+, Xe++) within the computational regions. The specifications for the thrusters are provided in Table 4.1.

During simulations, the thruster is assumed to be electrically connected to the spacecraft

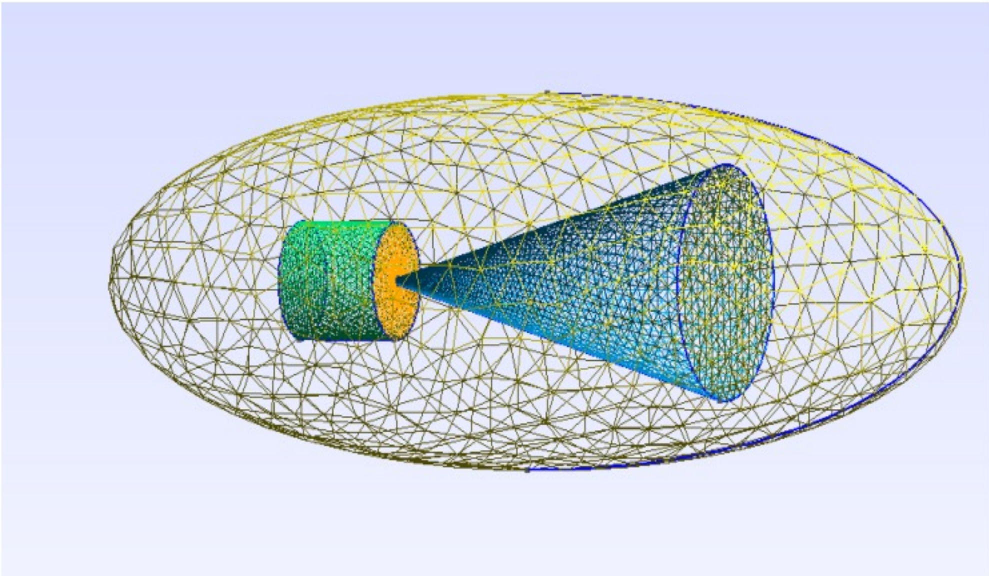

Figure 4.1: GMSH spacecraft model with a meshing grid (green/yellow), the void boundary is the simulation boundary, and the blue conical shape represents the ion plume.

Table 4.1: Parameters used for SPIS simulation. Plasma Parameters taken from (Rudolph, 2012; Holmberg et al., 2019)

Parameters	**Value**		
Geometry	1 m radius, 2 m long, cylinder		
Material	Indium Tin Oxide		
Secondary electron temperature	2eV		
Photoelectron temperature	3eV		
Ambient Ion type	O+		
Ion modelling	PIC		
Electron modelling	PIC		
Magnetic Field	Not considered		
Thruster Specification			
Electric Thruster	SPT-100 Hall	RIT-2X Thruster	
Thrust (N)	0.035	0.180	
Specific Impulse (s)	1840	2966	
Cathode Temperature (eV)	5	5	
Mass Flow rate (Xe) (kg/s)	1.91×10^6	$6.19 \times 10^{-}6$	
Current (A)	1.43	3.99	
Power (W)	723	6025	
Plasma Parameters			
Jovian Magnetospheric plasma (Rj)	Europa	Ganymede	Callisto
Plasma denisty (m-3)	2×10^8	4.5×10^6	0.5×10^6
Electron Temperature Te (eV)	20	20	100
Ion Temperature Ti (eV)	90	60	60
Ion ram speed (km/s)	60	400	400

chassis, while the spacecraft itself floats with the local plasma potential. This means that the anode and cathode of the thruster are isolated from the spacecraft (Liu et al., 2013; Tajmar and Wang, 2000). To manage excessive charging, a 500-kilo ohm resistor is introduced between the thruster and the spacecraft, providing a return path for leakage currents. The resistor ensures a high degree of isolation between the thruster and the spacecraft, thereby limiting potential charging issues. It is crucial to note that the ground of the spacecraft is distinct from the ground of the electric thrusters. Such configurations are adopted primarily to reduce spacecraft contamination caused by thruster plumes Liu et al., 2013. During the simulations, the magnetic field is not considered. In Figure 4.1 center of the cylinder (representing the spacecraft) is located at the origin of the Cartesian coordinate system (0, 0, 0). The orientation of the plane is as follows: the x-axis points along the thruster axis (i.e., the length of the cylinder), the y-axis points vertically upward along the plane of the paper, and the z-axis points outward from the plane. The Sun is at the left side.

4.4 SPIS Simulated Results

4.4.1 Variation of the spacecraft potential at Jovian's Magnetospheric Plasma

In Figure 4.2, the green, orange, and yellow lines depict the variations in spacecraft potential with the SPT-100 Hall thruster, the RIT-2X thruster, and without the thruster, respectively. Without the thruster, the potential of the spacecraft increases with an increase in the radial distance from Jupiter. The dark blue region signifies the negative charging of the spacecraft without the thruster in Europa's orbit. The light blue region corresponds to a potential near zero in Ganymede's orbit, and the white area has a significantly positive potential in Callisto's orbit. However, the spacecraft potential with the thruster on is low, stable, and negative throughout the magnetosphere of Jupiter.

At 9.5 R_j, without the thruster, the spacecraft charges negatively due to the dominance of the ambient thermal electron current. These ambient electrons hold a substantially higher density of 10^8 m^{-3} compared to other charged particles such as ambient ions (10^7 m^{-3}), photoelectrons (10^7 m^{-3}), and secondaries (10^7 m^{-3}). The mean energy of thermal electrons is large enough to cause a large rate of secondary electron emission. As evidenced in Figures 4.2 and 4.3, the high thermal electron current of 0.1mA leads to negative charging of the spacecraft at about -25 V. As we progress to the orbit of Ganymede at 15 R_j, the spacecraft charges to a positive potential of approximately 2 V. In this orbital, the spacecraft's charging remains influenced by thermal electron current; however, due

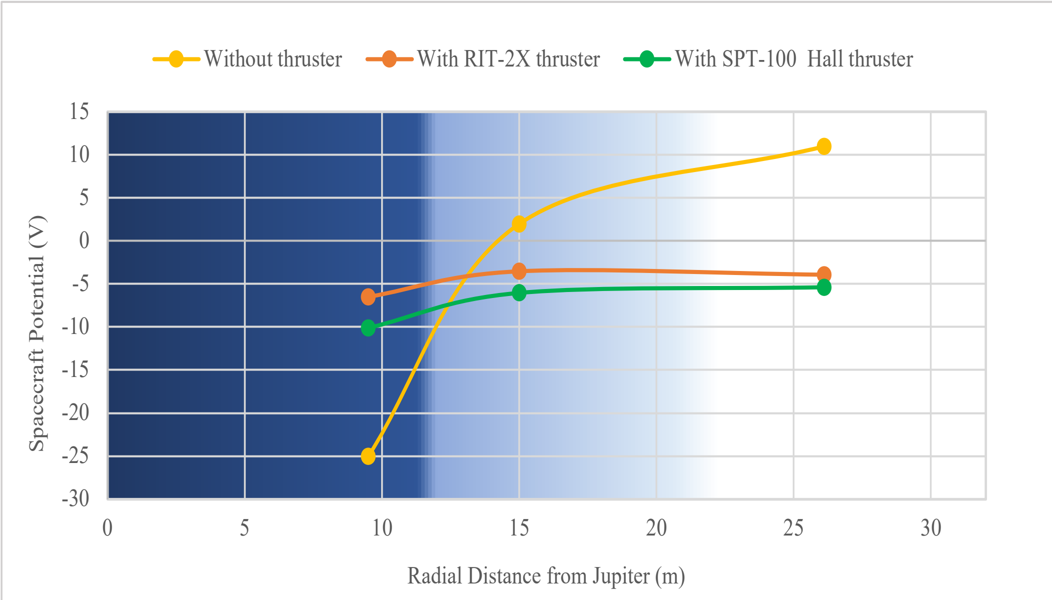

Figure 4.2: Spacecraft potential versus radial distance from Jupiter with and without the thruster. The dark blue region represents Europa at 9.5 R_j, the light blue region shows Ganymede 15 R_j, and the white region denotes Callisto at 26.1 R_j

to the higher emission of secondary electrons, the spacecraft's potential becomes positively charged. The emitted current of the secondary of about 0.017 mA is higher than the collected current of thermal electrons (0.011 mA).

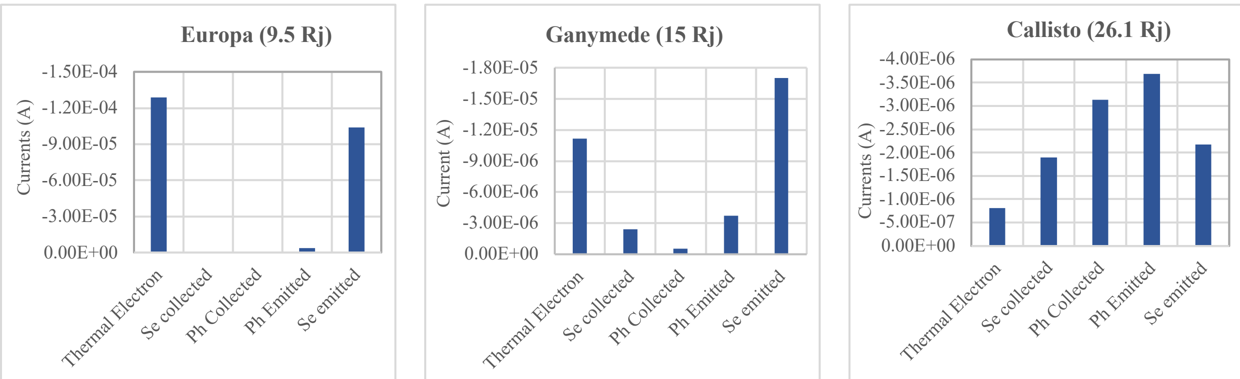

Figure 4.3: Collected and emitted currents without the thruster at the Europa, Ganymede, and Callisto. 'Se' stands for secondary electrons and 'ph' for photoelectrons.

Further away from Jupiter, the spacecraft's potential becomes significantly positive (11 V), driven by the dominance of photoelectrons. The main charging factor in the Callisto region is mainly due to the photoemission and then secondary electron emission due to the diminished thermal electron. The emitted current of photoelectrons of about 0.003 mA is much higher than the collected current of thermal electron 0.0008 mA (as shown in Figure 4.3). Observe the significantly reduced vertical scales in Figure 4.3 when transitioning from Europa to Callisto.

However, during the operation of the thrusters, a low, stable, and negative potential is observed. For the RIT-2X thruster, the potential ranges from -4 V to -6 V, while for the SPT-100 Hall thruster, it falls within the range of -10 V to -6 V (Figure 4.2). The presence of CEX-ions and thruster electrons results in the formation of a dense cloud surrounding the spacecraft, which interacts with the charged particles in close proximity to the spacecraft. These high-density CEX-ions and thruster electrons play a crucial role in neutralizing the accumulated charge on the spacecraft. The path followed by the thruster electrons mirrors that of the CEX-ions. Thruster electrons are attracted to positively charged spacecraft surfaces and repelled by negatively charged surfaces. The CEX-ions and thruster electrons act as a protective shield between the spacecraft and the surrounding plasma, thereby mitigating the impact of ambient electrons. Consequently, the operation of an electric thruster provides an additional current that effectively controls and stabilizes the spacecraft's potential at a low negative potential. For example, at 9.5 R_j, without a thruster, the spacecraft's potential reaches a significantly negative value of -25 V. However, when the thruster is activated, this potential is notably reduced to -10 V with the SPT-100 Hall thruster and -6.5 V with the RIT-2X thruster. It is worth noting that the RIT-2X thruster exhibits stronger stabilizing effects compared to the SPT-100 thruster, potentially due to its higher emission of CEX-ions. Therefore, the effectiveness of electric thruster neutralization depends on various factors including the density of emitted CEX-ions and thruster electrons, local plasma conditions, and the specific geometry of the spacecraft. Figure 4.4 shows the collected and emitted currents with the thruster on for Europa, Ganymede, and Callisto. Across these domains, the RIT-2X thruster consistently displays a dominant electron current ranging from 120 to 140 mA, accompanied by CEX-ions at 56.2 to 13 mA. Likewise, when considering the SPT-100 Hall thruster, the predominant currents are the thruster electron current, which varies from 5.5 to 10 mA, and the CEX-ions at 6 to 10 mA, surpassing all other currents.

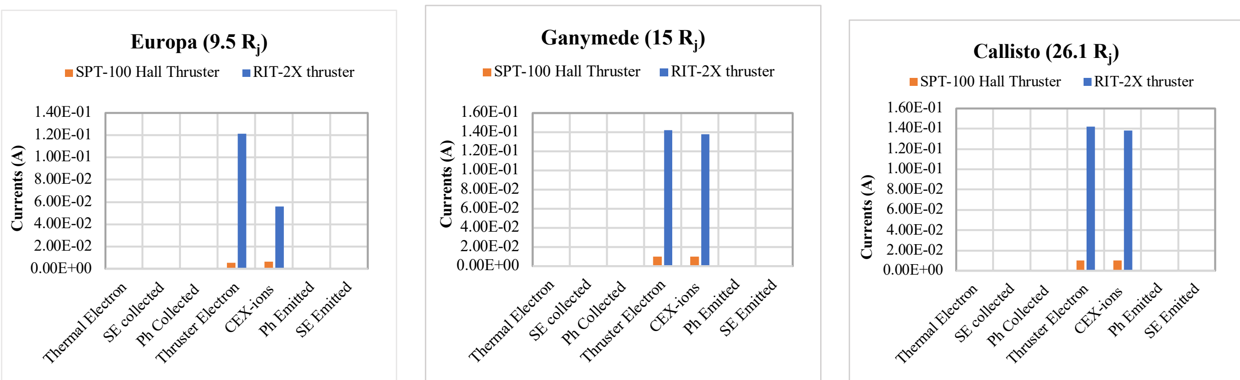

Figure 4.4: Collected and emitted currents with the thruster at the Europa, Ganymede, and Callisto.'Se' stands for secondary electrons and 'ph' for photoelectrons.

4.4.2 Spacecraft Charging Effects in the Absence of sunlight

Figure 4.5 illustrates the influence of photoelectrons on spacecraft potential within the radial distance range of 9.5 R_j to 26.1 R_j from Jupiter, both in the presence and absence of the thruster. Typically, when a spacecraft is exposed to sunlight, it becomes positively charged due to the emission of photoelectrons from its surface. In the absence of sunlight, the spacecraft tends to acquire a negative charge. Excessive negative charging can disrupt the distribution of charge, leading to variations in spacecraft potential and potential interference with sensitive instruments, thereby contaminating the data. Therefore, it is crucial to understand how spacecraft interact with electric thrusters in the absence of sunlight. To facilitate this, during this section's simulations, photoemission was eliminated.

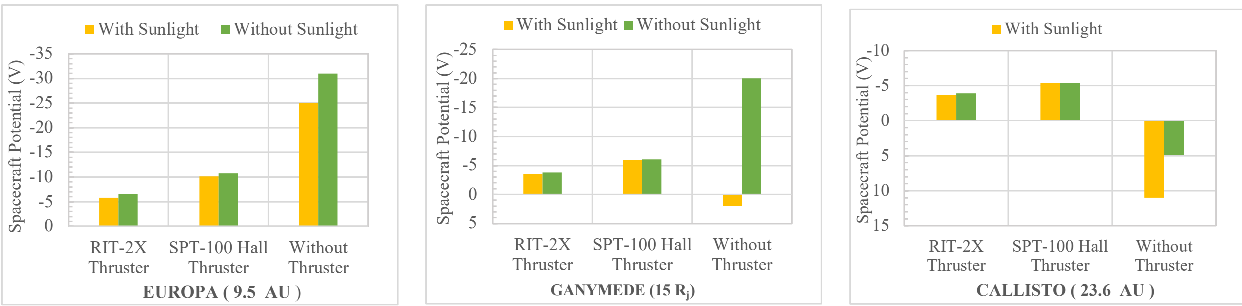

Figure 4.5: Spacecraft potential with and without photoelectrons at a.) Europa, b.) Ganymede, and c.) Callisto

As depicted in Figure 4.5, when the thruster is off and the sunlight is absent, there is a notable impact on spacecraft potential in the regions around Europa, Ganymede, and Callisto. In contrast, when the thruster is operating, the effect of photoemission is small, regardless of the presence or absence of sunlight.

Figure 4.5a demonstrates that in Europa's orbit, without the thruster, the spacecraft potential becomes highly negative, reaching -31 V instead of the -25 V observed in the absence of sunlight. The shift is attributed to the absence of photoemission, which leads to the dominance of thermal electrons accumulating on the spacecraft's surface. Similarly, in the Ganymede region in Figure 4.5b, the absence of sunlight causes the spacecraft to become significantly negatively charged, changing from 2 V to -20 V. In the case of Callisto in Figure 4.5c, the spacecraft potential, without sunlight, attains a lower positive potential of 5V instead of 11V. Changes in potential without sunlight are due to the variation in the density and temperature of ambient ions, electrons, and secondary electrons. Hence, in the absence of the thruster, the final spacecraft potential, be it positive or negative, is determined by the ambient plasma surrounding the spacecraft.

As depicted in Figure 4.5, the spacecraft potential remains largely unchanged upon thruster activation across the Jovian magnetosphere, regardless of whether photoelectrons are present or not. In fact, a notable decrease in spacecraft potential is observed both with and without the thruster when photoemission is off. For example, in Europa (Figure 4.5a), the potential decreases from -31 V (without thruster) to 10.1 V and 6.5 V with the SPT-100 and RIT-2X thrusters, respectively. Similarly, in the vicinity of Ganymede (Figure 4.5b), the potential drops from -20 V to 6.5 V and 3.5 V with the SPT-100 Hall thruster and the RIT-2X thruster, respectively. Thus, the electric thruster shows a significant reduction in spacecraft potential and mainatins a low negative potential across these areas, regardless of photoemission.

Furthermore, as depicted in Figure 4.5, it is evident that the RIT-2X thruster exhibits a more pronounced stabilizing effect and achieves a much lower negative potential compared to the SPT-100 Hall thruster. This difference may be attributed to the higher thrust and higher densities of CEX-ions and thruster electrons of the RIT-2X thruster. It is essential to highlight that the final spacecraft potential when thruster is on is primarily dependent on the densities of charge-exchange ions (CEX-ions)and thruster electrons. Previous simulations reported in Shinde, Held, and Cairns, 2024 indicate that increased densities of CEX-ions and thruster electrons relative to the ambient plasma result in a reduction in negative charging of the spacecraft and minimal influence of the ambient plasma on the spacecraft potential.

4.4.3 Ram, wake, and side potential profiles

Figure 4.6 demonstrates the intrinsically 2D (rotationally symmetric) nature of the potential structure of the spacecraft which is obtained by cutting Figure 4.1 along the y=1 plane for varying heliocentric distances. The ram direction is in the negative x-axis direction, and the wake direction is along the positive x-axis. The left images depict the potential with and without the thruster for the Europa region, the middle panel is Ganymede, and the right panel is for the Callisto. On the sides (e.g., the +/- z direction), the potential shows a relatively standard sheath.The sunlight directions are in the -x direction.

Figure 4.7 illustrates the changes in potential profiles in the ram (-x axis), wake (x axis), and side (-z axis) at Europa, Ganymede, and Callisto, both in scenarios with and without the thruster.The top panel of Figure 4.7a highlights the Europa region, depicting the ram, wake, and spacecraft sides.In the absence of the thruster, the spacecraft potential in the Europa region shows a significant negative charging of -25 V in the ram wake and side potential. However when the SPT-100 and RIT-2X thruster are on, the potential within the ram, wake, and spacecraft sides becomes significantly more positive. Specifically, the

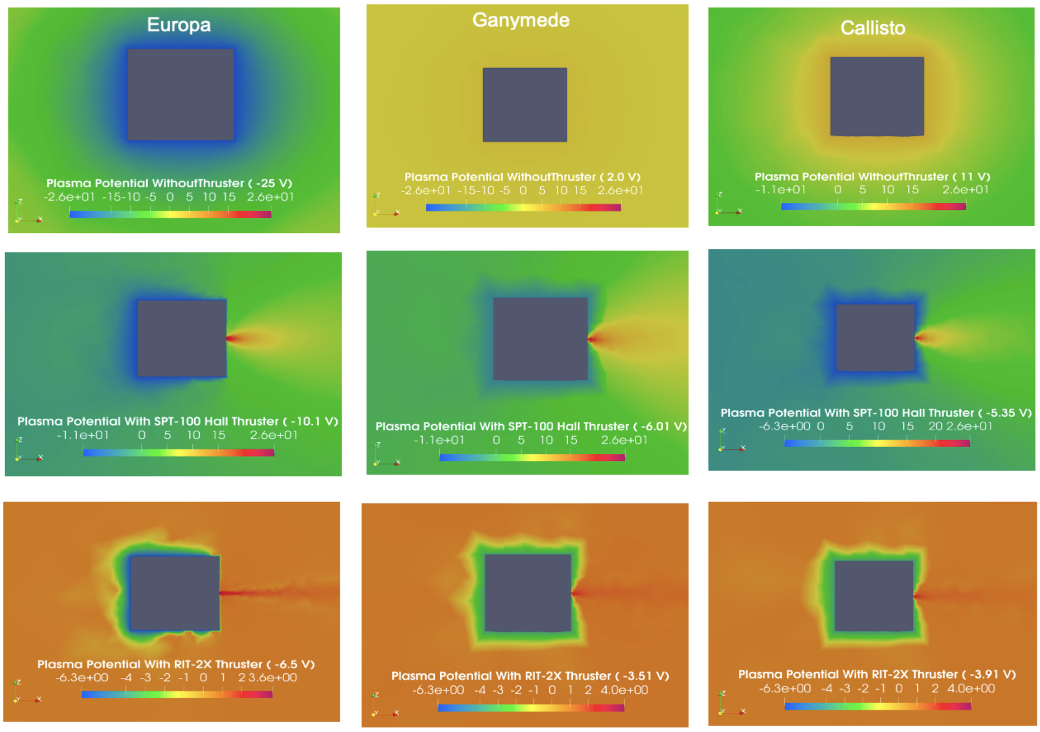

Figure 4.6: Cross comparisons of 2D spacecraft potential maps with and without thrusters at the Europa (left column), Ganymede (middle) and Callisto (right panel), corresponding to Figure 1, cut in y = 1 plane. sunlight directions are on the left

ram and side potential with the SPT-100 thruster charges around -10 to -11 V instead of -25 V (without thruster), while with the RIT-2X thruster, it falls within the range of -6 to -7 V, instead of -25 V without Thruster. The RIT-2X thruster demonstrates a remarkable decrease in negative potential by 19 V, largely attributed to the high density and collected currents of thruster electrons and CEX-ions than the SPT-100 Hall thruster.

Furthermore, Figures 4.7b (middle row) and 4.7c (bottom row) show the behavior of the ram, wake, and side potentials in the Ganymede and Callisto. Without a thruster on, the ram, wake and side potentials of Ganymede and Callisto tend to exhibit a positive potential of 2 and 11 V , respectively. However, when a thruster is on, the ram and side potentials charge negatively, charging to -3 to -4 V (for RIT) and -5 to -6 V (for SPT-100) for both Ganymede and callisto.

For all three orbits, the wake region consistently maintains a stable positive potential of 25 V for the SPT-100 Hall thruster, whereas the RIT-2X thruster keeps it at 3 V. Remarkably, these potential profiles remain relatively consistent irrespective of the spacecraft's radial distance from Jupiter when a thruster is operational, highlighting the dominance of the thruster plume in shaping the charging dynamics. Consequently, the wake region behind

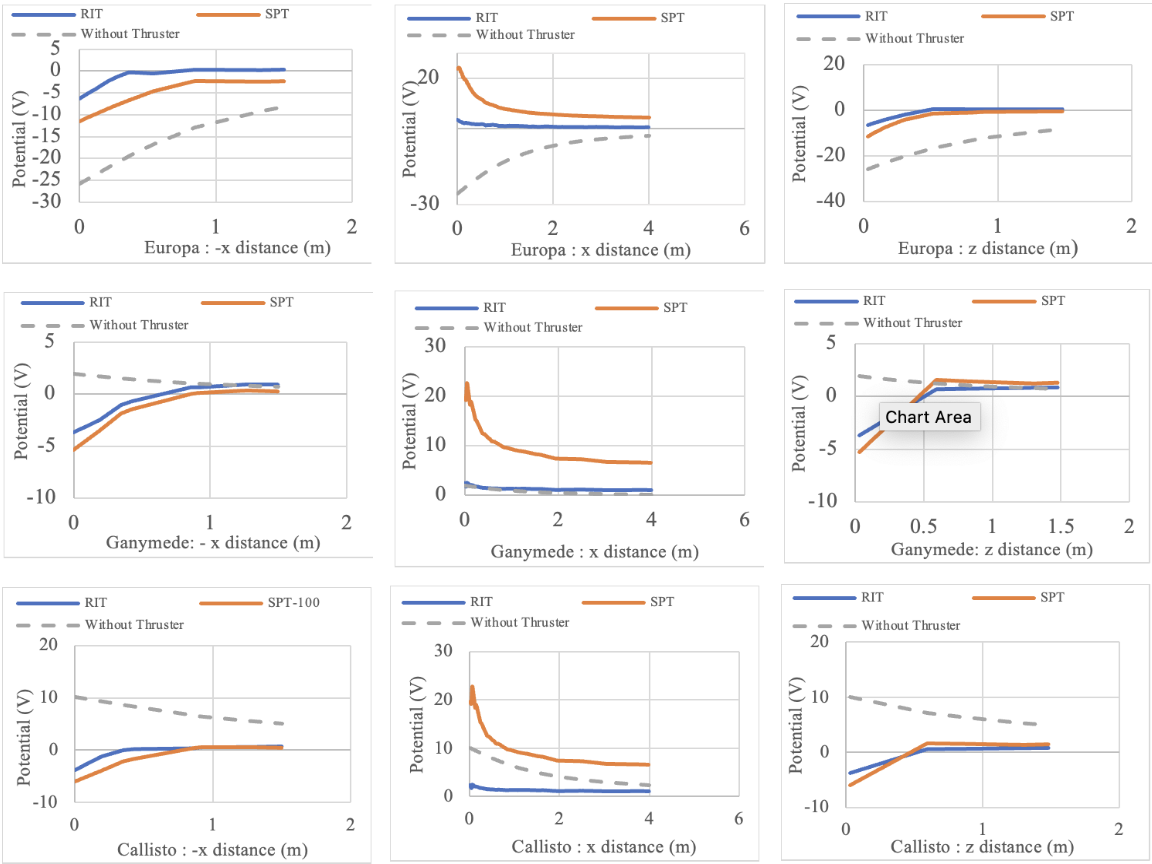

Figure 4.7: From top to bottom rows, the potential profile along the ram direction (-x axis), wake direction (x-axis) and the sheath direction (z-axis) obtained from Figure 6 a.) Europa (top row) b.) Ganymede (middle row) and c.) Callisto (bottom row)

the spacecraft becomes saturated with ions and electrons discharged by the thruster, establishing a plasma sheath that serves as a protective shield against incoming ambient ions and electrons, thereby enhancing spacecraft charge control and ensuring its secure and steady operation in the space environment. Thus, based on simulation results, the use of an electric thruster proved effective in achieving a low and stable negative spacecraft potential regardless of the presence or absence of sunlight in the Jovian magnetospheric plasma.

4.5 Conclusions

The study examined the variations in spacecraft potential within the Jovian magnetospheric plasma at 5.2 AU from the Sun, both with and without the use of an electric thruster.Three regions were considered: Europa, Ganymede, and Callisto, each located at different radial distances from Jupiter. When the thruster was off, the spacecraft's potential near Europa became highly negative, reaching approximately -25 volts. This negative potential was primarily due to the dominance of thermal electrons.As the spacecraft moved farther from Europa, the potential shifted from negative to positive values: +2 volts near Ganymede and +11 volts near Callisto. These changes were attributed to the dominance of secondary electron current at Ganymede and photoelectron current at Callisto.

When the thruster was activated, the spacecraft's negative potential near Europa significantly decreased.With the SPT-100 Hall thruster, the potential dropped from -25 V to 10 V, and with the RIT-2X thruster, it decreased from -25 V to -6.5 V, reducing the potential by 19 volts and 15 volts, respectively.This change was mainly due to the effects of thruster-emitted electrons and charge-exchange (CEX) ions.The difference in spacecraft potential between the two thrusters is attributed to the varying densities of CEX ions and thruster-emitted electrons, with the RIT-2X thruster having a much higher density relative to the ambient plasma compared to the SPT-100 Hall thruster.Near Ganymede and Callisto, the RIT-2X thruster maintained a negative potential between -3 and -4 volts, whereas the SPT-100 resulted in a slightly lower potential of -5 to -6 volts.Importantly, the spacecraft's potential remained stable, regardless of sunlight, when the thrusters were operating.Importantly, when the thrusters were operating, the spacecraft's potential remained unchanged regardless of sunlight.In contrast, without the thrusters, the spacecraft's potential became significantly more negative in the absence of sunlight.

The main findings of the study are : the high dominance of CEX ions and thruster electrons over the ambient plasma plays a crucial role in maintaining a consistently low negative potential within Jupiter's magnetosphere, irrespective of sunlight conditions.The RIT-2X thruster exhibited a stronger stabilizing effect compared to the SPT-100 Hall thruster, achieving a lower negative potential due to its higher density of CEX ions and thruster electrons, which contributed to reducing the spacecraft's negative charging.Additionally, the spacecraft's wake generated a stable positive potential, filled with ions and electrons expelled by the thruster, forming a plasma sheath that protected the spacecraft from incoming ambient ions and electrons, thereby maintaining a low negative potential.

In summary, the SPIS simulation results highlight the advantages of electric thrusters in stabilizing spacecraft potential within the Jovian magnetospheric plasma at 5.2 AU.These findings could be instrumental in spacecraft design, particularly in accounting for charging dynamics across different plasma environments and ensuring spacecraft safety for future missions.

CHAPTER 5

The Effects of SPT-100 and RIT-2X Thruster Plumes on Solar Panels at 0.044 AU and 1 AU

To be Submitted: Tejaswi L. Shinde, Iver H Cairns, Jason M. Held

5.1 Abstract

The study investigates how thruster electrons and charge-exchange (CEX) ions from the SPT-100 Hall thruster and the RIT-2X thruster influence the charging and potential of deployed, non-body-mounted solar panels and the spacecraft at distances of 1 AU and 0.044 AU. Simulations using SPIS software are conducted both with and without thrusters at these distances. Two configurations are examined: one where the front of the solar panel (made of non-conductive material) faces away from the thruster towards the Sun, and another where it faces both the thruster and the Sun. The main result aligns with previous findings that the operation of the SPT-100 and RIT-2X thrusters achieves a low negative spacecraft potential regardless of sunlight at 1 AU and 0.044 AU. However, there is a notable discrepancy in the solar panel potential between its front and back sides. The difference is mainly due to the non-conductive material on the front surface, which reduces negative charging compared to the conductive material, regardless of the thruster. Additionally, using a resistor between the spacecraft and the solar panel limits current flow, preventing excess charge accumulation on the spacecraft surface. Furthermore, the study compares the impact of thruster plumes when the front side of the solar panel faces the thruster versus when it is oriented away. The results show a more negative potential when the front side of the solar panel faces the thruster because of the high accumulation of thruster electrons. Although no major difference in spacecraft potential is found, there is a significant reduction in the collection of photoelectrons and secondaries compared to the case when the panel's front faces the Sun but is oriented away from the thruster.

Overall, the simulation results confirm that electric thrusters not only mitigate spacecraft surface charging but also reduce the solar panel potential to low positive (with the RIT-2X thruster) and low negative (with the SPT-100) levels, regardless of sunlight. A new insight from this study indicates that using dielectric material on the solar panels, along with the influence of CEX ions and thruster electrons, leads to a substantial decrease in the potential of the solar panel compared to the spacecraft surface or the back side of the panel in both thruster and non-thruster scenarios.

5.2 Introduction

The influence of a thruster's plume on spacecraft systems has become a significant concern due to CEX-ions and thruster electron backflow (Lai, 1989; Shan et al., 2015; Tajmar, Foing, et al., 2004). The backflow particles, returning to the surface of the spacecraft, can interact with its systems and solar arrays, potentially altering electrical properties and increasing the risk of parasitic current flow. Such currents can reduce solar panel efficiency and induce localized heating, leading to thermal stress and potential damage to solar cells. In addition, they may accelerate the degradation of the solar cell material and contribute to corrosion or contamination problems (Young et al., 2017; Sarrailh, Sebastien Hess, et al., 2022). Hence, it is important to study thruster-plume interactions with solar panels. The present study will focus solely on surface charging effects, excluding erosion, sputtering, and contamination issues.

In the previous investigations, simulations for the SPT-100 Hall thruster and the RIT-2X thruster revealed that the thruster backflow plume plays a dominant role in influencing both the spacecraft and the surrounding plasma under various plasma conditions (Shinde, Held, and Cairns, 2024; Shinde, Held, Cairns, and Deprez, 2024). The influence results in the spacecraft achieving a low negative potential and maintaining this stability across heliocentric distances from 0.044 - 1 AU. Importantly, regarding surface charging, the backflow plume does not negatively impact it; instead, it reduces the excess negative charge, particularly near the Sun and in scenarios without sunlight. For example, without the thruster, close to the Sun at 0.044 AU, the spacecraft attains a large negative potential of -28 V, but upon thruster operation the potential is kept to a small negative value in range of -3 to -4 V, as seen in Shinde, Held, and Cairns (2024); Shinde, Held, Cairns, and Deprez (2024). Consequently, the electric thruster exhibits the ability to regulate and maintain the spacecraft potential at a consistently low negative value, regardless of the presence or absence of sunlight, provided the plume plasma dominates the ambient plasma. It is essential to note that all simulations were conducted without the inclusion of solar panels.

As a result, the present study now shifts its focus to simulating the spacecraft integrated with both a thruster and solar panels, particularly in the near-Earth environment at 1 AU and the vicinity of the Sun at 0.044 AU. The main objective is to understand the complex interaction between solar arrays, the spacecraft, and charged particles from thruster plumes and the ambient environment (comprising thermal electrons, ions, photoelectrons, and secondary electrons). To achieve this, the Spacecraft Plasma Interaction Software (SPIS) will be used to predict spacecraft charging at the above two distinct locations. To further examine the influence of solar panel backflow plumes, we will assess two distinct scenarios: a) the front side of the solar panels directed towards the Sun and positioned away from the thruster, and b) the front side of the solar panels directed towards both the Sun and the thruster (as shown in Section 5.4.2). Note that the side of the panel facing the Sun will be referred to as the front side, and the side not facing the Sun will be referred to as the backside.

Section 5.3 will provide a comprehensive overview of the simulation setup and the environmental parameters considered. In Section 5.4, we analyze the variations in spacecraft potential under both sunlight and no sunlight conditions, with the front side of the solar panels positioned away from the thruster (in Section 5.4.1), considering distances of 1 AU and 0.044 AU. Section 5.4.2 presents findings for scenarios where the front side of the solar panels faces the thruster, considering distances of 1 AU and 0.044 AU.

5.3 SPIS Simulation Setup

The satellite model, depicted in Figure 5.1 and detailed in Table 5.1, is constructed using the GMSH software (*GMSH* n.d.). The satellite is a cube with dimensions of 1 meter in length, 1 meter in width, and 1 meter in height. It includes two deployed external solar panels, each measuring 3 meters in length, 1 meter in width, and 0.05 meters in height. The body of the spacecraft is coated with a conductive material made of Indium Tin Oxide while the back side of the solar panel is covered with conductive Carbon Fiber material. The front side of the solar panel facing the Sun is coated with solar cell material (Cerium + doped MgF_2), which is non-conductive. Plasma parameters for environments at 1 AU and 0.044 AU are derived from Guillemant (2014), as used in Chapters 2 and 3. Adhering to the SPIS user manual guidelines *Spis User Manual* (n.d.), the domain is defined based on the Debye length of ambient electrons (Section 1.5.2.1 of the thesis). The domain dimensions are typically set as one-third of the Debye length of ambient electrons, with a mesh resolution three times the Debye length. During these simulations, the spacecraft and electric thruster are decoupled using a resistor of 500,000 ohms, and similarly, the solar panels and spacecraft are decoupled using another resistor of 5000

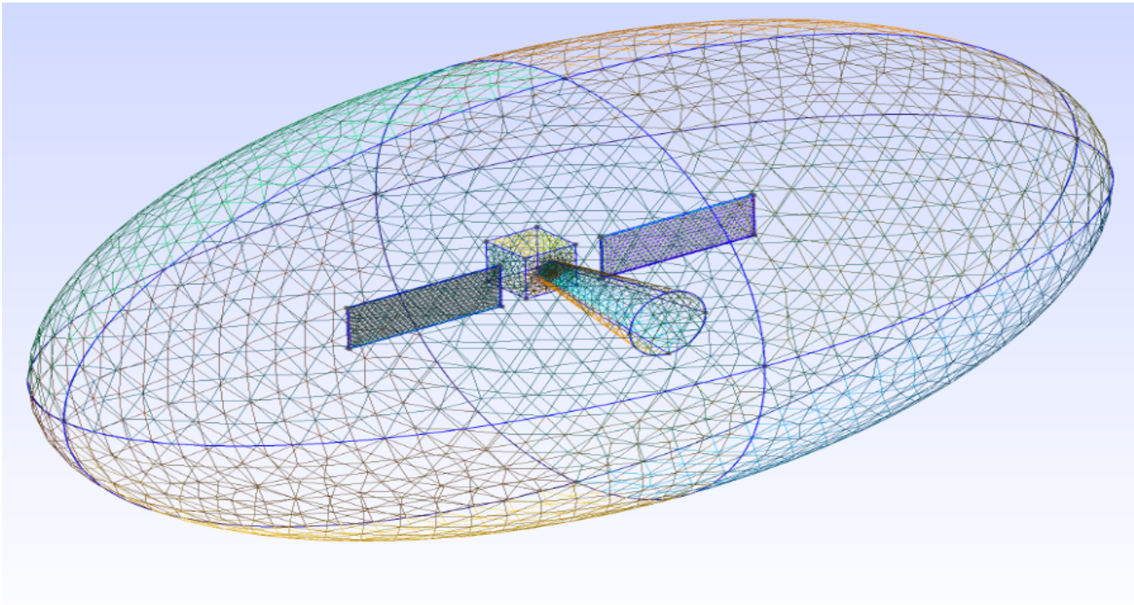

Figure 5.1: Integration of GMSH spacecraft model with the solar panels and the mesh grid. The void indicates the domain/simulation boundary and the conical shape symbolizes the ion plume.

ohms. This means that the solar panels, thruster, and spacecraft can all be at different potentials and not interact with each other. The resistor helps limit the flow of current and prevents excessive currents from damaging the spacecraft components. However, the net current around each loop of the electrical circuit considered is zero according to Kirchoff's current law.

Please note that the variance in spacecraft potential, with and without the SPT-100 and RIT-2X thruster, as depicted in this chapter in contrast to Chapters 2 and 3, arises from the utilization of distinct geometrical configurations. The geometry used in this study differs from that of Chapters 2 and 3. The primary factor contributing to the potential variance of the spacecraft is the modification of the total surface area and the exposure to sunlight, resulting in variations in the collection and emission of surface current. In addition, Appendix C includes a concise examination of how different spacecraft sizes and geometries influence spacecraft potential.

Table 5.1: Geometry Dimensions and Thrusters Specifications used in SPIS

Parameters	**Values**	
Geometry	Satellite Size : 1m x 1m x 1m Solar Panel Size : 3m x 1m x 0.5m	
Material	Satellite Material: Indium Tin Oxide Solar Panel's Front side : Cerium +Doped MgF2 Solar Panel's Back side : Carbon Fiber	
Photoelectron Temperature	3eV	
Ambient Ion Type	H+	
Ion and Electron Modelling	Particle In Cell (PIC)	
Magnetic field	Not considered	
Thruster Specification	**Values**	
Electric Thruster	SPT-100 Hall Thruster	RIT-2X Thruster
Thrust	35mN	180mN
Specific Impulse	1840	2966
Cathode Temperature	5	3
Mass Flow rate (Xe)	1.91×10^{-6} (kg/s)	6.19×10^{-6} (kg/s)
Current	1.43	3.99
Power	723	6025

5.4 SPIS Simulation Results

5.4.1 Case A: Solar Panel opposite the Thruster

5.4.1.1 With and without sunlight at 1 AU

Figure 5.2 illustrates the variation in the spacecraft potential at 1 AU by contrasting scenarios with and without the thruster, where the front side of the solar panel is oriented towards the Sun and away from the thruster. In Figure 5.2, the left side of the graph shows the spacecraft potential and the back side of the solar panel in the presence and absence of sunlight. It is important to note that the back side of the solar panel (not facing the Sun) shares the same potential as the spacecraft surface, since both surfaces are conducting - hence it is indicated by the red border. In contrast, the right-hand side of the plot shows the front-side surface potential of the solar panels both in the presence and absence of sunlight with and without the thruster. Figure 5.3 displays the 2D potential maps of the spacecraft, solar panels, and plasma at 1 AU with sunlight and with and without the SPT-100 Hall and RIT-2X thrusters, achieved by slicing Figure 5.1 in an x plane. In this configuration, the sunlight and solar wind originate in the left direction.

At 1 AU, the spacecraft charging effects are less critical than in near-Sun conditions,

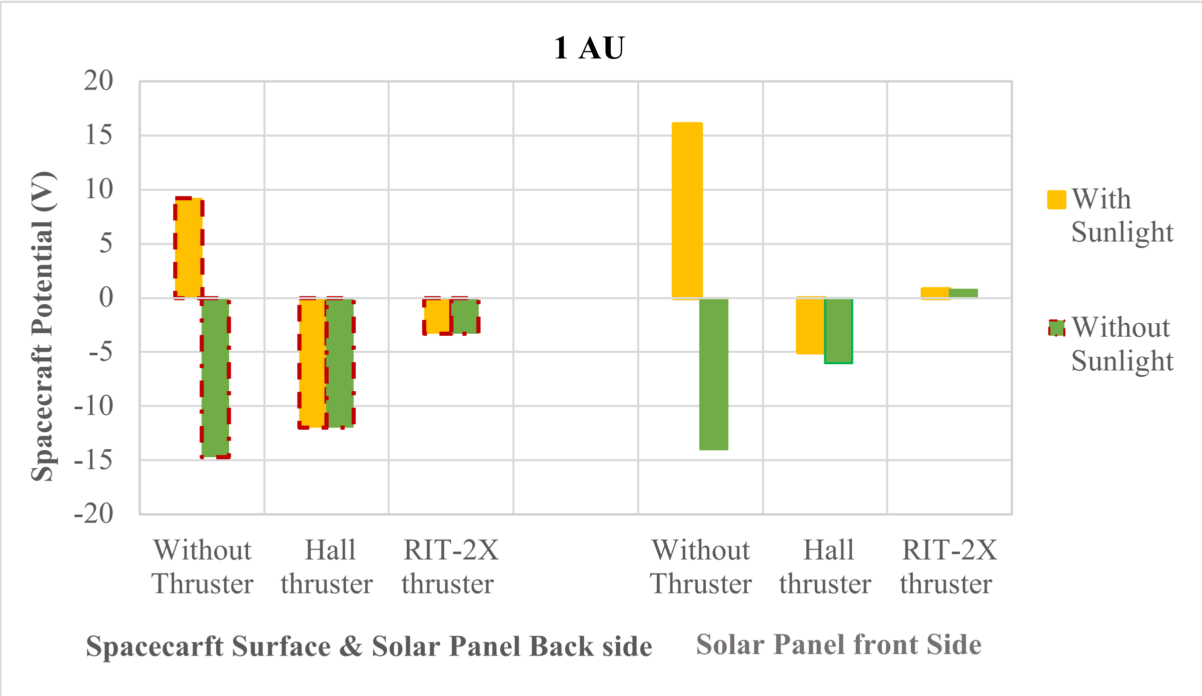

Figure 5.2: Influence of sunlight on Spacecraft and Solar Panel Surface Potential with and Without Thruster at 1 AU. Spacecraft Surface on the Left, Solar Panel Back Surface (Marked in Red Border) and Solar Panel Front Surface on the Right

mainly because of the low density and temperature of ambient electrons, with photoelectrons dominating. Due to high photoemission, the spacecraft becomes positively charged at 14.2 V and the front side of the solar panels at 16 V without the thruster. Without sunlight and a thruster, the spacecraft and backside of the solar panel charge negatively to approximately -14.7 V and the front side of the solar panel front side to -14 V, due to the high accumulation of ambient electrons. These results show the importance of photoemission at 1 AU in the presence and absence of sunlight when the thruster is not active.

In contrast, when thrusters are used, the potential of the spacecraft surface remains almost constant at -12 V for SPT and -3.34 V for RIT, regardless of whether there is sunlight or not. The main reason is due to the high density of CEX-ions and thruster electrons that dominate the spacecraft and surrounding plasma, making the effect of photoelectrons negligible, as demonstrated in Chapter 2 and Chapter 3. Similarly, the front side of the solar panel in sunlight equipped with SPT-100 Hall thruster charges at -5.02 V, showing a slight increase to -6.0 V in the absence of sunlight. With the RIT-2X thruster, the front side of the solar panel charges at 0.8 V in sunlight and at 0.76 V without sunlight. Therefore, the findings indicate that the use of the SPT-100 and RIT-2X thrusters helps to regulate and stabilize the potential of both the spacecraft surface and solar panels regardless of the presence or absence of sunlight. Similar behavior is observed in the earlier research

Shinde, Held, and Cairns (2024); Shinde, Held, Cairns, and Deprez (2024) and Chapter 2, 3, and 4, the thruster operations demonstrate a uniform pattern of behavior, unaffected by modifications in geometry or the incorporation of additional solar panels.

Note that the difference in spacecraft and solar panel potential between tw0 different thruster (SPT-100 and RIT-2X thrusters) is due to the varying number densities of CEX ions and thruster electrons. The RIT-2X thruster, with its high thrust of 180 mN, generates CEX ions and thruster electrons at a density of approximately $10^{16}\,\mathrm{m}^{-3}$, which is significantly higher than the ambient plasma density. This higher density helps stabilize the spacecraft more effectively compared to the SPT-100 Hall thruster, as discussed in Chapter 3. (Shinde, Held, and Cairns, 2024).

Figure 5.3 highlights the inherently 2D (rotationally symmetric) nature of the spacecraft potential structure, derived by slicing Figure 5.1 along the x=1 plane at 1 AU. The ram direction points along the positive z-axis, while the wake direction follows the negative z-axis. In the ram region, without the thruster (left corner), the spacecraft and the front side of the solar panel are enveloped in a strong sheath of positive ions because of the dominance of photoemission. The ram potential without the thruster reaches 8.48 V uniformly around the spacecraft, with the front side of the solar panel charging to 16 V. With the thruster on, CEX ions and thruster electrons overshadow the photoelectron effect, dominating the spacecraft and surrounding plasma. For the Hall thruster and RIT-2X thruster, the minimum ram potential of the spacecraft is -12.1 V and -3.34 V, respectively, while the front side of the solar panel reaches -5.01 V and 0.8 V, respectively.In the wake region at 1 AU, without the thruster, both the spacecraft surface and the rear side of the solar panel are at a similar potential of about 8.48 V, as both surfaces are conductive. In the wake region, the SPT-100 and RIT-2X thrusters create a stable positive potential of 20 V and 4 V, respectively, due to electric thruster plume emitting ions and electrons. The plume generates a plasma sheath in the wake region, mitigating the direct impact of ambient electrons on the spacecraft's surface

Figures 5.4 illustrates the currents collected and emitted from the surface of the spacecraft and the back sides of the solar panel, while Figure 5.5 depicts the collected and emitted currents on the front side of the solar panel. The backside of the solar panel, being similar to the spacecraft surface, is not represented distinctly in the plots.

As evident in Figure 5.5, at 1 AU, the spacecraft's positive potential of 8.48 V results from a high photoelectron emission current of approximately 0.01 mA, leading to a positive charge. Similary, the front side of the solar panel charges to a significantly higher positive potential of +16 V, driven by a photoemission emission current of 0.12 mA, which surpasses that of the spacecraft surface. The collected current of photoelectrons on the solar

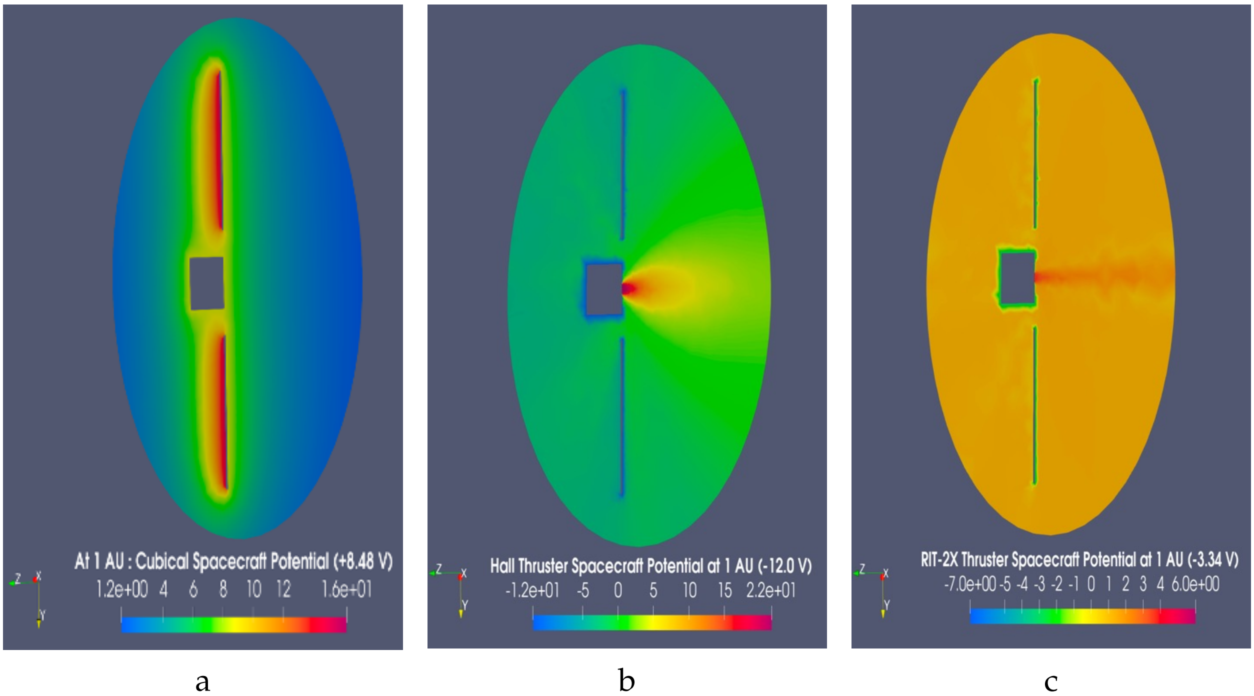

Figure 5.3: Cross comparisons of 2D potential maps with and without the SPT-100 Hall thruster and RIT-2X thruster at 1 AU, corresponding to Figure 1 and the 3D potential cut in the x = 1 plane. sunlight and solar wind come from the left (the -x direction) for each panel.

panel, approximately 0.11 mA, notably exceeds that of the spacecraft surface, which is approximately 0.027 mA. Therefore, the solar panel exhibits higher collection and emission of photoelectrons currents than those of the spacecraft surface.

Conversely, employing the SPT-100 Hall thruster results in the spacecraft surface and the rear side of the solar panel charging to a notably large negative potential of -12 V. The outcome arises from the high dominance of thruster electrons and CEX-ions, approximately 2 mA and 1.76 mA, respectively. The thruster electrons are attracted to the spacecraft surface due to its lower potential relative to the surrounding plasma, leading to significant negative charging. Meanwhile, the solar panel's front side encounters a minimal ram potential of -5.02 V. The less negative charge of the solar panel's front side can be attributed to several factors. Firstly, the material's non-conductive nature allows charge to accumulate locally because non-conductive surfaces do not allow charges to redistribute efficiently across their surface. This leads to a slower rate of charge dissipation compared to conductive materials, where charges can move freely and neutralize more quickly. As a result, non-conductive materials are more prone to localized charge buildup, which can mitigate total charge accumulation but may still lead to surface charging effects. Secondly, direct exposure to sunlight results in a high photoelectron emission current, approximately 0.1 mA, unlike the spacecraft surface, which is about 0.032 mA. Finally, the

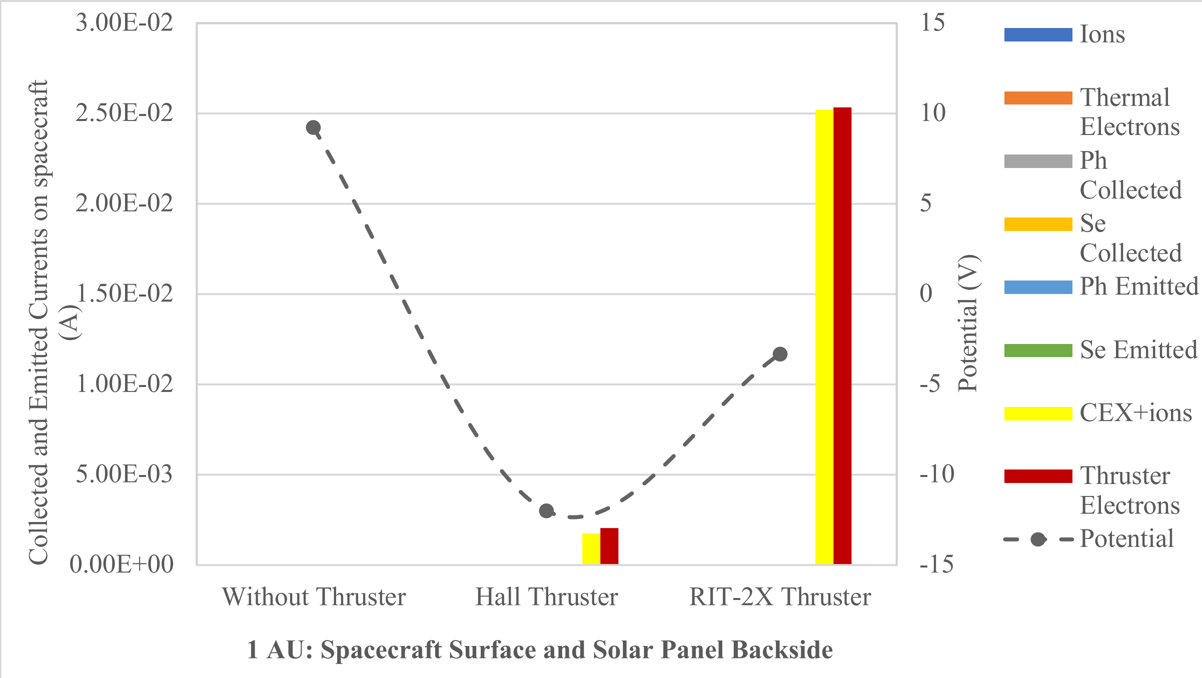

Figure 5.4: Collected and emitted currents at 1AU on the spacecraft surface and rear side of the solar panel (on the primary axis) and spacecraft potential (on the right-hand axis) versus heliocentric distance

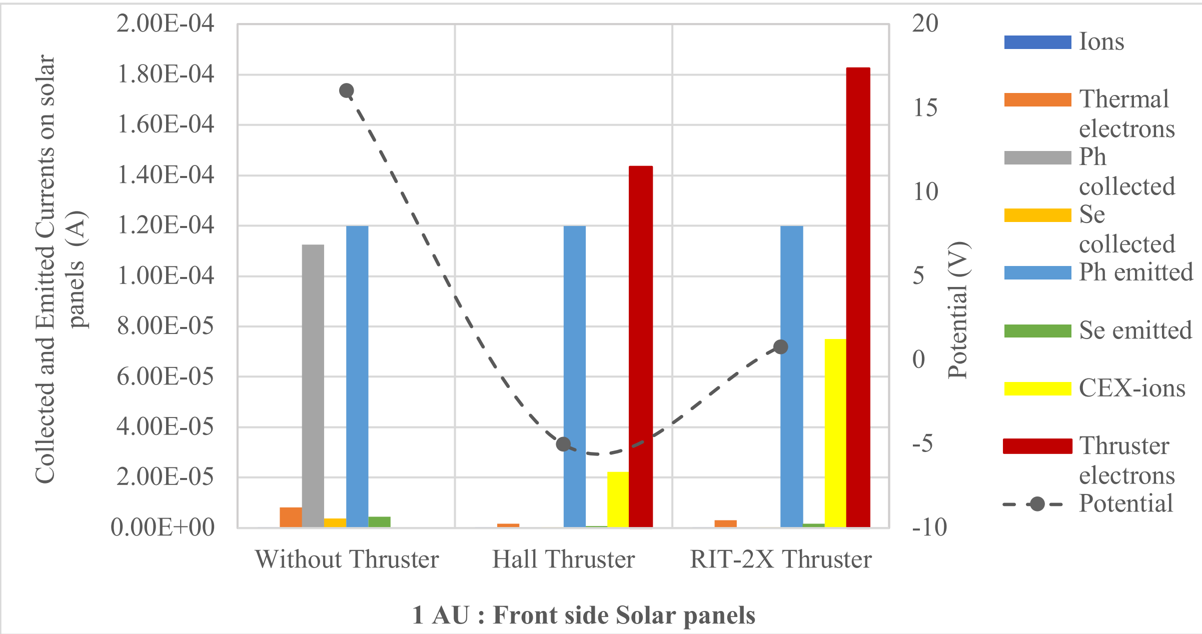

Figure 5.5: Collected and emitted currents on the front side of the solar panel (on the primary axis) and spacecraft potential (on the right-hand axis) versus heliocentric distance

accumulation of CEX-ions and thruster electrons on the front side of the surface is considerably lower than on the spacecraft surface, with about 0.02 mA of CEX-ions compared to 1.76 mA on the spacecraft surface or the rear side of the solar panel and 0.14 mA of thruster electrons compared to 2 mA on the spacecraft surface or the rear side of the solar panel.

However, with the RIT-2X thruster, there is a noticeable difference in spacecraft potential and solar panel potential charges compared to the SPT-100 Hall thruster. This is mainly attributed to the significantly higher density of CEX-ions and thruster electrons in relation to the ambient plasma density (Shinde, Held, and Cairns, 2024). At 1 AU, the front side of the solar panel charges at +0.8 V, while the back side and the spacecraft surface are approximately -4 V negatively charged. The disparity in potential between the front and back sides of the solar panels can be due to the choice of materials, resistors used between spacecraft and the front side of the solar panel and the area exposed to the sunlight. The front solar panel employs non-conductive material, whereas the backside utilizes a conductive material. Non-conductive materials are less prone to charge accumulation compared to conductive materials, as they can more effectively dissipate accumulated charge. As illustrated in Figure 5.5, the accumulation of thruster electrons (0.18 mA) and CEX-ion currents (0.075 mA) on the front side of the solar panel is significantly lower than that observed on the spacecraft surface or the back side of the solar panel, which amounts to approximately (25 mA).

5.4.1.2 With and without sunlight at 0.044 AU

At a distance of 0.044 AU, spacecraft charging becomes critical as a result of the increased density and temperature of thermal electrons. The dominance of thermal electrons establishes a strong potential barrier around the spacecraft, restricting the escape of photoelectrons and secondary electrons, as evidenced in prior research Shinde, Held, and Cairns (2024); Shinde, Held, Cairns, and Deprez (2024). Owing to the significant potential difference between the spacecraft and the surrounding plasma, low-energy photoelectrons and secondaries fail to overcome the barrier, resulting in a high accumulation of secondaries and photoelectrons on the spacecraft's surface. A similar phenomenon is observed when the spacecraft is integrated with the solar panels.

As depicted in Figures 5.6 and 5.7, the spacecraft surface attains a charge of -15.53 V, while the front side of the solar panel charges to a positive potential of approximately +4 V, and the back side maintains -15.53 V same as the spacecraft surface. Conversely, upon activation of the RIT-2X thruster, the spacecraft's potential significantly diminishes from

-15.53 V to -2.61 V (becoming more positive), while the front side of the solar panel decreases from +4 to +1.98 V (becoming less positive due to thruster electron accumulation). The dominance of CEX-ions and thruster electrons mitigates the direct impact of ambient electrons by mitigating negative charge. Consequently, the potential barrier diminishes substantially, facilitating the escape of photoelectrons and secondaries, thereby aiding in the dissipation of negative charge, as illustrated in previous studies Shinde, Held, and Cairns (2024); Shinde, Held, Cairns, and Deprez (2024). The reduction in the recollection rate of low-energy electrons could potentially enhance the accuracy of low plasma measurements.

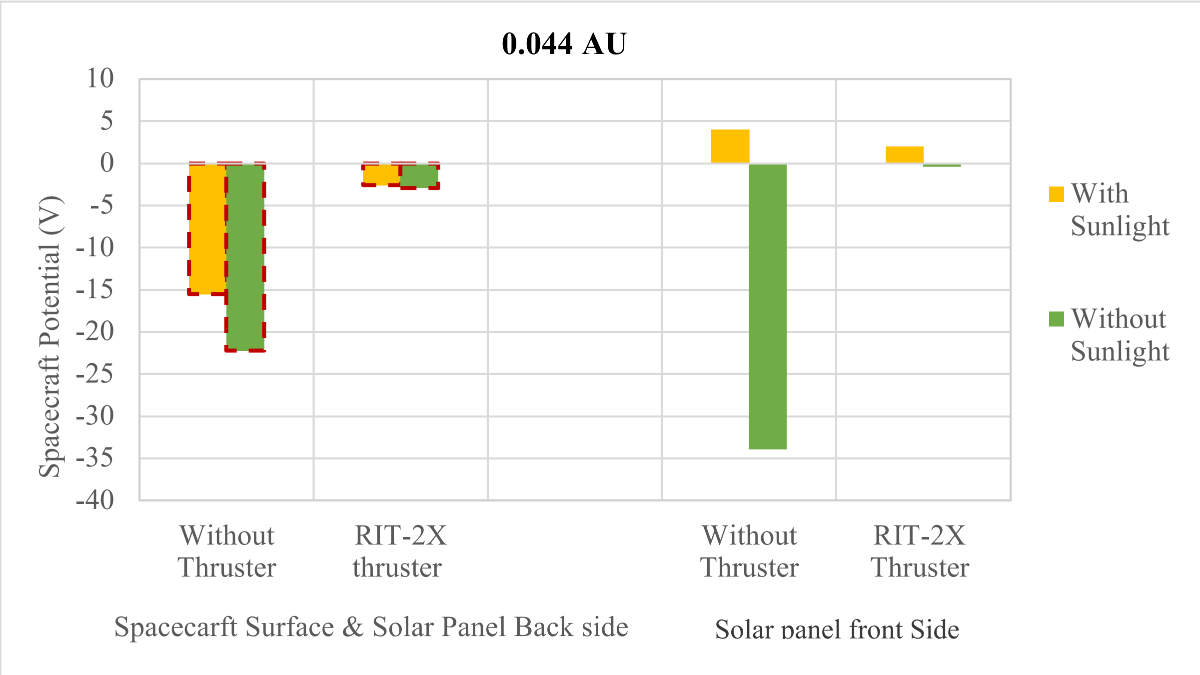

Figure 5.6: Influence of sunlight on Spacecraft and Solar Panel Surface Potential with and Without Thruster at 0.044 AU. Spacecraft Surface on the Left, Solar Panel Back Surface (Marked in Red Border) and Solar Panel Front Surface on the Right

In the absence of sunlight, the spacecraft without the thruster experiences a significant increase in negative potential, shifting from -15.53 V (in sunlight) to -22.2 V (without sunlight), attributed to lack of photoemission. Near the Sun, the recollection of photoelectrons becomes essential to maintain a low negative potential. Similarly, the front side of the solar panel undergoes a substantial increase in negative potential, transitioning from +4 (in sunlight) to -33.3 V (without sunlight-without thruster), mainly due to the accumulation of high-density ambient electrons. In contrast, when the RIT-2X thruster is operational, a notable reduction in spacecraft and solar panel potential is observed compared to the scenario without the thruster, regardless of sunlight presence or absence.

Without sunlight, the spacecraft surface potential charges to -2.9 V (without sunlight) instead of -2.6 V in sunlight, while the solar panel charges to -0.43 V (without sunlight) instead of 1.98 V in sunlight. As indicated in the previous research in Chapters 2 and 3 (Shinde, Held, and Cairns, 2024; Shinde, Held, Cairns, and Deprez, 2024), a higher density of backflow plumes relative to the ambient plasma density leads to a diminished impact of photoelectrons and secondaries on spacecraft potential.

Figure 5.7 illustrates the inherently two-dimensional (rotationally symmetric) characteristics of the spacecraft's potential structure. Figure 5.7 is derived by cutting Figure 5.1 along the x=1 plane at a distance of 0.044 AU. In the absence of the thruster (left corner), the spacecraft's surface in the ram direction becomes negatively charged, approximately -26 V. That charge is attributed to the high thermal electron density and temperature prevailing in the surrounding plasma, despite the presence of significant photoemission near the Sun. A localized minimum potential develops, acting as a barrier that traps photoelectrons and secondary electrons. Conversely, the solar panels exhibit a positive potential of 4 V due to the solar panel's non-conductive coating, which facilitates high photoemission and mitigates the impact of thermal electrons. With the RIT-2X thruster engaged (depicted on the right side of Figure 5.7), the strong electrostatic sheath is notably diminished. The reduction is primarily due to the increased dominance of CEX-ions and thruster electrons, reducing the effect of ambient plasma. As evident from Figure 5.7, the minimum ram potential at the spacecraft's frontal surface reaches -2.61 V, while the front side of the solar panel achieves a potential of +1.98 V.

In the wake region, without the thruster, both the rear side of the spacecraft and the solar panel acquire a negative charge of approximately -18 V, primarily influenced by the high density of thermal electrons. Conversely, with the RIT-2X thruster operational, in the wake region, the spacecraft rear side surface maintains a stable positive potential of +3.5 V instead of (-18 V without the thruster) while the rear side of the solar panel achieves a potential about +1.98 V (instead -18 V without the thruster). When the thruster is activated, ions and electrons emitted from it fill the wake region behind the spacecraft, creating a plasma sheath. That sheath acts as a barrier, preventing ambient electrons from directly impacting the spacecraft's surface. The presence of positive ions in the wake, facilitated by the electric thruster, significantly reduces spacecraft charging and helps manage potential barriers. These dynamics contribute to the safe and stable operation of the spacecraft in the space environment (Shinde, Held, and Cairns, 2024; Shinde, Held, Cairns, and Deprez, 2024).

Figures 5.8 and 5.9 show the measured currents collected and emitted on the surfaces of the spacecraft and the front of the solar panel, respectively. As depicted in Figure 5.8,

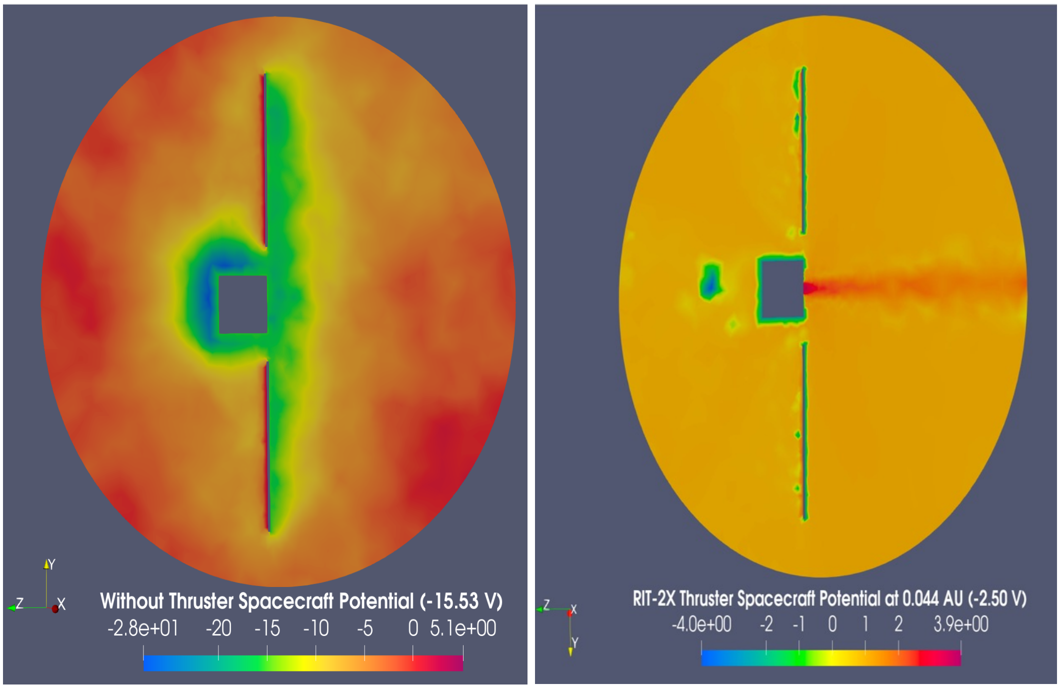

Figure 5.7: 2D potential maps with and without the RIT-2X thruster at 0.044 AU, corresponding to Figure 1 and the 3D potential cut in the x = 1 plane. sunlight and the solar wind come from the left (the -x direction)

the thermal electron collection current on both the spacecraft surface and the rear side of the solar panel is roughly 18 mA, significantly exceeding the 9.8 mA collected on the solar panel's front side, as shown in Figure 5.9. In addition, the currents of secondary and photoelectrons collected on the surface of the spacecraft are recorded at 23.7 and 13.5 mA, respectively, as shown in Figure 5.8. The high recollection of photoelectrons and secondary electrons is due to the strong electrostatic sheath surrounding both the spacecraft and the rear side of the solar panel (as shown in Figure 5.7), which restricts the escape of photoelectrons and secondary electrons to overcome the potential barrier, thus resulting in elevated recollection rates. This high rate of recollection could interfere with delicate on-board equipment, possibly leading to anomalies in spacecraft operation. In contrast, activating the thruster leads to a marked decrease in the electrostatic sheath, as indicated in Figure 5.7. This decrease substantially lowers the recollection rates of secondary electrons and photoelectrons on both the spacecraft surface and the rear side of the solar panel to 0.098 mA and 1.79 mA, respectively, as detailed in Figure 5.8.

With respect to the collected and emitted current of the front side of the solar panel, there are notable differences compared to the backside. In the absence of the thruster, the front surface of the solar panel charges positively by approximately 4 V, primarily attributed to its high photoelectron emission of 62 mA and low collection of thermal electrons at

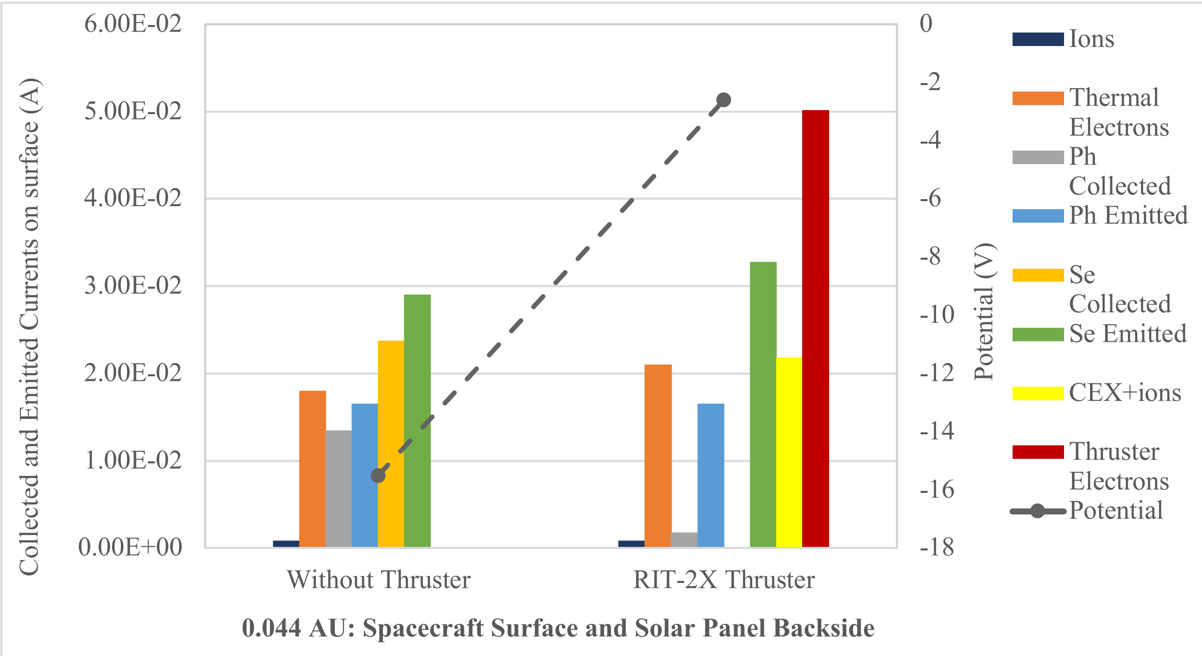

Figure 5.8: Collected and emitted currents at 0.044 AU on the spacecraft surface and rear side of the solar panel (on the primary axis) and spacecraft potential (on the right-hand axis) versus heliocentric distance

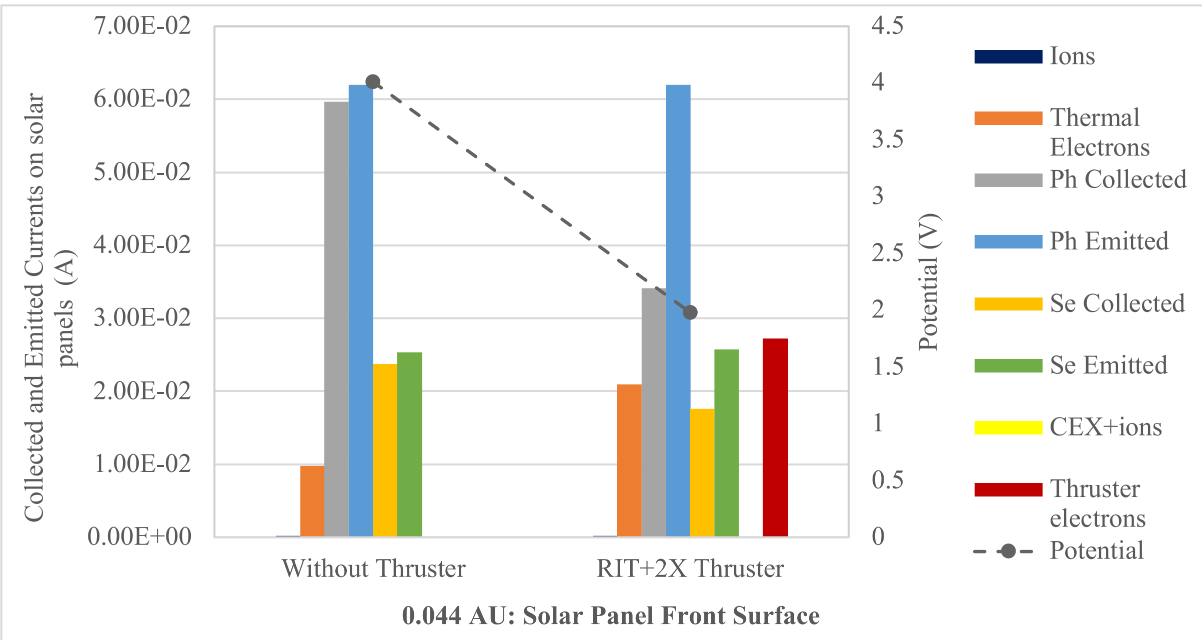

Figure 5.9: Collected and emitted currents on the front side of the solar panel (on the primary axis) and spacecraft potential (on the right-hand axis) versus heliocentric distance.

9.8 mA. This contrasts with the backside of the solar panel, which exhibits 16 mA of photoelectron emission and a large thermal electron collected current of 18 mA, leading to a negative charging of -15.3 V. The surface, coated with non-conductive Cerium-doped +MgF2 solar cell material, easily dissipates the accumulated charge, resulting in a more positive charge compared to the backside. However, after operation of the RIT-2X thruster, as illustrated in Figure 5.9, the front side of the solar panel exhibits a significant decrease in the collected current of thruster electrons, in contrast to the back side of the solar panel, reducing from 52 mA to 27 mA. Thus, the front side of the solar panel charges more positively +2 V than the back side of the solar panel charges about -2.61 V.

The findings align with previous research on simple cylinders simulated at heliocentric distances between 0.044 AU and 1 AU, and with observations from Jovian magnetospheric plasma studies discussed in Chapter 4 (Shinde, Held, and Cairns, 2024; Shinde, Held, Cairns, and Deprez, 2024). The use of electric thrusters in spacecraft, regardless of the presence of solar panels, has been shown to effectively lower the potential barrier. This leads to a reduced collection of low-energy electrons, which allows the spacecraft to maintain a less negative charge. However, it is important for the reader to recognize that this study exclusively concentrates on surface charging and does not delve into potential impacts such as internal charging, erosion, or contamination of solar or spacecraft surfaces resulting from backflow plumes. These plumes may result in contamination or erosion or trap currents and cause internal charging, potentially affecting the performance of solar panels. Such effects will be evaluated in future work.

5.4.2 Case B: Thruster-facing Solar Panel Configuration

To gain insight into the behavior of the solar panel's front surface when directly exposed to both the backflow plume and the Sun simultaneously, the positions of the thrusters were swapped. Similarly to the previous simulation, the front surface of the solar panel is non-conductive, while the backside and spacecraft surface are conductive. The Sun's direction is from the right side (+x direction). The simulation is conducted solely in the presence of sunlight at both 1 AU and 0.044 AU. The SPT-100 Hall thruster is simulated for the 1 AU scenario, whereas the RIT-2X is simulated for both the 1 AU and 0.044 AU locations.

5.4.2.1 In the Presence of sunlight at 1 AU:

As depicted in Figure 5.10, as expected, the spacecraft surface and backside of the solar panel potential remain unchanged even when the thrusters are facing the front side of the solar panel. With the SPT-100 Hall thruster, the spacecraft and backside side of the solar

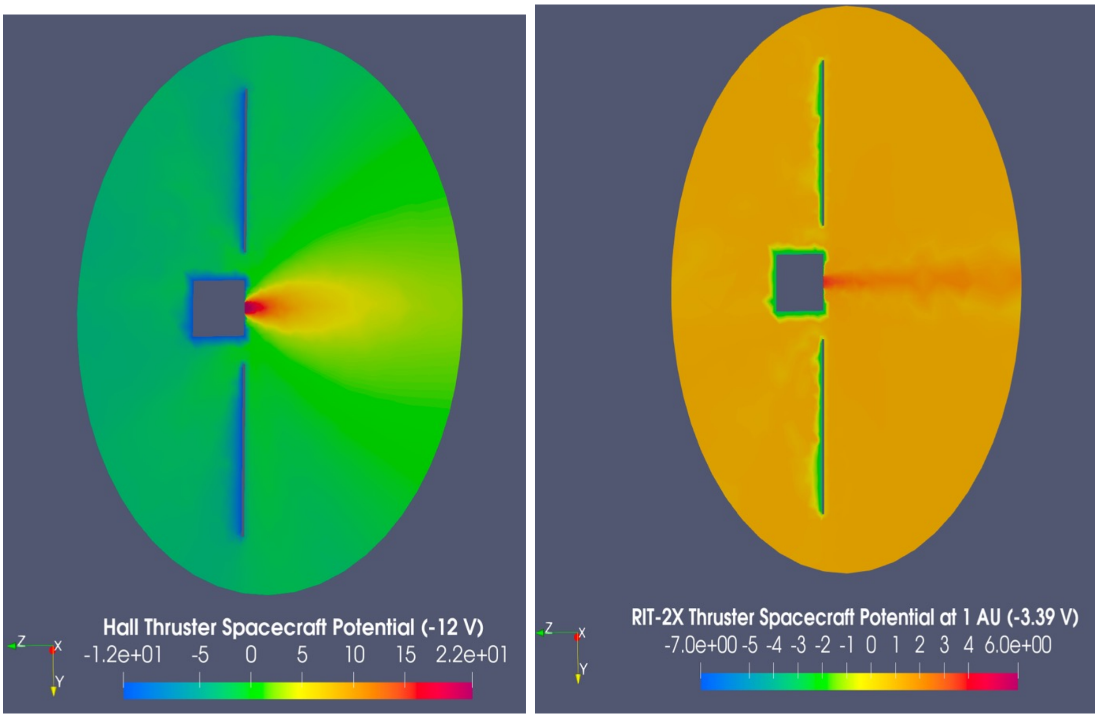

Figure 5.10: 2D potential maps with SPT-100 Hall thruster (on left) and RIT-2X thruster (on right) at 1 AU facing the thruster, corresponding to Figure 1 and the 3D potential cut in the x = 1 plane. sunlight is coming from the right (in +x direction).

panel charge to -12.4 V instead of -12 V, while the RIT charges to -3.37 V instead of -3.39 V. The slight increase in potential is due increase in thruster electron current accumulation. However, the front side of the solar panel does exhibit a change in spacecraft potential, albeit not a significant one. Ideally, since the solar panel is directly facing the thruster, the thruster electrons would induce a significant negative charge on the surface. However, due to the non-conductive material, the front side of the solar panel does not readily accumulate as much charge as the conductive surface. With the SPT-100 Hall thruster, the solar panel's front side charges to -6 V instead of -5.0 V, while with the RIT-2X thruster, it charges to +0.3 V instead of +0.8 V. The slight increase in negative charging can be attributed to the additional accumulation of thruster electron current on the solar panel surface.

As depicted in Figure 5.11, there is a notable difference in the collected current of thruster electrons and CEX-ions on the front side of the solar panel when facing the thruster compared to when it is oriented away from the thruster. Specifically, the collected current is substantially higher when the solar panel is facing the thruster. For instance, at 1 AU, the SPT-100 Hall thruster exhibits a collected current of thruster electrons at 0.15 mA, as opposed to 0.014 mA when the solar panel is not facing the thruster. Similarly, the RIT-2x

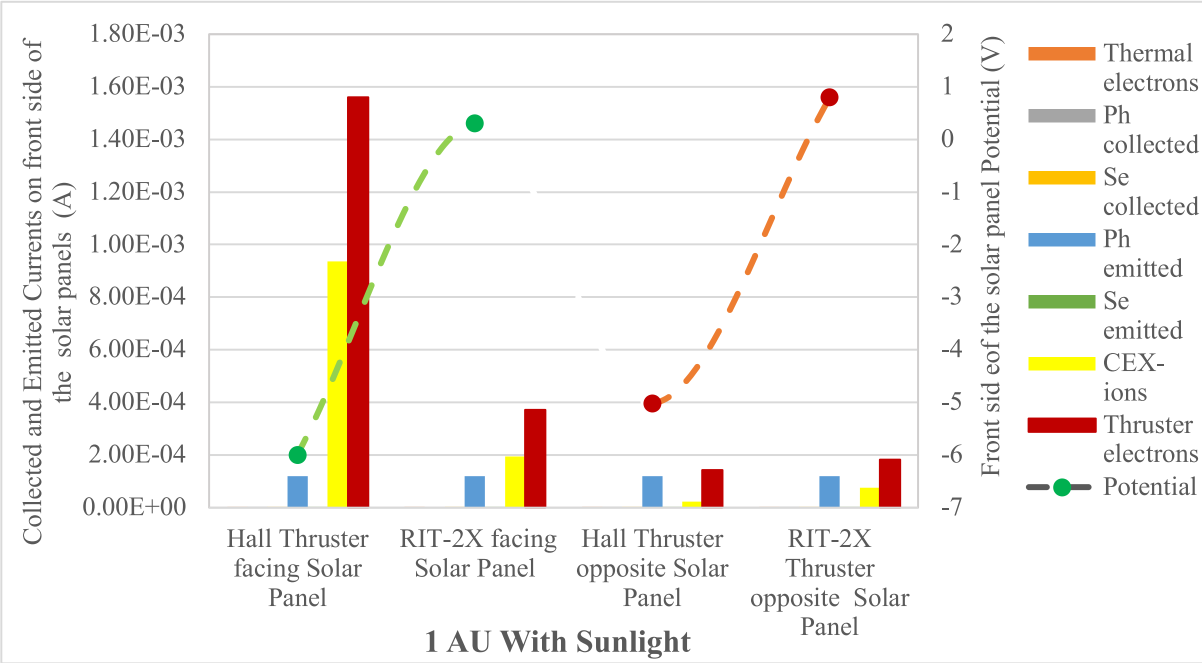

Figure 5.11: Comparison of collected and emitted currents on the front side of solar panels relative to the heliocentric distance at 1AU: Thruster-facing solar panel vs. Thruster-away from the solar panel Configurations

thruster shows a collected current of 0.037 mA when the solar panel faces the thruster, compared to 0.018 mA when it does not. Despite the significant accumulation of thruster electrons when the solar panel faces the thruster, the surface potential does not attain a large negative potential. Primarily, this is attributed to the low energies and temperatures of these electrons.

5.4.2.2 In the Presence of sunlight at 0.044 AU:

The simulation specifically focuses on the RIT-2X thruster, as the SPT-100 Hall thruster encountered convergence issues and was therefore excluded from this location. Figure 5.12 illustrates the solar panel facing the thruster at 0.044 AU, the spacecraft's potential and the backside of the solar panel remain unchanged, charging around -2.62 V instead of 2.60 V (when facing opposite to the thruster). In contrast, the front side of the solar panel, exposed to the thruster's backflow plume shows a slight variation in potential charging to 0.8 V instead of 1.98 V (when facing opposite to the thruster). The decrease in spacecraft potential (less positive) primarily is mainly due to the slight increase in the accumulation of thruster electrons compared with the configurations where thruster is not facing the solar panels. The front side of the solar panel does not charge to a large negative potential due to the non-conductive surface shielding of the solar cell which protects from substantial thruster electron accumulation and the direct impact of ambient electrons.

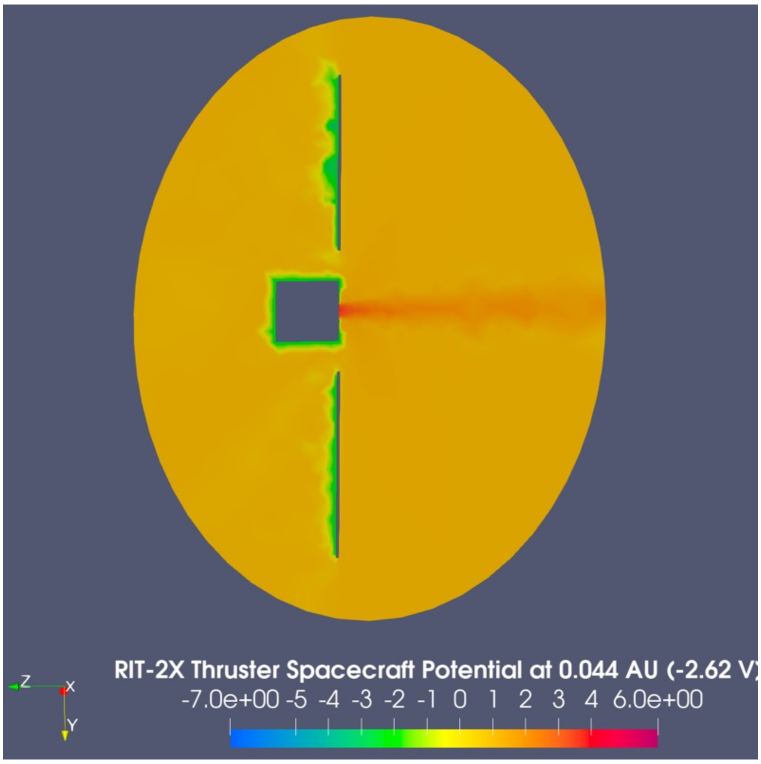

Figure 5.12: 2D potential maps with the RIT-2X thruster (on right) at 0.044 AU facing the thruster, corresponding to Figure 1 and the 3D potential cut in the x = 1 plane. sunlight is coming from the right (in +x direction).

Similarly to the situation at 1AU, when the solar panel faces the thruster, the collected current of thruster electrons significantly increases to approximately 83 mA compared to 27 mA when the solar panels are oriented away from the thruster. The rise in thruster electron current results in a reduction of the solar panel potential from 2V to 0.8V when facing the thruster. Another intriguing finding reveals a substantial decrease in the recollection of photoelectrons and secondary electrons, from 34mA to 0.01mA and from 17mA to 0.14mA respectively, at 0.044 AU when the thruster faces the solar panel (as shown in Figure 5.13). Thus, orienting the solar panel towards the thruster might result in diminished recollection of lower-energy electrons compared to facing the opposite direction.This, in turn, could potentially decrease interference with low plasma measurements and mitigate contamination or erosion of the solar panels.

In summary, regardless of whether the thruster faces the solar panel or is positioned opposite to it, no significant differences are seen in spacecraft potential nor the front and back sides of the solar panel at both locations, 1 AU and 0.044 AU. Therefore, at 1 AU and 0.044 AU, the accumulation of CEX-ions and thruster electrons plays a crucial role in maintaining the low negative potential of the spacecraft's surface, including its solar

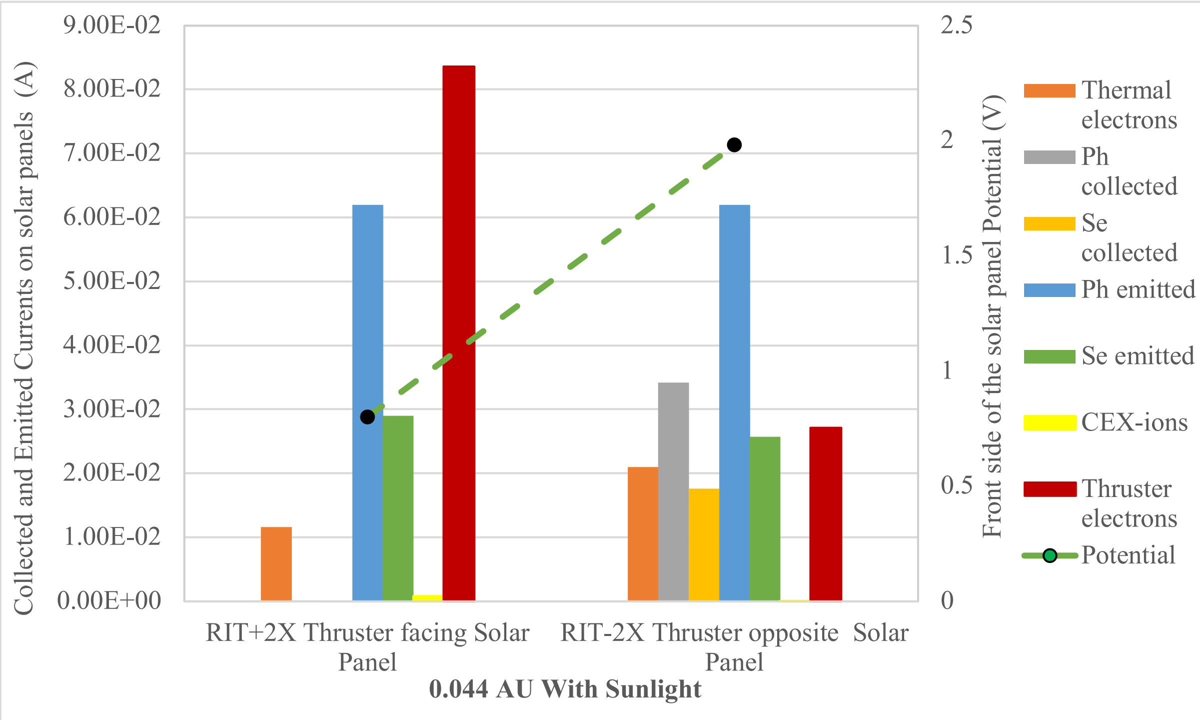

Figure 5.13: Comparison of collected and emitted currents on the front side of solar panels relative to the heliocentric distance at 1AU: Thruster-Facing solar panel vs. Thruster-away from the solar panel Configurations

panels, when compared to conditions without the thruster. However, changing the orientation of the solar panels relative to the thruster does not significantly affect the surface potential. These observations hold true when using the SPT-100 Hall thruster, RIT-2X thruster, and solar cells coated with Cerium + MgF2 material.

5.5 Conclusion

The primary objective of this study is to explore the impact of electric thruster backflow plumes on the potential of solar panels. The research shows the findings obtained at 1AU and 0.044 AU, under varying sunlight conditions, with and without thrusters. Two types of thrusters, namely the SPT-100 Hall thruster and the RIT-2X thruster, were analyzed using SPIS modeling software. The two configurations in which the impact of the electric thruster on the solar panels is analyzed were selected. The one facing opposite to the thruster and the other facing the thruster.

In the absence of the thruster, significant variations were evident in the potential of the spacecraft and solar panels, particularly without sunlight. In contrast, using the SPT-100 Hall thruster and the RIT-2X thruster resulted in notable reductions in spacecraft and solar panel potential at both 1 AU and 0.044 AU, regardless of whether the solar panel faced the thruster or not, and whether there was sunlight. The operation of these thrusters achieved a stable, low negative potential in all conditions. The RIT-2X thruster exhibited a stronger stabilizing effect by charging the solar panel positively due to the high density of CEX-ions and thruster electron density, thus reducing surface potential variations more effectively compared to the SPT-100 Hall thruster.

Notably, a significant difference in surface potential is observed between the front and back sides of the solar panel as a result of material selection differences, resitor places between front side of panel and spacecraft and area exposed to the sunlight. The front side of the solar panel, coated with non-conductive material (Cerium doped + MgF2), showed lower charging compared to the backside coated with conductive material (carbon fiber), both with and without thruster operation. Indeed, the CEX-ions and thruster electrons impacted the front side of the solar panel by maintaining a low negative potential, albeit to a lesser extent compared to the backside and spacecraft surface. The primary reason is due to the dielectric material's (non-conductive) ability to dissipate the charge more readily and not accumulate as much as conductive materials. Lastly, the operation of the thruster significantly reduces the recollection rate of photoelectrons and secondaries on the solar panels compared to those without the thruster.

In the second scenario, where the solar panel faces the thruster, a slight increase in negative potential is noted on the front side of the solar panel at both locations, 1 AU and 0.044 AU, as expected. The increase occurs because the surface is directly exposed to CEX-ions and thruster electrons, leading to the accumulation of more thruster electrons on the solar panel's front side compared to when it faces away from the thruster. However, there is no significant change in the spacecraft potential, indicating that the solar material, coated with cerium-doped+ MgF2, effectively prevents the surface from charging to a negative potential. Surprisingly, another important finding regarding changing the thruster position relative to the solar panel is the exceptional reduction in the recollection of photoelectrons and secondary electrons on the front side of the solar panel compared to when it faces away from the thruster or when the thruster is not in operation. Thus, the reduction suggests that the interference caused by low-energy electrons on sensitive instruments or solar panels may be significantly reduced, potentially mitigating contamination or erosion issues.

Thus, CEX-ions and thruster electrons significantly impact the solar panel surface potential by making it more positive compared to those without the thruster, regardless of the presence or absence of sunlight.The combination of an electric thruster, non-conductive material on the solar panels, and a resistor helps mitigate spacecraft charging. However, the authors would like to emphasize that while surface potential may remain unchanged, solar panels may store energy internally, leading to potential contamination or erosion issues, which were not addressed in this study.

CHAPTER 6

Conclusion

The thesis has sought to address the fundamental question of how electric thruster plumes impact spacecraft surface potential under varying plasma density and temperature conditions, both in the absence and presence of sunlight and both for two different electric thrusters and for no active thruster. It has also explored the effects of the Jovian magnetospheric plasma and, finally, the effect on the potential of deployed solar solar panels both connected to the spacecraft and not. Through the use of numerical simulations with the SPIS software, a more deeper understanding is achieved regarding the intricate dynamics of four primary interactions: the interaction between an electric thruster plume and the spacecraft, the interaction between the electric thruster plume and the local plasma (including the solar wind and Jovian magnetospheric plasma), the interaction between the spacecraft and solar wind conditions (without the thruster) over various heliocentric distances, and the interactions between the spacecraft and its solar panels.

Chapter 2 laid the foundations for the thesis by examining the spacecraft's potential variations across different heliocentric distances (0.067 to 1 AU) with and without the SPT-100 Hall thruster. It illustrated that in the absence of the thruster, the spacecraft's potential varied considerably (ranging from +9 V at 1 AU to -28 V at 0.044 AU from the Sun) with heliocentric distance. The variation is primarily attributed to the strong influence of photoemission at 1 AU, which gradually shifts to the dominance of thermal electrons closer to the Sun due to their high density and temperature, resulting in a strong potential barrier surrounding the spacecraft. The potential barrier further traps low-energy electrons, leading to a high recollection of photoelectrons and secondary electrons, thus causing the spacecraft to acquire a large negative potential at 0.044 AU. However, with the SPT-100 Hall thruster in operation, there was a notable reduction in potential variation, maintaining a low and stable negative potential in the range of -2 V (at 0.067 AU) to -6 V (at 1 AU) for heliocentric distances ranging from 0.067 AU to 1 AU. Chapter 2 also investigated the effects of photoelectrons and secondary electrons with and without the thruster on. The results showed that the elimination of photoelectrons or secondary electrons has a comparatively greater impact on spacecraft potential when the thruster is off (particularly at

1 AU), as opposed to when the thruster is on. In contrast, with the thruster on both CEX-ions and thruster electrons significantly contribute to the mitigation and regulation of spacecraft potential towards a less negative potential in situations where photoemission or secondary electrons are absent.

Thus, the main result from Chapter 2 demonstrated that the SPT-100 Hall thruster maintained a low negative potential throughout heliocentric distances, regardless of the presence or absence of sunlight and secondary electrons. The reduced variation in spacecraft potential is due to the strong dominance of charge-exchange ions (CEX) and thruster electrons, which establish the spacecraft's potential and act as a protective layer against the direct impacts of ambient electrons, photoelectrons, and secondary electrons. The negative potential is due to the thruster electrons having much larger charging current than the CEX ions, due to their larger speeds. Through 2D spatial profile analysis, it was found that the potential barrier reduced significantly, especially near the Sun, leading to a decrease in negative charge. Additionally, it was observed that the recollection of low-energy electrons on the spacecraft surface decreased substantially. Overall, these findings provide a comprehensive understanding of spacecraft charging resulting from the electric thruster's plume interaction with ambient plasma in various plasma environments, setting the stage for further investigation.

Chapter 3 presented detailed numerical simulations that compared two electric thrusters, the SPT-100 Hall thruster and the RIT-2X thruster, as well as the scenario without any thruster from 0.044 to 1 AU. The aim was to analyze how variations in thrust and backflow plume density affect the spacecraft potential at different distances from the Sun. The results revealed several key insights. Firstly, a low, stable, and negative spacecraft potential in the range of -3 to -4 V is achieved throughout heliocentric distances from 0.044 AU to 1 AU when the RIT-2X thruster is on. This variation in potential is significantly reduced compared to the SPT-100 Hall thruster (potential ranging from -2 to -6 V from 0.067 AU to 1 AU), primarily due to the increased density of CEX ions and thruster electrons (about $10^{16}\,\mathrm{m}^{-3}$) compared to the SPT-100 Hall thruster backflow plume (about $10^{11} - 10^{12}\,\mathrm{m}^{-3}$). The main finding is that when the CEX ion and thruster electron densities are much higher than the ambient plasma, the effect of the ambient plasma (such as photoelectrons, secondaries, and thermal electrons) becomes negligible. In such conditions, the spacecraft's final potential depends solely on the CEX ion and thruster electron current, regardless of the presence of sunlight. However, if the CEX ion and thruster electron densities are comparable to the ambient plasma, as observed in the SPT-100 case at 0.067 AU, then the ambient plasma contributes significantly to spacecraft charging (via the thermal electrons). Moreover, the absence of photoelectrons and secondary electrons contributes to making spacecraft more negative even when the thruster is active, albeit to a lesser extent compared to when the thruster is off. Overall Chapter 3 demonstrated that the RIT-2X thruster shows stronger stabilization effects, maintaining a consistently lower, stable negative potential ranging from -3 to -4 V, compared to the SPT-100 Hall thruster's range of -2 to -6 V, across heliocentric distances from 0.044 AU to 1AU.

Chapter 4 expanded upon these investigations by examining the influence of the SPT-100 Hall thruster and RIT-2X thruster on spacecraft charging in the Jovian magnetosphere. The analysis considered three distinct regions and their correspondingly different plasma conditions: Europa at 9.5 Jovian radii (R_j), Ganymede at 15 R_j , and Callisto at 26.1R_j. The Jovian magnetospheric plasma is different from the solar wind plasma (simulated in Chapter 2 and Chapter 3) in several ways. First, the plasma density varies with distance from Jupiter, with Europa having the highest at $2 \times 10^8\,\mathrm{m}^{-3}$ and Callisto the lowest at $0.5 \times 10^6\,\mathrm{m}^{-3}$. Second, electron temperatures also vary significantly, reaching up to 100 eV with Callisto, whereas near Europa and Ganymede the temperatures are around 20 eV. Third, the ion ram speed is notably lower near Europa at 60 km/s but increases to 400 km/s near Ganymede and Callisto, increasing with increasing radial distance. Fourth, the ion species in the Jovian magnetosphere is dominated by O^+ rather than H^+ in the solar wind.

In contrast, the solar wind plasma exhibits increasing density and temperature as the distance to the Sun decreases. At 1 AU, the density is $\approx 7 \times 10^6\,\mathrm{m}^{-3}$, rising sharply to $7 \times 10^9\,\mathrm{m}^{-3}$ at 0.044 AU. Electron temperatures follow a similar trend, starting near 8 eV at 1 AU and escalating to $\approx$ 85 eV at 0.044 AU. The ion ram speed generally decreases from 430 km/s at 1 AU to 300 km/s at 0.044 AU. Through analysis and simulation, this chapter found that both the electric thrusters effectively maintain a low, stable, and negative potential within a small range of -3 to -6 V in the Jovian magnetosphere when the thruster is on, as opposed to the varying range of -25 to +11 V without the thruster. The reason is as for the solar wind: the thruster electrons (and CEX ions) dominate the ambient plasma and photoelctric and secondary electron effects.

Chapter 5 expanded the preceding investigations by delving into understanding the impact of the backflow of the CEX-ions and thruster electrons on solar panels. The study simulated a satellite with deployed external solar panels, equipped with either an SPT-100 Hall thruster or an RIT-2X thruster, at two locations: 1 AU and 0.044 AU. Another preliminary study for Chapter 5, described in Appendix C, investigated how the size and shape of the spacecraft relative to ambient electron Debye length influences the spacecraft. Note that the satellite studied in Chapter 5 is a cubical spacecraft (1m x 1m x 1m) with a solar panel (3m x 1m x 0.5m), which is larger than the spacecraft discussed in Chapters 2 and 3.

Appendix C shows that the spacecraft potential depends on the Debye length and spacecraft size. If the Debye length is larger than the spacecraft size, the spacecraft potential does not vary regardless of the geometry. However, if the Debye length is comparable to or smaller than the spacecraft size, the spacecraft potential starts to vary regardless of the geometry.

The main finding of Chapter 5, consistent with Chapters 2 and 3 and Appendix C, is that CEX ions and thruster electrons help achieve a relatively low negative potential on the conductive spacecraft surface and the backside of the solar panels, regardless of the presence of sunlight. At 1 AU, the spacecraft potential with the SPT-100 Hall thruster on was -12 V with or without sunlight, and with the RIT-2X thruster, it was -3.3 V with or without sunlight. At 0.044 AU, the RIT-2X thruster maintained a potential of -3 V with or without sunlight. In contrast, without a thruster, the spacecraft potential was very different and significantly depended on sunlight: at 1 AU, it was +8.48 V in sunlight and -14.7 V without sunlight, while at 0.044 AU, it was -15.5 V in sunlight and -33.3 V without sunlight.

On the other hand, the (non-conducting, dielectric, Sun-pointing) front side of the solar panel maintained a stable potential with low positive values for the RIT-2X thruster (0.5 at 1AU to 2V at 0.044 AU) and low negative values for the SPT-100 Hall thruster (-5 to -6V at 1AU), irrespective of sunlight. The difference in potential between the front and back sides of the solar panels is due to several factors: first, the resistor used between the spacecraft and the front side of the solar panel that limits the current flow to the spacecraft; second, the distinct material compositions; and third, the area exposed to sunlight. The front side (non conductive, pointing towards Sun), charges more positively than the backside and the spacecraft surface (coated with conductive material). This is due to, first, the front side of the solar panel experiencing strong photoelectric effects, and second, the non-conductive front side dissipates charge more effectively, leading to significantly lower collection of thermal electrons, CEX ions, and thruster electrons. Additionally, the backside of the solar panel is not exposed to the Sun, resulting in a large accumulation of thermal electrons, and thruster charged compared to the front side.

Another significant finding is that facing the front side of the solar panel toward the thruster and the Sun results in a slight increase in negative potential compared to facing away, due to increased accumulation of thruster electrons. However, on the backside of the solar panel, the potential remains unchanged regardless of the panel's orientation to the thruster or away from it. This is primarily due to the use of a resistor that limits the current flow from the solar panels to the spacecraft. Thus, the potential on the front and back sides of the solar panel does not change significantly when the thruster's position is altered relative to the front side of the solar panel facing the Sun. Chapter 5 also outlines future research directions, proposing potential areas such as examining erosion and contamination issues on the solar panel, which were previously neglected. The low-energy CEX ions and thruster electrons may deposit on the solar panel, causing erosion and further degrading the material.

In conclusion, the numerical simulations and interpretations in this thesis advance our knowledge of spacecraft potential variations with and without the use of thrusters. The following points highlight the primary advances.

- Firstly, the high-density CEX ions and thruster electrons dominate spacecraft charging, resulting in a low-magnitude negative potential in most solar wind and magnetospheric environments, even without sunlight. The potential is negative due to the thruster electrons dominating the charging current due to their larger speeds. In contrast, without the thruster active, significant variations are observed with heliocentric distance due to the varying plasma density and temperature of the ambient plasma relative to the Sun. Far from the Sun, photoelectrons dominate, causing the spacecraft to become positively charged, which then transitions to a large negative potential very close to the Sun due to the high density and temperature of thermal electrons.

- Secondly, near the Sun without the thruster, the strong potential barrier formed by the high thermal electron density tends to trap low-energy electrons, causing them to return to the spacecraft's surface and potentially interfere with sensitive onboard instruments, leading to anomalies. However, when the thruster is on, the presence of additional current from charge exchange (CEX) ions and thruster electrons significantly reduces this potential barrier, thereby decreasing the recollection of low-energy electrons. Thus the reduction in recollection of photoelectrons and secondary electrons can play a crucial role in improving the accuracy of low plasma measurements.

- Thirdly, The importance of selecting the appropriate thruster based on plasma conditions is crucial. When the CEX ion and thruster electron densities are higher than the ambient plasma, they dominate spacecraft charging, making the impact of photoemission, thermal electrons, and secondary electrons on spacecraft potential negligible, as observed with the RIT-2X thruster in Chapter 3. However, if the CEX ion and thruster electron densities are smaller than or comparable to the ambient plasma density, then the impact of photoemission, secondary electrons, and thermal electrons becomes more prominent, though still less significant than without the thruster. Thus, comparing different electric thrusters, such as the SPT-100 Hall thruster and the RIT-2X thruster, helps to select the most suitable thruster for specific mission requirements, ensuring the spacecraft potential is maintained at a low negative value while the thruster is active.

- Finally, the simulation findings demonstrate how spacecraft potential is influenced by various factors, including spacecraft size, geometry, material composition, and the resistor connection between the spacecraft and the solar panel. Firstly, the results show that spacecraft potential depends on the Debye length relative to the spacecraft size, regardless of geometry. If the Debye length is larger than the spacecraft size, the potential remains consistent regardless of the shape. However, if the Debye length is comparable to or smaller than the spacecraft size, the potential varies significantly. Additionally, it was found that a cubical spacecraft experiences more stable variations in potential compared to a cylindrical spacecraft when the Debye length is larger than the spacecraft size. The difference is likely due to the cubical spacecraft's flat surfaces and sharp edges accumulating fewer charged particles compared to the cylindrical spacecraft's smooth surface. Secondly, the study shows that material composition influences surface potential, providing guidance for selecting appropriate materials for spacecraft components, including solar panels. A combination of dielectric material on the front side of the solar panel facing the Sun, along with the collection of CEX ions and thruster electrons, makes the front side of the solar panel significantly more positive compared to a surface covered with conductive material, regardless of sunlight exposure. Thirdly, the use of a resistor between the solar panel and the spacecraft (preliminary results not shown) and between the spacecraft and electric thruster (Chapter 2 and 3) helps to limit the current flow from solar panel and electric thruster to the spacecraft. Thus the resistor plays an important role in limiting the current flow and stabilizing the spacecraft potential. Without the resistor, the spacecraft could accumulate a larger charge, leading to potential differences that may interfere with spacecraft systems or cause electrostatic discharges.

In conclusion, the insights provided by this thesis offer a comprehensive understanding of how varying plasma density, different thrusters, different materials, various geometric shapes and sizes, the use of resistors, and the addition of solar panels influence spacecraft potential with and without electric thrusters. This knowledge is crucial for mission design and analysis, enabling a thorough assessment of charging effects, optimal thruster selection, and strategic positioning of solar panels and other instruments. Understanding charging dynamics will allow mission designers to select the appropriate components, thus ensuring the reliable operation of spacecraft systems and solar panels.

6.1 Limitations

The limitations of the research conducted on spacecraft charging using simulations with the SPT-100 and RIT-2X thrusters are multifaceted. Primarily, the research relies on numerical simulations and mathematical models within the Spacecraft Plasma Interaction Software (SPIS) suite, which has inherent limitations, as explained in detail in Section 1.5.3. These models are constructed based on various assumptions and approximations that may not fully capture the complexity of real-world scenarios. However, the papers by Wartelski, Theroude, et al. (2013); Wartelski, Ardura, et al. (2011) have endeavoured to validate the accuracy of the thruster plume model by comparing experimental data with the SPIS simulations. These comparisons demonstrated excellent agreement between the ion current simulated by SPIS and the experimental data for thrusters such as SPT-100 and RIT-10, as well as others.

In this thesis, the simulations are based on solar wind plasma conditions ranging from 0.044 AU to 1 AU and on Jovian magnetospheric plasma conditions. Replicating these plasma conditions in a vacuum chamber is challenging, making experiments critical yet difficult. Consequently, the simulated results could not be compared with either experimental data or real flight data, further compounding this limitation. In addition, the study neglected factors such as contamination, erosion, and internal charging with and without the thruster, all of which can significantly impact the charging dynamics of spacecraft. Addressing these limitations in future research endeavors is essential for advancing the understanding of spacecraft charging dynamics and enhancing the reliability of spacecraft systems in practical applications.

6.2 Future Work

The proposed research aims to address current challenges and expand our knowledge of spacecraft interactions with plasma, leading to innovative solutions that enhance mission performance and instrument protection.

- LEO Plasma Simulations
  The next phase of this research will involve conducting simulations of the LEO environment using the Spacecraft Plasma Interaction Software (SPIS) at altitudes ranging from 300 km to 900 km. The primary objective is to further elucidate the relationship between spacecraft potential and drag effects in the LEO environment.

Preliminary results suggest that increasing the spacecraft potential to positive values, rather than the negative values expected even in sunlight due to the very large ambient electron number densities, leads to increased drag as predicted by Capon et al. (2016). Future work will focus on understanding the influence of electric thruster plumes on drag effects.

- Extended Simulations for Solar and Deep Space Missions
  Complex simulations should be carried out for missions near the Sun, such as the Parker Solar Probe, and upcoming missions like the Europa Clipper. These simulations, also using SPIS integrated with an electric thruster, could aim to predict spacecraft potential and compare the results with real flight data. The goals are to gain a deeper understanding of the impact of electric thrusters on spacecraft potential and to explore how these effects influence the sensitive instruments onboard. Additionally, these simulations should analyze erosion and contamination issues on the spacecraft surface and solar panels.

- Effects of Electric Thruster Plumes on Low Energy Plasma Measurements
  An intriguing area for future research is the impact of electric thruster plumes on low-energy plasma measurements, with energies less than or similar in magnitude to the spacecraft potential. This includes investigating how high-density charge-exchange (CEX) ions and thruster electrons affect data from instruments such as Langmuir probes, which measure electron density, temperature, and plasma density. Additionally, it is important to consider the effects on instruments that measure thermal electrons and ions by detecting currents on detectors while varying the applied potential, a method that has been employed for many years. Understanding these influences is crucial for accurate plasma measurements and optimal instrument positioning.

- Thruster Orientation and Plasma Interaction
  To investigate how different thruster orientations, such as along-track or perpendicular to the orbit plane, affect spacecraft charging under varying plasma conditions. It is predicted that when the thruster backflow plume density significantly exceeds the ambient plasma density, the thruster will dominate the spacecraft and surrounding plasma environment, making orientation less critical. However, in environments where the plume density is comparable to the ambient plasma—particularly near the Sun—photoelectrons and secondary electrons will play a crucial role in reducing negative spacecraft charging. Exploring these dynamics across different orientations and plasma conditions will provide deeper insights into spacecraft charging behavior.

- Autonomous Mitigation Strategies and Quantum Sensors
  Efforts should be dedicated to developing autonomous mitigation strategies using electric thrusters, potentially involving quantum sensors for spacecraft potential detection. Quantum sensors, known for their high sensitivity and precision, could provide real-time data on potential variations, enabling rapid response and adjustment. These sensors can measure the local electric field and monitor charge buildup on the spacecraft surface. This real-time data will help activate discharge devices, such as electric thrusters, to mitigate charging. Furthermore, algorithms will be used to control and autonomously activate electric thrusters in response to detected changes in spacecraft potential, ensuring optimal performance and protection of sensitive instruments.

APPENDIX A

Charge-Exchange Plasma Effects of the SPT-100 Hall Thruster at Heliocentric Distances from 0.044 AU to 1 AU

Published as: Tejaswi Shinde, Iver Cairns, and Jason Held
AIAA 2023-1597, https://doi.org/10.2514/6.2023-1597

(Note that this refereed conference paper does not account for variations in the solar photon flux with heliocentric distance, unlike Chapter 2. Consequently, the results differ from those in Chapter 2, where the photoelectric effects are accurately included and significantly affect the system when the thruster is off compared to when it is on)

A.1 Abstract

Electrostatic charging varies the potential of the spacecraft by developing a sheath surrounding the spacecraft that disturbs low-energy plasma measurements. The floating potential of a satellite in the solar wind at various heliocentric distances can vary between positive and negative potentials of several tens of volts, affecting the collection of low-energy electrons and ions and contaminating low-energy plasma data. If the SPT-100 Hall thruster is operated, it is shown that the backflow CEX-ions and associated electrons dominate the background plasma and spacecraft interactions, making the spacecraft charge negatively due to the associated thruster electrons and stably for a wide range of heliocentric distances. The paper presents the detailed effects of electron and ion-induced charging of a simplified spacecraft with and without the thruster for various heliocentric distances (from 0.044 AU to 1 AU) using the Spacecraft Plasma Interaction System Software (SPIS). To study this, cross-comparisons with and without the thruster are performed to investigate the variations in spacecraft potential (magnitudes and 2D spatial profiles), trapping structures for electrons and ions, changes in the size of the electrostatic sheath surrounding the spacecraft, and the roles of the ambient particles (electrons and

ions), thruster ions and electrons, and both photoelectrons and secondary electrons. In particular, the study investigates the importance of secondary electrons during thruster operation near the Sun at 0.067 AU and at 1 AU. The main result is that the dominance of the CEX-ions and electrons of the thruster on the ambient plasma during thruster operation leads to the satellite potential being in a small range (-2 to -6 V, but typically -5 to -6 V for the range 0.1 to 1 AU), compared to the large range of -18 to +5 V without the thruster. This demonstrates an electric thruster's capability to maintain and control the spacecraft's potential for a wide variety of solar wind and space weather conditions.

A.2 Introduction

In recent years, there has been increasing interest in electric propulsion systems for commercial, scientific and interplanetary missions due to their high specific impulse, thruster controllability, and proven reliability (Goebel et al., 2023; Kuninaka et al., 2011; Garner et al., 2013; Liu et al., 2013). Several space missions have incorporated an electric thruster rather than a chemical thruster due to the increased propellant capacity and less propellant consumption which enables additional payload capacity for various scientific instruments (Goebel et al., 2023). However, the time-to-destination is significantly longer for electric propulsion, which results in a greater risk of spacecraft charging while traversing in a solar wind environment. The highly energetic particles of the solar wind cause the variation in the electrostatic potential of the spacecraft, which severely disturbs the particle and electric field measurements (Guillemant, 2014). Similarly, when an electric thruster encounters different plasma environments, a variation in spacecraft surface charging is expected (Na et al., 2019; Wang, 1997). The effects caused by electric thruster operations have long raised both scientific and operational concerns as the plume's backflow contaminates and interacts with spacecraft systems and results in ion-induced charging (Na et al., 2019; Wang, 1997;Lee et al., 2011; Filleul et al., 2021; Tajmar, 2002).

Backflow plumes consist of low-velocity charge-exchange ions (CEX ions) generated from a collision between fast-beam ions and propellant neutrals inside the main ion beam (Goebel et al., 2023). These ions flow back to the spacecraft and lead to two main effects. First, effluent deposition causes contamination of optical sensors, solar arrays, thermal control, and other communication instruments (Wang, 1997). Second, the CEX-ions and associated electrons will modify the properties of the solar wind flowing around the spacecraft by inducing an additional current that may influence the spacecraft potential and plasma instrument observations (Wang, 1997). Thus, it is important to study thruster-induced plasma and solar wind effects on spacecraft charging in various environments to avoid spacecraft operational anomalies and failures. Using solar wind effects on spacecraft charging at various heliocentric distances by Guillemant (2014) investigated variations in spacecraft potential, electrostatic sheath, and potential barrier depending on the distance to the Sun using the SPIS software. The main result was that the spacecraft charged to a few positive volts from 1 AU to about 0.3 AU, while below 0.3 AU, the potential barrier generated by photoelectrons and secondary electrons drives the potential negative. Due to the low energy of these electrons, they can surround the spacecraft and affect the plasma potential by generating a potential barrier, leading to the high recollection of low-energy electrons. These low-energy electrons could interfere with (up to a few tens of electron volts) plasma sensors and particle detectors, by biasing the particle distribution functions measured by the instruments (Guillemant, 2014).

Following observations of spacecraft charging on the Cluster spacecraft outside the Earth plasmasphere, Torkar et al. (2001) found that the spacecraft charges to a high positive potential due to high-energy photoelectron (K. Torkar et al., 2005). The development of an electrostatic sheath around the spacecraft is due to the photoelectrons energy being lower than the spacecraft potential, trapping the low-energy photoelectrons and eventually returning to the surface, thus causing an additional disturbance in the particle measurement. The disturbances are not limited to particle measurement, but also electric field measurement may suffer from spacecraft potential. Thus, to avoid this situation, the Cluster spacecraft was equipped with an indium ion emitter capable of producing ions at 5 to 9 keV energy in currents of some tens of micro amperes. Some results derived from the Active Spacecraft Potential Controller instrument (ASPOC) onboard the Cluster spacecraft demonstrated a significant reduction in spacecraft potential and improved particle measurements (Torkar et al., 2001). Similarly, beneficial effects were observed on the Double Star TC-1 spacecraft (K. Torkar et al., 2005).

This phenomenon confirms that the presence of an ion beam is advantageous for lowering the potential and improving particle measurements. This paper will conduct a similar investigation to evaluate the effects of the ion beam emitted from the SPT-100 Hall thrusters on spacecraft charging by using the Spacecraft Plasma Interaction Software (SPIS). Hall thrusters emit an ion beam and neutralizer electrons to create a quasineutral plasma, and the CEX-ions act as plasma contactors to lower the spacecraft potential. Although thruster-spacecraft interactions have been the subject of extensive experimental and theoretical studies, there is an incomplete understanding of the interaction between the thruster-generated plasma and the spacecraft in the presence of ambient plasma, photoelectrons, and secondaries. Hence, the earlier paper Shinde, Held, and Cairns (2022)] investigated the influence of photoelectrons and secondary electrons on spacecraft potential for two heliocentric distances at 1AU and 0.093 AU (Shinde, Held, and Cairns, 2022).

The main result is that CEX-ions and thruster electrons dominate the satellite plasma environment at 1 AU and 0.093 AU, leading to negative spacecraft potentials due to higher thruster electron charging rates. The photoelectron and secondary electron effects are larger at 0.093 AU than at 1AU, leading to more positive spacecraft potentials. This paper presents a detailed study of ion-induced charging from 0.044 AU to 1AU by comparing the variation in spacecraft potential and the evaluation of currents for various sources with the thruster on and off. Additionally, the paper investigates the detailed spatial profiles of the ram, wake, and electrostatic sheath structure with and without the thruster. Finally, the role of secondaries on spacecraft charging is investigated near-Sun the environment at 0.067 AU and far away from the Sun at 1AU. Section A.3 of this paper will explain the simulation setup and physical parameters of the SPIS software. Section A.4 represents the simulation results for A.4.1.) Near the Sun at 0.044 AU A.4.2) From 0.11 to 0.162 AU and A.4.3.) Below 0.25 AU. Section A.5 analyses the wake of the ram and the side potential profile of the spacecraft. Finally, A.6 investigates the effects of spacecraft charging without secondary electrons.

A.3 Simulation Modeling

The simulation tool used in the paper is SPIS, a 3D electrostatic solver based on the particle-in-cell (PIC) method to simulate the spacecraft charging effects in various environments (LEO, GEO) electric thruster operations). The spacecraft geometry used for all simulations is a cylindrical geometry (1m radius and 2m length) covered with indium tin oxide material (ITO). The domain dimension varies with Debye length (3x Debye length), and so do the mesh refinements. The domain meshing resolutions for all the simulations are maintained at less than one-third of the Debye length, and the number of tetrahedrons ranges from 50,000 to 100,000. Figure A.1 shows the satellite model using the GMSH software. The physical environment parameters corresponding to various heliocentric distances are taken from Guillemant (2014).

The varying parameters in the simulations are plasma properties such as densities, temperatures, solar wind velocity, solar flux, and timesteps for each population (ions, thermal electrons, secondary electrons, and photoelectrons). Moreover, the satellite is assumed to be static with respect to the Sun, so only the ion drift velocity is simulated (directed along the x-axis). All species (protons, thermal electrons, photoelectrons, and secondary electrons) are computed using a PIC model for a spacecraft integrated with the SPT-100 Hall thruster. The SPIS Hall thruster model uses the Monte Carlo method to simulate the CEX-ion collisions and various other species (Xe neutral, Xe+, Xe++) in the computational

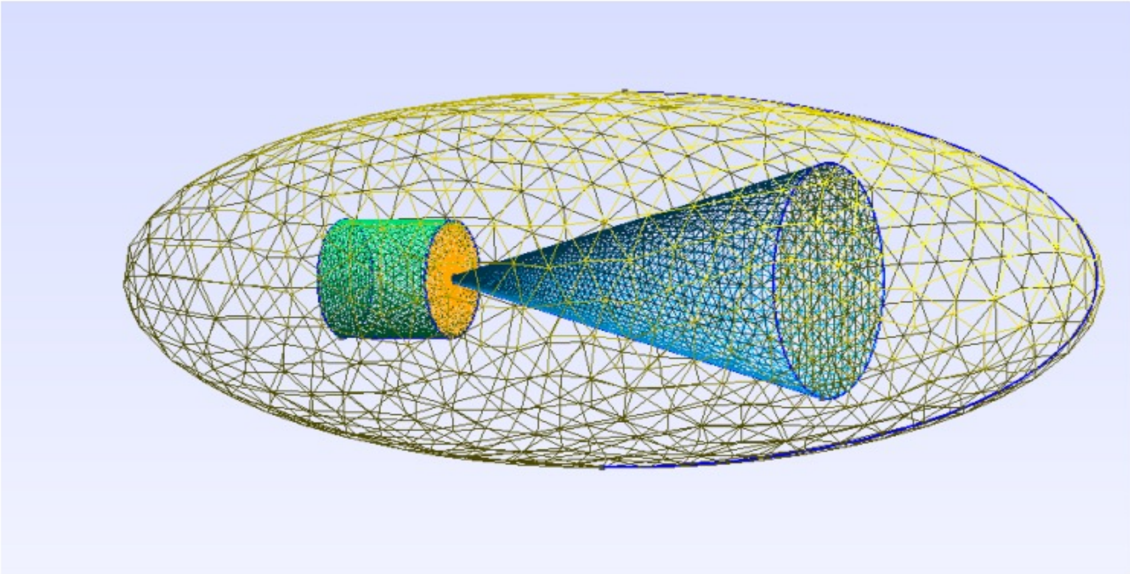

Figure A.1: GMSH model of the simple cylindrical spacecraft and meshing grid (green and yellow) used in the SPIS simulation. The ovoid boundary is the simulation box. The blue conical shape shows the ion plume

regions. The SPT-100 thruster specifications are described in Table A.1. During simulations, thrusters are assumed to be electrically connected to the spacecraft chassis, and the spacecraft floats with the local plasma potential (the anode and cathode of the thruster are isolated from the spacecraft) (Liu et al., 2013; Tajmar and Wang, 2000). A resistor is added between the thruster and spacecraft to provide a return path for this leakage. The resistor provides a high degree of isolation between the thruster and the spacecraft, thus limiting excessive charging. The ground of the spacecraft is different from the ground of the electric thrusters. The primary reason for operating in this manner is to reduce the contamination of the spacecraft caused by thruster plumes (Liu et al., 2013). The magnetic field is not taken into consideration. The vertices of the spacecraft cylinder in the x-y plane are A(0,1,0), B(2,1,0), C(2,0,0), and D(0,0,0). In the Figures below the y = 0 (x-z) plane is the reference plane shown, without loss of generality due to the cylindrical symmetry. The vector x lies along the thruster axis. The ram and wake start from points D and C and are directed in the -x and x directions, respectively.

A.4 Simulation Results

A.4.1 Simulation results from 0.044 AU to 1 AU

This section presents and discusses the results of three cases 1.) With and without the thruster at 0.044 AU 2.) Between 0.0162 and 0.11 AU 3.) below 0.25 AU. In all simulation

Table A.1: Gmsh Geometry Dimensions and Thruster Specifications.

Parameters	**Value**
Geometry	1m radius, 2m long, cylinder
Surface Material	Indium Tin Oxide
Photoelectron temperature	3eV
Thruster Electron Temperature	0.5-0.8eV
Ambient Ion type	H+
Ion modelling	PIC
Electron modelling	PIC
Magnetic Field	Not considered
Thruster Specification	
Ion Thruster	SPT-100 Hall
Thrust	0.035 N
Specific Impulse	1840s
Cathode Temperature	5 eV
Mass Flow rate (Xe)	1.91×10^{-6} Kg/s
Current	1.43 A
Power	723 W

cases, the photoelectron temperatures are kept constant, while the secondary electron temperature and ion drift velocity are varied with distance to the Sun. The Sun's incoming solar wind is directed from the left direction in all figures. To solve the equivalent electric circuit of the SPIS software, the resistance between the thruster and spacecraft is maintained at 500,000 ohms. Figures A.2 and A.3 illustrate the potential maps and log-density plots for each plasma population over heliocentric distances, while Figure A.4 illustrates the cross-comparison of population densities with and without the thruster at 0.044 AU. Figure A.5 compares the 2D variation in potential around the spacecraft with and without the thruster. Figures A.4 and A.5 show the cut model of the geometry along the y axis. Figures A.6 and A.7 show the collected and emitted currents for various helio distances with and without the thruster while Figures A.8 and A.9 illustrate the ram, and wake structural profiles with and without the thruster.

A.4.2 With and Without thruster from 0.044 AU to 0.093

As shown in Figure A.2 without the thruster the satellite potential converges to -18.43 V. The negative charging can be explained by the fact that close to the Sun the space charging effects become more critical due to the hot and dense ambient environment, despite higher secondary emission rates from the surfaces exposed to the plasma. The high thermal electron density of 10^9 m^{-3} dominates and charges the spacecraft negatively despite the high photoelectron density (as shown in Figures A.3 and A.4) (Guillemant, 2014; Ergun et al., 2010). This result might seem contradictory when considering photoemission, but it can be explained by the fact that the Debye length of the photoelectron is smaller than the spacecraft, which moves the local potential barrier close to the surface and the space charge may be considered as the 1D thin sheath. Chapter 1 and 2 and a previously reported paper provides a detailed explanation of the transition from thick to thin sheaths near the Sun environment)(Shinde, Held, and Cairns, 2022). Looking at the 2D potential structure from Figure A.5, the potential in the ram region at 0.044 AU (without the thruster) charges around -22.7 V due to the denser population of photoelectrons emitted from the sunlight, they have spread around until the wake region. In the wake region, the spacecraft charges to a high negative value of approximately -33.7 V mainly because of the high-density secondary electrons added due to the lack of ions in the region. Thus, the potential barrier generated by the photoelectrons and secondary electrons may have low energy (2-3 eV) surrounding the spacecraft. Due to the insufficient kinetic energy, they did not overcome the barrier resulting in high recollection and returned to the spacecraft's surface. The high recollection, especially because of the secondary electrons, can interfere with the low-energy plasma measurement and bias the particle distribution functions measured by the instruments.

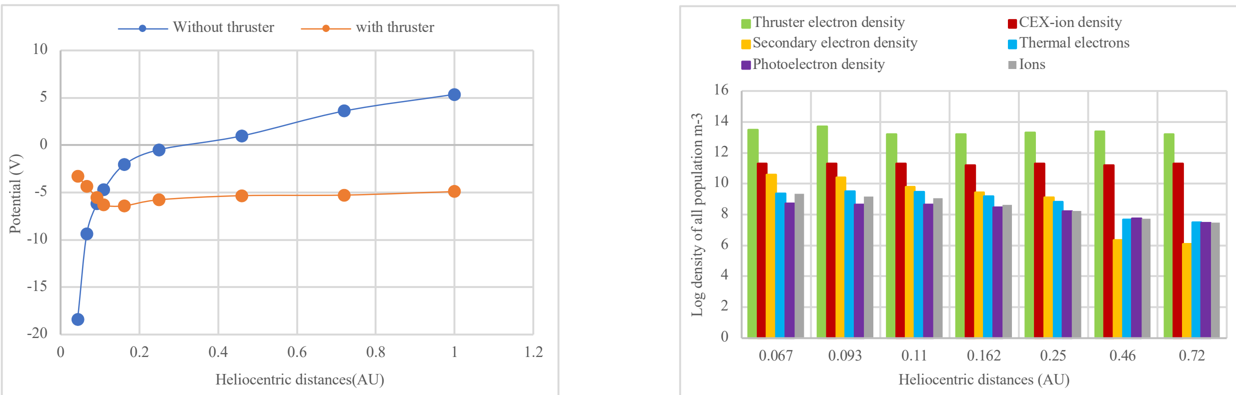

a. Spacecraft potential with and without the thruster vs heliocentric distances

b. Log of population densities vs heliocentric distance with the thruster on

Figure A.2: Illustration of Spacecraft potential and Population densities with the thruster on vs helio distances

However, with the thruster operating, as shown in Figures A.2 and A.4 the spacecraft charges to -2.85 V. Thus, a significant drop in the spacecraft potential at 0.044 AU occurs when the thruster is turned on. The explanation is that CEX- ions and electrons from the cathode dominate the surface and surrounding plasma because their number densities are much higher, $10^{10}\,\mathrm{m}^{-3}$ and $10^{11}\,\mathrm{m}^{-3}$, respectively (as shown in Figures A.3 and A.4). The CEX-ions reach every corner of the spacecraft and the associated thruster

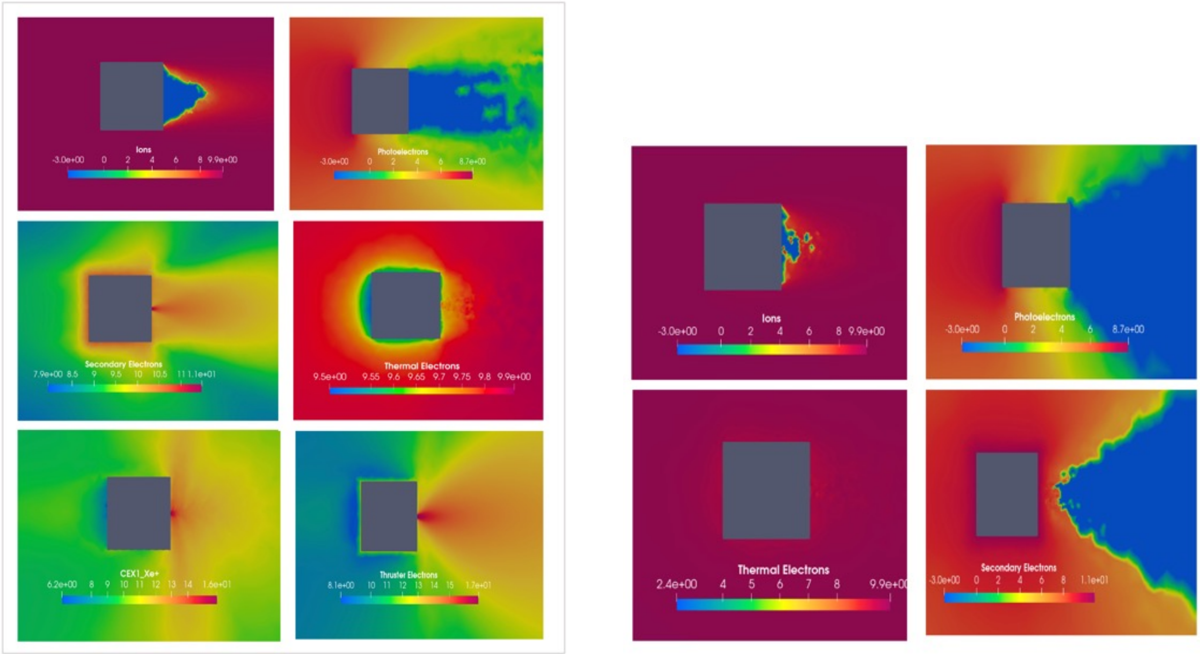

Figure A.3: Simulation result for the 0.044 AU case representing the population densities with (left) and without the thruster (right). The solar wind and Sun direction on the left side for all the simulations

electrons try to neutralize their charge and follow the same path. The high density-low energy charged particles emitted from the electric thruster provide an additional current to reduce the equilibrium potential of the spacecraft. As shown in Figure A.2, thruster operation achieves a low and stable potential over a wide range of heliocentric distances from 0.044 AU to 1AU. The flatness of the curve indicates that the constant ion beam current can stabilize and maintain the low potential compared to the situation without the thruster, since the CEX-ions and thruster electrons dominate the ambient plasma. The minor variability in the curve is due to changes in plasma conditions. Similar results were found by Torkar et al. in the sense that they demonstrated the indium ion emitter capable of reducing the spacecraft potential by adding an ion beam current (Torkar et al., 2001,K. Torkar et al., 2005). The results from both missions (Cluster and Double Star TC-1) confirmed that the use of an ion beam helps reduce the spacecraft potential and enhances the low-energy plasma measurement. However, these missions included a pure ion emitter, and in the present case, it is an operating SPT-100 Hall thruster producing quasi-neutral plasma. The thruster produces a similar density of slow CEX-ions and thruster electrons, but the thermal velocity of the electrons is larger for the same energy compared with the ions (ve » vi), and so the surface accumulates an electron larger than the CEX-ions, thus charging negatively.

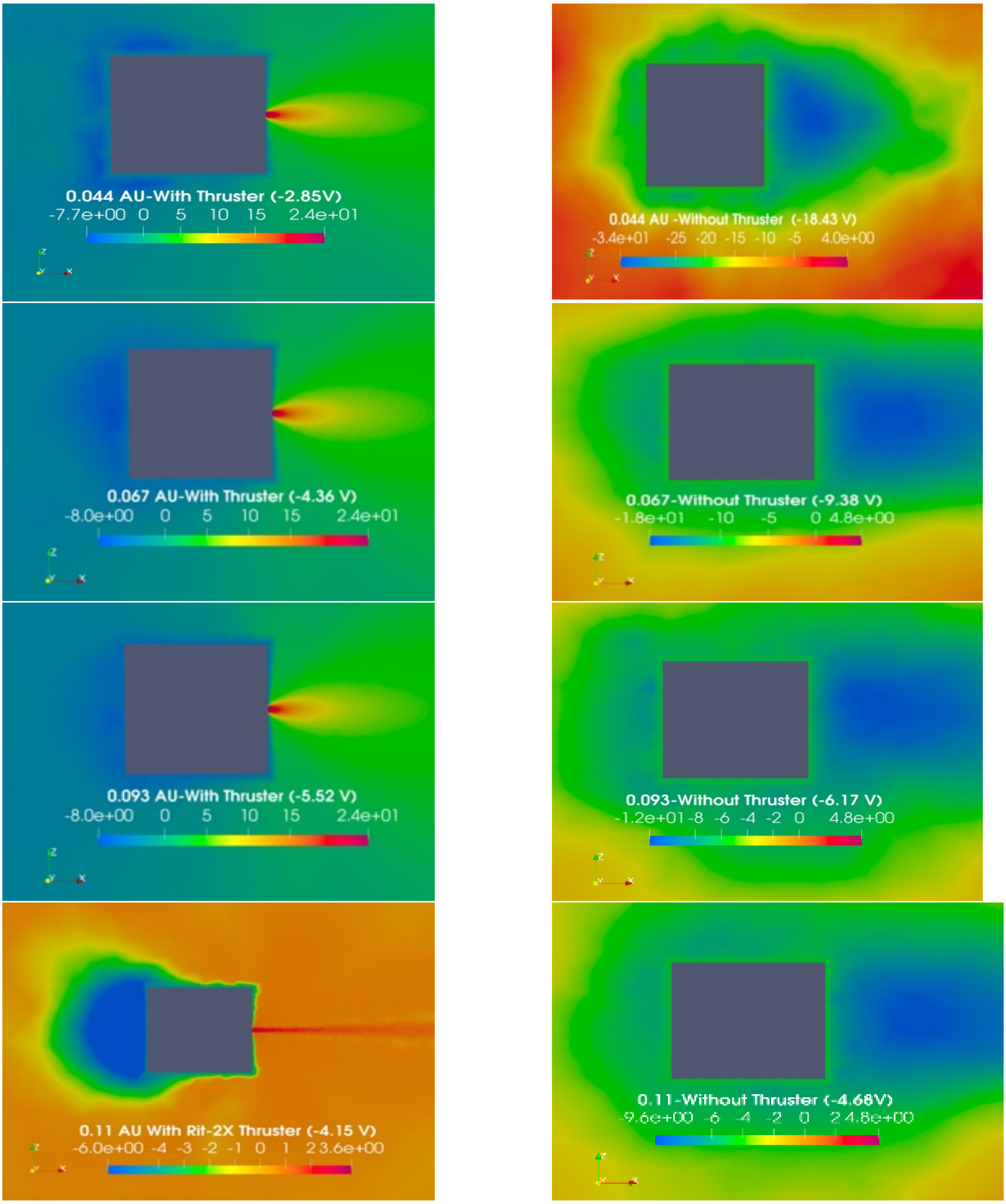
0.044 AU-With Thruster (-2.85V)
-7.7e+00 0 5 10 15 2.4e+01
0.044 AU -Without Thruster (-18.43 V)
-3.4e+01 -25 -20 -15 -10 -5 4.0e+00
0.067 AU-With Thruster (-4.36 V)
-8.0e+00 0 5 10 15 2.4e+01
0.067-Without Thruster (-9.38 V)
-1.8e+01 -10 -5 0 4.8e+00
0.093 AU-With Thruster (-5.52 V)
-8.0e+00 0 5 10 15 2.4e+01
0.093-Without Thruster (-6.17 V)
-1.2e+01 -8 -6 -4 -2 0 4.8e+00
0.11 AU With Rit-2X Thruster (-4.15 V)
-6.0e+00 -4 -3 -2 -1 0 1 2 3.6e+00
0.11-Without Thruster (-4.68V)
-9.6e+00 -6 -4 -2 0 2 4.8e+00

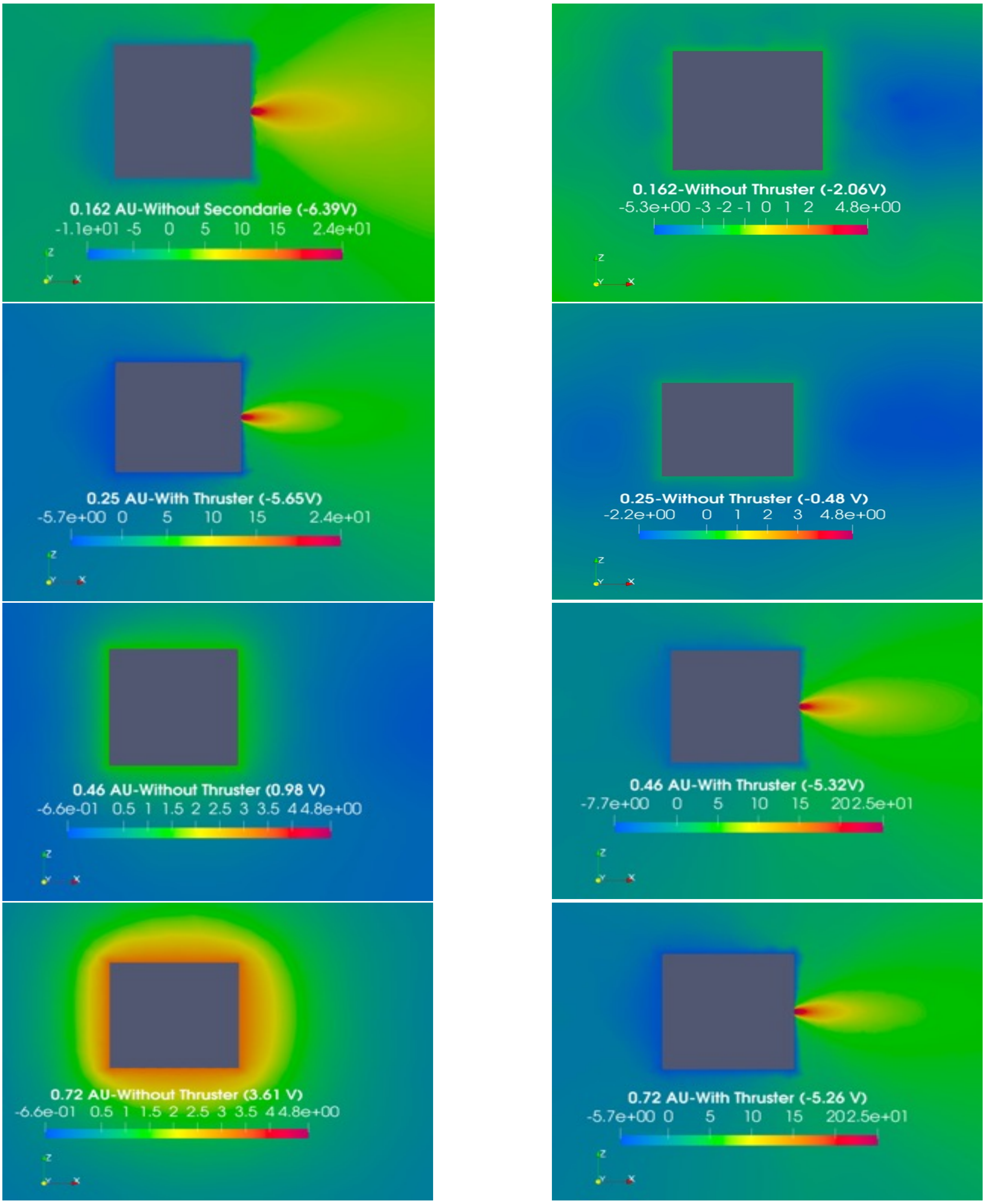
0.162 AU-Without Secondarie (-6.39V)
-1.1e+01 -5 0 5 10 15 2.4e+01
0.162-Without Thruster (-2.06V)
-5.3e+00 -3 -2 -1 0 1 2 4.8e+00
0.25 AU-With Thruster (-5.65V)
-5.7e+00 0 5 10 15 2.4e+01
0.25-Without Thruster (-0.48 V)
-2.2e+00 0 1 2 3 4.8e+00
0.46 AU-Without Thruster (0.98 V)
-6.6e-01 0.5 1 1.5 2 2.5 3 3.5 4 4.8e+00
0.46 AU-With Thruster (-5.32V)
-7.7e+00 0 5 10 15 20 2.5e+01
0.72 AU-Without Thruster (3.61 V)
-6.6e-01 0.5 1 1.5 2 2.5 3 3.5 4 4.8e+00
0.72 AU-With Thruster (-5.26 V)
-5.7e+00 0 5 10 15 20 2.5e+01

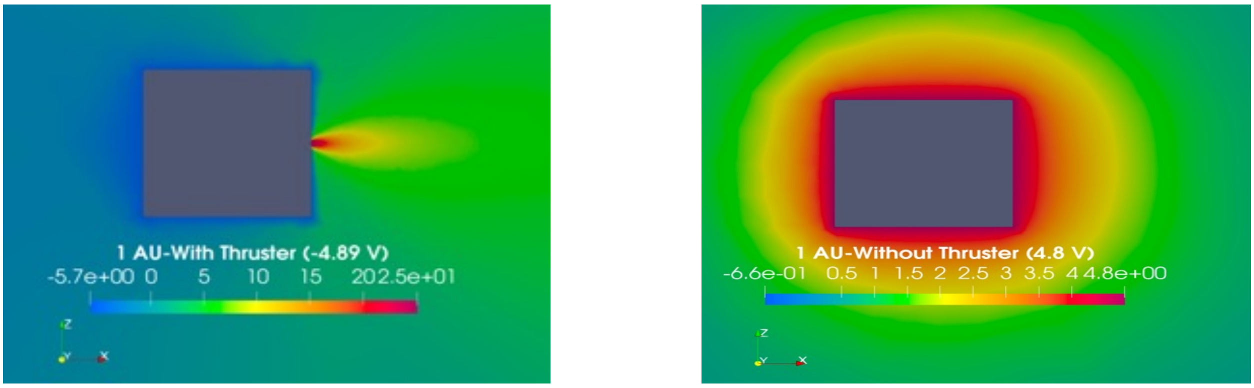

Figure A.4: Cross comparison of spacecraft potential with and without the thruster for various helio distances from 0.044 AU to 1 AU

Figures A.5 and A.6 show the collected and emitted currents with and without the thruster versus the heliocentric distance. The collection current of secondary electrons is higher without the thruster case than with the thruster, as shown in Figure A.5. With the thruster, the spacecraft collects secondary electrons of 18 mA, while it collects 67 mA without the thruster (for 0.044 AU). The thermal electron collection current is constant in both cases. Another finding shows that with the thruster close to the Sun, particularly at 0.044 AU, the secondary electron emission current of 73 mA is higher than the collected current of 18 mA, resulting in a lowering of the spacecraft potential (as shown in Figure A.6). The secondary electron emission helps to carry away negative charge, unlike in the thruster case. Looking at 2D the structure of the ram and wake potential in Figure A.4, the spatial size of the sheath and the potential barrier are significantly reduced when the thruster is operated. Thus, the result implies that the use of a thruster no longer restricts the escape of secondary electrons as they easily overcome potential barriers which lead to a reduction of returns of secondary electrons back to the spacecraft. The low rates of secondary electron recollection will have a negligible effect on spacecraft and the instruments and will enhance low-energy plasma measurements' accuracy. However, this study does not include the effects of erosion, contamination, and deposition of charged particles on the spacecraft instrument, which will be an interesting perspective for future studies.

A.4.3 With and Without thruster from 0.11 to 0.25 AU

In this region, the same model works as for 0.044 AU when the thruster is on. The CEX-ions reach every corner of the spacecraft and the associated thruster electrons dominate the spacecraft and surrounding plasma. However, the spacecraft potential shows minor variability in this case compared to other helio distances despite the constant ion beam current. As shown in Figures A.2 and A.4, the spacecraft potential for 0.162 AU and 0.11

AU changes to -6.39 V and -6.30 V, respectively. The small increase in the spacecraft potential is mainly due to the low emission of secondary electrons. As shown in Figure A.6, the thruster electrons collecting current is in the range of 7.0-7.4 mA higher than the secondary electron emission current of 2.0-2.4 mA, which means that the spacecraft collects more electrons, resulting in a negative charging of the spacecraft. On the other hand, in the earlier section A.4.2 at the 0.044 AU with the thruster, the spacecraft potential is comparatively lower than at 0.11 AU and 0.162 because the thruster electron collected current of 39 mA is lower than the secondary electron emission current of 73 mA (as shown in the Figure A.6). Thus, the study suggests that when the thruster is on, the secondary electrons play a significant role in minimizing the spacecraft potential, since they help to carry away negative charge. From Figures A.5 it is evident that between 0.011 to 0.25 AU, without the thruster, the spacecraft potential (on the secondary axis) decreases non-monotonically and is more positive compared to when the thruster operates. A possible reason is due to the high secondary electron emission current (3.9 mA) compared to the thermal electron collection (2.1mA) which reduces the return of electrons on the spacecraft. Taken together with and without the thruster, the study confirms that the higher the secondary electron emission, the lower the spacecraft potential.

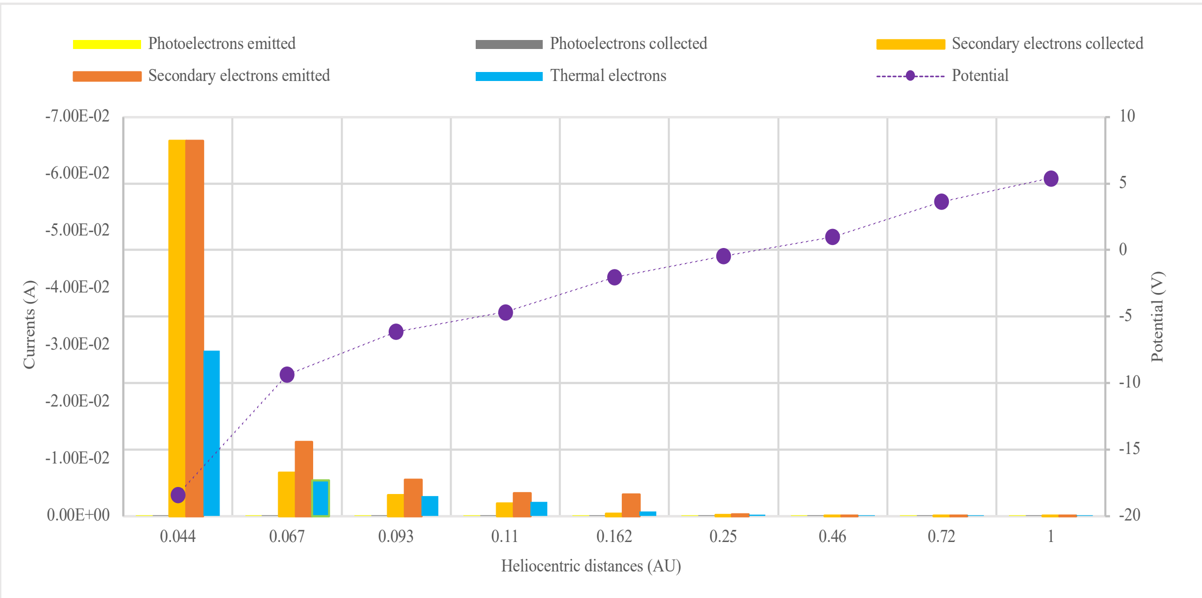

Figure A.5: Without the thruster collected and emitted currents versus heliocentric distances

A.4.4 With and Without thruster from 0.25 to 1 AU

Far away from the Sun, the charging effects are less critical. Considering the case far away from the Sun, this region is dominated by photoelectrons without the thruster due to their

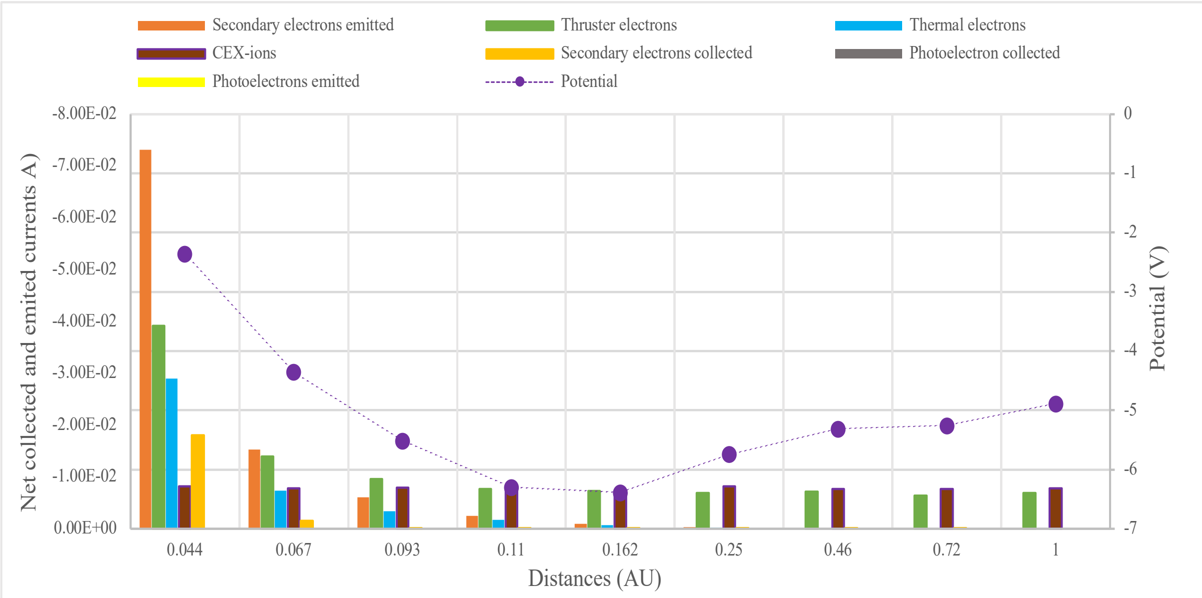

Figure A.6: With the thruster collected and emitted currents versus heliocentric distances

much higher density of $10^8\ \mathrm{m}^{-3}$ compared to other densities (ambient ions $10^7\ \mathrm{m}^{-3}$, thermal electron $10^7\ \mathrm{m}^{-3}$, secondary electron densities $10^7\ \mathrm{m}^{-3}$). The decreasing mean energy of thermal electrons reduces the secondary emission rate (Guillemant, 2014). Moreover, the ambient ions become a source of secondary electrons due to proton impact (SEEP) on the spacecraft surface and increase the secondary electron density nearby. As shown in Figure A.2, above 0.25 AU the spacecraft potential (without the thruster) is positive and decreases monotonically. The positive charging of the spacecraft can be explained by the fact that since the photoelectron Debye length is larger than the spacecraft size, the sheath does not have a potential barrier to restrict the escape of photoelectrons and secondaries. It can be seen in Figure A.4 that the ram and wake potentials are comparatively lower than in the cases of a near-Sun environment. Because there is no blocking from a potential barrier, the photoelectrons can easily escape the sheath, and we obtain a current balance with a positive spacecraft potential. The collected current of photoelectrons without the thruster is 0.045 mA, higher than the thermal and secondary electron currents of 0.014 mA and 0.0065 mA, respectively (as shown in Figure A.5). In contrast, below 0.3 AU, the collected thermal and secondary currents gradually start increasing faster than the photoelectron current, and we obtain the negative charge on the spacecraft. Thus, the study indicates the importance of secondary and photoelectron currents in both the far- and near-Sun environments without the thruster. Both are important currents that determine the final spacecraft's potential. Far away from the Sun, the positive charging is mainly due to the photoelectron current, while near-the-Sun environment the recollection of photoelectrons and secondaries is more important and leads to negative charging of the spacecraft.

Similar simulations were performed with the thruster far away from the Sun's environment. The CEX-ions and thruster electrons dominate the spacecraft and surrounding plasma. At 1 AU, it is visible from Figure A.2 and A.4 that the spacecraft potential charges to 5.37 V positive while with the thruster it turns to -4.89 V. Negative charging is due to the low-energy electrons emitted from the cathode being drawn back to the spacecraft because they follow the same path as CEX-ions. The higher speed of electrons (ve » vi) compared to ions with similar energy and density results in the accumulation of more electrons on the surface, thereby increasing the negative charge. Above 0.25 AU, no significant changes in the spacecraft potential are observed. A low and stable negative potential is observed from 1AU to 0.25 AU but negatively charged. This is due to the collected current of 0.078 mA of thruster electron being larger in this region and dominating other currents, and thus we obtain a negative charge of the spacecraft (as shown in Figure A.6). As mentioned earlier, the higher the collected current, the larger the negative charge since more electrons are accumulated. However, near the Sun environment from 0.093 AU to 0.044 AU, it is evident that the emitted current is higher than the collected current, which leads to spacecraft charging less negatively due to high secondary electron emission (for example at 0.044 AU, the spacecraft potential with the thruster is around -2.87 V).

A.4.5 Ram wake and side potential profiles

Figure A.7 shows the evolution of the potential in the ram direction, with and without the thruster and for different heliocentric distances, corresponding to profiles of Figure A.4 along the x-axis (directed towards the Sun). With the thruster on, from 0.044 AU to 1AU the ram potential structure always shows more negative potentials at the spacecraft than at large $|x|$ but develops a localized minimum in potential near x = 0.2 m interior to 0.16 AU (dotted lines) that can act as a potential barrier or a trap (depending on particle charge). A similar minimum in potential occurs inside 0.16 AU even when the thruster is off, although the potential is much more negative than when the thruster is on. For example, at 0.044 AU, the potential barrier changes from -21.8 to -4.32 V when the thruster is turned on, which reduces the recollection rate of secondaries back to the spacecraft.

Similarly, Figure A.8 shows the wake structure with and without the thruster. A stable positive potential of approximately +25 V is observed at the satellite when the thruster is on, with the potential increasing monotonically with decreasing helio distance, presumably due to constant ion beam current. On the other hand, the wake potentials are always

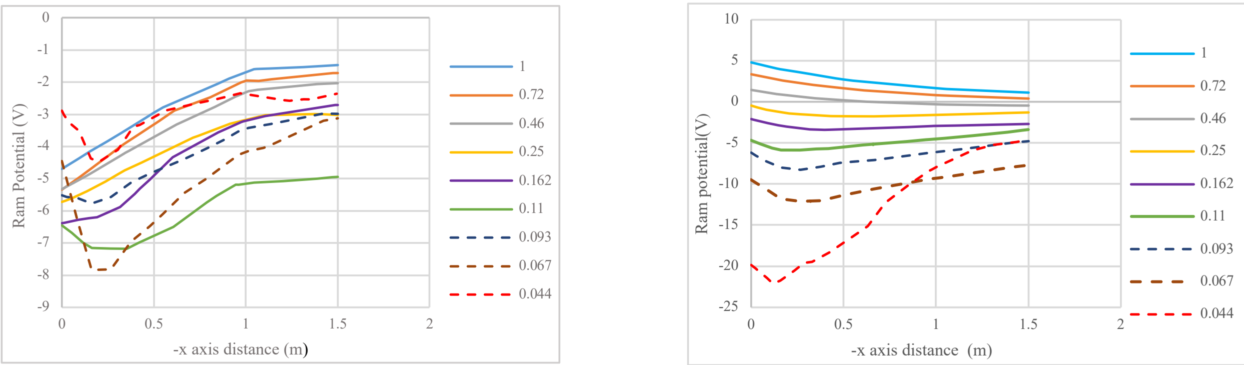

Figure A.7: The plot shows the potential profile along the ram direction (-x axis). The origin of the graph is at point D in Figure A.1. The left panel is with the thruster on, and the right panel is without the thruster

negative at heliocentric distances interior to 0.46 AU without the thruster. Moreover, interior to 0.16 AU the profile develops a localized minimum near x = 1 m with a magnitude that increases as the heliocentric distance decreases. For instance, at 0.044 AU this wake barrier reaches -34 V when the thruster is off, tending to force the recollection of a large fraction of secondary electrons emitted from the spacecraft.

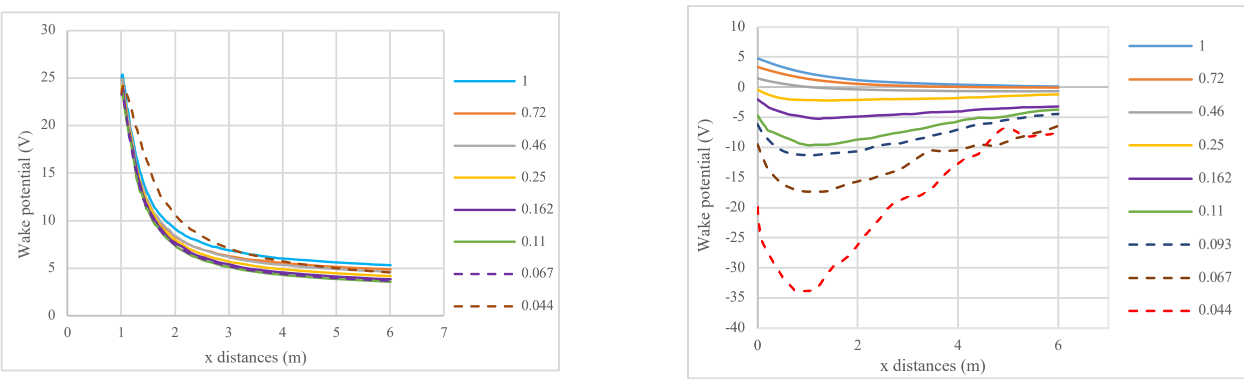

Figure A.8: The plot shows the potential profile along the wake direction (x-axis). The origin of the graph is at point C in Figure A.1. The left panel is with the thruster on, and the right panel is without the thruster

Figure A.9 shows the electrostatic sheath with and without the thruster in the z-direction. The reduction in the electrostatic sheath surrounding the spacecraft is reduced when the thruster is switched on. Thus, the study suggests that the backflow plume emitted from the thruster helps to reduce the size of the electrostatic sheath and potential barrier surrounding the spacecraft and minimizes the return of low-energy charged particles (secondaries or photoelectrons) at the surface, thereby causing minimal additional disturbance for low-energy plasma sensors and particle detectors. However, without the thruster, below 0.11 AU shows a large potential barrier that traps the electron and ions and forces recollection. A significant change in ram, wake potential, and larger spatial size of sheaths is observed.

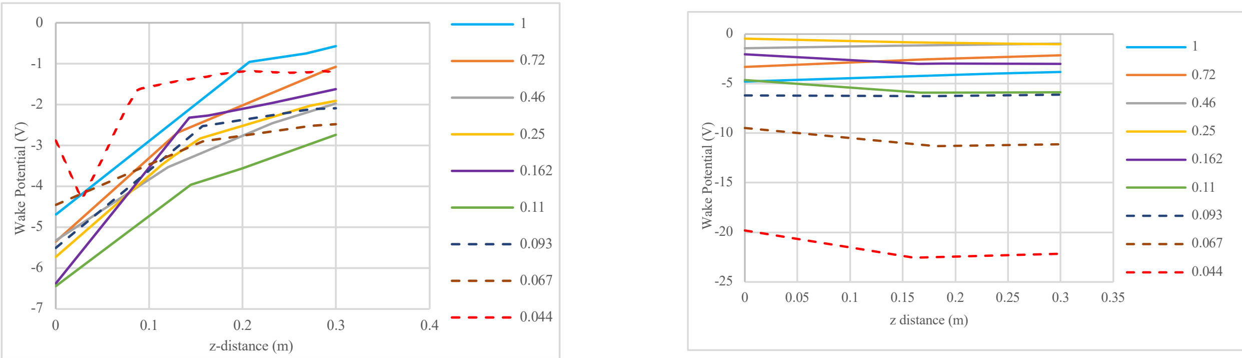

Figure A.9: The plot shows the potential profile along the sheath direction (z axis). The origin of the graph is in the z-direction from Figure A.1. The left panel is with the thruster on, and the right panel is without the thruster

A.4.6 Effects on spacecraft charging with and without the Secondary electrons

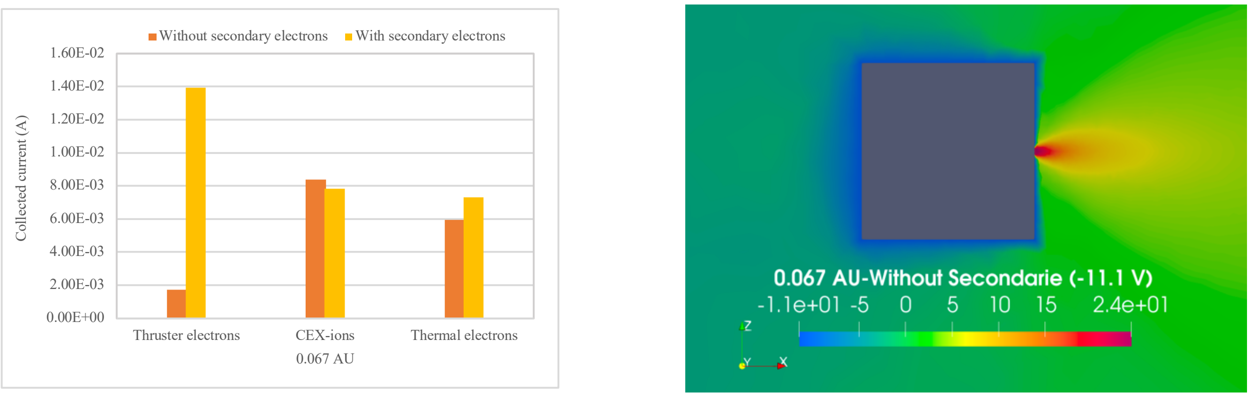

Figure A.10: Collected currents and spacecraft potential with and without secondaries at 0.067 AU when the thruster is on

Figures A.10 and A.11 demonstrate the influence of secondary electrons on potential near the Sun environment at 0.067 AU and far away from the Sun at 1 AU. The emission of secondary electrons during thruster operation depends on both ambient and thruster electrons, as shown next. Simulations were performed with and without the secondaries to observe the behaviour of the spacecraft. At 0.067 AU the final spacecraft potential without secondary electrons converges to -11.1 V instead of -4.25 V since the spacecraft is not emitting electrons anymore, as shown in Figure A.10. On the elimination of secondary electrons, the thruster electrons are greatly decreased while the collection of CEX-ions and thermal electrons remain constant. No potential barrier is observed and the spacecraft charges to a large negative potential. Thus, the near-Sun environment results show that secondary electron emission greatly influences the spacecraft and surrounding plasma potentials during thruster operation and that most secondaries are due to thruster electrons hitting the spacecraft.

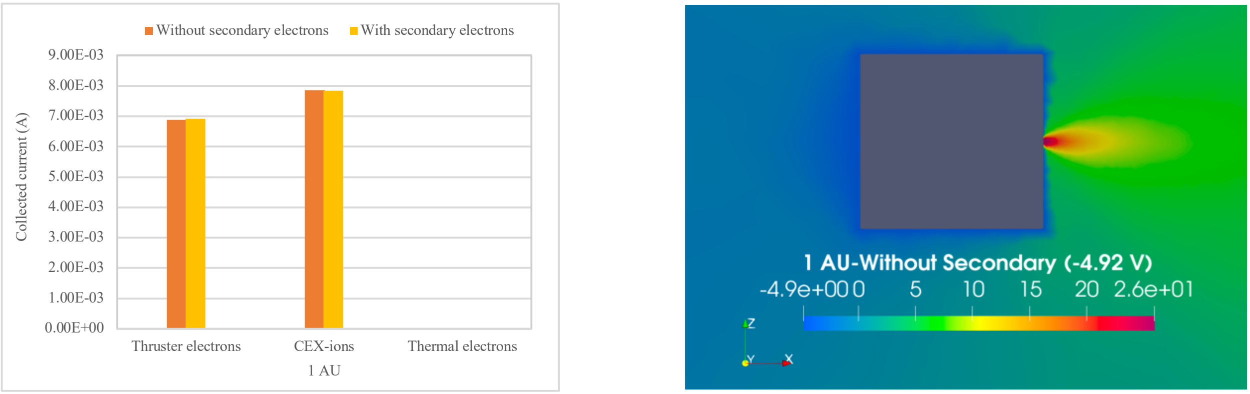

Figure A.11: Collected currents and spacecraft potential with and without secondaries at 1 AU when the thruster is on

In contrast, at 1AU, the spacecraft shows a negligible difference in surface potential with and without secondary electron emission. The spacecraft potential is -4.95V (without secondary electrons) instead of -4.85 V (with secondary electrons), as shown in Figure A.11. This is because the thermal electrons (from the ambient plasma) are dominated by the thruster electrons. The low mean energy of thermal electrons decreases the secondary electron emission rate, and thruster electrons dominate the spacecraft and the surrounding plasma. In Figure A.11, it is evident that the collected current of thermal electrons is much lower than the currents of thruster electrons and CEX-ions with and without secondaries. Hence, far away from the Sun, the secondary electrons have negligible influence on spacecraft potential. However, thruster electrons strongly influence this region, making the spacecraft charge negatively. Overall, the findings suggest that during the thruster operation an additional source of electrons (thruster electrons) helps to generate more secondary electrons, which then results in a smaller, more positive spacecraft potential. In such conditions despite high thermal electron density and temperature, the spacecraft charges to a lower negative potential due to the CEX-ions and associated thruster electrons emitted from the thruster. The electric thruster helps to provide a stabilizing effect by balancing the negative charge. However, there are still many unanswered questions about the thruster-induced secondary effects on low-energy plasma measurements, as they may interfere with and contaminate the measured data. Investigating the CEX-ions generated secondaries and their effects on spacecraft will be one area of future study to fully understand plume effects on spacecraft and instruments.

A.5 Conclusion

The simulations investigated the plasma thruster-induced charging effects and led to a better understanding of the electric thruster-spacecraft interactions for various plasma conditions from 0.044 AU to 1 AU. The study has shown variations in space charge and potential barriers with and without the thruster. The spacecraft potential tends to settle at a low negative potential (ranging from -2 V to -6V) during thruster operation due to the backflow plume originating from the ion plume of the SPT-100 Hall thruster, which brings CEX-ions and thruster electrons back to the spacecraft. Near the Sun, at 0.044 AU, the operation of the thruster leads to a significant drop by approximately 16 V in a spacecraft potential compared to the thruster being off, due to the plume ions and electrons dominating the ambient plasma and, to a lesser extent, to high secondary electron emission that helps to carry away negative charge. Without the thruster, the spacecraft charges to a large negative potential of -18.4 V, due to the interaction of the dominant ambient thermal electrons with photoelectrons and secondary electrons generating an electrostatic barrier that results in the recollection of photoelectrons and secondary electrons by the spacecraft. Outside 0.25 AU with the thruster on the spacecraft, the potential is essentially constant at -5 to -6V. In contrast, without the thruster on the potential, it decreases monotonically from a positive value of approximately +5V to a strongly negative value of approximately -19V near 0.044 AU, primarily due to the thermal electrons' increasing energy and number density.

Other important findings include: (1) When the thruster is on, the dominance of the CEX-ions and thruster electrons reduces and maintains a low negative spacecraft potential over the various heliocentric distances considered. (2) During thruster operation, the spatial size of the sheath and the potential barrier is significantly reduced and no longer restricts the escape of secondary electrons, reducing their recollection. Hence, the low rate of recollection of secondary electrons may have a negligible effect on spacecraft and their instruments, and so will enhance the accuracy of low-energy plasma measurements. (3) Near the Sun, the secondary electrons greatly influence the potential of the spacecraft, while they have negligible effects farther away from the Sun. For instance, on the elimination of secondary electrons, the spacecraft charges to a more negative potential around -11.1 V instead of -4.45V (with secondaries) at 0.067 AU. Hence, close to the Sun, the backflow plume at energies of several keV can stabilize the spacecraft to lower potential. Overall, these findings have significant implications for understanding how the operation of the thruster can help maintain and control spacecraft charging under various solar-wind conditions.

This new understanding should help to improve the preflight design assessment of electric thruster-induced charging and ensure the safety of the sensitive instruments onboard. Numerical simulations are a more complete way to get valuable insight into charging characteristics compared to ground testing. However, the study did not evaluate the impact of ion-induced plasma on the particle measurement instruments. Thus, a future study will assess the effects of the electric thruster plume on different instruments. Concerning further development, different types of thrusters and spacecraft geometry will be simulated.

Appendix B

Simulation Study of Hall Thruster and their Effects on the Spacecraft at 1 AU and 0.093 AU

(Note that this refereed conference paper does not account for variations in the solar photon flux with heliocentric distance, unlike Chapter 2. Consequently, the results differ from those in Chapter 2, where the photoelectric effects are accurately included and significantly affect the system when the thruster is off compared to when it is on)

Published as: Tejaswi Shinde, Iver Cairns, and Jason Held
IEPC 2022-324, https://www.electricrocket.org/IEPC_2022_Papers.html

B.1 Abstract

The article provides the first 3D PIC (Particle in Cell) simulations for Hall thruster-induced spacecraft charging at 1 AU and 0.093 AU using the Spacecraft Plasma Interaction System Software (SPIS). The baseline context is a cross-comparison of the spacecraft charging effects with and without SPT-100 Hall thruster effects, with the aim of providing 3D results for the total net charge and potential structure surrounding the spacecraft. In addition, the study investigates the effects of photoelectrons and secondary electrons on spacecraft charging during electric thruster operation. The simulated results highlight the importance of ion-induced charging impact on spacecraft, which lays a foundation for future improvement in pre-flight design modeling and space-charge reduction techniques.

B.2 Introduction

When in orbit, electric thrusters encounter different plasma environments, and a variety of spacecraft surface charging is expected. Variations in surface potential can pose a serious threat to plasma measurement instruments due to the reflection or acceleration of low-energetic charged particles (Na et al., 2019). Surface charging occurs mainly due to dynamic interactions between the spacecraft-plasma environment and thruster-generated plume exposed to the solar wind environment (Wang, 1997). The effects caused by electric thruster operations have long raised both science and technology concerns as the plume's backflow contaminates and interacts with spacecraft systems and results in ion-induced charging (Wang, 1997); (Goebel et al., 2023). Backflow plumes consist of low-velocity charge-exchange ions (CEX ions) generated from a collision between fast beam ions and propellant neutrals inside the main ion beam (Goebel et al., 2023). These ions flow back to the spacecraft and lead to two main effects. First, effluent deposition causes contamination of optical sensors, solar arrays, thermal control, and other communication instruments (Wang, 1997). Second, the ions will modify the properties of solar wind flowing around the spacecraft by inducing an additional current that can influence the observations of the plasma instrument (Wang, 1997). Thus, for longer-duration missions, the effects of an ion thruster on the payload system must undergo a careful assessment before the flight to avoid spacecraft operational anomalies and failures.

Recent studies on electric propulsion-spacecraft interactions were presented by authors such as (Roussel et al., 2008; Lee et al., 2011; Tajmar, 2002; Filleul et al., 2021 and Mier-Hicks et al., 2017) who modeled the effects of ion plumes on the spacecraft. All of these studies found that the charge-exchange ions emitted by an electric thruster play a fundamental role in varying the spacecraft's potential with respect to the local environment. However, these studies neglected the effects of photoelectrons and secondary electrons and the effects on the spacecraft potential of ion thruster operation. Photoelectron currents play an important role in neutralizing the spacecraft's potential since the continuous interaction of solar radiation with the spacecraft's surface makes the potential more positive due to the removal of electrons from the surface.

Similarly, the emission of ions from the electric thruster, as well as the return of some CEX-ions, contribute to lowering or increasing the spacecraft potential since the ions correspond to positive currents either leaving or reaching the spacecraft, respectively. Such effects can be particularly important when the spacecraft charges negatively near geosynchronous orbit (the GEO region) (Lee et al., 2011). There has been no study concerning the interaction of photoelectrons and CEX-ions and their combined effects on spacecraft potential. Therefore, in this paper study of the spacecraft-ion plume-solar wind interaction phenomenon will be performed using the Spacecraft Plasma Interaction Software (SPIS) in the presence of ambient plasma, photoelectrons, and secondary electrons. To do so, the SPT-100 Hall thruster is modeled using SPIS software to understand the behavior of spacecraft on changing solar wind parameters at 1AU, while keeping the same geometry model. Section II presents the SPIS modeling setup, which includes environment parameters, spacecraft dimensions, and covering material. Section III presents simulation results for two main cases 1) without the thruster for 1 AU and 0.093 AU and 2) with the SPT-100 Hall thruster at 1 AU and 0.093 AU.

B.3 Simulation setup

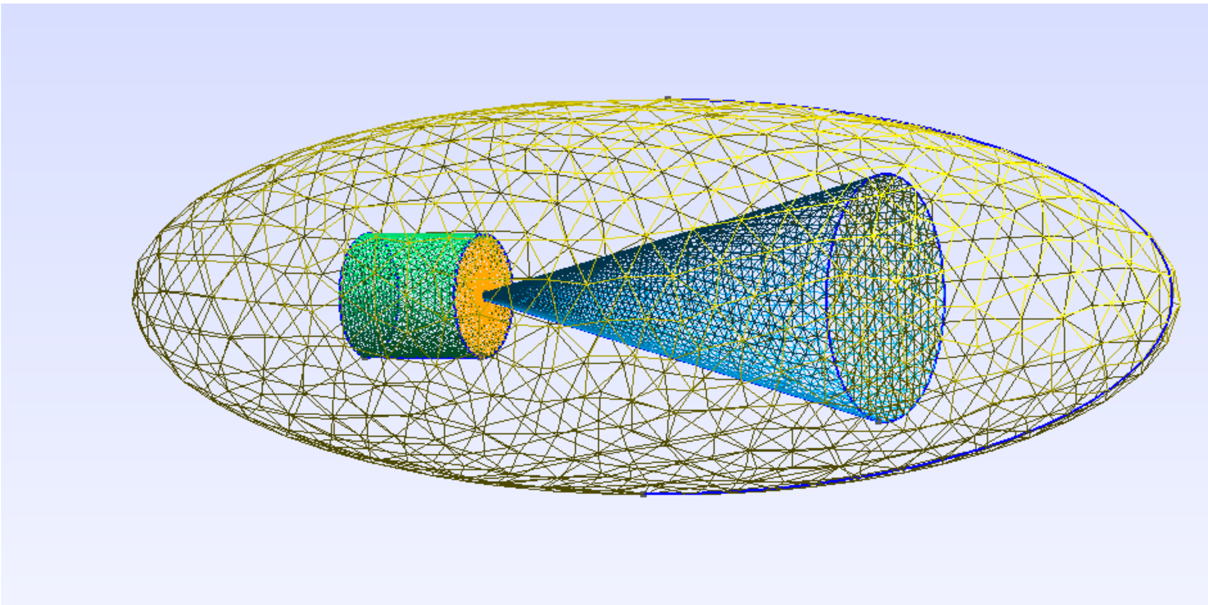

Figure B.1: GMSH model of the simple cylindrical spacecraft and meshing grid (green and yellow) used in the SPIS simulation. The void boundary is the simulation box. The blue conical shape shows the ion plume

The spacecraft geometry used for all simulations is a cylindrical geometry (1m radius and 2m length) covered with indium tin oxide material (ITO). The domain dimension varies with Debye length (3 x Debye length) and so do the mesh refinements. The domain meshing resolutions for all the simulations are maintained at less than one-third of the Debye length and the number of tetrahedrons ranges from 50,000 to 100,000. Figure 1 shows the GMSH model for the satellite. The physical environment parameters corresponding to heliocentric distances are taken from Guillemant (2014). The varying parameters in the simulations are plasma properties such as densities, temperatures, solar wind velocity, solar flux, and timesteps for each population (ions, thermal electrons, secondary electrons, and photoelectrons). Moreover, the satellite is assumed to be static with respect to the solar wind so only ion drift velocity is simulated only along the x-axis. All species (protons, thermal electrons, photoelectrons, and secondary electrons) are computed using a PIC model for a spacecraft integrated with the SPT-100 Hall thruster. The SPIS Hall

Table B.1: Gmsh Geometry Dimensions and Thruster Specifications.

Parameters	**Value**
Geometry	1m radius, 2m long, cylinder
Surface Material	Indium Tin Oxide
Photoelectron temperature	3eV
Thruster Electron Temperature	0.5-0.8eV
Ambient Ion type	H+
Ion modelling	PIC
Electron modelling	PIC
Magnetic Field	Not considered
Thruster Specification	
Ion Thruster	SPT-100 Hall
Thrust	0.035 N
Specific Impulse	1840s
Cathode Temperature	5 eV
Mass Flow rate (Xe)	1.91×10^{-6} Kg/s
Current	1.43 A
Power	723 W

thruster model uses the Monte-Carlo method to simulate the CEX-ion collisions and various other species (Xe neutral, Xe+, Xe++) in the computational regions. The SPT-100 thruster specifications are described in Table B.1. During simulations, the thrusters are assumed to be electrically connected to the spacecraft chassis and the spacecraft floats with the local plasma potential (the anode and cathode of the thruster are isolated from the spacecraft) (Liu et al., 2013; Tajmar and Wang, 2000). A resistor is added between the thruster and spacecraft to provide a return path for this leakage. The resistor provides a high degree of isolation between the thruster and the spacecraft, thus preventing excessive charging. The ground of the spacecraft is different from the ground of the electric thrusters. The primary reason for operating in this manner is to reduce the spacecraft contamination caused by thruster plumes (Liu et al., 2013). However, in the future, other electrical configurations will be explored to understand their impact on the spacecraft's potential during thruster operation.

B.4 Simulation results

The simulation results display the densities and final spacecraft potential with and without the thruster. The photoelectron temperatures are kept constant while the secondary electron temperature and ion drift velocity are varied with distance to the Sun (Guillemant, 2014). The Sun's incoming solar wind is directed from the left direction in all Figures. The capacitance is evaluated by the trial-and-error method to obtain convergence using 1×10^{-5} F and 1×10^{-6} F for 1 AU and 0.093 AU, respectively. The expected capacitance 1e-11 F obtained using equation 2 from Reference Guillemant (2014) did not lead to convergence of the simulation, leading to the use of the trial-and-error method to obtain the convergence. To solve the equivalent electric circuit of the SPIS software the resistance between the thruster and spacecraft is maintained at 500,000 ohms.

B.4.1 Without the SPT-100 Hall thruster

This section presents and discusses the PIC results for the 3D distribution of the electric potential and particle densities in the absence of the thruster for 1 AU and 0.093 AU plasma conditions. Figures B.2 and B.4 show density maps for each plasma particle while Figures B.3 and B.5 show the variation in spacecraft potential with photoelectrons, without photoelectrons, and secondary electrons.

B.4.1.1 S1 Simulation: Far away from the Sun At 1AU

Far away from the Sun, space charging effects are less critical due to high photoelectron density. As illustrated in Figure B.2, it is apparent that the space environment in this region is highly dominated by photoelectrons with a density of $10^8\,\mathrm{m}^{-3}$ due to its considerably lower thermal electron temperature and density. The decreasing mean energy of thermal electrons reduces the secondary emission rate (Guillemant, 2014). Moreover, the ambient ions become a source of secondary electrons due to proton impact (SEEP) on the spacecraft surface and increase the secondary electron density in the region. Thus, the balance of these currents determines the spacecraft potential, which then very much depends on secondary and photoelectron emission currents (Guillemant, 2014; Grard et al., 1983; Muranaka et al., 2012; Ergun et al., 2010). The positive charging of the spacecraft of approximately 5.37 V in Figure B.3.a can be explained by the fact that since the photoelectron Debye length is larger than the spacecraft size, it tends to have a thick sheath (potential barrier farther from the emitting surface which no more restricts the escape of photoelectrons from a 3D sheath) (Guillemant et al., 2012). Overall, a spacecraft with a conductive surface can be positively charged due to the following reasons (Ergun et al., 2010): 1) The photoelectron electron emission is greater than the thermal electron current over the total area. 2) The photoelectron Debye length is larger than the spacecraft size $\lambda_{ph} >> R_{sc}$. 3) The thermal electron energy is smaller than the characteristic energy of the escaping photoelectron. 4) The photoelectron number density at the spacecraft surface greatly exceeds the ambient electron number density, allowing the photoelectron plasma to dominate the ambient plasma surrounding the spacecraft (Ergun et al., 2010).

From Figure B.3.a it is evident that photoemission is important to avoid negative charging of the spacecraft. The results show a significant transition from a spacecraft's potential of +5.37 V to -16.5 V when photoemission is turned off (Figures B.3.b). A possible reason is that photoemission helps to reduce an electron sheath surrounding the spacecraft, which results in reducing the ambient electrons surrounding the spacecraft and making it charge less negatively. A similar finding is reported by Muranaka et al. (2012) showing that photoelectrons reduce the electron sheath surrounding the spacecraft which results in more positive potential (Muranaka et al., 2012). Another interesting result is that on eliminating secondary electrons (but with photoelectrons) the spacecraft tends to charge to a negative potential around -7.43 V (Figure B.3.c). Thus at 1 AU secondary emission and photoemission have a great influence on spacecraft and surrounding plasma potential.

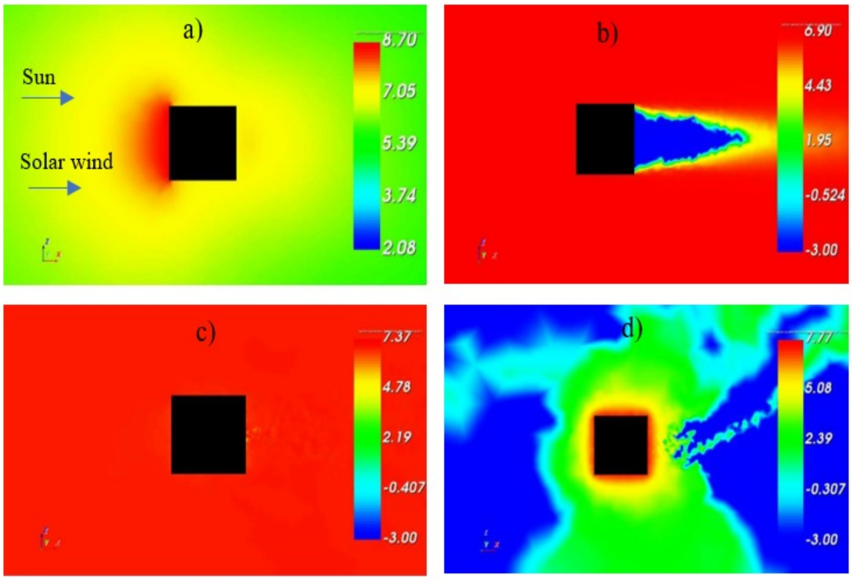

Figure B.2: Population density logarithmic maps without the thruster for 1AU a) photoelectrons, b) H+ ion density, c) ambient electron density, d) secondary electrons density

B.4.1.2 S2 Simulation: Near-Sun environment at 0.093 AU

When spacecraft orbits close to the Sun the space charging effects become more critical due to the hot and dense ambient environment, which leads to higher secondary emission rates from the surfaces exposed to the plasma. Figure B.4 shows that close to the Sun, thermal electron number densities of 10^9 m^{-3} dominate near the surface despite the high

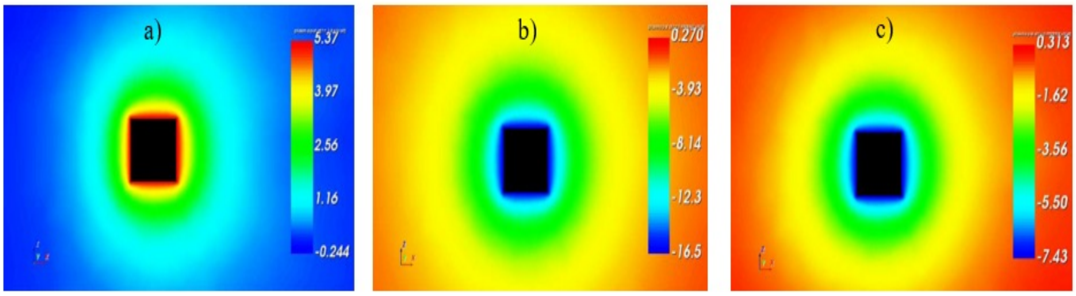

Figure B.3: Maps of the plasma potential for the 1 AU case without the thruster: a) with photoelectrons, b) without photoelectrons, c) without secondary electrons.pa

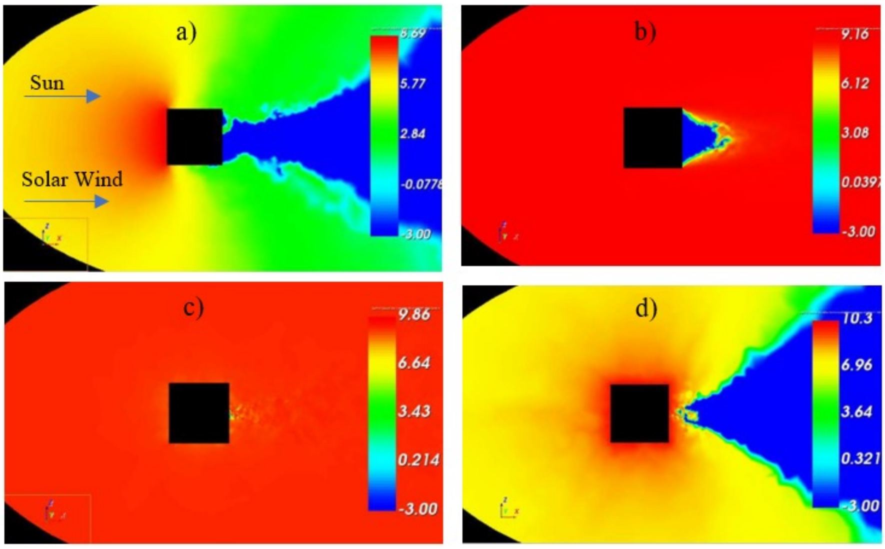

Figure B.4: Population density logarithmic maps without the thruster for 0.093 AU a) photoelectrons, b) H+ ion density, c) ambient electron density, d) secondary electrons density

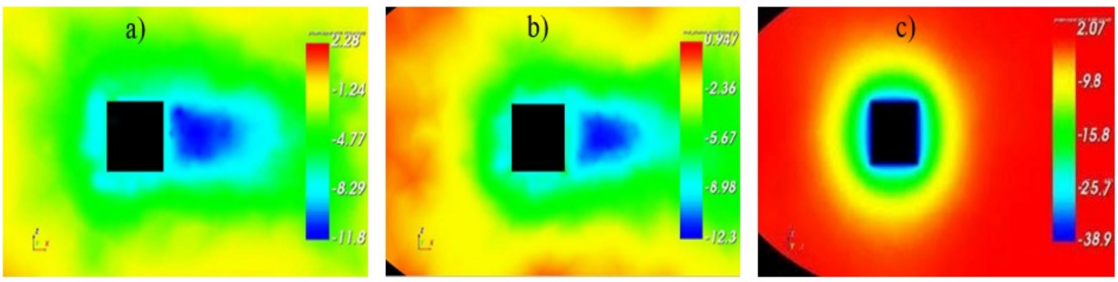

Figure B.5: Maps of the plasma potential at 0.093 AU case without the thruster: a) with photoelectron (-7.29 V), b) without photoelectron (-7.98), c) without secondary electrons (-38.9 V) photoelectron number density of 10^8 m^{-3}. This result may seem contradictory when considering photoemission, but it can be explained by the fact that the Debye length of the photoelectron is smaller than the spacecraft, which moves the local potential barrier close to the surface and the space charge may be considered as a 1D thin sheath (Guillemant, 2014). In this case, the photoelectrons and secondary electrons emitted with low energies (2-3 eV) surround the spacecraft and cannot escape since they have insufficient kinetic energy to overcome the potential barrier developed by the high-density thermal electrons. Hence photoelectrons and secondary electrons return to the spacecraft's surface which results in a reducing the spacecraft's potential (Guillemant, 2014). Figure B.5.a shows the final surface potential to be -7.29 V with photoemission which charges more positively than without photoelectrons (-7.98 V). Similarly, on the elimination of secondary electron emission (but with photoemission), the spacecraft charges to a large negative potential of -38.9 V as the spacecraft emits zero electrons (Guillemant, 2014). Thus, secondary electrons are very important as they help to carry away the negative charge and make spacecraft potential more positive (Lai, 1989). The sudden rise in negative potential might be due to zero electron emission that allows the accumulation of more and more electrons on the spacecraft's surface. Thus, the study confirms that the recollection of photoelectrons and secondary electrons is very efficient at 0.093 AU and helps to lower the floating potential, even when the structure is charged negatively. Similar results were found in the near-Sun environment by Ergun et al. (2010) and Guillemant (2014) demonstrating that 85-95 per cent of photoelectrons and more than 80 per cent of the secondary electron returned to the surface to maintain a negative floating potential (Ergun et al., 2010) and (Guillemant, 2014). Note that the difference in potential in our simulation compared to Guillemant's result is believed due to different meshing and boundary conditions.

In the near-Sun environment, despite the presence of photoelectrons, a spacecraft charges negatively due to the flowing reasons (Ergun et al., 2010): 1) The thermal electron currents are greater than the other electron current over the total area 2) The photoelectron Debye length is smaller than spacecraft size, which can be referred to as the thin sheath limit $\lambda_{ph} << R_{sc}$ 3) The thermal electron temperature is higher than the characteristic energy of escaping photoelectron.

B.4.2 With the SPT-100 Hall thruster

B.4.2.1 S3 Simulation: Far away from the Sun at 1 AU

2D maps of the plasma potential and population densities are presented in Figure B.6 and B.7, respectively. The final potential of the spacecraft integrated with the operating SPT-100 Hall thruster reaches -4.84 V (as shown in Figure B.7.a), different from the potential of

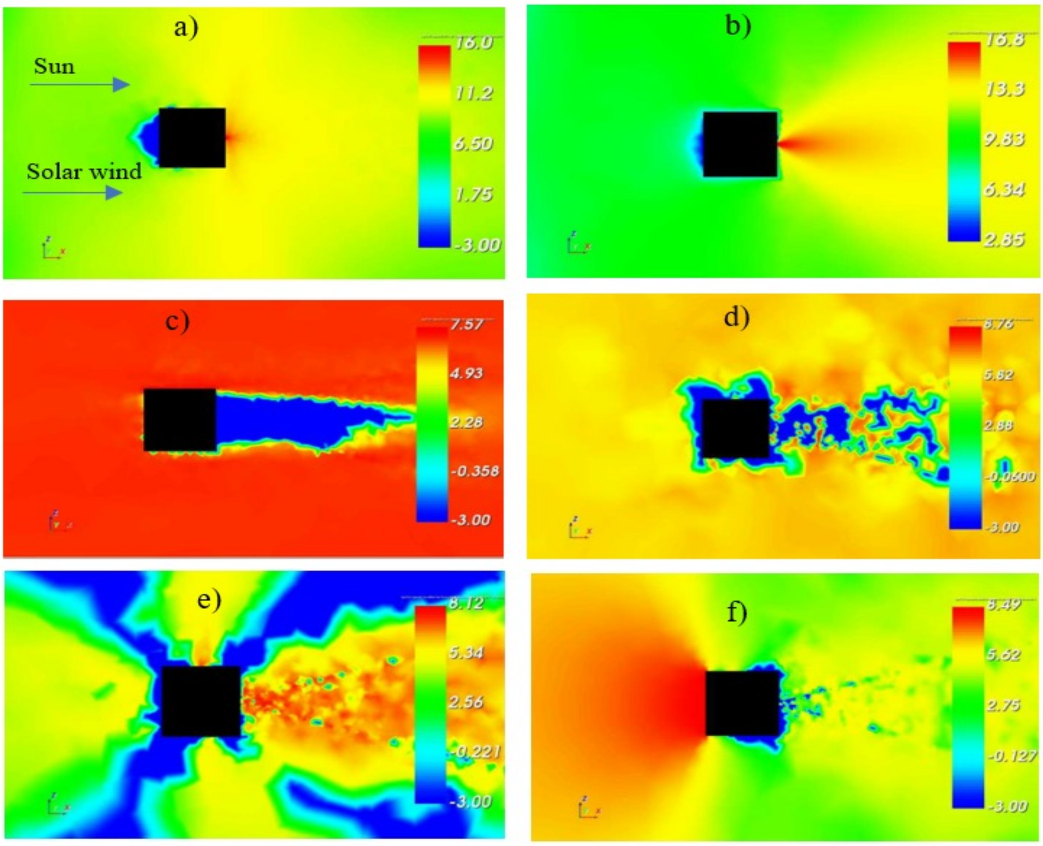

Figure B.6: Population density logarithmic maps with the thruster for 1AU: a) CEX-ion, b) thruster electrons, c) ambient ions H+, d) thermal electrons, e) secondary electrons, f) photoelectrons

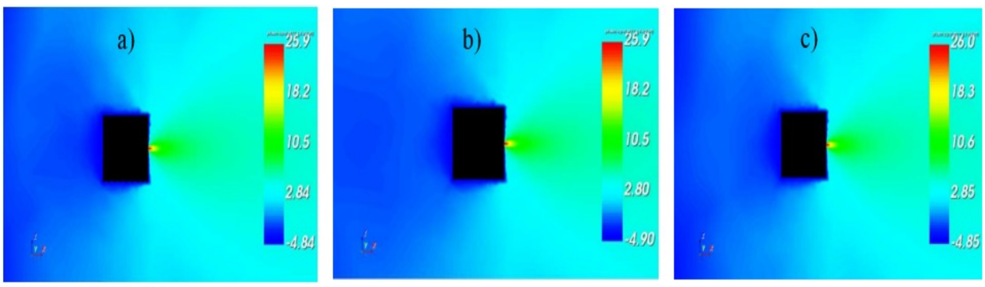

Figure B.7: Maps of the plasma potential at 1 AU case with the thrusters operating: a) with photoelectron (-4.84 V), b) without photoelectron (-4.90 V), c) without secondary electrons (-4.85 V)

+5.37 without the thruster operating (as shown in Figure B.3.a). The CEX-ions will reach every corner of the spacecraft as expected due to their low kinetic energy that gets radially deflected from the main ion beam of the thruster. The CEX-ion density of $10^{11}\,\mathrm{m}^{-3}$ and thruster electrons of $10^{10}\,\mathrm{m}^{-3}$ tends to dominate the surface more than any other densities ($10^{7}\,\mathrm{m}^{-3}$ ions, $10^{8}\,\mathrm{m}^{-3}$ electrons, $10^{8}\,\mathrm{m}^{-3}$ photoelectrons, and $10^{8}\,\mathrm{m}^{-3}$ secondary electrons). A possible explanation for the negative charging of the spacecraft might be due to the potential barriers developed by a high density of CEX-ions that control the surrounding plasma and dominate the collected particles. The low-energy electrons emitted from the neutralizer are drawn back to the spacecraft following the same path as CEX-ions. The larger speed of electrons (ve » vi) compared to ions for similar energy and density results in the accumulation of more electrons on the surface, thereby increasing the negative charge. Hence, we can infer that at 1 AU the positively charged spacecraft can shift to a negative potential on thruster operation because of the accumulation of negative charge by the thruster electrons. Moreover, the photoelectrons and secondary electrons have a negligible effect on lowering the negative potential spacecraft, since their densities are relatively small compared to the thruster electrons (as shown in Figure B.6). There are still many unanswered questions about the generation of the secondary electrons by CEX-ions and thruster electrons and their effects on the spacecraft's potential. If the ion-induced secondary electron density is comparable with the thruster electron density, then the secondaries might help to carry away the negative charge and make the spacecraft positive Lai, 1989. However, the CEX-ions and thruster electrons have low energies so they may not have sufficient energy to produce the secondaries. Thus further investigation is required to understand the ion-induced generated secondary effect on spacecraft charging.

Figure B.7 shows that during thruster operation, the photoelectrons are not that efficient in changing the negative potential of the spacecraft when the photoemission is zero (Figure B.7.b). Similarly, without secondary electron emission, the spacecraft shows a negligible difference in surface potential of -4.85 V (Figure B.7.c). This is due to photoelectrons and secondary electrons (generated by ambient plasma) being relatively small compared to the thruster electrons so the thruster electron current dominates the charging. On the other hand, without the thruster in the earlier S1 case (as shown in Figure B.3.b and B.3.c), the spacecraft charges to -16.5 V and -7.43V on eliminating photoelectrons and secondary electrons, respectively. Thus, the study suggests that far away from the Sun, solar wind effects can be neglected when the thruster is operating as they do not contribute significantly to charging the spacecraft more positively.

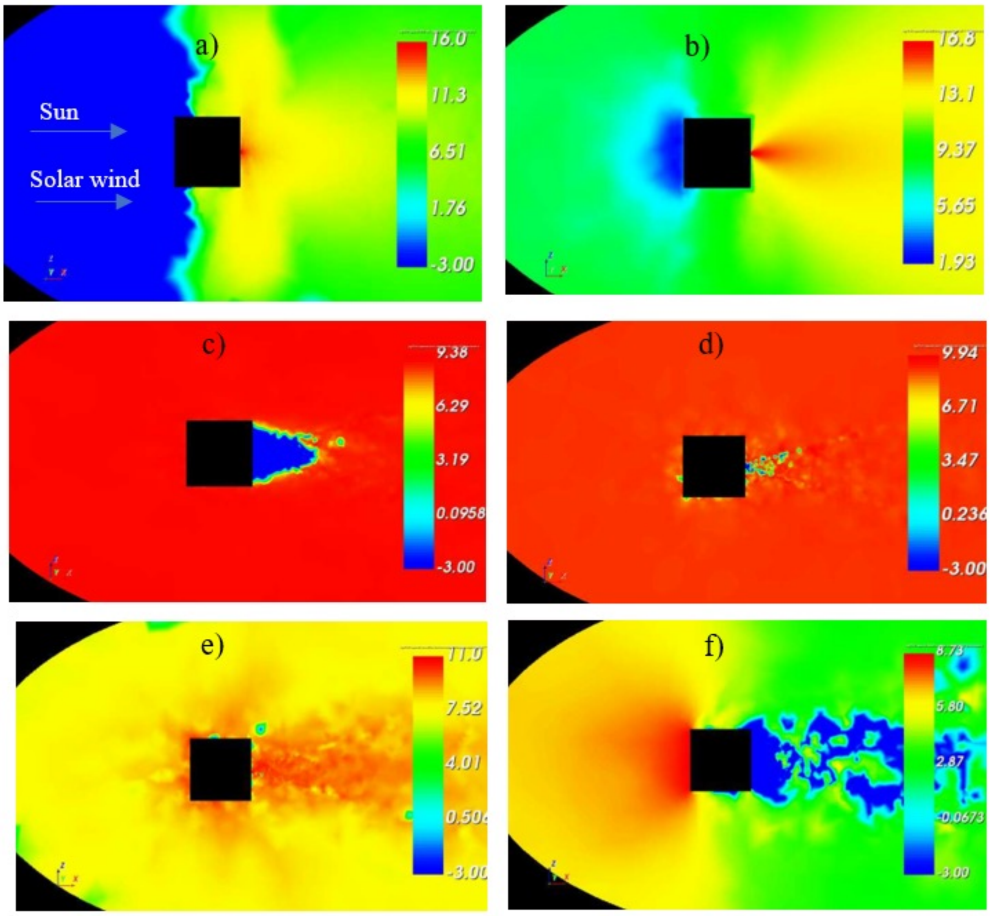

Figure B.8: Population density logarithmic maps with the thruster for 0.093 AU: a) CEX-ion, b) thruster electrons, c) ambient ions H+, d) thermal electrons, e) secondary electrons, f) photoelectrons

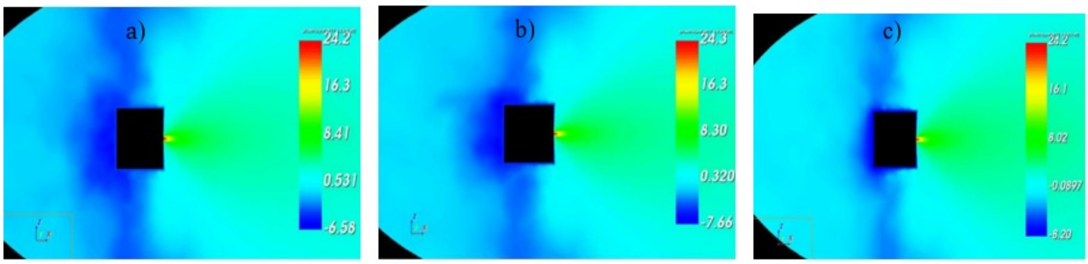

Figure B.9: Population density logarithmic maps with the thruster for 0.093 AU: a) CEX-ion, b) thruster electrons, c) ambient ions H+, d) thermal electrons, e) secondary electrons, f) photoelectrons

B.4.2.2 S4: Near-Sun environment at 0.093 AU

In this section, we present and discuss the simulation results of the spacecraft integrated with the SPT-100 Hall thruster at 0.093 AU. Number density and plasma potential maps are shown in Figures B.8 and B.9, respectively. Solar wind and sunlight incident are from the left along the x direction. In distinction to the S2 case at 0.093 AU, it is found that without the thruster the spacecraft charges to a negative potential of -8.29 V (As shown in Figure B.5.a) due to the high thermal electron density and temperature that tends to dominate the surface charging. Interestingly, in the S4 case, on the operation of the thruster, the spacecraft shows a slight reduction in surface potential by approximately 2V. The spacecraft potential at 0.093 AU with SPT-100 Hall to -6.58 V, is more positive than without the thruster at 0.093 AU (as shwon in Figure B.9.a). A possible explanation for the reduction in the surface potential at 0.093 AU is essentially the same as for the 1 AU case when the thruster is on. The CEX- ions and thruster electrons dominate the surface and surrounding plasma since their number densities are so much larger, 10^{11} m^{-3} and 10^{10} m^{-3}, respectively (as shown in Figure B.8). So, therefore, the same model works as at 1 AU (with the thruster S3 case): The CEX-ions reach every corner of the spacecraft and the associated thruster electrons try to neutralize their charge and follow the same path. Since the thermal velocity of electrons is larger for the same energy and densities compared with the ions (ve » vi), the surface accumulates a larger negative charging current than the CEX-ions, so the satellite charges up negatively. However, in this case, the reduction in potential is mainly due to the photoelectrons and secondary electrons (generated by plasma) which are denser and more effective at 0.093 AU than at 1 AU but, again, make small, more positive, changes to the satellite potential. Thus, the study suggests that the negative charging of the spacecraft at 0.093 AU with the thruster is mainly due to CEX-ions and thruster electrons that dominate the region while photoelectrons and secondary electrons may be mildly effective in discharging a negatively charged spacecraft.

Figure B.9.b shows that surface potential becomes more negative in the absence of photoelectrons and secondary electrons (by 1V). Thus photoelectrons and secondary electrons are more important at 0.093 AU than at 1AU in reversing the negative charging, as explained earlier in the S2 case. Note that these results may differ with changes in the covering material, the geometry of the spacecraft exposed to the environment, as well as changes in the plasma and radiation environment. In this paper, we observed that changes in plasma conditions at different distances from the Sun change the surface potential. Future work will be performed to see the changes in spacecraft behaviour on changing the geometry, covering material, and propellants.

B.5 Conclusion

Far away and near the Sun environmental effects of ion-induced charging are investigated using the SPIS software. These preliminary results show variations in spacecraft potential near 1 AU and 0.093 AU with and without a Hall thruster in the presence of solar wind plasma, photoelectron, and secondary electron effects. Near 1 AU with the SPT-100 Hall thruster, the spacecraft potential charges to a negative potential (-4.84 V) due to a high density of CEX-ions and thruster electrons. Since the thermal velocity of electrons is higher than for the CEX-ions the surface accumulates more electrons from the electric thruster's neutralizer. Hence far away from the Sun at 1AU, the solar wind effects are negligible and do not contribute to discharging the negative potential when the thruster is on. Similarly, close to the Sun (0.093 AU), with the SPT-100 Hall thruster, the spacecraft charges to a negative potential of -6.54 V, more positive than without the thruster at 0.093 AU (S2 case). Photoelectrons and secondaries are mildly important in reducing the excess negative charge. Thus close to the Sun, solar wind effects have a greater influence on reducing the negative potential. Taken together, the results of the SPT-100 Hall thruster model simulations using the SPIS software suggest that the CEX-ions and thruster electrons dominate the satellite's plasma environment and charge at both 1 AU and 0.093 AU, leading to negative spacecraft potentials due to the higher thruster electron charging rates. The photoelectron and secondary electron effects are larger at 0.093 AU than at 1AU and so lead to more positive spacecraft potentials. Overall, this research lays the groundwork for finding techniques to reduce negative charging caused by thruster plume backflow currents. The thruster plume-generated CEX-ions and thruster electrons have the potential to contaminate and affect the result of certain in-situ measurements when operating. Although the geometry model used in this paper did not consider instruments or solar arrays, future studies could assess the combined effects on the CEX-ions and the solar wind to fully understand their impacts. There are other considerations worthy of investigation, including determining the effects of different spacecraft covering material, Sun-thruster orientation, and operation in the fast solar wind. Three controlling parameters that require further investigation include 1) Variation in the CEX-ion temperature 2) Secondary electrons generated by CEX-ion temperature, and 3) Secondary electrons generated by thruster electrons impact.

APPENDIX C

Variation in Spacecraft Potential with Different Sizes and Geometries

The aim is to understand how spacecraft potential depends on spacecraft size and geometry at distances of 1 AU and 0.044 AU from the Sun. As observed in Chapter 5, the spacecraft potential at distances from 0.044 AU to 1 AU ranged from +14.2 V to -16 V, differing from the potentials in Chapters 2 and 3, which ranged from +9.2 V to -28 V under the same conditions. The differences are shown here to mainly be due to the use of different geometries, different sizes relative to the ambient electron Debye length, the addition of a solar panel, and the use of dielectric material. This Appendix explores these effects in detail: first, the dimensions of cylindrical and cubical spacecraft are varied from 30 cm to 8 m to see how the spacecraft potential changes; second, the effects of various geometries, including a simple cylinder, a cubical spacecraft, and a cubical spacecraft with solar panels, on spacecraft potential at 1 AU and 0.044 AU are examined. In this second case, simple cylindrical and cubic spacecraft are coated with ITO material and have the same dimensions: 1 m in radius and 1 m in length for the cylinders, and 1 m x 1 m x 1 m for the cubical spacecraft. The SPIS software is used for the simulations.

C.1 Different spacecraft sizes and potential variation

Figure C.1 shows the relationship between the spacecraft potential and the spacecraft size for cylindrical and cubic geometries at 1 AU from the Sun. The x-axis represents the spacecraft size in meters, while the y-axis shows the spacecraft potential in volts.

The results are as follows.

- For spacecraft sizes smaller than one-eighth of the ambient electron Debye length (8 meters), that is, less than about 1 m, the potential remains closely constant (within 10%) at around 9.5 V for both cylindrical and cubical geometries.

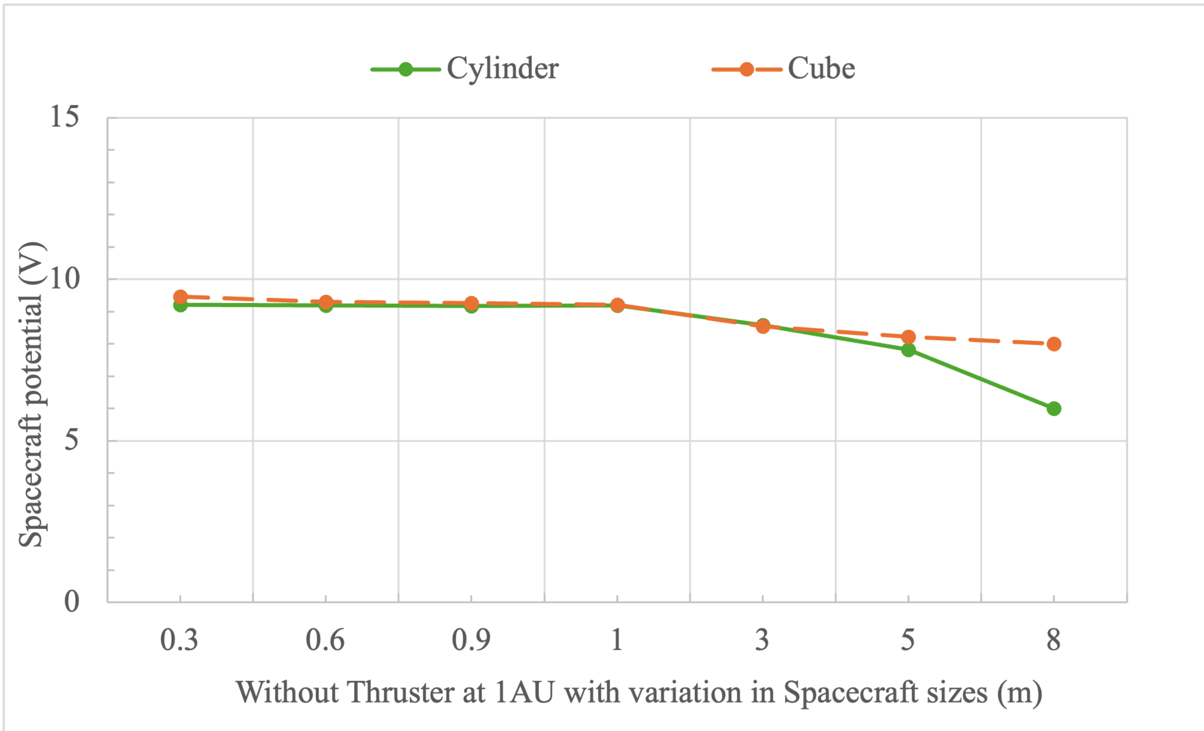

Figure C.1: Spacecraft potential variation with size and geometry at 1 AU without thruster

- This is because when the spacecraft size is much smaller than the Debye length, the electric field generated by the spacecraft does not significantly disturb the surrounding plasma. The potential distribution remains relatively uniform, and thus the spacecraft potential does not vary significantly with size.
- As the spacecraft size increases further, somewhere between about 1/8th and 1/3rd of the Debye length, the potential starts to decrease approximately linearly with increasing size. When the spacecraft size becomes comparable to or larger than the Debye length, the spacecraft's electric field can significantly perturb the surrounding plasma. The perturbation affects the spacecraft's potential more noticeably, leading to variations.
- Both cylindrical and cubical spacecraft exhibit similar trends, but there is a slight difference in potential values, especially as the size increases beyond the Debye length (e.g., a 10% versus a 30% reduction for the cubic and cylindrical geometries, respectively). This difference is possibly due to the geometric effects on how the spacecraft interacts with the plasma and its exposure to the sunlight. For a cylindrical spacecraft facing the Sun, the rounded surface allows for a more uniform distribution of plasma particles, leading to a smoother charge accumulation. However, the edges

at the ends of the cylinder can create regions of higher electric field strength, enhancing localized charge accumulation. In contrast, a cubical spacecraft, with its flat surfaces and sharp edges, experiences more pronounced variations in charge accumulation and potential distribution. The flat surfaces directly facing the Sun collect more plasma particles, while the sharp edges can act as points for intensified electric fields, resulting in higher localized charge buildup. Thus, the differences in the geometric shapes of cylindrical and cubical spacecraft significantly influence their interactions with the plasma, affecting charge and potential distribution.

- For spacecraft sizes equivalent to or greater than the Debye length (such as at 0.044 AU, where the Debye length is 0.8 meters), the spacecraft potential varies significantly, as shown in Figure C.1. When the spacecraft size is comparable to the Debye length, the electric field around the spacecraft is not fully screened by the plasma, leading to more pronounced variations in potential. At 0.044 AU, a cylindrical spacecraft with a size of 1-meter charges to -28 V, whereas a cubical spacecraft charges to -12 V. A detailed discussion of this phenomenon is presented in the next section.

C.2 Different spacecraft geometry at 1AU and 0.044 AU

Figure C.2 compares 2D maps of the spatial distribution of the potential about and on a spacecraft for two geometries: a cylinder with a 1-meter radius and 1-meter length, and a cube with dimensions of 1 meter in length, width, and height. Both geometries are coated with the same material, Indium Tin Oxide, and are evaluated at two different distances from the Sun: 1 AU and 0.044 AU.

Figure C.2 shows the potential structure about these two spacecraft geometries at these two distances to be inherently 2D, rotationally symmetric, and qualitatively identical. In the case of the cylindrical and cubical spacecraft, the ram direction aligns with the negative x-axis, while the wake direction aligns with the positive x-axis. At 1 AU, both geometries exhibit a minimum ram and wake potential of 10 V, distributed uniformly around the spacecraft. However, as proximity to the Sun increases at 0.044 AU, a localized minimum develops, acting as a potential barrier or trap depending on the particle charge. For the cylindrical spacecraft, a ram barrier of approximately -35 V is observed, with the wake barrier reaching approximately -40 V, as depicted in Figure C.2. Conversely, for the cubical spacecraft, the potential barriers are significantly reduced compared to cylindrical counterparts, with ram and wake barriers ranging from -12 V to -14 V. A detailed study on

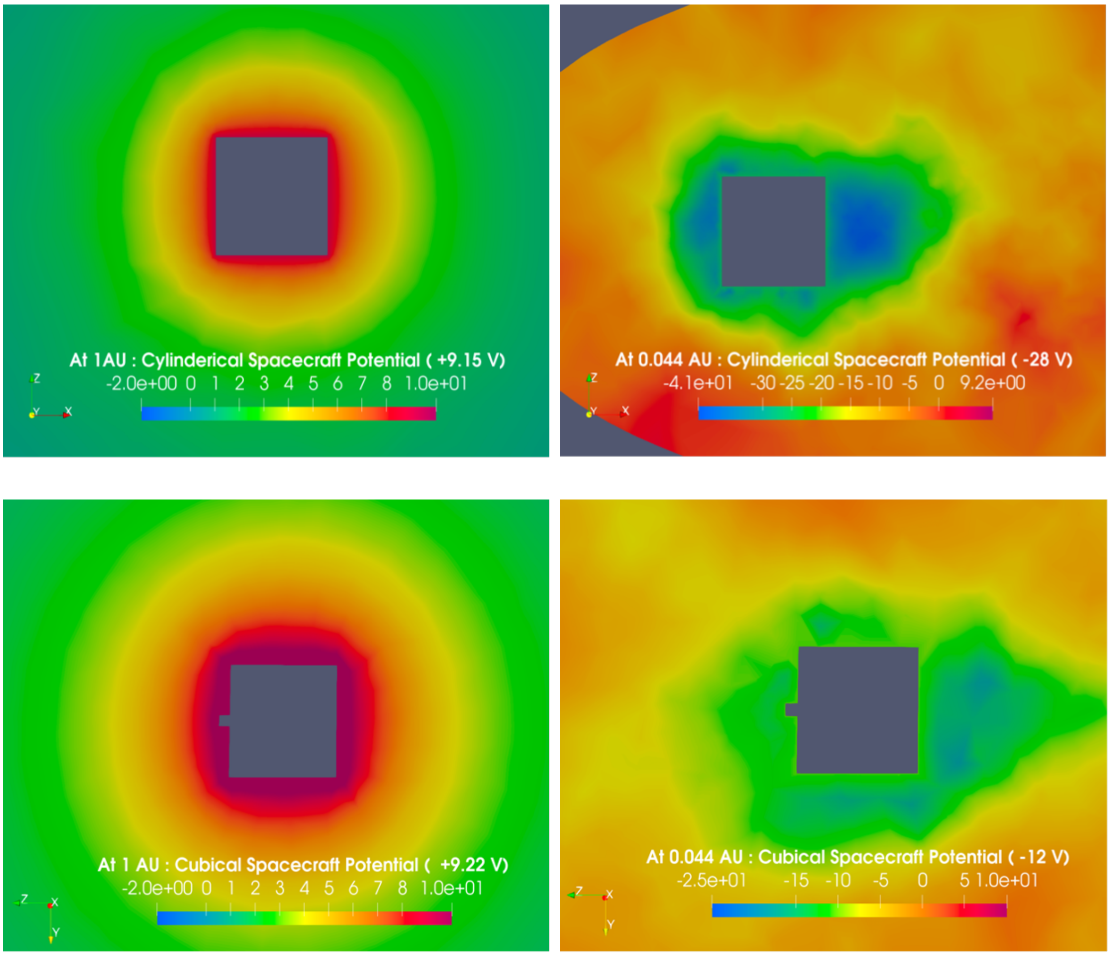

Figure C.2: Spacecraft potential distributions for cylindrical (1m in radius and 1 m long) and cubical geometries (1m x 1m x 1m) at 1 AU and 0.044 AU. The top panels show the potential for the cylindrical spacecraft to be (left) +9.15 V at 1 AU and (right) -28 V at 0.044 AU. The bottom panels show the potential of the cubic spacecraft to be (left) +9.22 V at 1 AU and (right) -12 V at 0.044 AU. sunlight is incident from the left side in both cases.

the ram, wake, and side structures of cylindrical and cubical spacecraft will be conducted in the future.

At 1 AU, both geometries exhibit very similar spacecraft potentials, with the cylindrical spacecraft reaching +9.15 V and the cubical spacecraft at +9.22 V. The large Debye length of 8 m at 1 AU, resulting from the lower plasma density of 10^6 m^{-3} of ambient ions and electrons, allows the emitted photoelectrons to dominate the charging process. The mean energy of the thermal electrons is low, leading to reduced secondary electron emission. It appears that the combination of small spacecraft size compared with the Debye length and relatively small secondary electron emission leads to the minimal difference in potentials between the cylindrical and cubical geometries at this heliocentric distance.

In contrast, at 0.044 AU, a significant difference in spacecraft potential is observed between the two geometries. The cylindrical spacecraft reaches a potential of -28 V, while the cubic spacecraft has a potential of -12 V. The variation in potential between the cylindrical and cubic spacecraft appears to arise from the Debye length at 0.044 AU, which is approximately 0.8 meters. This is nearly equivalent to the spacecraft size of 1 meter, resulting in significant differences in spacecraft potential by analogy with Figure C.1. Another possible reason involves the different surface areas and edge lengths for the two geometries, which plausibly influence the charge distributions. The cubic spacecraft, with its sharp edges, creates strong local electric fields that promote secondary electron emission, making its potential more positive compared to the cylindrical spacecraft. The cubic spacecraft has a total surface area of 6.0 square meters, with each face being 1 square meter. On the other hand, the cylindrical spacecraft, with a continuous smooth surface, collects more electrons, resulting in a much more negative potential. The cylindrical spacecraft has a surface area of approximately 12.6 square meters (considering a cylinder with length and radius of 1 meter). The curvature of the cylinder provides a larger collection area, which might be larger than the area exposed to the Sun due to projection effects, facilitating the collection of high-energy electrons. The larger collection area allows the cylindrical spacecraft to accumulate more charge, leading to a more negative potential.

These simulations and interpretations demonstrate the crucial role of spacecraft geometry in determining spacecraft potential across different environments, primarily dependent on the relationship between the Debye length and spacecraft size. At 1 AU, where the spacecraft size (1 m) is smaller than the Debye length (8 m), the geometry has minimal impact. However, if the spacecraft size exceeds the Debye length at 1 AU, which is greater than 8 meters, then the spacecraft potential will undergo significant variations. These findings emphasize the importance of considering the Debye length relative to the size of the spacecraft and its influence on the potential of the spacecraft.

C.3 Cubical Spacecraft with Solar Panels

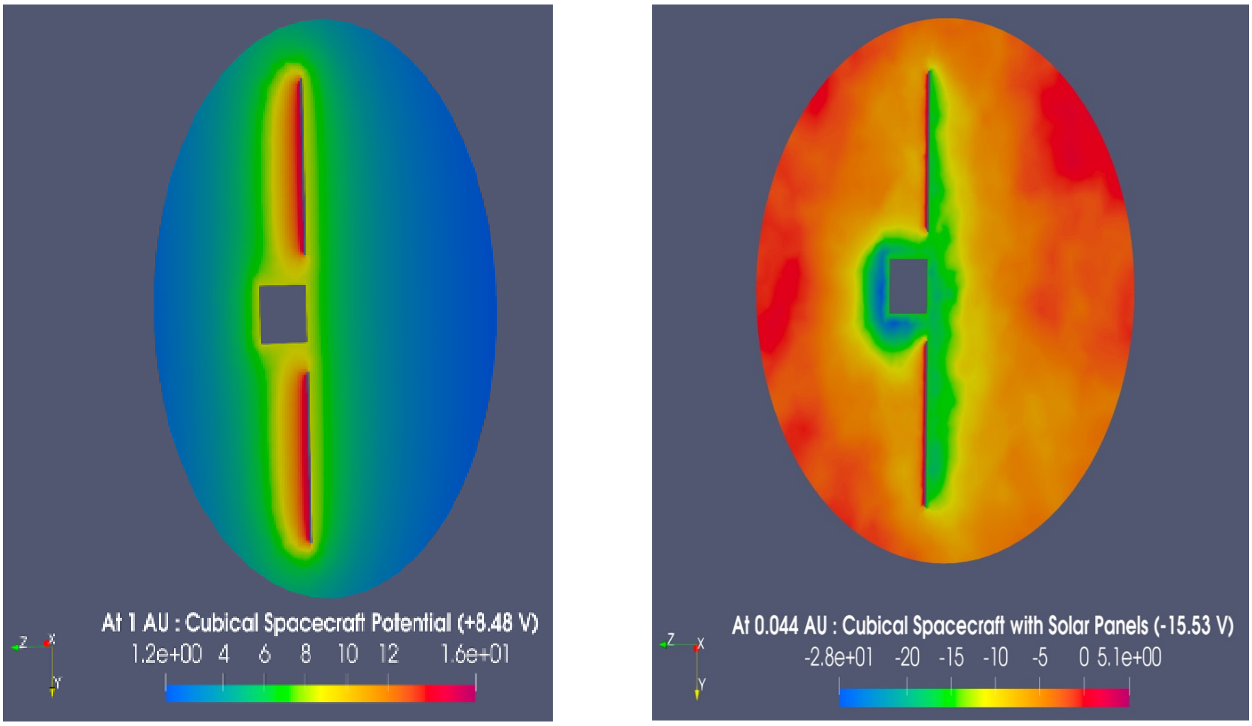

a. 1 AU b. 0.044 AU

Figure C.3: 2D potential distributions of a cubical spacecraft (1m in length, width, and height) with solar panels (3m in length, 1m in width, and 0.5 m in height) at 1 AU (left) and 0.044 AU (right). sunlight is incident from the left side in both cases.

Figure C.3 illustrates the potential distributions of, and around, a cubic spacecraft equipped with deployed solar panels in the solar wind at two distances from the Sun, 1 AU and 0.044 AU. The spacecraft and solar panels are each connected with a resistor of 5000 ohms, influencing the overall charging dynamics. The solar panel facing the Sun is referred to as the front side, while the opposite side is the backside. In both cases, the Sun is incident from the left side, as depicted in Figure C.3.

At 1 AU, the cubic spacecraft, equipped with solar panels, charges to +8.48 V. This value is slightly lower than the potentials of the simple cubic and cylindrical spacecraft (without solar panels), which are +9.15 V and +9.22 V, respectively, as shown in Figure C.2. Figure C.1 demonstrates that when the spacecraft size becomes comparable to or larger than 1/3rd or 1/8th of the Debye length, the spacecraft potential decreases approximately linearly with increasing size. In the present scenario, the addition of solar panels (3m in length, 1m in width, and 0.5m in height) increases the linear size (and surface area) of the spacecraft-solar panel system, making it comparable to the Debye length at 1 AU (8 m). Consequently, based on Figure C.1, the potential is expected to decrease, which it does to +8.48 V, compared to the simple cubic spacecraft (+9.15 V) and the simple cylindrical spacecraft (+9.22 V).

Notably at 1 AU, as depicted in Figure C.3's left panel, the potential of the front (Sunward, dielectric) side of the solar panel charges to +16 V, which differs considerably from the spacecraft surface potential (+ 8.48 V) and the potential (+8.48 V) of the backside (anti-Sunward, conducting) of the solar panels. This is believed to be primarily due to the use of non-conductive material on the front side of the solar panel and conductive material on the spacecraft surface and backside of the solar panel. Additionally, a resistor of 5000 ohms is placed between the spacecraft and the front side of the solar panel to restrict current flow from the solar panel and prevent damage to the spacecraft's electrical components.

Moreover, Figure C.3 illustrates the 2D potential distribution around the spacecraft - solar panels system. In the ram region, the spacecraft and the front side of the solar panel facing the Sun charge to positive potentials of +8.48 V and +16 V, respectively, owing to high photoemission. Conversely, in the wake region, both the spacecraft and the rear side of the solar panel charge to the same potential of approximately +8.48 V, given the uniform use of conductive material on both. The potential of the front side of the solar panel differs from that of the backside and the spacecraft surface. This difference arises primarily due to the presence of the resistor and secondarily due to the use of non-conductive materials. The resistor restricts the current flowing from the solar panel to the spacecraft. Meanwhile, non-conductive materials are less prone to accumulating charge compared to conductive materials, as they can more effectively dissipate accumulated charge, as detailed in Chapter 5.

In contrast, at 0.044 AU, the surface of the cubical spacecraft with the solar panels (as shown in the right panel of the Figure C.3), charges to -15.5 V, while the solar panel alone charges to +4 V. In this scenario, the Debye length at 0.044 AU is 0.8 m, equivalent to the spacecraft size but much smaller than the solar panels and the whole spacecraft - solar panels system, resulting in significant variations in spacecraft potential with geometry predicted based on sections II and III and Figures C.1 and C.2.

Furthermore, in Figure C.3's right panel, at 0.044 AU there is a noticeable presence of a strong electrostatic sheath enveloping both the spacecraft surface and the rear side of the solar panel. The phenomenon arises from the high thermal electron density and temperature, which dominate charging of the spacecraft and affect the surrounding plasma. In the ram region, the spacecraft surface facing the sunlight charges to approximately -27 V, attributed to a strong potential barrier that entraps photoelectrons and secondary electrons. Conversely, in the wake region, both the spacecraft surface and the rear side of the solar panel charge to around -19 V. The possible difference in the potential is due to the presence of photoemission on the ram side and its absence on the wake side, along with other factors like plasma flow dynamics and sheath formation. On other hand, the front side of the solar panel charges to a positive potential of 2 V due to the high photoelectron emission and thermal electron collection. Please find the detailed study in Chapter 5.

C.4 Conclusion

The simulation results at 1 AU and 0.044 AU from the Sun for cubical and cylindrical spacecraft highlight the dependence of spacecraft potential on size and geometry and the ambient electron Debye length. These results demonstrate how spacecraft potential is influenced by the Debye length in relation to spacecraft size for both cylindrical and cubical geometries at different heliocentric distances.

At 1 AU, for cylindrical and cubical spacecraft with sizes less than 1 meter, the potential remains relatively constant (within 10%) at around 9.2 V for both geometries. This stability is because the Debye length (8 meters) is significantly larger than the spacecraft size. In this scenario, the spacecraft's electric field does not significantly disturb the surrounding plasma, resulting in minimal variation in potential. However, as the spacecraft size increases to between approximately 1/8th and 1/3rd of the Debye length, the potential begins to decrease roughly linearly with increasing size. When the spacecraft size becomes comparable to or larger than the Debye length, the spacecraft's electric field can significantly perturb the surrounding plasma, causing noticeable variations in potential. Both cylindrical and cubical spacecraft exhibit similar trends, though cylindrical spacecraft tend to vary more at larger sizes than cubical ones, possibly due to their continuous, smooth surfaces facilitating higher electron collection.

Additionally, the study compared the spacecraft potentials for two geometries: a cylinder with a 1-meter radius and 1-meter length, and a cube with 1-meter dimensions in length, width, and height. In each case the surfaces are coated with Indium Tin Oxide and evaluated at 1 AU and 0.044 AU. At 1 AU, both cylindrical and cubical spacecraft charge to a constant potential of around +10 V because the Debye length is much larger than the spacecraft size. However, at 0.044 AU, significant variations in potential with geometry are observed, with cylindrical and cubical spacecraft charging to about -28 V and -12 V, respectively. This variation is primarily due to the Debye length at 0.044 AU (0.8 meters) being comparable to the spacecraft size, leading to noticeable differences. The difference in potentials between cylindrical and cubical spacecraft is also possibly due to the change in geometry; the sharp edges of the cubical spacecraft tend to develop strong electric fields, which enhance secondary electron emission and lower the negative potential.

Finally, at 1 AU, the addition of solar panels increases the surface area to a size comparable to the Debye length, leading to a slight decrease in spacecraft potential by 10 percent compared with simple cubic and cylindrical spacecraft. The spacecraft potential with the solar panels charges to +8.48 V, while the front and back sides of the panels charges to +16 V and +8.48 V, respectively. The change in spacecraft potential is consistent with the Debye length effect. In contrast, at 0.044 AU, the spacecraft potential charges to -16 V, compared to the simple cubic geometry at -12 V and the simple cylindrical geometry at -28 V, while the solar panel charges to +4 V. The significant variation is due to the Debye length of 0.8 m being much smaller than the solar panel-spacecraft system , which causes a substantial change in the spacecraft potential.Furthermore, the observed difference between the front and back sides of the solar panel is due to the resistor connection between the front side of the solar panel (non-conductive, Sunward) and the spacecraft, which limits current flow. Additionally, the use of non-conductive material on the front side tends to accumulate less charge compared to the back side of the solar panel (conductive, anti-Sunward).

References

Allen, Van et al. (1974). "The magnetosphere of Jupiter as observed with Pioneer 10: 1. Instrument and principal findings". In: *Journal of Geophysical Research* 79.25, pp. 3559–3577.

Amo, JA Gonzalez del and DM Di Cara (2022). "European Space Agency Electric Propulsion Activities". In: *European Space Agency, ESTEC, Keplerlaan* 1, p. 2200.

Ashkenazy, J et al. (2007). "Venμs technological payload-the Israeli Hall effect thruster electric propulsion system". In: *47th Israel Annual Conf. on Aerospace Sciences, Tel-Aviv & Haifa, Israel*.

Bame, SJ et al. (1993). "Magnetospheric plasma analyzer for spacecraft with constrained resources". In: *Review of Scientific Instruments* 64.4, pp. 1026–1033.

Bedingfield, Keith L and Richard D Leach (1996). *Spacecraft system failures and anomalies attributed to the natural space environment*. Vol. 1390. National Aeronautics and Space Administration, Marshall Space Flight Center.

Biagioni, Leonardo, Andrea Passaro, and Alessandro Vicini (2003). "Plasma Thruster Plume Simulation: Effect of the Plasma Quasi Neutrality Hypothesis". In: *34th AIAA Plasmadynamics and Lasers Conference*, p. 4173.

Capon, Christopher J, Melrose Brown, and Russell R Boyce (2016). "Charged aerodynamics of a low earth orbit cylinder". In: *AIP Conference Proceedings*. Vol. 1786. 1. AIP Publishing.

Carrington (1859). "Description of a singular appearance seen in the Sun on September 1, 1859". In: *Monthly Notices of the Royal Astronomical Society, Vol. 20, p. 13-15* 20, pp. 13–15.

– (1863). *Observations of the spots on the sun from Nov. 9, 1853, to March 24, 1861, made at Redhill, by Richard Christopher Carrington: Illustrated by 166 Plates*. Williams and Norgate.

Chen, FF (1965). *Chapter 4, in" Plasma Diagnostics Techniques", RH Huddlestone and SL Leonard, ed.*

Chopra, KP (1961). "Interactions of rapidly moving bodies in terrestrial atmosphere". In: *Reviews of Modern Physics* 33.2, p. 153.

Cranmer, Steven R (2009). "Coronal holes". In: *Living Reviews in Solar Physics* 6, pp. 1–66.

Cravens, Thomas E et al. (1997). *Physics of solar system plasmas*. Cambridge University Press Cambridge.

D'Azambuja (1952). "L'oeuvre de Bernard Lyot". In: *L'Astronomie, Vol. 66, p. 265* 66, p. 265.

Deprez (2024). *Personal communications with Gregory Deprez, technical expert of SPIS software*. Personal communication.

Dichter, Bronislaw K et al. (2015). “Specification, design, and calibration of the space weather suite of instruments on the NOAA GOES-R program spacecraft”. In: *IEEE Transactions on Nuclear Science* 62.6, pp. 2776–2783.

Divine and Garrett (1983). “Charged particle distributions in Jupiter’s magnetosphere”. In: *Journal of Geophysical Research: Space Physics* 88.A9, pp. 6889–6903.

Egeland (2009). “Kristian Birkeland: The first space scientist”. In: *Journal of atmospheric and solar-terrestrial physics* 71.17-18, pp. 1749–1755.

Ergun, RE et al. (2010). “Spacecraft charging and ion wake formation in the near-Sun environment”. In: *Physics of Plasmas* 17.7.

Filleul et al. (2021). “BepiColombo: A Platform for Improving Modeling of Electric Propulsion-Spacecraft Interactions”. In: *Frontiers in Space Technologies* 2, p. 639819.

Garner, Charles E and Marc Rayman (2013). “In-Flight Operation of the Dawn Ion Propulsion System Through Year One of Cruise to Ceres”. In: *49th AIAA/ASME/SAE/ASEE Joint PropulsionConference*, p. 4112.

Garrett (1981). “The charging of spacecraft surfaces”. In: *Reviews of Geophysics* 19.4, pp. 577–616.

Garrett and Hoffman (2000). “Comparison of spacecraft charging environments at the Earth, Jupiter, and Saturn”. In: *IEEE transactions on plasma science* 28.6, pp. 2048–2057.

GMSH (n.d.). URL: https://gmsh.info/.

Goebel, Ira Katz, and Ioannis G Mikellides (2023). *Fundamentals of electric propulsion*. John Wiley & Sons.

Goertz (1981). “The orientation and motion of the predawn current sheet and Jupiter’s magnetotail”. In: *Journal of Geophysical Research: Space Physics* 86.A10, pp. 8429–8434.

Golub, Leon and Jay M Pasachoff (2010). *The solar corona*. Cambridge University Press.

Gombosi, Tamas I et al. (2018). “Extended MHD modeling of the steady solar corona and the solar wind”. In: *Living reviews in solar physics* 15, pp. 1–57.

Gonzalez, WD et al. (1994). “What is a geomagnetic storm?” In: *Journal of Geophysical Research: Space Physics* 99.A4, pp. 5771–5792.

Gopalswamy, Natchimuthuk, S Sirajul Hasan, and Ashok Ambastha (2010). *Heliophysical Processes*. Springer.

Grard, Knott, and Pedersen (1983). “Spacecraft charging effects”. In: *Space Science Reviews* 34.3, pp. 289–304.

Guillemant (2014). “Study and simulations of spacecraft/plasma interaction phenomena and their effects on low energy plasma measurements”. PhD thesis. Université Paul Sabatier-Toulouse III.

Guillemant et al. (2012). “Solar wind plasma interaction with solar probe plus spacecraft”. In: *Annales Geophysicae*. Vol. 30. 7. Copernicus Publications Göttingen, Germany, pp. 1075–1092.

Gurnett, Donald A and Amitava Bhattacharjee (2005). *Introduction to plasma physics: with space and laboratory applications*. Cambridge university press.

Holmberg et al. (2019). “Simulations of JUICE spacecraft charging and its impact on particle measurements in Europa’s ionosphere and the Jovian magnetosphere”. In: *EPSC-DPS Joint Meeting 2019*. Vol. 2019, EPSC–DPS2019.

Holzer, Thomas E (1989). “Interaction between the solar wind and the interstellar medium”. In: *Annual review of astronomy and astrophysics* 27.1, pp. 199–234.

Johnson, Charles Y and Edith B Meadows (1955). “First investigation of ambient positive-ion composition to 219 km by rocket-borne spectrometer”. In: *Journal of Geophysical Research* 60.2, pp. 193–203.

Katz, I et al. (1979). “The capabilities of the NASA charging analyzer program”. In: *Spacecraft Charging Technology-1978*. Vol. 2071, p. 101.

Khurana et al. (2004). “The configuration of Jupiter’s magnetosphere”. In: *Jupiter. The planet, satellites and magnetosphere* 1, pp. 593–616.

Kohl, John L et al. (2006). “Ultraviolet spectroscopy of the extended solar corona”. In: *The Astronomy and Astrophysics Review* 13, pp. 31–157.

Köhnlein, W (1996). “Radial dependence of solar wind parameters in the ecliptic (1.1 $R_\odot$-61 AU)”. In: *Solar Physics* 169, pp. 209–213.

Kuninaka, Hitoshi and Jun’ichiro Kawaguchi (2011). “Lessons learned from round trip of Hayabusa asteroid explorer in deep space”. In: *2011 Aerospace Conference*. IEEE, pp. 1–8.

Lai (1989). “An overview of electron and ion beam effects in charging and discharging to spacecraft”. In: *IEEE Transactions on Nuclear Science* 36.6, pp. 2027–2032.

Lai and Cahoy (2016). “Spacecraft charging”. In: *Encyclopedia of Plasma Technology-Two Volume Set*. CRC Press, pp. 1352–1366.

Lai and Rezy Pradipta (2022). *Physics of Satellite Surface Charging: Causes, Effects, and Applications*. CRC Press.

Lang (2001). *The Cambridge encyclopedia of the Sun*.

– (2009). “Space weather”. In: *The Sun from Space*, pp. 337–405.

Langmuir, Irving (1960). *Surface Phenomena The Collected Works of Irving Langmuir*.

Lee, Juyoung et al. (2011). “Simulation of the spacecraft electric propulsion interaction on DubaiSat-2 using SPIS”. In: *32nd International Electric Propulsion Conference. Wiesbaden, Germany: 1EPC*, pp. 1–15.

Liu, Thomas M and Mitchell LR Walker (2013). "Integration of Electric Propulsion Systems with Spacecraft–An Overview". In: *The 33rd International Electric Propulsion Conference, The George Washington University, USA, Vol. IEPC*.

Loureiro (2010). *Modelling of plasma thruster plumes for spacecraft-plume impingement analysis*.

Meadows, Arthur Jack (2016). *Early Solar Physics: The Commonwealth and International Library: Selected Readings in Physics*. Elsevier.

Meitzler, Richard et al. (2023). "Investigating Europa's radiation environment with the Europa Clipper radiation monitor". In: *Space Science Reviews* 219.7, p. 61.

Mier-Hicks, Fernando and Paulo C Lozano (2017). "Spacecraft-charging characteristics induced by the operation of electrospray thrusters". In: *Journal of Propulsion and Power* 33.2, pp. 456–467.

Mikaelian, Tsoline (2009). "Spacecraft charging and hazards to electronics in space". In: *arXiv preprint arXiv:0906.3884*.

Miller, J Scott et al. (2002). "Xenon charge exchange cross sections for electrostatic thruster models". In: *Journal of Applied Physics* 91.3, pp. 984–991.

Mulen, EG et al. (1980). "P78-2 SCATHA environmental data atlas". In: *NASA. Lewis Research Center Spacecraft Charging Technol., 1980*.

Muranaka, Hosoda, and Iku Shinohara (2012). "Numerical Analysis of Potential Structure around Solar Sail in Solar Wind Plasma". In: *Transactions of The Japan Society for Aeronautical and Space Sciences, Aerospace Technology Japan* 10.ists28, Po_4_1–Po_4_6.

Na et al. (2019). "Numerical simulation of ion thruster plume to spacecraft charging". In: *2019 14th IEEE International Conference on Electronic Measurement & Instruments (ICEMI)*. IEEE, pp. 1555–1561.

Parker (1958). "Dynamics of the interplanetary gas and magnetic fields." In: *Astrophysical Journal, vol. 128, p. 664* 128, p. 664.

– (1963). "Interplanetary dynamical processes." In: *New York*.

Porst et al. (2017). "The RIT 2X propulsion system: current development status". In: *35th International Electric Propulsion Conference (08–12 October 2017*.

Priest, Eric (2014). *Magnetohydrodynamics of the Sun*. Cambridge University Press.

Roussel et al. (2008). "Modeling of FEEP plume effects on MICROSCOPE spacecraft". In: *IEEE transactions on plasma science* 36.5, pp. 2378–2386.

Rudolph (2012). *Spacecraft-plasma interaction modelling of future missions to Jupiter*.

Russell (2001). "The dynamics of planetary magnetospheres". In: *Planetary and Space Science* 49.10-11, pp. 1005–1030.

Sarrailh, Sebastien Hess, et al. (2022). “Multiscale simulations of plasma plume collection by solar array and erosion of interconnects”. In: *International Electric Propulsion Conference (IEPC) 2022*.

Sarrailh, Jean-Charles Matéo-Vélez, et al. (2015). “Spis 5: new modeling capabilities and methods for scientific missions”. In: *IEEE Transactions on Plasma Science* 43.9, pp. 2789–2798.

Sentís (2023). *Plume-Spacecraft Interaction Analysis: Study on the Plume Effects of Hall-Effect Thrusters (HET) and High-Efficiency Multistage Plasma Thrusters (HEMPT).*

Shan et al. (2015). “Numerical simulation of the interaction between Hall thruster CEX ions and SMART-1 spacecraft”. In: *Mathematical problems in engineering* 2015.

Shinde, Held, and Cairns (2022). “Simulation Study of Hall Thruster and their Effects on the Spacecraft at 1 AU and 0.093 AU”. In.

– (2023). “Charge-Exchange Plasma Effects of the SPT-100 Hall Thruster at Heliocentric Distances from 0.044 AU to 1 AU”. In: *AIAA SciTech 2023 Forum*, p. 1597.

– (2024). “A Comparative Study of Spacecraft Charging Effects with and Without Thrusters from 0.044 AU to 1 AU”. In: p. 1141.

Shinde, Held, Cairns, and Deprez (2024). “Hall Thruster Plume Effects on Spacecraft Charging from 0.067 AU to 1 AU”. In: *Authorea Preprints*.

Singh, Jagdev et al. (2011). “Proposed visible emission line space solar coronagraph”. In: *Current Science*, pp. 167–174.

Snyder, Conway W, Marcia Neugebauer, and UR Rao (1963). “The solar wind velocity and its correlation with cosmic-ray variations and with solar and geomagnetic activity”. In: *Journal of Geophysical Research* 68.24, pp. 6361–6370.

Sorensen, J (2006). *Solar Orbiter Environmental Specifications*.

SPIS - Spacecraft Plasma Interaction Software (n.d.). URL: https://www.spis.org/.

Spis User Manual (n.d.). URL: https://www.spis.org/download/1234.

Tajmar (2002). “Electric propulsion plasma simulations and influence on spacecraft charging”. In: *Journal of spacecraft and Rockets* 39.6, pp. 886–893.

Tajmar, Bernard Foing, et al. (2004). “Charge-exchange plasma contamination on SMART-1: First measurements and model verification”. In: *40th AIAA/ASME/SAE/ASEE Joint Propulsion Conference and Exhibit*, p. 3437.

Tajmar and Wang (2000). “Three-dimensional numerical simulation of field-emission-electric-propulsion neutralization”. In: *Journal of Propulsion and Power* 16.3, pp. 536–544.

Thiebault, Benoit et al. (2015). “SPIS 5.1: An innovative approach for spacecraft plasma modeling”. In: *IEEE Transactions on Plasma Science* 43.9, pp. 2782–2788.

Torkar, K et al. (2005). “Spacecraft potential control for Double Star”. In: *Annales Geophysicae*. Vol. 23. 8. Copernicus Publications Göttingen, Germany, pp. 2813–2823.

Torkar et al. (2001). "Active spacecraft potential control for Cluster–implementation and first results". In: *Annales Geophysicae*. Vol. 19. 10/12. Copernicus GmbH, pp. 1289–1302.

Vernazza, Eugene, and Rudolf Loeser (1973). "Structure of the solar chromosphere. Basic computations and summary of the results". In: *Astrophysical Journal, Vol. 184, pp. 605-632 (1973)* 184, pp. 605–632.

– (1976). "Structure of the solar chromosphere. II: The underlying photosphere and temperature-minimum region". In: *Astrophysical Journal Supplement Series* 30, pp. 1–60.

– (1981). "Structure of the solar chromosphere. III: Models of the EUV brightness components of the quiet Sun". In: *Astrophysical Journal Supplement Series* 45, pp. 635–725.

Vokhmyanin, MV and NV Zolotova (2018). "Sunspot positions and areas from observations by Galileo Galilei". In: *Solar Physics* 293.2, p. 31.

Waldmeier, M (1956). "Synoptische Karten der Sonnenkorona. Mit 16 Textabbildungen". In: *Zeitschrift für Astrophysik, Vol. 38, p. 219* 38, p. 219.

Wang (1997). "Ion Thruster Plume Plasma Interactions in the Solar Wind". In.

Wartelski, Carlos Ardura, et al. (2011). "The Assessment of Interactions between Spacecraft and Electric Propulsion Systems Project". In.

Wartelski, Christophe Theroude, et al. (2013). "Self-consistent simulations of interactions between spacecraft and plumes of electric thrusters". In: *33rd Int. Electric Propulsion Conf.* Citeseer.

Whipple Jr, EC (1976). "Theory of the spherically symmetric photoelectron sheath: A thick sheath approximation and comparison with the ATS 6 observation of a potential barrier". In: *Journal of Geophysical Research* 81.4, pp. 601–607.

Young et al. (2017). "Ageing Effects of a Hall Thruster Plume on Solar Array Performance and ESD Susceptibility". In: *35th International Electric Propulsion Conference*.

Zank et al. (2022). "The early history of heliospheric science and the spacecraft that made it possible". In: *Space Science Reviews* 218.4, p. 34.

Zirker, Jack B (1977). "Coronal holes and high-speed wind streams". In: *Reviews of Geophysics* 15.3, pp. 257–269.